Parametric Investigation of the Mechanical Response of Two-dimensional Composite Scarf Joints via Finite Element Modeling

by

Arsalan Adil

B.S., Aerospace Engineering
Mississippi State University, 2012

Submitted to the Department of Aeronautics and Astronautics
in partial fulfillment of the requirements for the degree of

Master of Science in Aeronautics and Astronautics

at the

MASSACHUSETTS INSTITUTE OF TECHNOLOGY

June 2015

Author .....
Department of Aeronautics and Astronautics
May 11, 2015

Certified by .....
Professor Paul A. Lagacé
Professor of Aeronautics and Astronautics and Engineering Systems
Thesis Supervisor

Accepted by .....
Professor Paulo C. Lozano
Associate Professor of Aeronautics and Astronautics
Chair, Graduate Program Committee

Parametric Investigation of the Mechanical Response of Two-dimensional Composite Scarf Joints via Finite Element Modeling

by

Arsalan Adil

Submitted to the Department of Aeronautics and Astronautics on May 11, 2015, in partial fulfillment of the requirements for the degree of Master of Science in Aeronautics and Astronautics

Abstract

A parametric investigation was conducted in order to characterize the mechanical response of two-dimensional composite scarf joints subjected to extensional loading, to determine the associated response sensitivities to joint parameters, and to establish the fundamental operative joint mechanics. The geometric parameters of equal scarf angles, adhesive thickness, and unequal scarf angles, and the laminate parameter of similar laminate configurations of both adherends of $[\pm\theta_2/0_2]_S$, $[\pm\theta/0]_{2S}$, and homogenized $[\pm\theta_2/0_2]_S$ (equivalently homogeneously orthotropic) were explored for values of θ of 45° and 15°. The ply regions of the laminates were modeled as transversely isotropic T700/2510 carbon/epoxy composite material, and the adhesive region as isotropic FM 300-2K polymer film adhesive. Linear elastic plane strain analyses were performed via finite element modeling. The results indicate that the overall mechanical response of two-dimensional composite scarf joints in the joint region is influenced by the global/macroscopic joint features of 'effective' through-thickness stiffness properties of the configuration in the joint region, and equilibrium considerations along the bondline, and by the local joint features manifested at the tips of the adherends at the ends of the joint region and through ply-by-ply level mismatch in stiffness properties within the adherend. The global peaks in the magnitudes of strains occur in the adhesive, and the distributions of strains in the adhesive essentially reflect the distributions of strains along the bondline in the adherend. The distributions of strains in the adherend along the bondline reflect the distribution of stiffness properties of the adherend through the thickness, and are governed by the local effects of mismatch in stiffness properties between the θ and 0° plies along with the lengthscale of the effective ply thickness. Sharp changes in the magnitudes of strains occur near the acute and obtuse tips of the adherend, and these are related to the overall lengthscales of the configuration and show similar aspects to those occurring in laminated structures with ply drop-offs. The magnitudes of strains show the greatest sensitivity to variations in the scarf angle of the configuration, increasing with increasing values of scarf angle and associated changes in bondline length, but show little sensitivity to variations in the adhesive thickness of the configuration. For the asymmetric configurations of unequal scarf angles, the response characteristics exhibit combined effects of variations in scarf angles and adhesive thickness, and exhibit significant asymmetry

in the cross-sectional distribution of far-field longitudinal strain. Recommendations for further work are presented.

Thesis Supervisor: Professor Paul A. Lagacé
Title: Professor of Aeronautics and Astronautics and Engineering Systems

Acknowledgments

No piece of work is solely a culmination of isolated endeavor. I feel obliged to express sincere gratitude to several people that have contributed through their influence to the development and completion of this research. First and foremost, I am particularly grateful to my research advisor, Professor Paul A. Lagacé, for imparting careful instruction, continuous supervision, and mentoring throughout the course of this research. I am grateful to my peers at TELAMS: Holly Jeffrey, Thomas Fronk, and Elizabeth Jones for providing diligent technical insights and supportive discussions. I found their association extremely beneficial.

In the course of my institutional affiliation with MIT, I have been inexplicably fortunate to have befriended extraordinary individuals who made this entire experience very fulfilling, and thus merit specific mention herein. I am particularly indebted to my friend Anas al-Bastami, who has often times transcended formalities and the peripheries of ordinary friendship to act as a sincere brother, and to him I offer my earnest gratitude. I am grateful to my friends Nasruddin Nazerali and Usman Ayyaz, whose fellowship has been a resourceful blessing during the course of my graduate study at MIT. In recollections external to MIT, I express my gratitude to Omar Shubailat, Muhammad Nadeem, Ibrahim Abdoulahi, and Harpreet Grewal, whose friendship has been invaluable over the past few years, and in whose fellowship transpired some of the most fondly memorable moments in the US with indelible memories to cherish. I cannot emphasize enough their influence and contribution to my person.

I offer my gratitude to Professor Haitham el-Kadiri, with whom I conducted research over a significant portion of the formative years of my undergraduate education. This naturally proved instrumental to my personal acquisition of scientific acumen and ultimately in the completion of this research.

Lastly, but most importantly, the completion of this work bears the signature of my family's support, encouragement, and motivation. To them I offer my most profound gratitude for bearing patiently my prolonged absence from home for over the past six years and more. My absence at imperative family occasions is heartfelt, and I can only hope this work may serve as an apt tribute to their endurance.

Dedication

I dedicate this work to my parents, Malik Waris Khokhar and Najma Waris, who persuaded me to embark on the high road of knowledge in pursuit of my academic ambitions in an unbeknown foreign land. Were it not for their prudent vision, uncompromising resolve for excellent education, and unwavering trust in my abilities, these words would never have been inked. This work is a fulfilling fruition to their innumerable prayers.

In The Name of God,

Most Gracious, Most Merciful. [Q:1:1]

Foreword

This work was performed at the Technology Laboratory for Advanced Materials and Structures (TELAMS) of the Department of Aeronautics and Astronautics at the Massachusetts Institute of Technology. This work was sponsored by The Boeing Company under the General Terms Agreement between MIT and Boeing as Boeing Award Number MIT-BA-GTA-1.

Table of Contents

List of Figures

List of Tables

Nomenclature

E	extensional modulus of adhesive
E_{eff}	effective longitudinal stiffness of scarf joint in joint region
E_{ii}	extensional modulus of ply in the i-direction (i = 1, 2, 3)
F_i	net force in the i-direction (i = 1, 3)
E_{xx}	effective longitudinal stiffness of laminated adherend
G_{ij}	shear modulus of ply in the i-j plane (i, j = 1, 2, 3)
L	length of scarf joint model
ΔL	distance between end of joint region and edge of scarf joint model
L_{joint}	length of joint region
t_a	adhesive thickness
$t_{adherend}$	adherend thickness
t_{ply}	ply thickness
u_{app}	prescribed displacement on boundary edge of model at x equal to L
x	axis along length of joint
x_a	joint axis in x-direction with origin at $(\Delta L + L_{joint})$
x_a^*	joint axis with normalized distances along x-axis in adherend 2 at arbitrary location in z
x_j	general joint axis parallel to bondline
x_{jbi}	joint axis along bondline i in adhesive (i = 1, 2)
x_{jbi}^*	joint axis with normalized distances along bondline i in adhesive (i = 1, 2)
x'_{jbi}	joint axis along bondline i in adherend (i = 1, 2)

x'^{*}_{jbi}	joint axis with normalized distances along bondline i in adherend (i = 1, 2)
x_{jm}	joint axis along midline of adhesive
x^{*}_{jm}	joint axis with normalized distances along midline of adhesive
y	axis along width of joint
z	axis along thickness of joint
$\{x, y, z\}$	Laminate/Joint Coordinate System
$\{x_1, y_1, z_1\}$	Ply Coordinate System
$\{X', Y', Z'\}$	FEM/Abaqus Coordinate System
α_i	scarf angle of adherend i (i = 1, 2)
ϵ_{ij}	tensorial strain component relative to the Joint Coordinate System (i, j = 1, 3)
ϵ^{∞}_{11}	average far-field longitudinal strain at model edge (x equal to L)
ϵ_{m}	normalized peak magnitude of strain in normalized isostrain contour field plot
ν	Poisson's ratio of adhesive
ν_{ij}	Poisson's ratio of ply in the i-j plane (i, j = 1, 2, 3)
σ_{ij}	tensorial stress component relative to the Joint Coordinate System (i, j = 1, 3)
σ^{∞}_{11}	average far-field longitudinal stress at model edge (x equal to L)

Chapter 1

Introduction

Advanced polymer matrix composites are an important class of materials that continue to be explored and researched for increased applications. These materials constitute of high strength/stiffness fibers embedded in a less stiff polymer matrix material that binds the fibers and provides inter-fiber load transfer capability. The aerospace industry, in particular, has invested significant attention towards the use of carbon fiber-reinforced composites over the past few decades. The motivation for such notable attention primarily originates from the savings in weight and favorable mechanical properties that carbon fiber-reinforced composites provide in comparison to the other main class of materials in use for practical structural applications in aircraft – metallic alloys. Composites are known for their high stiffness-to-weight and strength-to-weight ratios (ratio of material stiffness or strength to density), surpassing those of aluminum-based alloys. These are referred to as "specific" properties. This attribute of composites is perhaps the most favorable from the prospect of aerospace industrial applications wherein weight savings are prioritized.

Henceforth in this document the word "composites" will generally allude to advanced polymer matrix composites. A distinctive feature of these materials is the lack of material isotropy at the macroscopic level. This emerges from the micromechancial structural composition of these materials through the presence of fiber-matrix material combination. The carbon fibers in carbon fiber-reinforced composites are embedded in specific directions in the matrix material, and this directionality is indexed by

angular orientation, also known as ply angle. Plies of varying angular orientations are stacked over each other to yield a laminated composite, and this is generally the final form used for direct structural fabrication. This results in the presence of reinforced fibers in specified directions. This directional specification allows better load-carrying capability in these directions, whereas the capability in transverse directions is reduced due to lack of transversely reinforced fibers. Composites therefore essentially allow manipulation of directional strength in the structure. Similar issues apply to stiffness properties.

In recognition of such control over strength at the benefit of saving structural weight, aerospace companies such as Boeing and Airbus have indicated growing interest in the use of composites. As an example, the primary structure of the new Boeing 787 Dreamliner, including the wings and the fuselage, is fabricated from carbon fiber-reinforced composites on the order of 50% by structural weight [1]. This statistic is important to the commercial success of the proposed flagship airliner, since structural weight reduction directly relates to reduced fuel consumption and augmented range. In a rapidly advancing world where efficient energy consumption has become a key priority, such advancements in the aerospace industry are invaluable and imperative. This, however, is not the only benefit that composites bring forth. Composites also provide significant structural benefits by enhancing fatigue life of aircraft and eliminating modes of failure characteristic to metallic structures [2]. These benefits are, of course, realized during the operational service life of the aircraft. Composite strucutres do, however, introduce other modes of damage such as delamination, fiber-matrix debonding, and matrix cracking, that require special design considerations for prevention [3].

The existing knowledge base of composite materials and their structures is not as comprehensive and rigorous as that of metals. This is largely a consequence of the extent of experience, based in terms of time and broader applications, of metallic structures versus high grade advanced composites. For example, the research investment in the study of composites has gone up only since the 1970's and 1980's.

Aircraft and spacecraft structures in operational service are inevitably vulnerable

to structural damage, wear and tear, and degradation. Existing repair mechanisms for metallic structures can be directly applied to restore structural strength in laminated carbon fiber-reinforced composite structures. However, implementing such repair mechanisms may not yield similar results and design benefits for composites as it may for metallic structures. This can primarily be attributed to the essentially different natures of composite and metallic materials. Repair mechanisms therefore need to be investigated that work well for damaged composite structures. A repair of a composite structure may be considered as removal of damaged material within the structure followed by replacement with a patch of material of virgin strength. In other instances, there may not be any removal of material necessary and an overlay patch material of virgin strength may be sufficient.

Mechanically fastened or bolted joints find widespread use in metallic structures. Bolted joints are economical and simple to implement, and provide certain obvious advantages such as ability to disassemble the patch and parent materials, and relatively easy in-service inspection. However, bolting composite parts is not particularly advantageous. Drilling holes in composites can lead to significant structural degradation of the laminate. Holes are geometric features that give rise to stress concentrations in their close vicinity within the structure. Composites also exhibit poor bearing properties, and these compound with fatigue vulnerability of the bolts, in cases where they are metallic, to make bolted joints even more disadvantageous in composites [2]. Furthermore, additional fastening elements such as washers and spacers are required to prevent damaging the composite adherends when bolting them together. This inevitably causes increase in structural weight.

Mechanically fastened joints are not the only repair mechanisms in use for composite structures. Adhesive joints can also be used, and they provide various advantages over mechanically fastened joints, despite some of the problems associated with them. Adhesive bonding of composite structures can preserve the external contours and geometric features of the original structure after repair, and result in lighter joints as no metallic fastening components such as bolts and rivets are required. To date, adhesive joints have been predominantly employed in secondary load-bearing structural

elements, with some occasional use in primary load-bearing structural components of aircraft [2]. Adhesive joints generally result in significantly lower stress concentrations in the joint region in comparison to bolted joints. However, adhesive joints in composites do have their drawbacks. Strong and reliable adhesive joints require high quality surface preparation of adherends and strict process control. Adhesive joints do not permit simple in-service inspection or ability to disassemble, and therefore joint strength may be difficult to ascertain in any quantifiable way when the repaired structure is in operational service. In addition, adhesive joints may also impose geometric limitations for the structural components and may not be implementable for all structural geometries.

The structural behavior of one particular type of adhesive joint for laminated composites, namely the scarf joint, is explored in this study. The two main types of adhesive joint configurations in use for composites applications are the lap joint and the scarf joint. Each has its own advantages and disadvantages. Significant research has been conducted on lap joints, but existing knowledge about scarf joints between composite adherends is limited. This lack of a comprehensive knowledge base about composite scarf joints is an important motivation for conducting this investigation. A parametric study is performed to investigate the structural sensitivities of composite scarf joints to various geometric parameters and laminate configurations. The findings from this study can be potentially useful in practical applications wherein a more involved and comprehensive knowledge of composite scarf joints from a structural standpoint is required to furnish a reliable and feasible design. In the next chapter, some of the fundamental prior research that has been conducted in regard to composite scarf joints is reviewed along with a discussion of their associated implications and limitations.

Chapter 2

Previous Work

A review of prior studies and investigations relating to scarf joint repairs, and a discussion of the associated knowledge acquired from these works are presented in this chapter. This is followed by a discussion of the limitations of these works and the relevance of their findings in the context of motivation for undertaking this work.

There exists a considerable amount of literature involving work oriented towards understanding the structural characteristics of adhesively bonded scarf joints. Various technical aspects of the structural behavior of scarf joints have been explored. These aspects range from one parametric study of scarf joints to strength assessments, failure issues, and joint optimization. Most of the studies have focused on two-dimensional idealizations of scarf repairs, although some studies have also considered three-dimensional idealizations. A significant amount of prior work has been numerical in nature, and most of the findings are based on finite element modeling. Some analytical models for determining the stress and strain states in simple two-dimensional idealizations of scarf joints have also been developed. Such analytical models usually result in numerical or closed-form solutions to a set of governing ordinary differential equations for simple cases of two-dimensional scarf joints with homogeneously isotropic or orthoropic adherends and perfect scarf joint geometry, as presented later in Figure 3.1. Such analytical models lack the comprehensiveness to analyze cases of perturbed scarf joint geometries exhibiting physical issues such as manufacturing imperfections, or complicated cases wherein the adherends are lam-

inated composites with varying stiffness properties from ply to ply. Experimental investigations have also been presented in the literature relating to composite scarf joints. These investigations have focused mainly on establishing ultimate strength of composite scarf joints and exploring failure issues.

Some of the earlier studies on scarf joints can be traced back to Adkins and Pipes [4], who explore analytically the sensitivity issues involving mismatch in adherend stiffnesses and blunt adherend tips. More importantly, they adapt the analytic formulations of Erdogan and Ratwani [5] and of Reddy and Sinha [6] that model the adhesive as a shear-tension spring (originally due to Volkerson [7]), to cases of orthotropic laminated adherends with tip bluntness. The original adhesive shear-tension spring model studies indicate the possibility of producing uniform stress distributions in scarf joints with identical homogeneous adherends and that these homogeneous stresses are lower for smaller scarf angles. Adkins and Pipes have extended the analytic formulations to show that scarf joints with smaller scarf angles are highly sensitive to mismatch in adherend stiffnesses and adherend tip bluntness. Thus, the benefits of shallow scarf angles come at a cost. The solutions to their modified shear-tension spring equations exhibit boundary layer characteristics for small scarf angles and significant adhesive stress concentrations in the boundary layer. Similar modeling efforts have been carried out by Marcolefas et al. [8]. They have attempted to develop a method of analysis for the case of a metal-to-composite scarf joint in which the metal and adhesive exhibit nonlinear behavior. Their analysis results in the determination of the stress distribution in the joint through numerical solutions of the model equations under tensile and compressive loading. Additionally, they propose a case-specific failure criterion for the scarf joint considered. Gleich [9] provides an analytical study of a two-dimensional scarf joint configuration involving identical isotropic adherends of similar lengths and thicknesses. The adherends are modeled as plates with bending and extensional stiffnesses, and the adhesive as an elastic layer with uniform stresses across its span. The resulting governing differential equations are then solved numerically through finite difference discretization for shear and peel stress distributions in the joint.

Gunnion and Herszberg [10] have performed a structured parametric study of composite scarf joints through finite element modeling. The study investigates the stress distribution along the adhesive bondline and shows the dependence of peak values to perturbations in scarf angle, adhesive thickness, ply thickness, laminate thickness, and variations in laminate configurations and over-laminates. The joint configuration with an over-laminate can be considered as comprising a standard scarf joint with an overlapping laminate on the top or bottom of both adherends, covering the adhesive region adhering the adherends, and extending to some finite distance over the adherends. Their overall findings indicate that the average peel and shear stresses along the bondline are not affected by the stacking sequence, laminate thickness, adhesive thickness, and mismatched stiffnesses of the adherends. An increase in the scarf angle causes an increase in the average peel stress at the bondline but a reduction in the average shear stress. The use of over-laminates results in a reduction of both the average peel and shear stresses at the bondline.

Wang and Gunnion [11] further investigate the adequacy of the two-dimensional idealization of a composite scarf joint in assessing the performance of a scarf joint. They propose a design methodology for scarf joint repair in composite structures by adopting strain-based failure criteria for the adhesive (maximum strain) and composite adherends (von Mises strain) to yield improved designs for strength. Harman and Wang [12] have attempted to optimize the scarf profile in cases involving scarf joints between adherends of dissimilar moduli in the sense of having uniform stress distributions within the adhesive to endow equal load-bearing capability to the entire adhesive region by design in expectation of enhanced joint strength and reduction in the amount of required material removal. Other attempts of optimization of scarf joint configuration include that of Breitzman et al. [13]. Their work has focused on the composition of the repair patch and they have attempted to determine optimal patch ply stacking sequences that minimize the von Mises stress in the adhesive region.

Other notable efforts directed towards the study of scarf joints include consideration of laminated orthotropic composite adherends with significant focus on damage

and strength assessment of composite scarf joints. Of these efforts, Kumar et al. have tested CFRP (carbon fiber-reinforced polymer) composite scarf joints for failure in uniaxial tension and compression [14, 15]. CFRP composite scarf joints were subjected to compresive and tensile loads until failure occurred. The ultimate compressive and tensile joint strengths were determined. It was observed that the ultimate tensile and compressive joint strengths decreased monotonically with increasing scarf angle. The failed specimens were also imaged through scanning electron microscopy. It was observed that the failure mechanism that dominates in compressive failure in scarf joints for cases of scarf angles of less than 3° is fiber microbuckling. For larger scarf angles, cohesive shear deformation of the adhesive film was more dominant in causing failure. For the case of uniaxial tension, the dominant failure mode for scarf angles of less than 2° was fiber fracture and pull-out. For larger scarf angles, tensile failure was observed to be caused by cohesive shear failure of the adhesive film. Finite element modeling was also performed wherein the adherends were modeled as homogeneously orthotropic continua and failure strengths were predicted by prescribing a failure criterion combining aspects proposed by Hashin [16] and Lee [17]. Goh et al. [18] have conducted experiments to determine the effects of bondline flaws, such as disbonds, on the load-bearing capability of scarf joints. Their results reveal that the load-bearing capability of scarf joints decreases with increasing size of bondline flaw at a faster rate than with the decrease in effective bonding area. Fractographic analysis also revealed that fracture occurred in the matrix of the composite adherend adjacent to the adhesive-adherend interface at a distance equal to a small fraction of a ply thickness. Kim et al. [19] have explored the interaction of laminate damage in the adherend with disbonding in the adhesive to combined in-plane and impact loading. Their findings reveal that composite scarf joints experience impact damage due to a combination of adhesive disbonding and matrix cracking, and that the damage size increases with increasing levels of in-plane pre-strain loading. Additional investigations of strength and failure assessments include the study of Kawakami and Feraboli [20] regarding lightning strike damage resistance and tolerance of composite scarf joints, and the experimental work of Jen [21] on fatigue life evaluation of scarf

joints.

Other studies have investigated the onset of failure in composite scarf joints by implementing cohesive damage models for ductile adhesives using finite element modeling. Damage models were implemented to simulate damage onset and growth in the adhesive to match empirical evidence of mixed mode interlaminar-intralaminar failure established through experimentation of small angle specimens [22]. Elastic finite element analyses were performed using cohesive laws determined from inverse methods for pure modes to identify critical regions where damage initiation could occur. Pinto et al. [23] performed further strength analysis through finite element modeling of three-dimensional scarf joints with repair width, scarf angle, and overlay plies as variable parameters. Particular studies have also been performed to characterize the performance of three-dimensional scarf joints with circular patches [24].

Kimiaeifar et al. [25] performed work to quantify the reliability of scarf joints by using a probabilistic model. The reliability is assessed through a design equation depending on partial safety factors and material properties and loads. The ultimate goal of the work is to predict a reliable probability of failure using scarf angle, failure criterion, and load.

In the existing literature on scarf joints, a distributed range of technical aspects has been explored. Analytical formulations of simple scarf joint idealizations with homogeneous isotropic adherends that furnish stress distributions within the joint are pursued, as well as numerical work to determine stress fields along the adhesive bondline using finite element models. In the case of numerical work, the variation of stress distribution in the adhesive with certain joint parameters such as scarf angle, adhesive thickness, ply thickness, laminate thickness, over-laminates, and adherend laminate configurations has been considered in one study [10]. The two important conclusions from this study indicate low sensitivity of adhesive stresses to mismatched adherend laminate configurations and significant reduction in peak stresses with use of over-laminates. The other results presented involve a qualitative assessment of the effects of the studied joint parameters on the average and peak stresses, but only at the bondline. General conclusions, however, cannot be drawn about the underlying

mechanics of load transfer in composite scarf joints and their mechanical response. Overall, the bulk of the previous work performed on scarf joints, however, focuses on strength and failure issues regarding scarf joints and optimization of scarf joint configuration.

Most of the existing literature on composite scarf joints does not address a significant number of issues required to comprehensively characterize the mechanical behavior of composite scarf joints. What can be noted is the lack of systematic parametric studies of composite scarf joints and investigations into the structural response dependency on the associated composite scarf joint parameters. Thus, there is a need to develop a fundamental understanding of composite scarf joint mechanics. Furthermore, while there has been substantial work directed towards the optimization of scarf joints, this has generally been conducted around specific configurations and without defining the qualitative or quantitative reasons that drive the optimization in the context of design of a scarf joint. The motivation for current work is therefore to address this knowledge gap and to undertake a study of composite scarf joints so as to provide a characterization of their mechanical behavior, and thereby produce a technical knowledge base to facilitate design of composite scarf repairs for practical applications.

Chapter 3

Objectives and Approach

The overall objectives of this work and the definition of the problem investigated, along with an outline of the approach and modeling considerations involved in addressing the problem, are presented in this chapter. Section 3.1 includes a discussion of the primary objective of this study and the approach undertaken to attain the primary objective. The two-dimensional composite scarf joint geometric configuration is presented in Section 3.2 along with the definition of pertinent joint parameters. This is followed in Section 3.3 by a detailed discussion of the selection and quantification of joint parameters chosen for investigation in this work, including the associated reasons for the specific choices.

3.1 Overall Objective and Approach

An account of the existing knowledge about scarf joints is provided in the previous chapter and the literature reviewed therein. Guided by the survey of existing literature, a systematic and structured investigation of the mechanical response of scarf joints with consideration of various joint parameters was undertaken in this work. The mechanical response is defined to be the stress and strains fields occurring in the joint when subjected to a prescribed loading condition such as a uniform extensional displacement.

The principal objective of this study is to determine key parameters and their

influences on the mechanical behavior of a two-dimensional composite scarf joint. As indicated, the mechanical behavior in this work is defined as the stress and strain states occurring within the adherends and adhesive material in the structural configuration subjected to a uniform extensional displacement. Proper characterization of the mechanical response of two-dimensional composite scarf joints requires an accurate and representative identification of the physical joint parameters to which the response may be sensitive. Parameters of geometric and material nature relating to the two-dimensional composite scarf joint were thus considered in this work in order to characterize the mechanical response and the related sensitivities. Linear static plane strain analyses were used with varying geometric and material configurations to account for the variations in the joint parameters. The reasons for the choices of the various aspects of the approach are subsequently described.

For the purpose of simplicity, the foremost recognition to be made is that the primary response characterization can be made by investigating a two-dimensional idealization of the scarf joint profile. This should provide a fundamental level of understanding about the mechanical behavior of a composite scarf joint, and particularly in determining the influence of various parameters on the joint response. The methodology for response investigation and characterization can then be extended to study three-dimensional configurations and response differences subsequently compared. This will naturally allow for a more convenient design analysis approach once the scarf joint responses from both types of analyses are used in conjunction with possible experimental results. In cases where numerical methods are used, a two-dimensional analysis can be more computationally economical than a three-dimensional one. The two-dimensional composite scarf joint geometry considered in this study is presented in Section 3.2. It is expected that the two-dimensional geometric configuration, as depicted in Figure 3.1, is a representative reduction of the three-dimensional scarf repair that may find typical use in aircraft wing skins and structural elements with similar external geometric features. It is thus particularly relevant to investigate the mechanical response of two-dimensional composite scarf joints to static extensional loading.

Polymeric adhesives used in scarf joints possess extensive load-bearing capability when deforming in their nonlinear stress-strain regime. Aircraft structures, however, are designed to experience deformation strictly in the elastic regime. The entire structure must deform only elastically to react out the loads it is subjected to during its entire service life. Under such consideration, a primary aspect regarding the mechanical response of a two-dimensional scarf joint that must be addressed is its mechanical behavior within the elastic regimes of the adhesive and the adherends when subjected to extensional loading. In order to pursue a comprehensive characterization of the mechanical response of scarf joints and exploit the full load-bearing capability of the adhesive, the mechanical response in the nonlinear stress-strain regime of the adhesive may also be investigated subsequently in order to fully assess the complete design potential of scarf joints. In this work, exploration was limited to the mechanical response of two-dimensional scarf joints in the linear stress-strain regime of the adhesive and the adherends in order to establish initial understanding of the baseline response.

In the two-dimensional case, the physical deformation of the joint is assumed to occur only in the two-dimensional plane of consideration (plane strain deformation), and all strains in the third direction, the y-direction, are consequently equal to zero. The problem under investigation is then essentially a plane strain linear elasticity problem with prescribed boundary conditions of uniform extensional displacements and material definitions varying from ply to ply within the laminated composite adherends and from adhesive to ply across the adherends. This permits investigation of the baseline response sensitivities to the joint parameters.

The domain over which the solution to this elasticity problem is sought is simply the two-dimensional geometry of the composite scarf joint. The complications in the geometry of the composite scarf joint introduced through the presence of the adhesive region and the variation of material properties over the joint domain are prohibitive to determining a closed-form analytical solution to the problem. Therefore, numerical solutions to the governing equations must be sought. Finite element analysis is currently the most commonly used numerical technique in obtaining such numerical solutions, particularly in relation to performing structural analyses for most practical

purposes.

Two-dimensional finite element models were used in this work to investigate the mechanical response and load transfer mechanisms of composite scarf joints in relation to various geometric and material parameters. This will provide a technical foundation that can serve as a basis for designing composite scarf joints for practical applications and provide fundamental insight into the mechanics of load transfer within the joint.

3.2 Two-dimensional Composite Scarf Joint Configuration

The definition of the geometric configuration of the two-dimensional composite scarf joints investigated in this work is described in this section. This geometric configuration is shown in Figure 3.1 and is formulated to address the overall objective and associated approach of the study, as discussed in Section 3.1.

Definitions of the geometric parameters associated with the two-dimensional composite scarf joint configuration shown in Figure 3.1 are provided subsequently. The total geometric length of the joint along the x-axis is denoted by L. The length along the x-axis spanning only the joint region, that is the region between the extremities of the adhesive along the x-axis, is denoted by L_{joint}.

The adherends are both laminated composites, although they need not be necessarily identical in configuration. They were, for this work, however, defined to possess similar laminate configuration and thickness (equal ply count and ply thickness), which is denoted by $t_{adherend}$ in Figure 3.1. Adherends with identical laminate configurations ensure that the stiffness mismatch does not play any role in the mechanical response sought in this investigation. The laminate thickness was preserved invariable in order to avoid inducing geometric eccentricity in this work. It is noted that such geometric eccentricity can exist practically due to manufacturing imperfections, or for design measures. The adhesive thickness is denoted by t_a.

The scarf angles for the joint are denoted by α_1 and α_2, with the subscript corre-

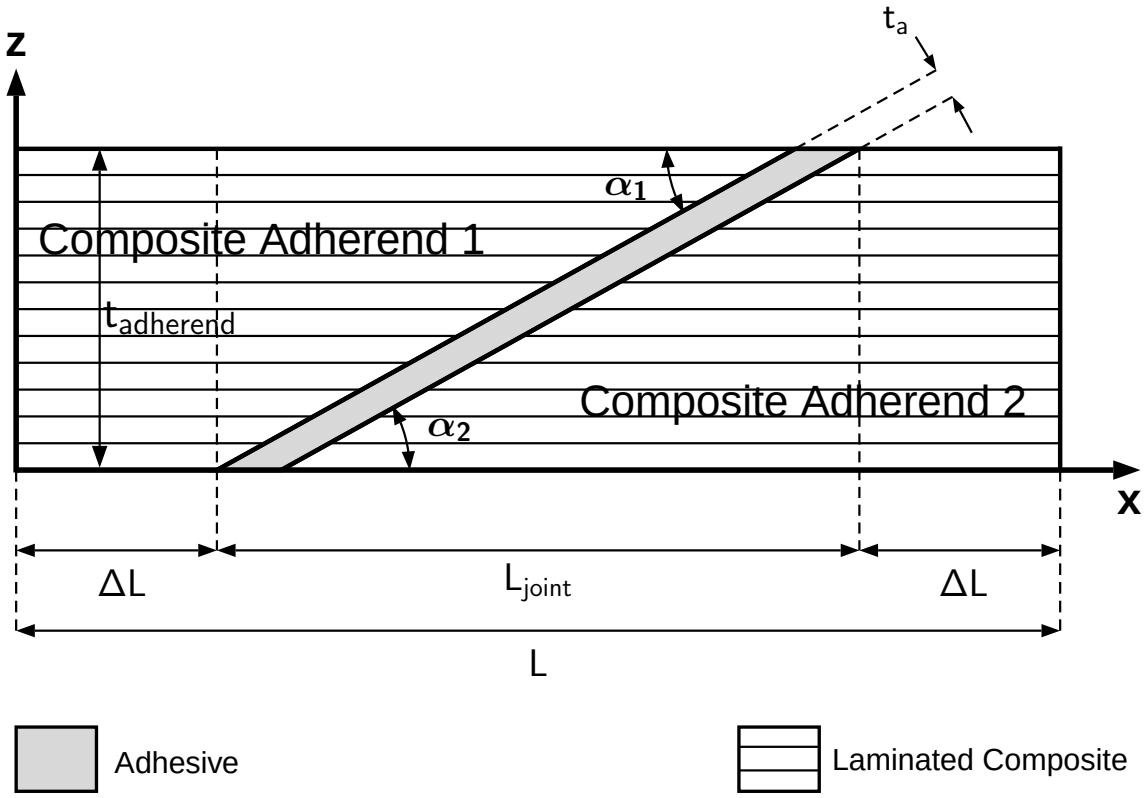

Figure 3.1 Two-dimensional composite scarf joint geometry.

sponding to the associated composite adherend. The scarf angles for either adherends may not be equal as well. Again, this can be attributed to manufacturing imperfections, or a result of design issues. Such a situation is parameterized by varying the values of the unequal scarf angles, α_1 and α_2, as shown in Figure 3.1. In this work, the scarf angle α_1 was always set to 10°. This situation will also have a varying adhesive thickness (t_a) along the scarf line. As the adhesive thickness varies in the case of unequal scarf angles along the scarf length, it was defined in this work to have a minimum value of 0.008 in at the base of the joint for the cases of (10°, 8°) and (10°, 9°), and at the top of the joint for the cases of (10°, 11°) and (10°, 12°). This implies that the adhesive thickness increases along the scarf length from a minimum value of 0.008 in from the base for the first two cases of unequal scarf angles, but from a minimum value of 0.008 in from the top of the joint for the latter two cases. For the case of equal scarf angles, the joint length (L_{joint}) is related to the geometric parameters of laminate thickness ($t_{adherend}$), adhesive thickness (t_a), and scarf angle ($\alpha = \alpha_1 = \alpha_2$) through Equation 3.1:

$$L_{joint} = \frac{t_{adherend} \cos\alpha + t_a}{\sin\alpha}. \tag{3.1}$$

The characterization of the mechanical response was developed through the classification of the stress and strain states within the joint for the parameters defined in the next section. A discussion of the considerations involved and the approach adopted in selecting and quantifying the parameters for this investigation is presented in the next section.

3.3 Selection and Quantification of Scarf Joint Parameters

Numerous parameters related to a two-dimensional scarf joint can be identified to which the mechanical response may be sensitive. These may be related to the geometry of the scarf joint or the material that constitutes the scarf joint. In this

Table 3.1 Table of two-dimensional composite scarf joint parameters investigated

Parameter Considered	**Parameter Values**		
	t_a [in]	**α**	**Laminate**
Baseline	0.008	10°	$[\pm 45_2/0_2]_S$
α	0.008	5° 15°	$[\pm 45_2/0_2]_S$
α unequal (α_1, α_2)	0.008 (min)	(10°, 8°) (10°, 9°) (10°, 11°) (10°, 12°)	$[\pm 45_2/0_2]_S$
t_a	0.004 0.006 0.010 0.012	10°	$[\pm 45_2/0_2]_S$
Laminate	0.008	10°	$[\pm 15_2/0_2]_S$ $[\pm 15/0]_{2S}$ $[\pm 45/0]_{2S}$ *Homogenized** $[\pm 45_2/0_2]_S$ *Homogenized** $[\pm 15_2/0_2]_S$

* Note: Stiffness values of adherend set to be homogeneously orthotropic from Classical Laminated Plate Theory for indicated laminate with no spatial variation within adherend.

work, in order to provide a well-defined scope of study and to establish fundamental knowledge about the mechanical behavior of two-dimensional composite scarf joints, four parameters were identified and selected for investigation. These are three geometric parameters, the scarf angle of each adherend, α_1 and α_2, and the adhesive thickness, t_a, and one material parameter, the adherend laminate configuration. The two scarf angles were considered in a manner to investigate geometric configurations with equal scarf angles ($\alpha = \alpha_1 = \alpha_2$) and unequal scarf angles (α_1, α_2).

The model parameters that were explored were selected with the aim of fulfilling the primary objective of this study of determining the key parameters and their influences on the mechanical behavior as elicited through the stress and strain fields. The basic joint response was initially established by setting and investigating a baseline case. The specifications of this baseline case were chosen in relevance to typical practical applications and earlier studies. For the baseline case, the following parameters were chosen: equal scarf angles of α_1 and α_2 equal to 10°, an adhesive thickness value of 0.008 in, and identical 12-ply laminate adherends with a laminate configuration of $[\pm 45_2/0_2]_S$. A balanced and symmetric laminate configuration for the baseline case was selected for practical purposes. This was done in order to investigate the behavior of laminates commonly employed in industrial practice where only plies of 0°, ±45°, and 90° orientations are generally considered. As all cases investigated in this study are two-dimensional and not subjected to any transverse (out-of-plane) loading, the 90° ply orientation was thus eliminated from all adherend configurations considered. Balanced and symmetric configurations find particular use in practical applications as a result of their favorable mechanical properties brought about by balance of ply orientations and symmetry about the laminate mid-plane. This case is indicated in Table 3.1 and is the one from which changes in parameters were worked. The adhesive material was selected to be FM300-2K polymer film adhesive, and the carbon/epoxy composite material for the adherends was selected to be T700/2510. These choices were based upon availability and industrial usage of such materials in existing applications. The physical value of the adhesive thickness of 0.008 in was selected for the baseline case, which is the manufactured physical thickness of the film adhesive [26].

Similarly, the cured ply thickness (t_{ply}) for T700/2510 carbon/epoxy composite material is 0.006 in [27]. This results in a laminate thickness of the adherends ($t_{adherend}$) of 0.072 in for a laminate of twelve plies.

Parametric variations from the baseline case were chosen with various increments in values based on consideration of typical applications, prior work, and practical issues. Each parameter was varied individually in each case while maintaining the others invariable. This allows the sensitivity to each parametric variation, as manifested in the stress and strain fields within the joint to be addressed individually, relative to the baseline case. The various parametric cases considered are all listed in Table 3.1.

Initially, two different cases based on selected increments for each parameter were examined in order to establish first order assessment of the influence on the mechanical response. The increments for the geometric parameters were chosen in consideration of practical issues that may cause such variations in reality, such as manufacturing imperfections. In such situations, the deviation in these parameters is expected to be within a reasonable percentage of the original value of the parameter. These increments are therefore an estimation of such deviations from original values that are expected to occur in practice. Thus, scarf angle increments of 5° were chosen to investigate the response sensitivity to (equal) scarf angle variation in the initial phase. The 5° increment size was chosen in order to investigate sensitivity issues in the mechanical response of two-dimensional composite scarf joints and also allow for modeling convenience in conjunction. This results in scarf angles of 5° and 15°, in addition to the baseline case of 10°. The mechanical response sensitivity to unequal scarf angles were explored with a 20% difference between scarf angles in the preliminary stage. This results in unequal scarf angle configurations of $(10°, 8°)$ and $(10°, 12°)$. The results can thus be compared to those for the baseline case of equal scarf angles to discern the influence of unequal scarf angles on the mechanical response. The adhesive thickness was varied by 50% increments of the baseline thickness value of 0.008 in. This results in adhesive thicknesses of 0.004 in and 0.012 in along with the baseline value of 0.008 in.

The parametric variations in laminate configurations from the baseline case are $[\pm 15_2/0_2]_S$, $[\pm 45/0]_{2S}$ and $[\pm 15/0]_{2S}$. The effect of effective ply thickness stacking sequence on the mechanical response of scarf joints was investigated along with variation of off-axis ply orientation angles. The 15° ply orientation was chosen in addition to the 45° orientation for investigation because its presence renders the laminate particularly susceptible to delamination issues [28]. In addition, the presence of 15° ply orientation allows for investigation of influence of varying longitudinal and transverse stiffnesses compared to the 45° case. The use of 15° plies also significantly reduces the ply stiffness mismatch within the laminate compared to the 45° case.

After initial characterization and examination of influence from results from these cases, another set of complementary values for the joint parameters were chosen for response investigation where more refined steps were identified to be needed in order to fully capture the influence of the particular parameter. The results from the entire study were then analyzed in conjunction in order to characterize the response sensitivities of two-dimensional composite scarf joints. For those parameters where this was indicated to be needed, half of the previous increment size was used. This was done for the cases of unequal scarf angles and adhesive thickness, resulting in unequal scarf angle values of $(10°, 9°)$ and $(10°, 11°)$ (10% deviation from baseline), and adhesive thickness values of 0.006 in and 0.010 in (25% deviation from baseline).

In addition to actual laminates, the response to homogeneously orthotropic elastic adherends was also explored. This was done in order to isolate the effects of homogeneous material orthotropy from ply-to-ply stiffness variation in the laminated adherends. Two homogeneously orthotropic adherend cases were thus chosen such that the stiffness properties correspond to the effective homogeneously orthotropic stiffness properties of the laminates of $[\pm 45_2/0_2]_S$ and $[\pm 15_2/0_2]_S$. These cases form a third set wherein the ply stiffness mismatch is completely eliminated and its influence is thereby explored through comparison with the former cases. The ply stiffness mismatch is maximum for the case of $[\pm 45_2/0_2]_S$ and intermediate for the case of $[\pm 15_2/0_2]_S$.

Chapter 4

Finite Element Modeling

The basic findings of this work and the ensuing discussions draw entirely from the results of the finite element models for the parametric cases of two-dimensional composite scarf joints discussed in Section 3.3. This chapter entails discussions of the details of the finite element modeling performed in this work. This includes a discussion of the approaches, assumptions, and considerations involved in assembling the finite element models, keeping in view the needed level of fidelity in order to generate response characterization from the model results that is well representative of actual composite scarf joints. The typical finite element model geometry is presented and discussed in Section 4.1. A discussion of the material properties and considerations in modeling the composite plies and adhesive follows in Section 4.2. The details of formulating the prescribed boundary conditions applied to all finite element models are discussed in Section 4.3. Section 4.4 involves a discussion of the discretization aspects of the finite element models, including the type of elements employed and the mesh density used in the laminate and adhesive regions. All finite element modeling was performed using the computer-based finite element analysis suite Abaqus [29], and the models involved linear static plane strain analyses. Finally, an assessment of model lengths through comparison of the far-field longitudinal strains is presented in Section 4.5

4.1 Model Geometry

Most of the geometric dimensions for all finite element models were determined by the physical material dimensions such as ply thickness (t_{ply}), adhesive thickness (t_a), and the choice of parameters. These are noted for each case considered in Table 3.1. The dimensionalized geometry of a typical two-dimensional composite scarf joint finite element model can be related to the physical characterization shown in Figure 3.1. The laminate thickness, $t_{adherend}$, was preserved as an invariable parameter across all the cases studied as a consequence of choosing 12-ply laminated adherends composed of the same composite material (T700/2510) for all cases. The joint length, which is a function of the scarf angle, adhesive thickness, and laminate thickness, was determined through Equation 3.1 and its appropriate adaptations for the case of unequal scarf angles for the various models. The relation reveals that the joint length is variable and must change as the scarf angle and adhesive thickness are varied.

The length ΔL, as shown in Figure 3.1, is the distance between either of the vertical edges of the configuration and the joint region where the adhesive layer exists. The length ΔL must vary if L, the total model length, is to be kept constant. Alternatively, ΔL may be kept constant while L is allowed to vary. In this work, ΔL was kept constant and chosen to be three times the laminate thickness, $t_{adherend}$, in all cases. This gives a value of ΔL equal to 0.216 in. This was done in order to ensure that the distance ΔL was sufficiently large in order to allow the strain state outside the joint region to lose the effects introduced by the presence of the adhesive region in the joint and become sufficiently uniform through the thickness of the configuration at the far-field location where the uniform displacements are applied. A discussion of the resulting far-field strains for all the models is presented in Chapter 5, and an assessment of the length, ΔL, in this regard is presented in Section 4.5. The resulting dimensions of L_{joint} and L are given in Table 4.1 for all finite element models. The total length of the model, L, is found through Equation 4.1:

$$L = L_{joint} + 2\Delta L. \tag{4.1}$$

The geometric dimensions α, (α_1, α_2) for the case of unequal α's, t_a, t_{ply}, and $t_{adherend}$ for all finite element models are given in Table 3.1 as per the parametric choices.

4.2 Material Properties

The laminated composite adherends in this work were modeled as being constituted of T700/2510 carbon/epoxy unidirectional plies, and the adhesive as being constituted of FM300-2K polymer film adhesive. The T700/2510 unidirectional plies exhibit transversely isotropic material properties at the ply level. The experimentally obtained stiffness properties for a T700/2510 unidirectional ply are given in Table 4.2 [30]. The properties for the isotropic FM300-2K film adhesive are a Young's Modulus of 0.348 Msi and a Poisson's ratio of 0.400 [31]. The adhesive material region was modeled as being linearly isotropic.

The variation of these transversely isotropic material properties for each ply across different ply orientations in the composite adherend region must be taken into account in the finite element modeling. Abaqus does not allow definition of out-of-plane material coordinate systems for the definition of material orientation in two-dimensional models wherein the plane of consideration is the two-dimensional plane of modeling. Consequently, for the models in this study the ply stiffness properties for each ply orientation were transformed to correspond to the default global axis system in Abaqus, or the finite element model coordinate system (FEM Coordinate System). A sequential schematic of the coordinate systems relative to which the ply stiffness properties were transformed sequentially in order to facilitate definition of these properties for the finite element models is shown in Figure 4.1.

The orthogonal coordinate system, $\{x_1, x_2, x_3\}$, or the Ply Coordinate System, denotes the original material ply coordinates. The x_1-axis is aligned with the fiber direction in the ply, the x_2-axis denotes the in-plane direction transverse to the x_1-axis, and the x_3-axis is the direction orthogonal to the plane spanned by the x_1- and x_2-axes. The Laminate/Joint Coordinate System, {x, y, z}, represents the laminate coordinate system of a typical two-dimensional composite scarf joint as denoted in

Table 4.1 Geometric length dimensions, L_{joint} and L, of each finite element model

Variable Parameter	**Parameter Value**	**L_{joint} [in]**	**L [in]**
Baseline	10°	0.454	0.886
α	5°	0.915	1.347
	15°	0.300	0.732
α unequal (α_1, α_2)	(10°, 8°)	0.558	0.990
	(10°, 9°)	0.501	0.933
	(10°, 11°)	0.450	0.882
	(10°, 12°)	0.447	0.879
t_a	0.004 in	0.431	0.863
	0.006 in	0.443	0.875
	0.010 in	0.466	0.898
	0.012 in	0.477	0.909
Laminate	$[\pm 15_2/0_2]_S$	0.454	0.886
	$[\pm 15/0]_{2S}$	0.454	0.886
	$[\pm 45/0]_{2S}$	0.454	0.886
	*Homogenized** $[\pm 45_2/0_2]_S$	0.454	0.886
	*Homogenized** $[\pm 15_2/0_2]_S$	0.454	0.886

* Note: Stiffness values of adherend set to be homogeneously orthotropic from Classical Laminated Plate Theory for indicated laminate with no spatial variation within adherend.

Table 4.2 Stiffness properties for T700/2510 carbon/epoxy unidirectional ply

Property	**Value**
E_{11}	18.2 Msi
E_{22}	1.22 Msi
E_{33}	1.22 Msi
G_{12}	0.613 Msi
G_{13}	0.613 Msi
G_{23}	0.399 Msi
ν_{12}	0.309
ν_{13}	0.309
ν_{23}	0.596

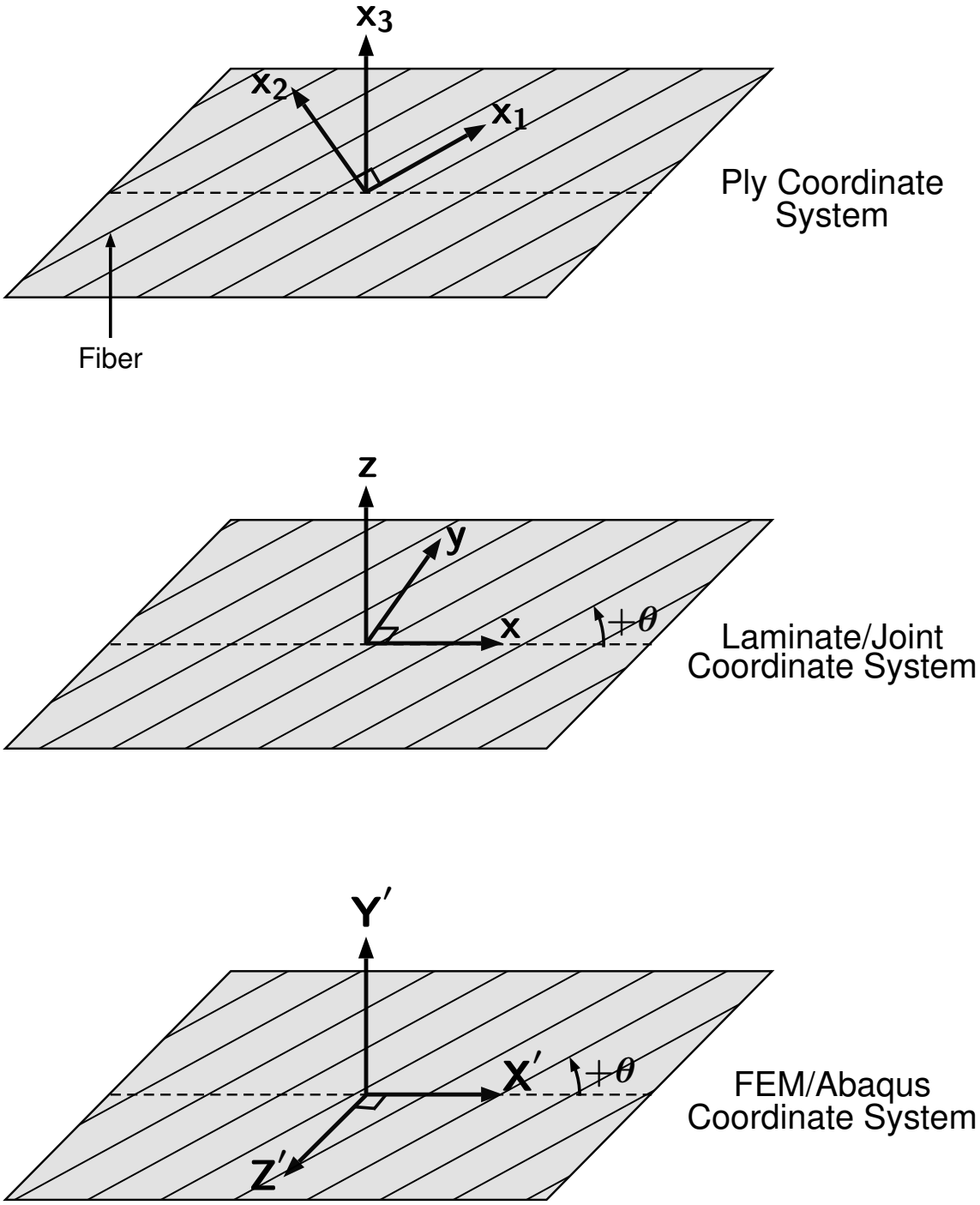

Figure 4.1 Definition of axes systems used and their associated transformations: (*upper*) Ply Coordinate System, (*middle*) Laminate/Joint Coordinate System, and (*lower*) FEM/Abaqus Coordinate System.

Figure 3.1. This is obtained via a rotation about the x_3-axis of the material coordinate system through the ply angle in the opposite direction (negative θ rotation for positive θ ply angle and vice versa). Note that a rotation is considered positive in the counterclockwise direction. The x_3-axis is preserved as the z-axis in the new orientation. All final results and evaluations are presented in Chapter 5 relative to the Laminate/Joint Coordinate System. The default Abaqus coordinate system, also referred to as the FEM Coordinate System in this work, is denoted by {X', Y', Z'}. This is obtained via a 90° counterclockwise rotation about the x-axis. The x-axis is preserved as the X'-axis in the new orientation. The z-axis becomes the Y'-axis, and the y-axis becomes the Z'-axis with the positive direction reversed. The FEM Coordinate System was employed for the purposes of building and running finite element models only.

The specific transformation relations employed in transforming each set of ply stiffness properties are given in Appendix A. The transformation relations are, in principle, simply an extension of the Classical Laminated Plate Theory (CLPT) mechanics to three dimensions. The transformations of axes only serve to allow definition of material properties for modeling convenience in Abaqus.

The transformed material properties for each ply orientation relative to the FEM Coordinate System were ultimately used as input to define the mechanical properties of associated material regions corresponding to the relevant ply regions of the laminated adherend in each finite element model. Each material region of different ply orientation was defined using the anisotropic linear elastic material option in Abaqus for material definitions. It may be noted from the outset that the transformed material constants for each ply also provide insight into the nature of coupling effects that can be expected in the stress and strain field responses relative to the laminate axes.

For the case of modeling homogenized $[\pm 45_2/0_2]_S$ and $[\pm 15_2/0_2]_S$ laminates, the variation of material properties from ply to ply was eliminated and the adherends were modeled as homogeneously orthotropic linear elastic plates having the equivalent laminate-level stiffness characteristics of $[\pm 45_2/0_2]_S$ and $[\pm 15_2/0_2]_S$ laminates, respectively. The orthotropic linear elastic plate properties for the homogenized ad-

herends were obtained simply as the average of the transformed material properties of each ply orientation in the associated laminate for the homogenized adherend, again with Classical Laminated Plate Theory as a basis.

4.3 Boundary Conditions

The two-dimensional finite element models of composite scarf joints investigated in this work were subjected to uniform extensional displacement boundary conditions. This was done in order to simulate physical situations wherein composite scarf joints are expected to be used in the repair of structures, such as wing skins on aircraft. Such structures generally need to transmit extensional loads, amongst other types of loading. The boundary conditions used in this study therefore seek to model this particular loading condition. This allows work to be conducted to determine the effects of the various parameters considered for a controlled situation that is representative of loading that occurs practically. This can be relayed to other situations. In this work, this has been achieved by applying uniform extensional displacements to the vertical edge of the two-dimensional composite scarf joint model at x equal to the model length, L, and keeping the vertical edge at x equal to 0 fixed with 0 displacements.

A need exists to provide an ability for direct comparison of the mechanical response across all the parametric cases investigated based on equal load-carrying capability. This is due to the fact that a parent structure may need to transmit the same load after a scarf joint repair. The applied uniform displacements, u_{app}, were therefore selected to correspond to equivalent load-carrying capability for all the parametric cases in this study. Since all the finite elements models entail geometric linearity in the strain-displacement relations, and material linearity in the stress-strain relations, the structural response of the models for a prescribed displacement can be scaled to any other applied displacement corresponding to a different loading situation if the behavior involved continues to fall within the linear regime.

The mechanical response for the different parametric cases varies depending upon

the parametric configuration of the joint. This results from variations in the effective stiffness of the scarf joint due to the variations in the geometric parameters of the joint and the laminate configuration of the adherends. Due to these variations, it is not possible to determine a priori the exact displacements at the far-field location for each parametric case that correspond to an equivalent applied load for all cases. Thus, a consistent method to choose the applied displacement corresponding to an equivalent load-carrying situation needs to be established.

The applied displacements in this work were chosen as estimated far-field values by using an estimate of the far-field longitudinal strain in the joint, corresponding to a uniformly distributed load of 100 lbf at the vertical edge at x equal to the model length, L. The load magnitude of 100 lbf was chosen in order to ensure that the mechanical response remains within the linear regime. The uniform far-field stress corresponding to a uniformly distributed load of 100 lbf is obtained by dividing by the cross-sectional area equal to the adherend thickness of 0.072 inches times a unit width of 1 inch in the y-direction. The resulting value of 1389 psi is the uniform tensile stress in the x-direction in the three-dimensional case. The estimated far-field strain in the joint is simply the uniform tensile stress divided by the effective longitudinal laminate stiffness of the adherend, E_{xx}. The estimated far-field strain is therefore only variable with the adherend stiffness since the equivalent load (100 lbf) and the cross-sectional area (constant $t_{adherend}$) are preserved as invariable across all the parametric cases. The effective longitudinal stiffness, E_{xx}, for the laminate adherends of $[\pm 45_2/0_2]_S$, $[\pm 45/0]_{2S}$, and homogenized $[\pm 45/0]_{2S}$ is 7.61 Msi, and this yields a value of 182.5 μstrain for the estimated longitudinal far-field strain. Similarly, for the laminate adherends of $[\pm 15_2/0_2]_S$, $[\pm 15/0]_{2S}$, and homogenized $[\pm 15/0]_{2S}$, the effective longitudinal stiffness, E_{xx}, is 16.0 Msi, and this yields a value of 86.8 μstrain for the estimated longitudinal far-field strain. The applied displacements for each parametric case are then obtained by multiplying the estimated longitudinal far-field strain by the respective model length, and are listed in Table 4.1. The simplified

relation for the computation of applied displacements is shown in Equation 4.2:

$$u_{app}[\text{in}] = \frac{1389\,[\text{psi}]\,L\,[\text{in}]}{E_{xx}\,[\text{psi}]}. \tag{4.2}$$

The applied uniform far-field displacement for each model is listed in Table 4.3. The applied uniform far-field displacement boundary conditions are also illustrated in Figure 4.2.

The results obtained from these specific models can be scaled, as previously noted, by determining appropriate ratios to scale all results. The underlying assumption is that all behavior stays within the linear regimes. These ratios depend upon whether the far-field condition is based on displacement or load. If based on displacement, it is necessary to determine the ratio of the values of the desired uniform extensional displacement to that of the applied uniform extensional displacement, u_{app}, as used in the model. All results for the field variables from the actual model are then multiplied by that ratio to determine the values for the field variables for that desired displacement. For the case of desired applied distributed load, it is first necessary to determine the resulting load being carried for the case modeled. First, the longitudinal far-field strains occurring at the edge at x equal to L, as obtained via the model, are averaged, and then multiplied by the effective longitudinal laminate stiffness of the adherend, E_{xx}, to yield the corresponding effective uniform tensile stress. The effective uniform tensile stress can then be multiplied by the cross-sectional area, which is equal to the adherend thickness of 0.072 inches times a unit width of 1 inch in the y-direction, in order to determine the value of the average distributed load transmitted in the modeled case. It is then necessary to determine the ratio of the values of the desired distributed load to that of the average distributed load for that model. All results for the field variables from the actual model are then multiplied by that ratio to determine the values for that desired load.

Table 4.3 Applied far-field displacement, u_{app}, for each finite element model

Variable Parameter	**Parameter Value**	$\mathbf{u_{app}}$ **[in]**
Baseline	10°	0.0001618
α	5°	0.0002458
	15°	0.0001336
α unequal (α_1, α_2)	(10°, 8°)	0.0001808
	(10°, 9°)	0.0001702
	(10°, 11°)	0.0001610
	(10°, 12°)	0.0001618
t_a	0.004 in	0.0001576
	0.006 in	0.0001597
	0.010 in	0.0001639
	0.012 in	0.0001604
Laminate	$[\pm 15_2/0_2]_s$	0.0000769
	$[\pm 15/0]_{2s}$	0.0000769
	$[\pm 45/0]_{2s}$	0.0001618
	*Homogenized** $[\pm 45_2/0_2]_s$	0.0001618
	*Homogenized** $[\pm 15_2/0_2]_s$	0.0000769

* Note: Stiffness values of adherend set to be homogeneously orthotropic from Classical Laminated Plate Theory for indicated laminate with no spatial variation within adherend.

4.4 Model Discretization

The purpose of this work, as has been noted earlier, is to establish a fundamental level understanding of the mechanical response and its associated parametric sensitivities for two-dimensional composite scarf joints. As this understanding is to be based on the results of the finite element modeling performed in this work, the modeling considerations and aspects involved directly influence the results, and therefore the primary understanding that is sought. Within this context, the type of finite elements used for discretization influences the modeling output and results. In this work, all two-dimensional scarf joint models were discretized using three-noded (linear), plane strain, displacement-based elements, named as CPE3 in the Abaqus standard element library. Plane strain conditions arise from the base assumption about the structural configuration of composite scarf joints, as discussed in Chapter 3. As it is assumed that the scarf joint configuration has significant geometric extension in the y-direction to prohibit any deformation out of the x-z plane, a plane strain condition exists at any given cross-section of the configuration. Linear triangular elements were used in order to reduce the computational cost of executing the models, yet ensuring adequate resolution of the resulting stress and strain fields in order to capture their steep variations in the model region.

Each ply was discretized with two elements in the through-thickness direction. This is illustrated in Figure 4.2 wherein a characteristic mesh of a typical two-dimensional composite scarf joint finite element model is shown in the joint region. The use of two elements per ply thickness was based on the consideration of issues related to modeling lengthscale. It was ensured that the lengthscale associated with the elements was at least greater by an order of magnitude than the lengthscale associated with fiber diameter in the plies. Thus, stress and strain fields generated from such modeling are maintained at a lengthscale where the assumption of fiber-matrix continuum in regard to stiffness properties remains valid.

The adhesive material is assumed to be homogeneously isotropic. The adhesive region is discretized with three elements through the adhesive thickness. Mesh seeds

were thus applied to each model in Abaqus at the horizontal adhesive edges and the vertical edges of each ply to yield the discussed number of through-thickness elements for the adhesive and ply regions. The number of elements in the x-direction was not restricted and the discretization in the x-direction was achieved to yield appropriate element aspect ratios at the adjoining regions between the plies and the adhesive. The characteristic mesh of a typical two-dimensional composite scarf joint finite element model along with the applied boundary conditions is shown in Figure 4.2, with an enlarged view of the mesh structure near the adhesive tip and the adjoining ply tip regions shown in Figure 4.3. The mesh density was kept higher in the adhesive region compared to the adherends in order to capture any higher stress and strain gradients within the adhesive region. The adhesive region is expected to be sensitive in producing higher stress and strain gradients due to the entire load being transmitted from one adherend to the other via the adhesvive. The adhesive layer is relatively thin, that is on the order of a ply thickness, and is significantly less than the adherend thickness. Large sensitivities in the mechanical response of the scarf joint are expected to occur within the adhesive.

4.5 Assessment of Model Lengths

An assessment of the sufficiency of the finite element model length between the joint region and the edges of the model was performed. The sufficiency of this length was assessed based on the recovery of uniform distribution of far-field longitudinal strain through the thickness of the laminated adherend. The true physical state of far-field strain at the model edge at x equal to L is purely longitudinal and has uniform distribution through the thickness of the adherend. Thus, the fidelity of a modeled case can be assessed by considering the level to which the far-field state of strain in the model becomes purely longitudinal. This is based on the uniformity of the state of strain through the thickness of the adherend in this region.

An additional finite element model of the case with twice the length between the joint region and the model edges compared to that for the baseline case, $2\Delta L$ (0.432

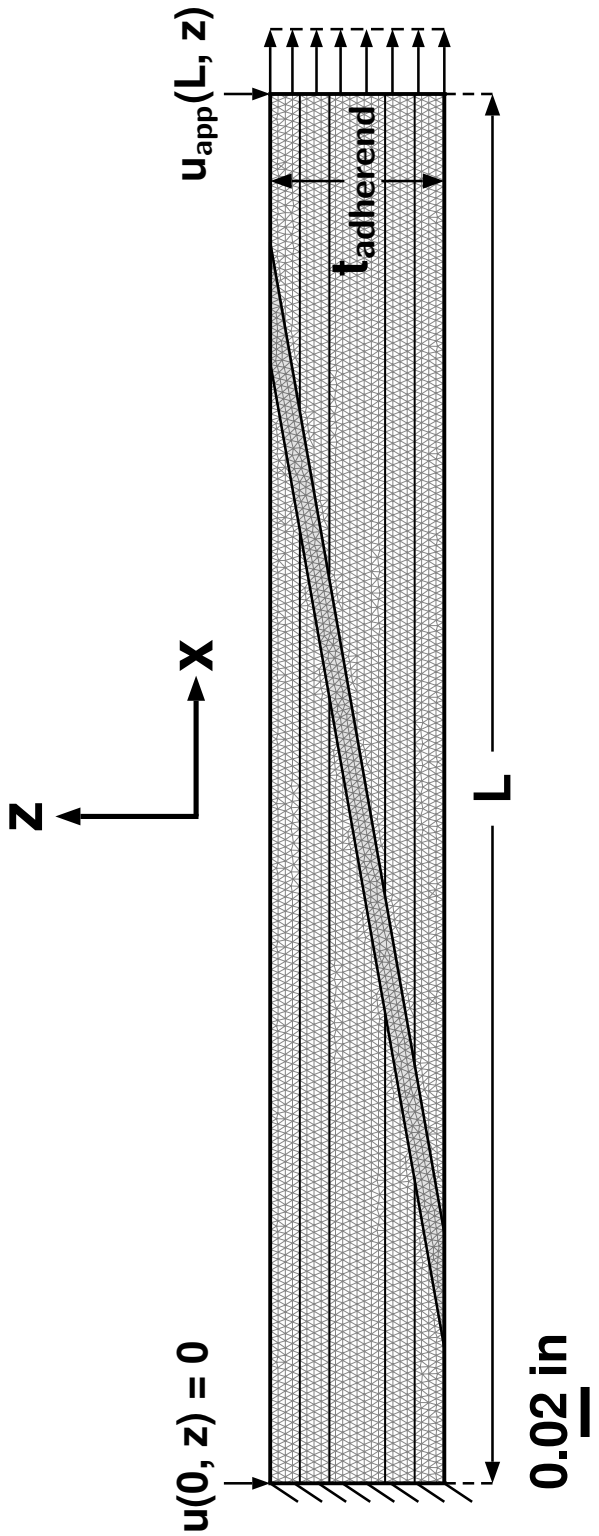

Figure 4.2 Discretized mesh of a typical two-dimensional composite scarf joint finite element model with applied boundary conditions.

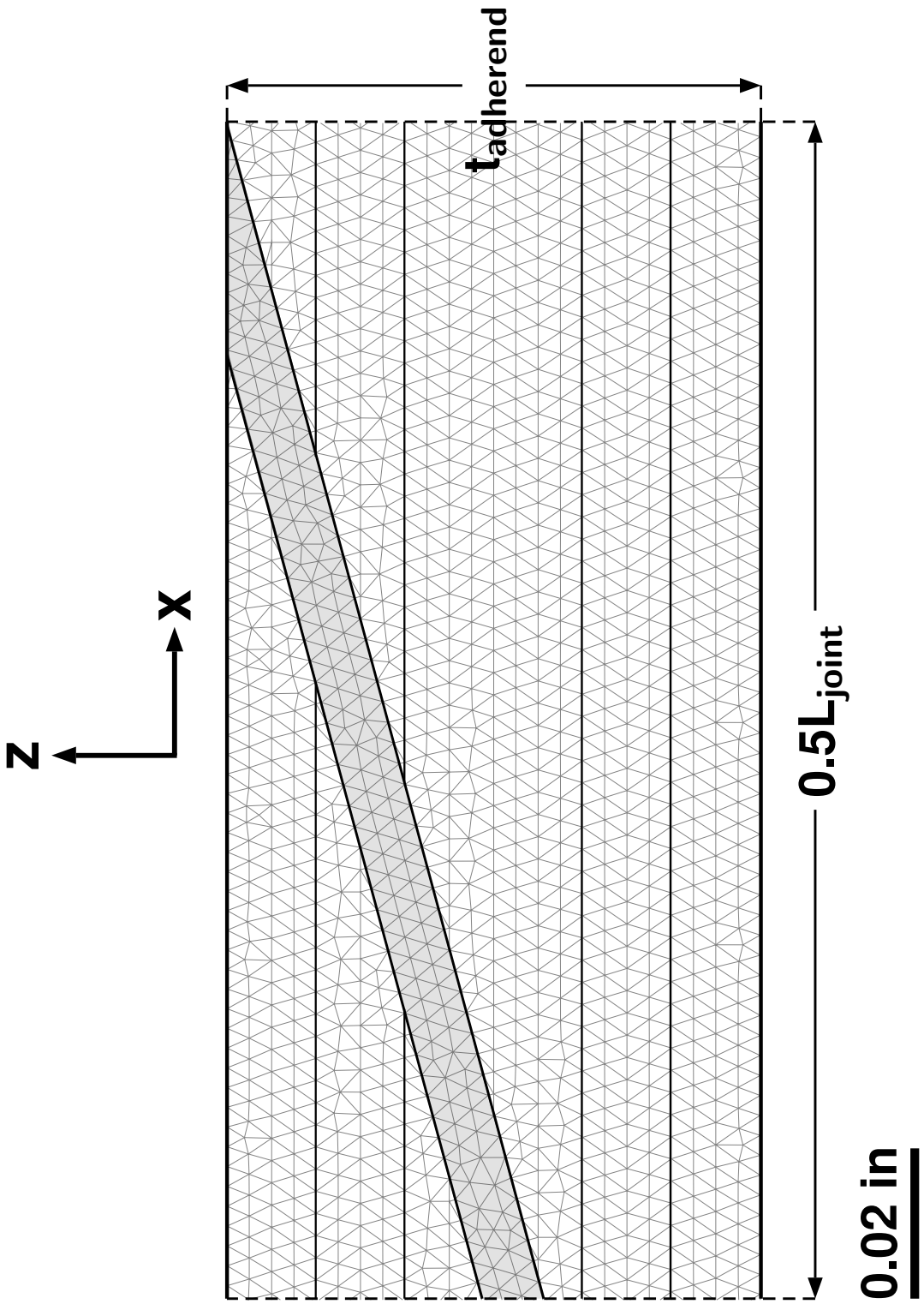

Figure 4.3 Enlarged view of the mesh at the adhesive tip region and the adjoining ply tips of a typical two-dimensional composite scarf joint finite element model.

in), with prescribed displacement boundary conditions corresponding to equivalent load-carrying capability for this case, was run in order to compare the distributions of far-field longitudinal strain through the thickness of the adherend for the two cases. All other parameters for this case were retained to be similar to those for the baseline configuration, and the length of the joint region was kept constant. The magnitudes of the differences in the values of the longitudinal strain from the average far-field longitudinal strain, ϵ_{11}^{∞}, are assessed at the far-field location through the thickness of the adherend. The magnitudes of these differences are reported as percentages of the average far-field longitudinal strain, ϵ_{11}^{∞}, in Table 4.4 for specific locations through the thickness of the adherend. These locations in the adherend correspond to the six effective mid-ply locations for the $[\pm 45_2/0_2]_S$ laminate configuration of the adherend.

The magnitudes of percentage differences in the values of local far-field longitudinal strain from the average far-field longitudinal strain, ϵ_{11}^{∞}, indicate uniformity of the distribution of longitudinal strain through the thickness of the adherend to within 0.15% of ϵ_{11}^{∞} for the baseline case with ΔL, and to within 0.04% of ϵ_{11}^{∞} for the case with 2ΔL. In this work, the length for the baseline case of ΔL between the joint region and the model edges is thus considered to be sufficiently long to allow recovery of purely longitudinal far-field strain behavior corresponding to that of a perfect laminate, with sufficiently uniform distribution of longitudinal strain through the thickness of the adherend.

Table 4.4 Magnitudes of percentage differences in the values of longitudinal strain at the end of the model from the average far-field longitudinal strain, ϵ_{11}^{∞}, at different locations through the thickness of the adherend of $[\pm 45_2/0_2]_S$ for the cases of ΔL and $2\Delta L$

Location in z (in)	**Difference for** ΔL	**Difference for** $\mathbf{2}\Delta L$
0.066	0.15%	0.04%
0.054	0.04%	0.02%
0.042	0.09%	0.01%
0.030	0.10%	0.01%
0.018	0.02%	0.03%
0.006	0.03%	0.04%

Chapter 5

Results

The results obtained through the finite element modeling of all the two-dimensional composite scarf joint cases investigated in this work are presented in this chapter. The findings of this work are primarily captured through the mechanical response exhibited in the strain distributions along defined coordinate axes in the scarf joint region, along with isostrain contour field plots. The isostrain contour field plots, which indicate the overall global joint response, are given in Appendix B. The strain results throughout are presented in terms of the tensorial components. The strain distributions along the coordinate axes associated with the joint provide localized qualitative and quantitative assessment of the mechanical behavior of the joint. This chapter is devoted to their documentation.

The results in this chapter are documented in association with variation of individual parameters. This allows the associated sensitivities for each parametric case to be assessed directly. The strain results for different laminate configurations of the adherends, similar for both adherends within one joint configuration, are presented in Section 5.1, and response sensitivities are described. In addition, the general characteristics of the mechanical response of two-dimensional composite scarf joints are described. The results for different scarf angles, equal for both adherends within one joint configuration, are presented in Section 5.2. The results for different adhesive thicknesses are presented in Section 5.3. The results for different scarf angles for adherend 2, with the scarf angle for adherend 1 always equal to 10°, are presented in

Section 5.4. In the latter three sections, description of the response sensitivities to the parameters is emphasized.

The presentation of strain results requires definition of the axes used. The defined axes can be categorized into two types, and are shown in Figure 5.1. The first set of axes is obtained by rotating the x-axis by the associated scarf angles, α_1 and/or α_2. These axes are identified by the subscript j, and thus denoted as x_j. One of these axes, x_{jm}, runs at the midline of the adhesive along the scarf length beginning at the bottom of the configuration (z = 0 in), and has a relative angle of $(\alpha_2 + \alpha_2)/2$. The interface between the adhesive and adherend 1 is defined as bondline 1. This has an axis, x_{jb1}, beginning at the top of the configuration (z = 0.072 in), that runs towards the bottom of the configuration, and has a relative angle of α_1. The interface between the adhesive and adherend 2 is defined as bondline 2. This has an axis, x_{jb2}, beginning at the bottom of the configuration (z = 0 in), and has a relative angle of α_2.

The distance along each of these axes is normalized to be between 0 and 1, running from its starting point to the other end of the configuration. Thus, the normalized distance along the adhesive midline, denoted as x^*_{jm}, is obtained by dividing the true values of x_{jm} by the length of the configuration along the adhesive midline, $[t_{adherend}/\sin((\alpha_1 + \alpha_2)/2)]$. Similarly, the normalized distances along the two bondlines, denoted as x^*_{jb1} and x^*_{jb2}, are obtained by dividing the true values of x_{jb1} and x_{jb2} by the length of the configuration along the bondline. This is equal to the adherend thickness, $t_{adherend}$, divided by the sine of the associated angle, α_1 or α_2. The strain distributions along the x_j-axes are thus all plotted versus the corresponding normalized values, x^*_j. It is also noted that the strain plots along x^*_{jb1} and x^*_{jb2} indicate strain values in the adhesive. However, the use of a prime on x^*_{jb}, x'^*_{jb}, indicates strain values within the adherends. Thus, strain plots along x'^*_{jb1} and x'^*_{jb2} indicate strain values in the adherends. Strain plots along x^*_{jb1} are only included for the case of unequal scarf angles ($\alpha_1 \neq \alpha_2$), in which case the geometric asymmetry yields different strain values along the two bondlines. The ply interface locations along x'^*_{jb2}, and adjacent locations along x^*_{jb2} and x^*_{jm}, for the cases of $[\pm\theta_2/0_2]_S$ are listed in Table 5.1, and

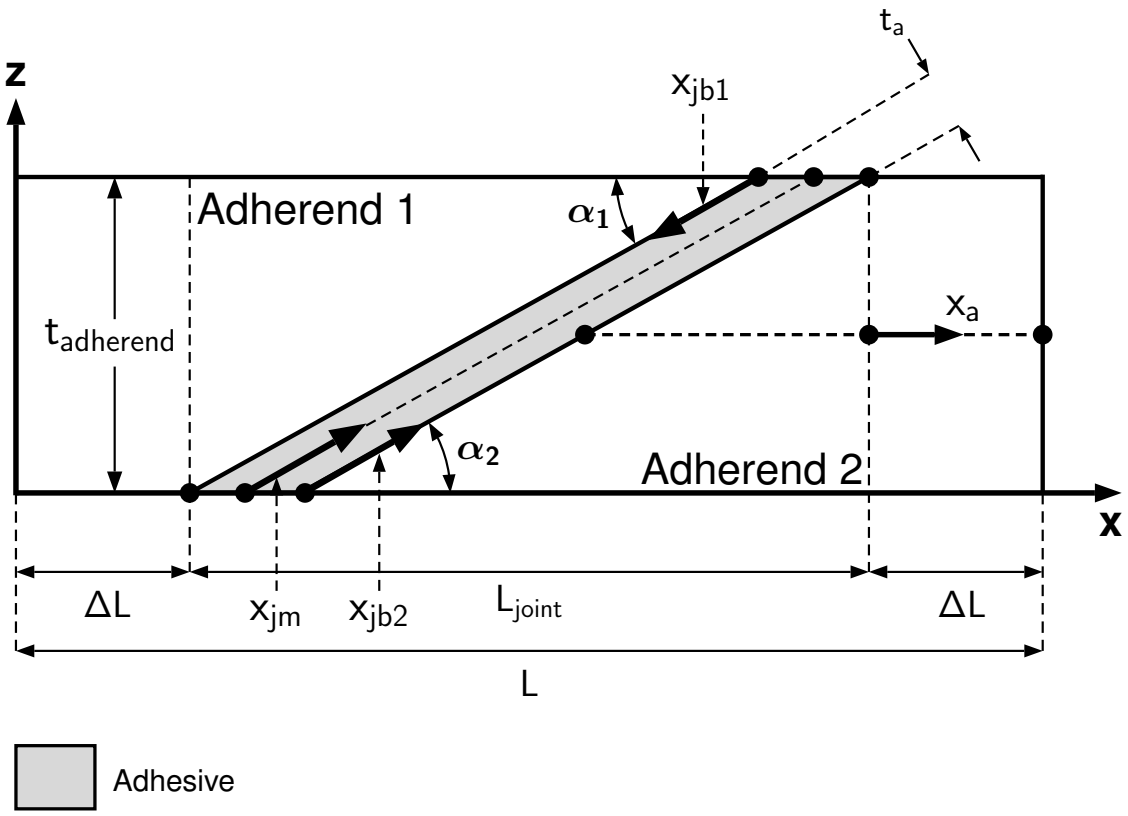

Figure 5.1 Definition of coordinate axes, x_{jb1}, x_{jm}, x_{jb2}, and x_a, used for plots of normalized strain distributions for all parametric cases.

those for the cases of $[\pm\theta/0]_{2S}$ are listed in Table 5.2.

The second set of axes runs parallel to the x-axis with the origin at the end of the joint region at x equal to $(L_{joint} + \Delta L)$ within adherend 2. The axes are distinguished by the subscript a, and thus denoted as x_a. These axes are used at specific through-thickness locations, and thus for specific values of z. Each of these axes runs from bondline 2 within the adherend to the edge of the scarf joint at x equal to L. This implies that each axis has negative values for values of x less than $(L_{joint} + \Delta L)$, and positive values for values of x greater than $(L_{joint} + \Delta L)$ along these axes. The values along these axes are normalized by the adherend thickness, $t_{adherend}$, and denoted by x_a^*. The strain distributions in this regard are also plotted versus the normalized values, x_a^*. The acute ply tip locations along x_a^* for the cases of $[\pm\theta_2/0_2]_S$ for cases of equal scarf angles are listed in Table 5.3.

The values of strain within the adhesive along the x_{jb}-axes are plotted at a third of the distance of the characteristic element length from each bondline (0.001 in). Similarly, strain values within the adherend along these axes are also plotted at one third of the distance of a characteristic element length from each bondline (0.001 in). Within this distance, the strain values are representative of the strain variation occurring at the bondline in the adhesive or the adherend for each case.

The strain plots presented in this chapter include distributions of longitudinal strain, ϵ_{11}, and shear strain (tensorial), ϵ_{13}, along the specific coordinate axes as defined previously. These two strain components sufficiently establish the fundamental mechanics and response of two-dimensional composite scarf joints and the load transfer mechanisms within the joint. The distributions of transverse normal strain in the adhesive, ϵ_{33}, generally exhibit similar trends to those for the distributions of longitudinal strain, ϵ_{11}. This is demonstrated through the distributions of normalized strains of ϵ_{11} and ϵ_{33} along the adhesive midline for the baseline case shown in Figure 5.2. In regions in the adhesive where the distributions of normalized strains remain relatively uniform, the magnitudes of transverse normal strain are related to those of longitudinal strain via the Poisson's ratio of the adhesive, ν, with the ratio being approximately 2ν, as indicated by plane strain conditions. However, in regions of

Table 5.1 Ply span intervals for $[\pm\theta_2/0_2]_S$ laminates along x_j^*-axes

x_j^* **Interval**	**Ply Angle**
$0.0 \leq x_j^* < 0.167$	$+\theta$
$0.167 < x_j^* < 0.333$	$-\theta$
$0.333 < x_j^* < 0.667$	0
$0.667 < x_j^* < 0.833$	$-\theta$
$0.833 < x_j^* \leq 1.0$	$+\theta$

Note: Interval boundaries, except 0.0 and 1.0, indicate actual ply interface locations inside adherend along x'^*_{jb2}, and adjacent ply interface locations along x^*_{jb2} and x^*_{jm}.

Table 5.2 Ply span intervals for $[\pm\theta/0]_{2S}$ laminates along x_j^*-axes

x_j^* Interval	Ply Angle
$0.0 \leq x_j^* < 0.083$	$+\theta$
$0.083 < x_j^* < 0.167$	$-\theta$
$0.167 < x_j^* < 0.250$	0
$0.250 < x_j^* < 0.333$	$+\theta$
$0.333 < x_j^* < 0.417$	$-\theta$
$0.417 < x_j^* < 0.583$	0
$0.583 < x_j^* < 0.667$	$-\theta$
$0.667 < x_j^* < 0.750$	$+\theta$
$0.750 < x_j^* < 0.833$	0
$0.833 < x_j^* < 0.917$	$-\theta$
$0.917 < x_j^* \leq 1.0$	$+\theta$

Note: Interval boundaries, except 0.0 and 1.0, indicate actual ply interface locations inside adherend along x'^*_{jb2}, and adjacent ply interface locations along x^*_{jb2} and x^*_{jm}.

Table 5.3 Acute ply tip locations for $[\pm\theta_2/0_2]_S$ laminates along x_a^* for scarf angles of 5°, 10°, and 15°

Acute Ply Tip Angle (interface location)	**x_a^* Location**		
	$\boldsymbol{\alpha = 5°}$	$\boldsymbol{\alpha = 10°}$	$\boldsymbol{\alpha = 15°}$
$+\theta$ ($z = 0.060$ in)	-1.905	-0.945	-0.622
$-\theta$ ($z = 0.048$ in)	-3.810	-1.890	-1.244
0 ($z = 0.024$ in)	-7.620	-3.780	-2.488
$-\theta$ ($z = 0.012$ in)	-9.525	-4.725	-3.110
$+\theta$ ($z = 0.0$ in)	-11.430	-5.670	-3.732

Table 5.4 Average far-field longitudinal strain, ϵ_{11}^{∞}, for each finite element model

Variable Parameter	**Parameter Value**	$\boldsymbol{\epsilon_{11}^{\infty}}$ **[**$\boldsymbol{\mu}$**strain]**
Baseline	10°	151.0
α	5°	161.0
	15°	141.5
α unequal (α_1, α_2)	(10°, 8°)	133.0
	(10°, 9°)	142.0
	(10°, 11°)	140.0
	(10°, 12°)	126.0
t_a	0.004 in	165.0
	0.006 in	158.0
	0.010 in	145.0
	0.012 in	139.0
Laminate	$[\pm 15_2/0_2]_S$	67.3
	$[\pm 15/0]_{2S}$	67.2
	$[\pm 45/0]_{2S}$	152.1
	*Homogenized** $[\pm 45_2/0_2]_S$	153.4
	*Homogenized** $[\pm 15_2/0_2]_S$	67.2

* Note: Stiffness values of adherend set to be homogeneously orthotropic from Classical Laminated Plate Theory for indicated laminate with no spatial variation within adherend.

high gradients in strains, the ratio of magnitudes of transverse normal strain to those of longitudinal strain varies. Nevertheless, the general characteristics of the distributions of both strains remain the same, and no additional observations are gathered from the distributions of transverse normal strain, ϵ_{33}. Therefore, the results for the distributions of transverse normal strain are not presented in this chapter.

The strain distributions in each plot are normalized by the average value of far-field longitudinal strain, ϵ_{11}^{∞}, as determined for each model. The average value of far-field longitudinal strain is the average of the values of longitudinal strain, ϵ_{11}, occurring at the edge of each model at x equal to L. The values of ϵ_{11}^{∞} for each parametric case are listed in Table 5.4. For all cases, except for those with unequal scarf angles, the strain fields in the joint region are anti-symmetric about the rectangular coordinate system originating at the geometric center of the scarf joint at x equal to L/2 and z equal to $t_{adherend}/2$, with one axis being aligned with the adhesive midline, x_{jm}, as shown in Figure 5.1. This can be attributed to anti-symmetry of the geometry, material, and loading about such a coordinate system for the associated cases of two-dimensional composite scarf joints investigated.

5.1 Effects of Laminate Configuration

The strain distributions for the two-dimensional composite scarf joints with various laminate configurations of the adherend investigated in this work are presented in this section. The general characteristics of the strain response of the two-dimensional composite scarf joints are described in relation to these specific cases of laminate configurations of the adherend. In addition, the sensitivities exhibited in the strain response to the variations in these configurations are also detailed.

The distributions of longitudinal strain, ϵ_{11}, along bondline 2 in adherend 2 and in the adhesive show high values of strain at the location of the acute tip of the adherend. As indicated in Figures 5.3 and 5.4, the longitudinal strain has peak values in the adherend at the acute tip, at $x_{jb2}^{\prime *}$ equal to 0.0. Conversely, the greatest reduction in longitudinal strain in the adherend occurs at the location of the obtuse tip of the

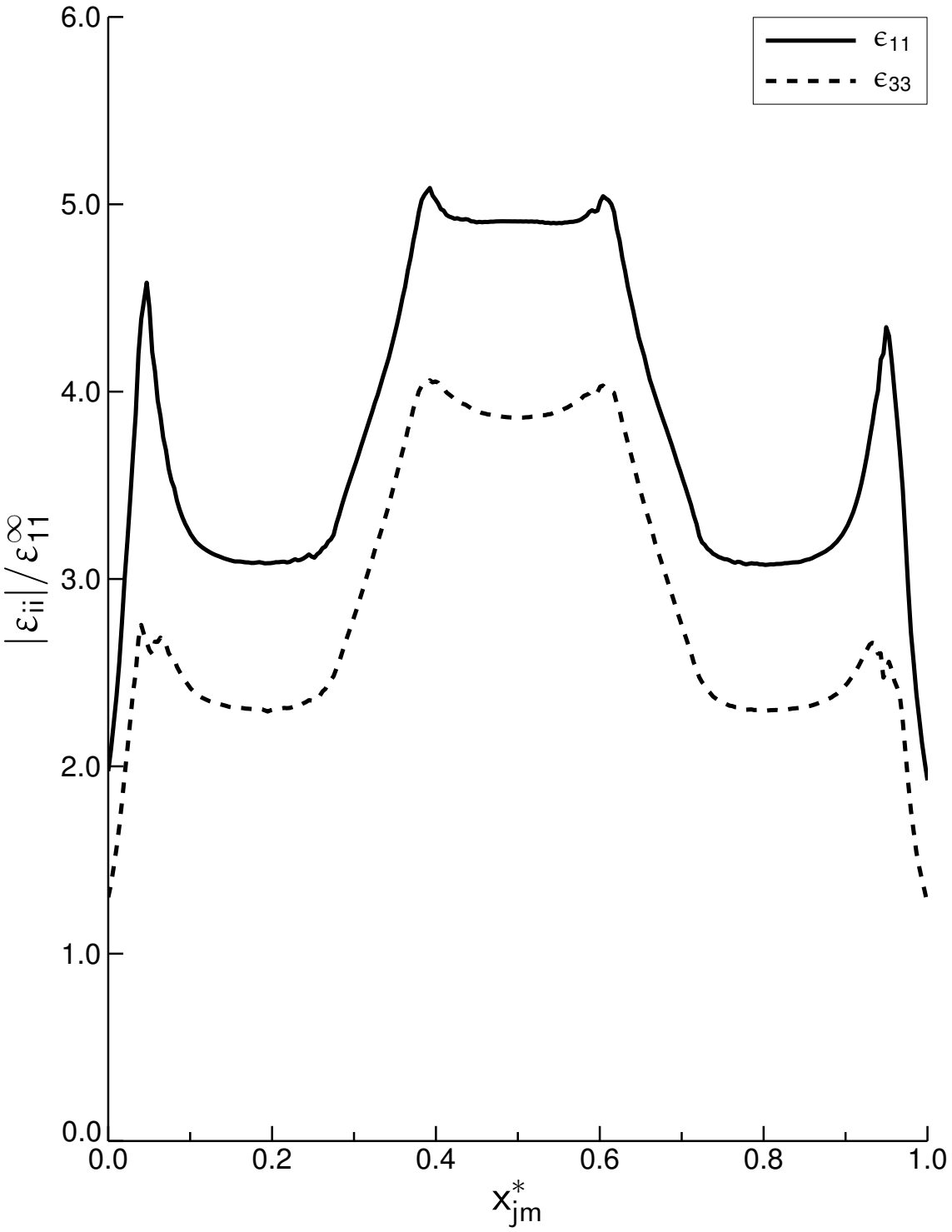

Figure 5.2 Plot of normalized magnitude of ϵ_{11} and ϵ_{33} versus x_{jm}^{*} at midline in adhesive for the baseline case with equal scarf angles of 10°, adhesive thickness of 0.008 in, and laminate configuration of $[\pm 45_2/0_2]_S$.

adherend, at x'^{*}_{jb2} equal to 1.0. At each end in the adherend, there exists a region of normalized length approximately equal to 0.1 with high strain gradient to the end value. Between these regions, the longitudinal strain remains relatively uniform for the cases of homogenized $[\pm\theta_2/0_2]_S$, with there being no difference in the value of normalized strain for the two values of θ considered, 45° and 15°.

For the laminated cases of $[\pm\theta_2/0_2]_S$ and $[\pm\theta/0]_{2S}$, the effect of mismatched stiffness properties arising from the presence of plies at angles of $+\theta$ and $-\theta$ along with those at 0° is evident through the sharp increases and decreases in longitudinal strain at the locations of ply interfaces along the bondline. The distributions of normalized longitudinal strain for the cases of $[\pm 15_2/0_2]_S$ and $[\pm 15/0]_{2S}$ very closely follow the distributions for the corresponding homogenized cases, to the extent of almost overlapping them, with deviations of no larger than 10% of the normalized value of longitudinal strain at ply interface locations along the bondline. However, the cases of $[\pm 45_2/0_2]_S$ and $[\pm 45/0]_{2S}$ show significant variations in the distributions of normalized longitudinal strain along the bondline compared to those for the corresponding homogenized cases. The local maxima of longitudinal strain occurring between the normalized distances of 0.1 and 0.9 for the case of $[\pm 45/0]_{2S}$ are all of relatively similar normalized magnitude of approximately 2.0. This value is slightly smaller than the corresponding normalized value of 2.3 for the single local maximum of longitudinal strain occurring in the same interval for the case of $[\pm 45_2/0_2]_S$. Similarly, the local minima of longitudinal strain occurring in the interval for the case of $[\pm 45/0]_{2S}$ are all of similar normalized magnitude of approximately 0.75, as compared with the corresponding normalized magnitude of 0.70 for the single local minimum for the case of $[\pm 45_2/0_2]_S$. Thus, the magnitude of the variation in longitudinal strain with respect to the average far-field value for the case of $[\pm 45/0]_{2S}$ is smaller compared to that for the case of $[\pm 45_2/0_2]_S$.

It is important to note that for the case of $[\pm 45/0]_{2S}$, the region of high strain gradient at each end is accompanied by a change in the sign of strain gradient over a normalized length of approximately 0.1, wherein the longitudinal strain reaches a local maximum value. In comparison to the case of $[\pm 45_2/0_2]_S$, similar behavior

occurs but over a normalized distance of approximately 0.2 from either ends of the bondline. In addition, the distribution of longitudinal strain for each case experiences a slight reduction in magnitude at the normalized distance of 0.89 along bondline 2. This point along the bondline has the same location in x as the location of the acute tip of the other adherend (adherend 1).

The distributions of longitudinal strain, ϵ_{11}, in the adhesive along bondline 2 are directly related to the corresponding distributions in adherend 2 along bondline 2. This can be seen in the plots of normalized longitudinal strain in the adhesive along the bondline, as shown in Figures 5.5 and 5.6. In general, increases and decreases in strain values in the adhesive occurring at various locations along the bondline are tied to associated increases and decreases in strain values in the immediately adjacent region in the adherend. The distributions of normalized longitudinal strain along the bondline in the adhesive over the normalized distances between 0.2 and 0.8 are related to those in the adherend by ratios of approximately 4.5 and 3.0 for the cases of homogenized $[\pm 15_2/0_2]_S$ and homogenzied $[\pm 45_2/0_2]_S$, respectively. The magnitudes of normalized longitudinal strain occurring for the cases of laminates having 15° plies are higher compared to those for the cases of laminates having 45° plies. This indicates the greater mismatch in longitudinal stiffness properties between the adhesive and the adherend for the cases having 15° plies compared to those having 45° plies.

The distributions of longitudinal strain, ϵ_{11}, in the adhesive along the midline exhibit significant resemblance to the distributions of longitudinal strain along the bondline, both in the adhesive and in the adherend. The normalized distributions are shown in Figures 5.7 and 5.8 for the cases of different laminates. For these cases, the distributions of longitudinal strain are symmetric about x^*_{jm} equal to 0.5, in consistency with the symmetry of the various aspects of the configuration of a two-dimensional composite scarf joint, as discussed in the introduction to this chapter. The local increases and decreases in longitudinal strain are reduced in magnitude, the local variations are shifted, and the overall strain gradients are also reduced in magnitude. Overall values of longitudinal strain at the adhesive midline for the cases

of homogenized $[\pm 15_2/0_2]_S$ and homogenized $[\pm 45_2/0_2]_S$ remain the same as those occurring in the adhesive at the bondline. The average values of normalized longitudinal strain for the cases of homogenized $[\pm 15_2/0_2]_S$ and homogenized $[\pm 45_2/0_2]_S$ are 5.5 and 3.7, respectively, over the normalized distances between 0.2 and 0.8.

The distributions of normalized shear strain, ϵ_{13}, at bondline 2 in adherend 2 are presented in Figures 5.9 and 5.10 for the cases of $[\pm\theta_2/0_2]_S$, homogenized $[\pm\theta_2/0_2]_S$, and $[\pm\theta/0]_{2S}$. These distributions exhibit similar characteristics to those for longitudinal strain. In particular, the distributions of shear strain remain relatively uniform, except near the end regions. This is specifically true for the homogenized cases. In addition, high values of shear strain occur at the acute tip of the adherend for all cases. However, the peak magnitude of shear strain does not always occur at the acute tip of the adherend for the cases of laminated adherends. The local maxima in shear strain for the case of $[\pm 45/0]_{2S}$ all have relatively similar normalized magnitude of approximately 3.4, slightly less than the normalized magnitude of 3.7 for the single local maximum for the case of $[\pm 45_2/0_2]_S$. Similarly, the local minima in shear strain away from the end regions for the case of $[\pm 45/0]_{2S}$ have negative values and also have a relatively similar normalized magnitude of approximately 1.8. This is slightly larger than the normalized magnitude of approximately 1.7 for the single local minimum for the case of $[\pm 45_2/0_2]_S$, which is also negative in value. The laminated cases of $[\pm 15_2/0_2]_S$ and $[\pm 15/0]_{2S}$ also show greater variations in the distributions of shear strain compared to those for longitudinal strain at ply interfaces. These variations are within differences of 50% of normalized values of shear strain at some ply interface locations. In all cases, the local maxima and minima for shear strain occur at the same locations as where the local maxima and minima for longitudinal strain occur. Another noteworthy feature in the distributions of shear is the sharp reduction in shear strain occurring near the normalized distance of 0.89 in the adherend along the bondline for all cases. This behavior is also exhibited in the distributions for longitudinal strain, but is significantly amplified in the distributions for shear strain.

The distributions of normalized shear strain, ϵ_{13}, along bondline 2 in the adhesive are shown in Figures 5.11 and 5.12 for all cases. The shear strain remains entirely

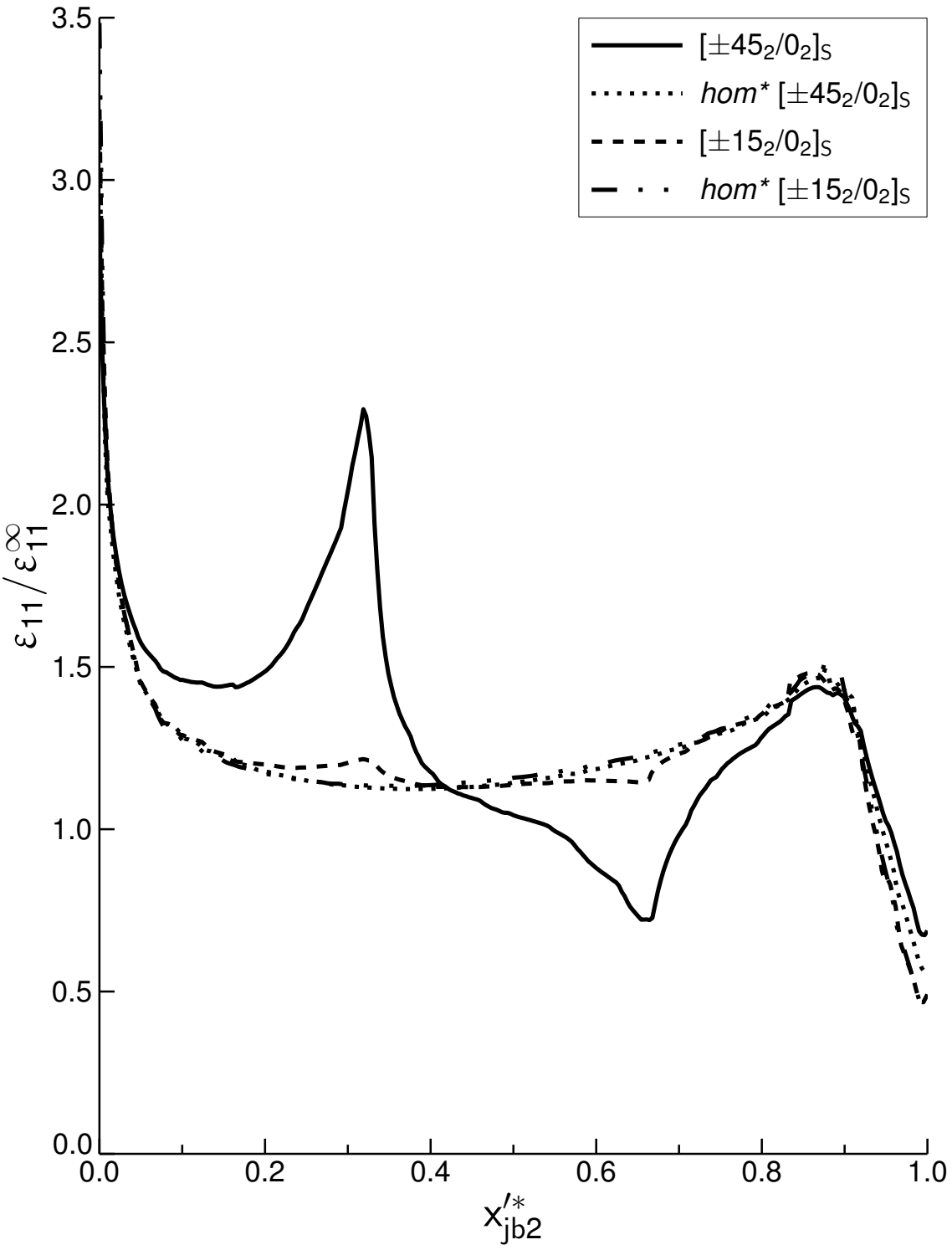

Figure 5.3 Plot of normalized ϵ_{11} versus x'^{*}_{jb2} at bondline 2 in adherend for the cases of laminate configurations of $[\pm 45_2/0_2]_S$, *homogenized* $[\pm 45_2/0_2]_S$, $[\pm 15_2/0_2]_S$, and *homogenized* $[\pm 15_2/0_2]_S$.

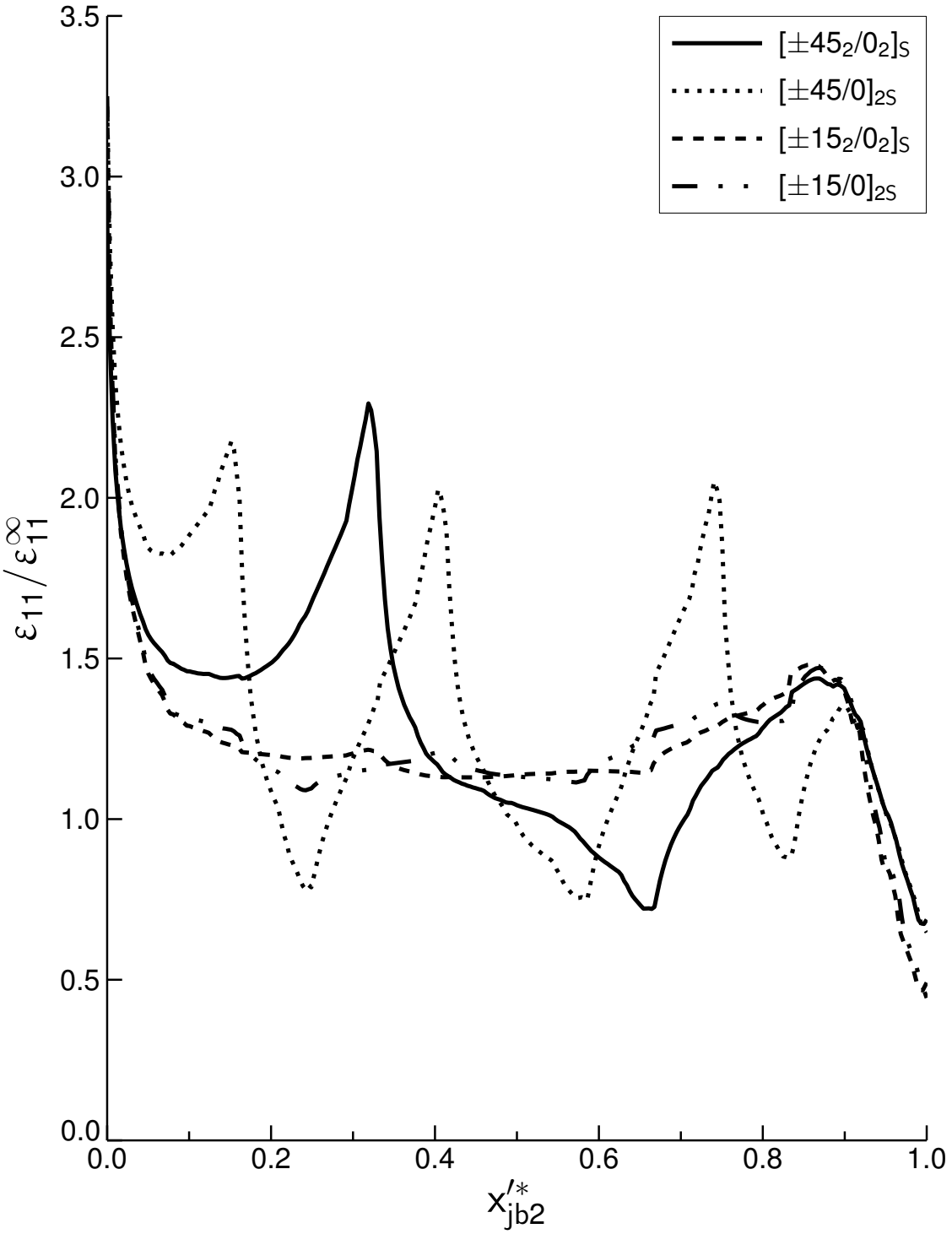

Figure 5.4 Plot of normalized ϵ_{11} versus x'^{*}_{jb2} at bondline 2 in adherend for the cases of laminate configurations of $[\pm 45_2/0_2]_S$, $[\pm 45/0]_{2S}$, $[\pm 15_2/0_2]_S$, and $[\pm 15/0]_{2S}$.

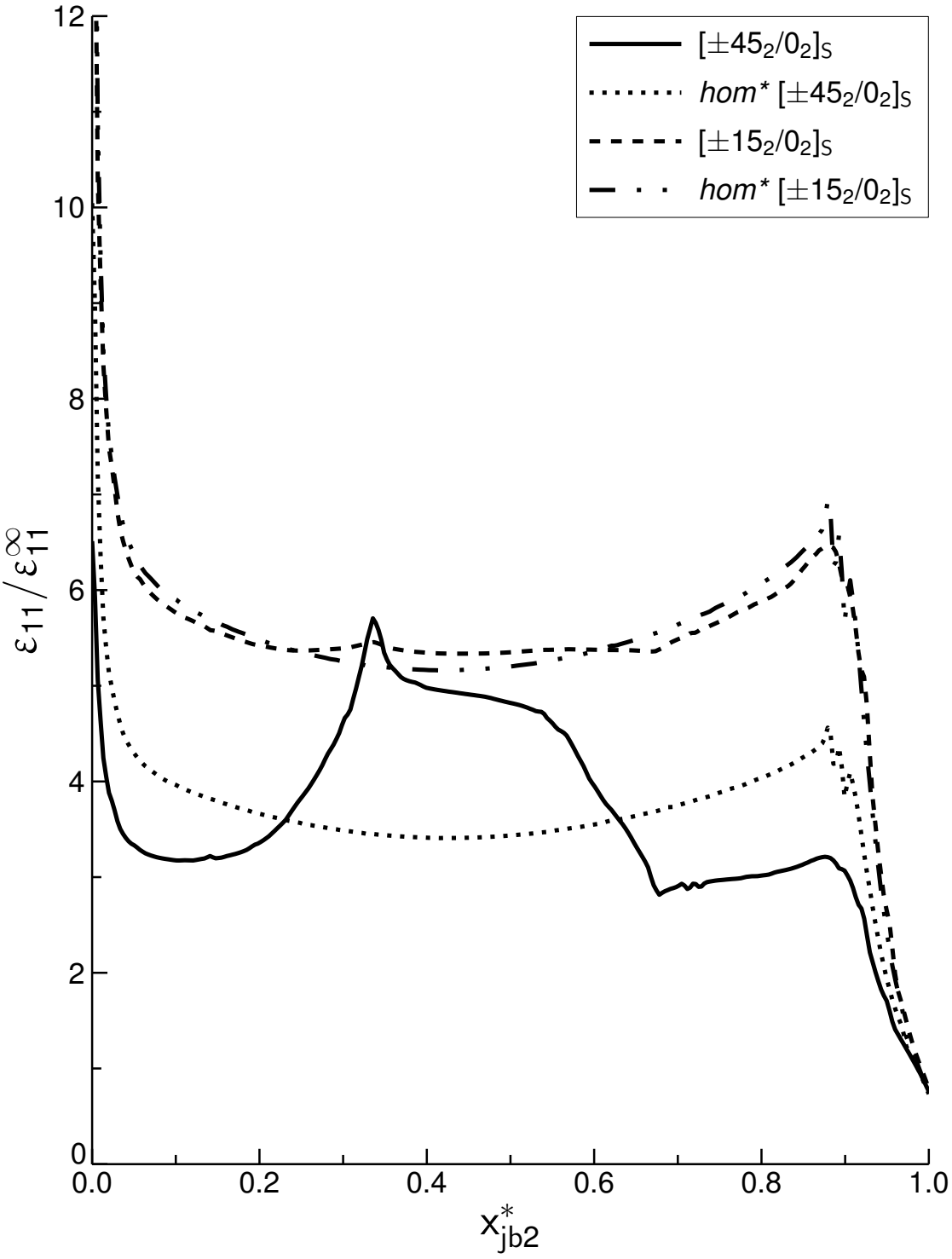

Figure 5.5 Plot of normalized ϵ_{11} versus x^*_{jb2} at bondline 2 in adhesive for the cases of laminate configurations of $[\pm 45_2/0_2]_S$, *homogenized* $[\pm 45_2/0_2]_S$, $[\pm 15_2/0_2]_S$, and *homogenized* $[\pm 15_2/0_2]_S$.

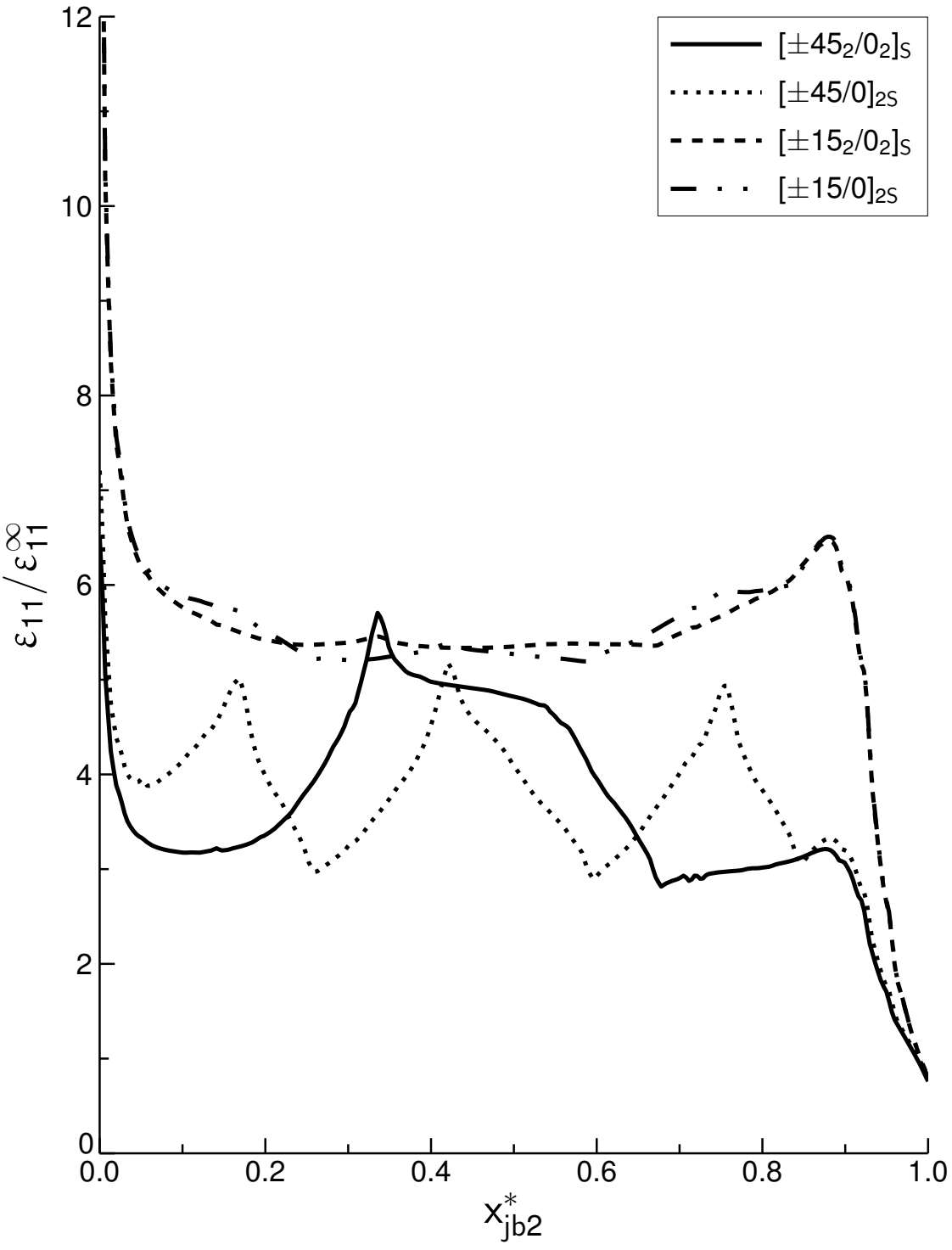

Figure 5.6 Plot of normalized ϵ_{11} versus x_{jb2}^{*} at bondline 2 in adhesive for the cases of laminate configurations of $[\pm 45_2/0_2]_S$, $[\pm 45/0]_{2S}$, $[\pm 15_2/0_2]_S$, and $[\pm 15/0]_{2S}$.

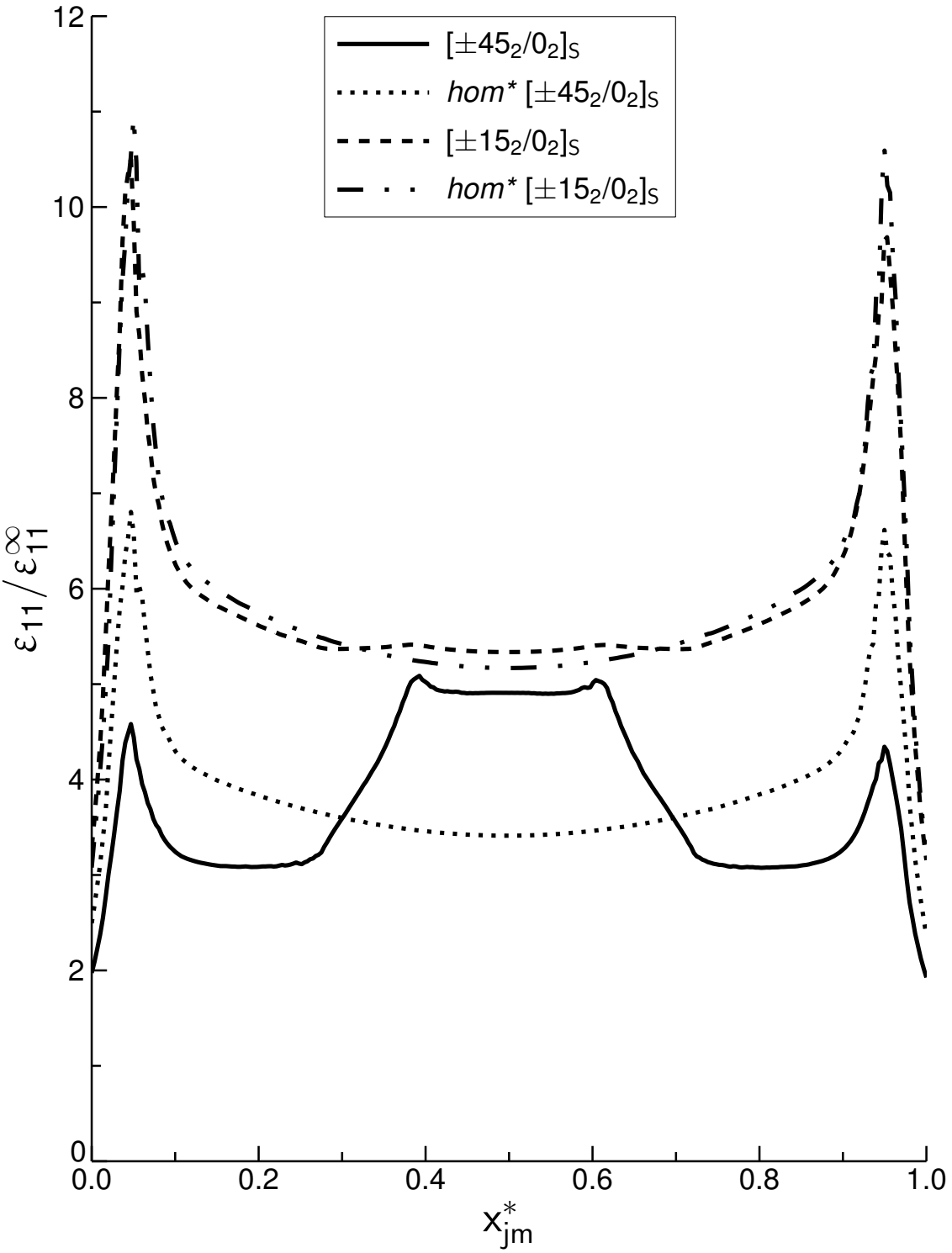

Figure 5.7 Plot of normalized ϵ_{11} versus x^*_{jm} at midline in adhesive for the cases of laminate configurations of $[\pm 45_2/0_2]_S$, *homogenized* $[\pm 45_2/0_2]_S$, $[\pm 15_2/0_2]_S$, and *homogenized* $[\pm 15_2/0_2]_S$.

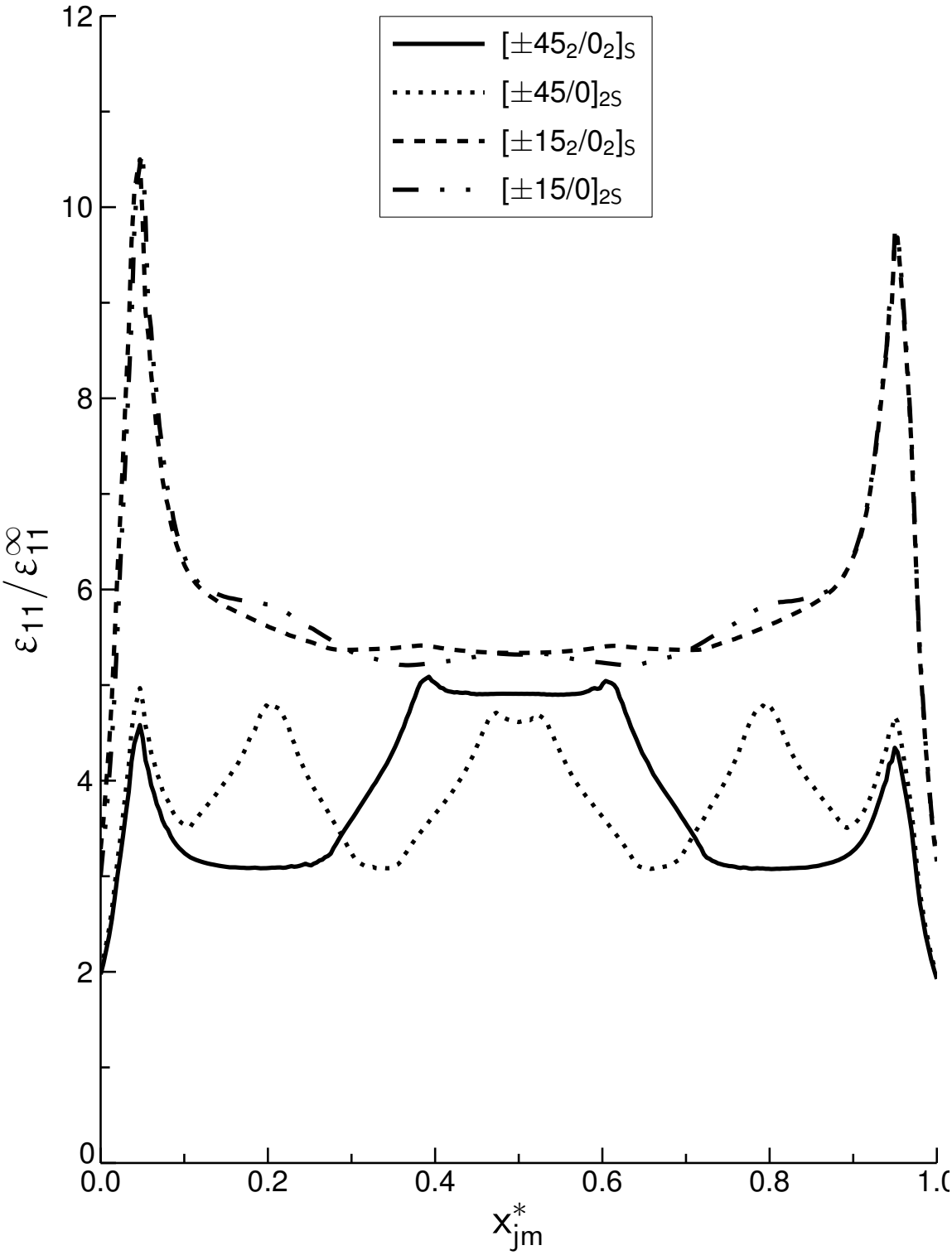

Figure 5.8 Plot of normalized ϵ_{11} versus x^*_{jm} at midline in adhesive for the cases of laminate configurations of $[\pm 45_2/0_2]_S$, $[\pm 45/0]_{2S}$, $[\pm 15_2/0_2]_S$, and $[\pm 15/0]_{2S}$.

negative in value, and the sharp reductions in shear strain occurring at the normalized distance of 0.89 in the adherend along the bondline are not as sharp in the adjacent adhesive region along the bondline. The largest magnitudes of shear strain occur near the acute tip of the adherend within a distance of a characteristic element length from the tip (0.003 in) for the laminated cases of $[\pm 15_2/0_2]_S$ and $[\pm 15/0]_{2S}$, and for the cases of homogenized $[\pm 15_2/0_2]_S$ and homogenized $[\pm 45_2/0_2]_S$. The corresponding normalized values are -26.8, -27.1, -28.1, and -15.8, respectively. However, the peak magnitudes of shear strain for the laminated cases of $[\pm 45_2/0_2]_S$ and $[\pm 45/0]_{2S}$ occur at the normalized distance of approximately 0.45, having normalized values of -20.0 and -16.3, respectively. Local variations in shear strain occur in the adhesive along the bondline at locations adjacent to the ply interface junctions, as exhibited in the distributions of longitudinal strain.

The distributions of normalized shear strain, ϵ_{13}, at the adhesive midline are shown in Figures 5.13 and 5.14 for all cases. These distributions exhibit similar characteristics to those in the adhesive at the bondline, but additionally exhibit symmetry about the midpoint of the adhesive midline, as illustrated in the distributions of longitudinal strain, and as must occur as previously described. This results in a reduction in the magnitudes of local gradients in shear strain occurring near the beginning of the adhesive midline, but a slight increase in those occurring near the end. In addition, the overall magnitudes of shear strain remain similar to those along the bondline in the adhesive.

The distributions of normalized longitudinal strain, ϵ_{11}, for the cases of $[\pm\theta_2/0_2]_S$ and homogenized $[\pm\theta_2/0_2]_S$ along x_a^*-axes, as defined in Figure 5.1, at various locations in adherend 2 through the thickness (values of z) are presented in Figures 5.15 through 5.22. The locations through the thickness were chosen such that the effects of varying stiffness through the adherend could be isolated in the distributions of strains within the adherend. These locations were chosen to be the midply locations for the cases of $[\pm\theta_2/0_2]_S$, and the top and bottom of the adherend of the overall configuration. The locations for these axes were retained in the cases of homogenized laminates in order to investigate the corresponding distributions of strains in the absence of mismatch

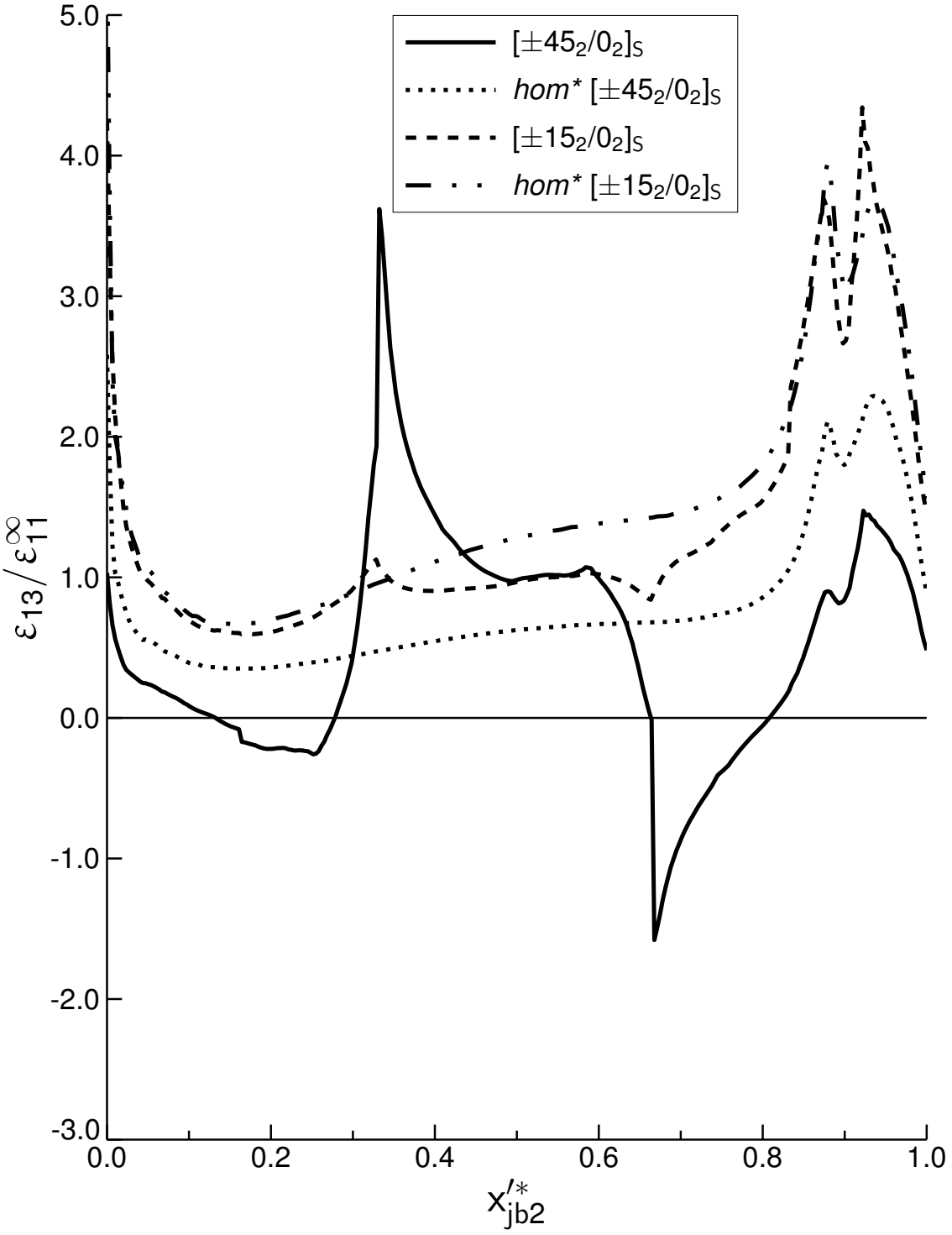

Figure 5.9 Plot of normalized ϵ_{13} versus x'^{*}_{jb2} at bondline 2 in adherend for the cases of laminate configurations of $[\pm 45_2/0_2]_S$, *homogenized* $[\pm 45_2/0_2]_S$, $[\pm 15_2/0_2]_S$, and *homogenized* $[\pm 15_2/0_2]_S$.

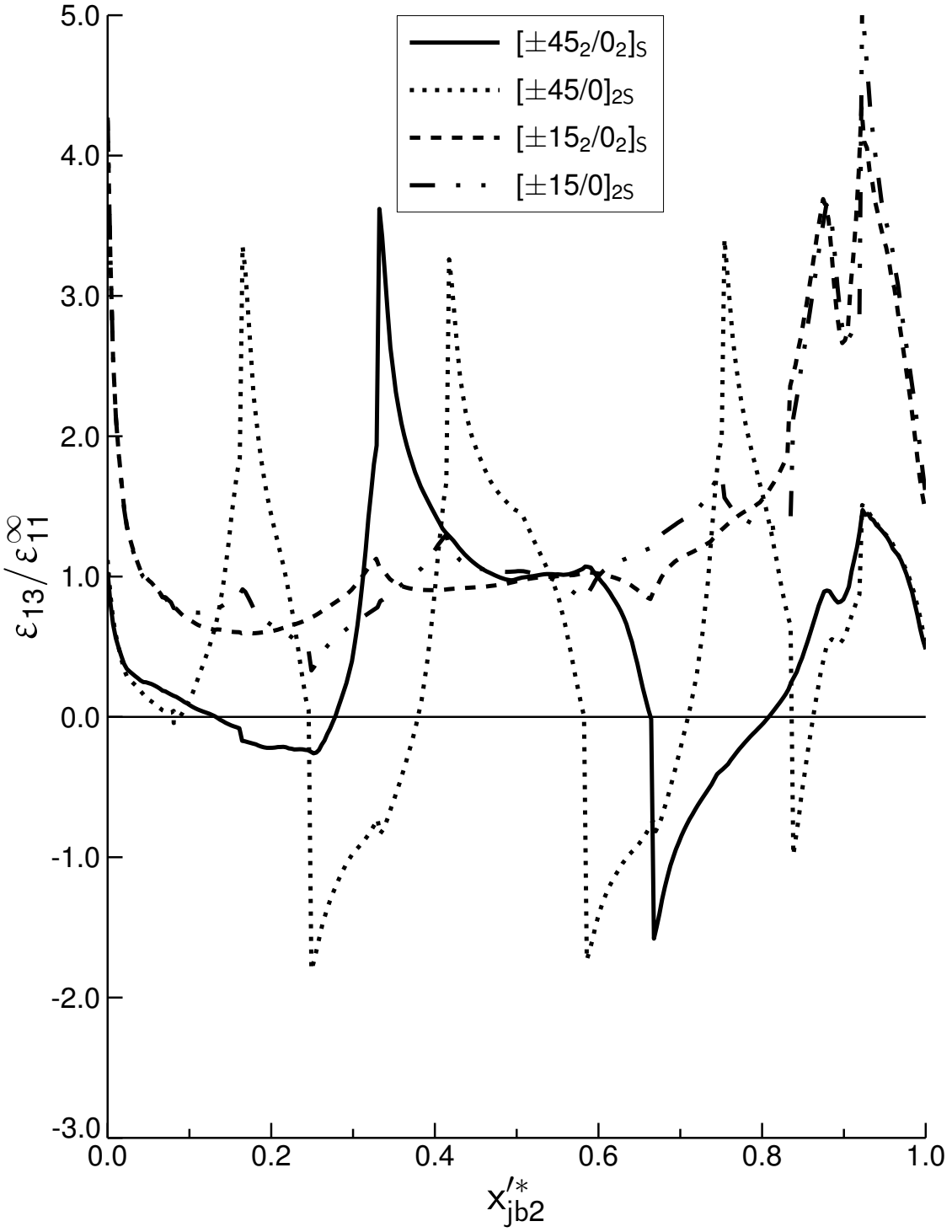

Figure 5.10 Plot of normalized ϵ_{13} versus x'^{*}_{jb2} at bondline 2 in adherend for the cases of laminate configurations of $[\pm 45_2/0_2]_S$, $[\pm 45/0]_{2S}$, $[\pm 15_2/0_2]_S$, and $[\pm 15/0]_{2S}$.

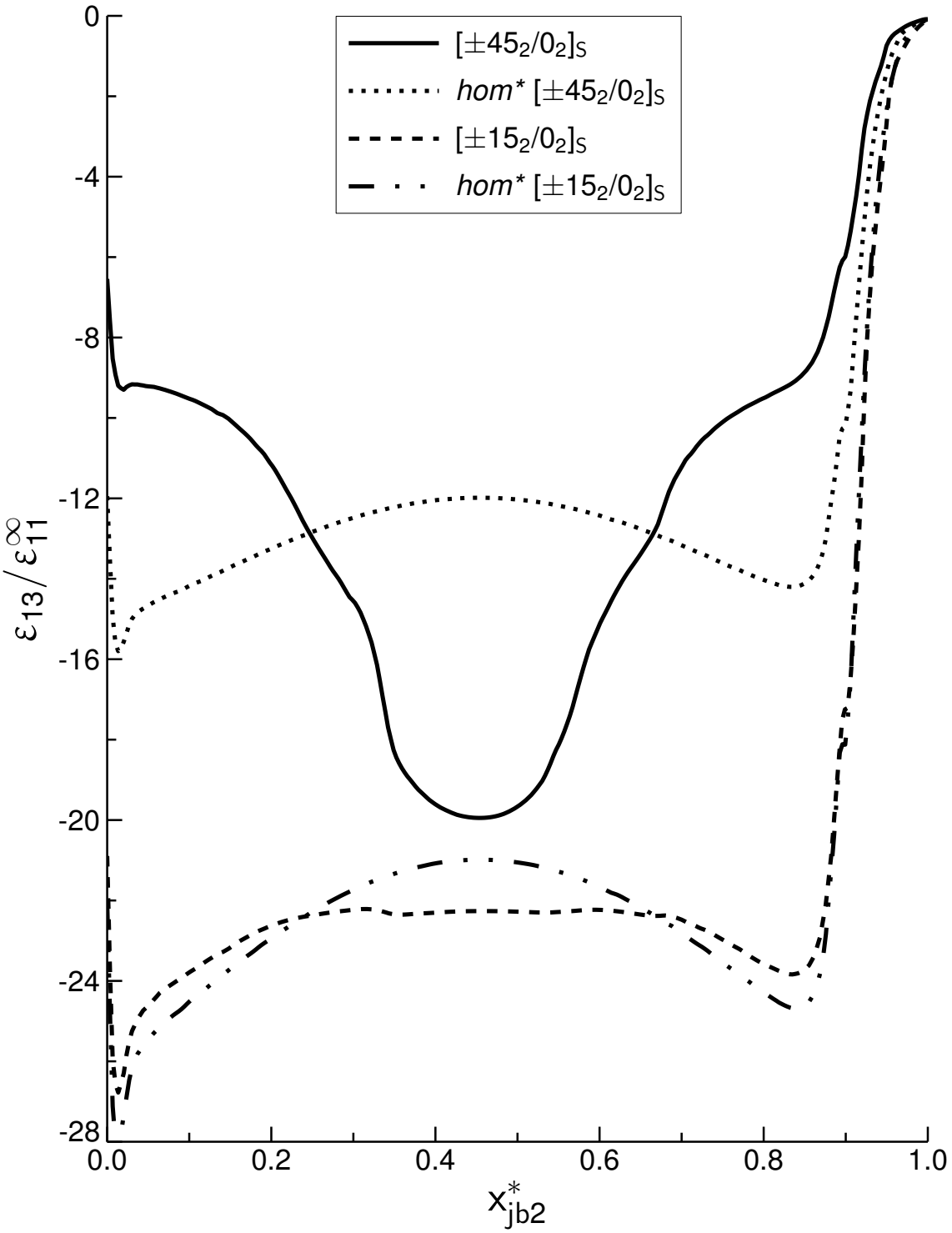

Figure 5.11 Plot of normalized ϵ_{13} versus x^*_{jb2} at bondline 2 in adhesive for the cases of laminate configurations of $[\pm 45_2/0_2]_S$, *homogenized* $[\pm 45_2/0_2]_S$, $[\pm 15_2/0_2]_S$, and *homogenized* $[\pm 15_2/0_2]_S$.

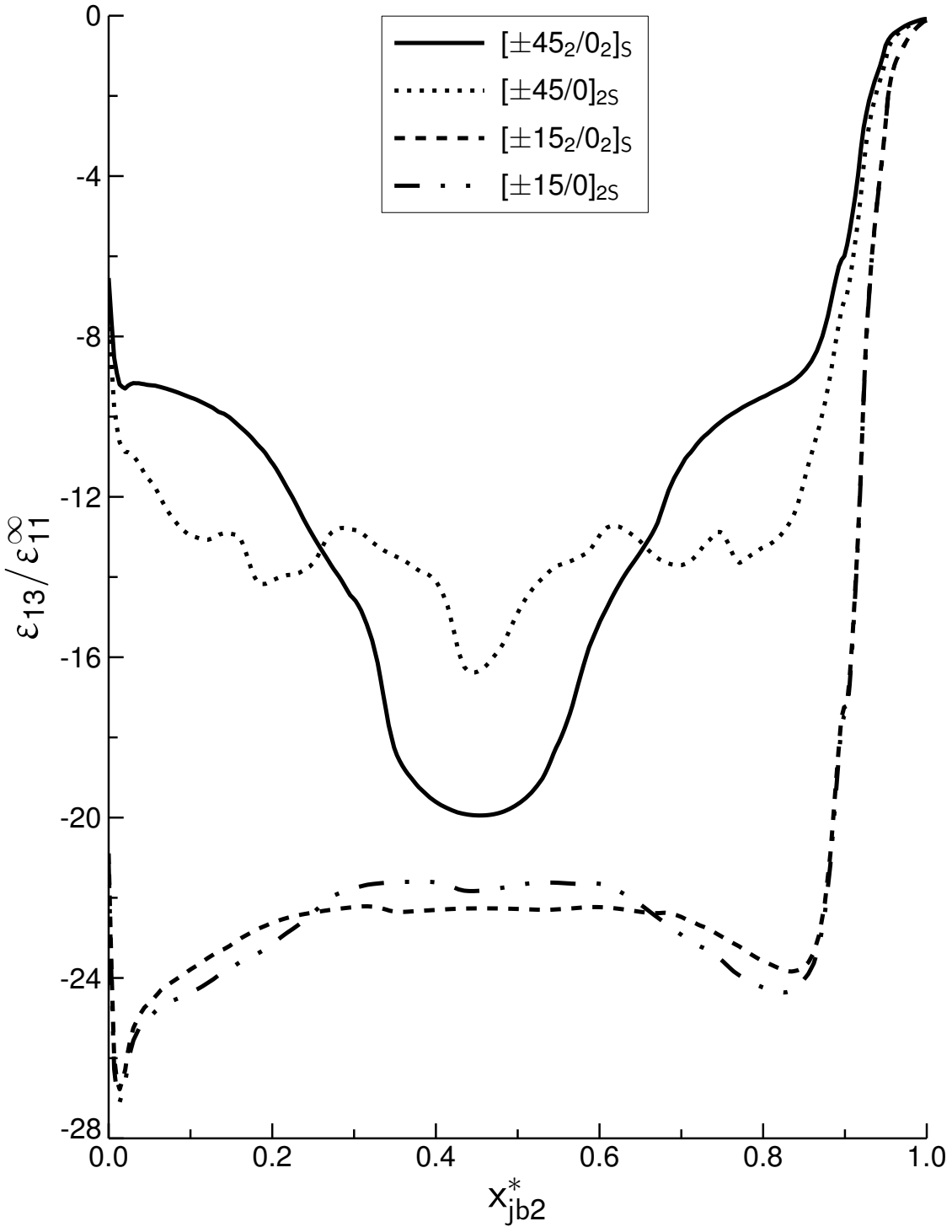

Figure 5.12 Plot of normalized ϵ_{13} versus x^*_{jb2} at bondline 2 in adhesive for the cases of laminate configurations of $[\pm 45_2/0_2]_S$, $[\pm 45/0]_{2S}$, $[\pm 15_2/0_2]_S$, and $[\pm 15/0]_{2S}$.

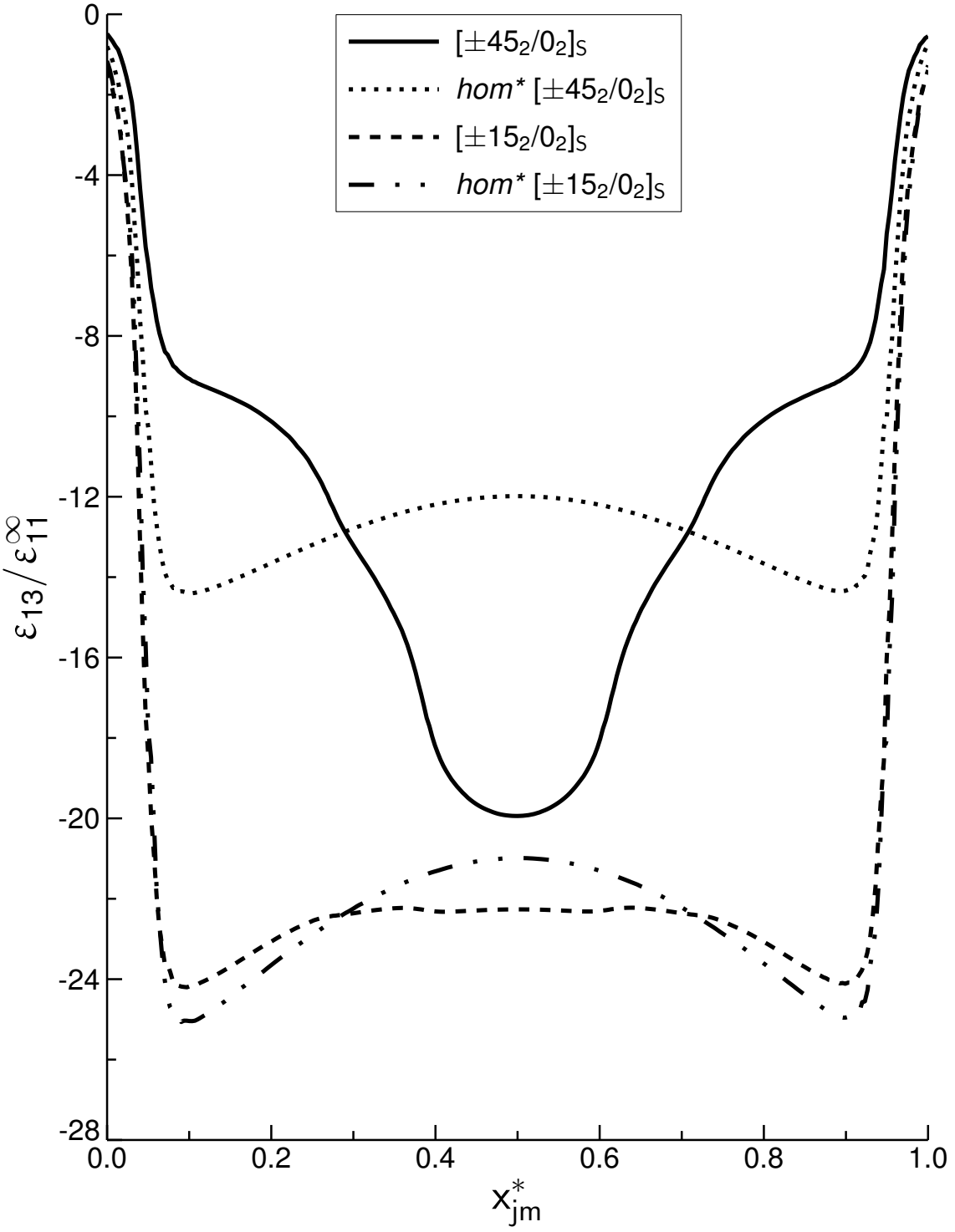

Figure 5.13 Plot of normalized ϵ_{13} versus x^*_{jm} at midline in adhesive for the cases of laminate configurations of $[\pm 45_2/0_2]_S$, *homogenized* $[\pm 45_2/0_2]_S$, $[\pm 15_2/0_2]_S$, and *homogenized* $[\pm 15_2/0_2]_S$.

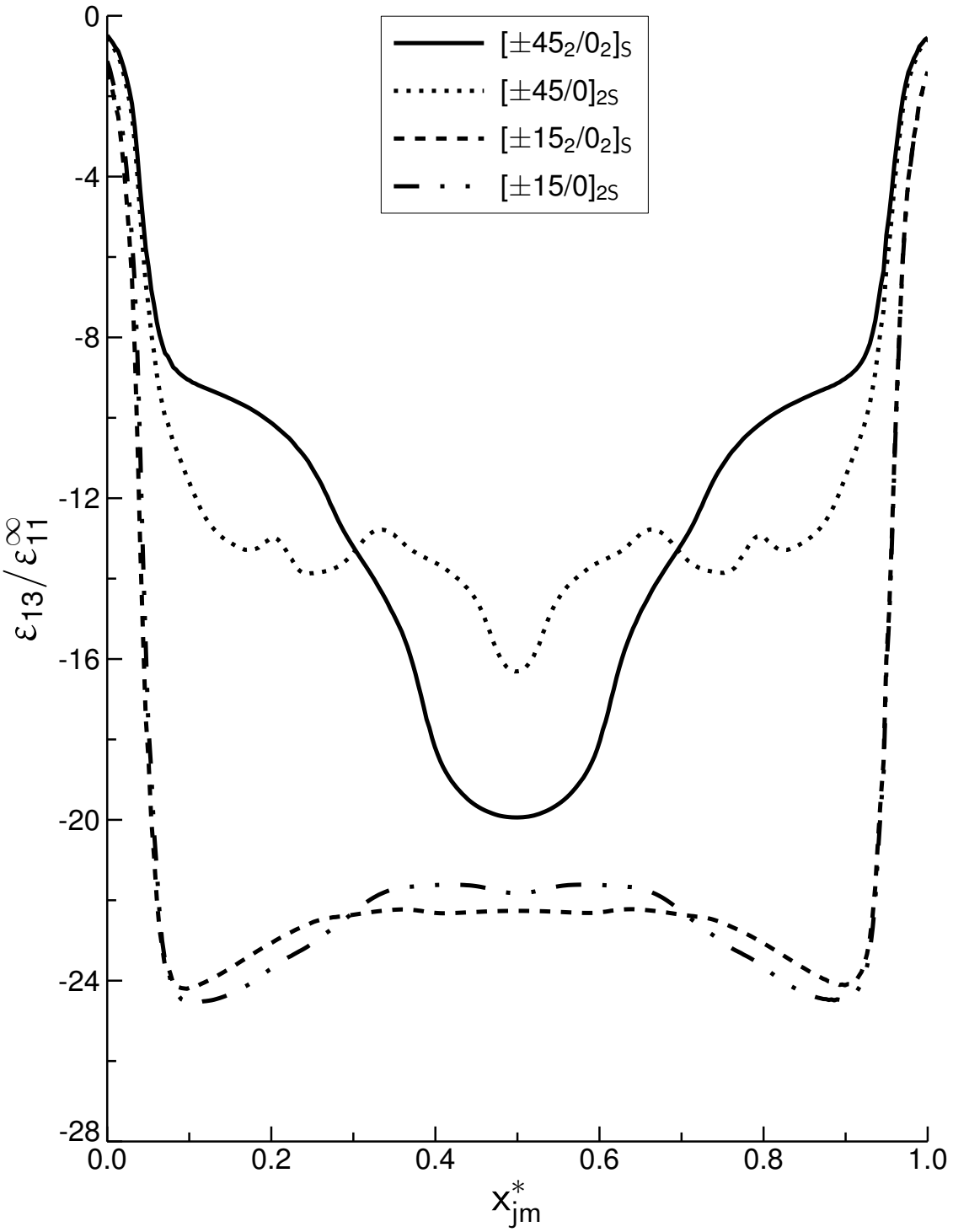

Figure 5.14 Plot of normalized ϵ_{13} versus x^*_{jm} at midline in adhesive for the cases of laminate configurations of $[\pm 45_2/0_2]_S$, $[\pm 45/0]_{2S}$, $[\pm 15_2/0_2]_S$, and $[\pm 15/0]_{2S}$.

in stiffness properties within the adherend. Similar plots are presented for the cases of $[\pm\theta/0]_{2S}$ in Figures 5.23 and 5.24. For these cases, strain distributions along x_a^*-axes at the top and bottom of the adherend, in conjunction with similar strain distributions for the cases of $[\pm\theta_2/0_2]_S$, were found to be sufficient to characterize the strain behavior in the adherend in these cases, and thus are the only ones presented. For these plots, negative values of x_a^* span the joint region within the adherend, whereas positive values of x_a^* span the region immediately outside the joint region to the edge of the model.

The distributions of longitudinal strain exhibit similar behavior for all cases outside the joint region. In this region, the distributions show negative gradients in longitudinal strain for the through-thickness locations of z equal to 0.072 in, 0.066 in, 0.018 in, 0.006 in, and 0.0 in, and positive gradients in longitudinal strain for the through-thickness locations of z equal to 0.054 in, 0.042 in, and 0.030 in, starting at x_a^* values between 1 and 2. The largest gradients in longitduinal strain in this region occur farther from the centerline, which is located at z equal to 0.036 in. Variations in longitudinal strain occur near x_a^* equal to 0 throughout the thickness of the adherend. The point x_a^* equal to 0 identifies the beginning of the joint region, and physically represents the location beyond which (for x_a^* less than 0) the effective stiffness composition of the configuration through the z-direction, at any cross-section in x, changes due to varying stiffness contributions of each of the adherends and the adhesive.

The distributions of longitudinal strain for the homogenized cases and the laminated case of $[\pm 15_2/0_2]_S$ follow each other closely, showing similar trends along x_a^* within the adherend at all locations through the thickness. This indicates the strain behavior of the adherend in the absence of varying stiffness for the homogenized cases, and the intermediate case of $[\pm 15_2/0_2]_S$ approximating the homogenized cases in characteristic response. Within the joint region, that is for negative values of x_a^*, the magnitude of longitudinal strain generally increases towards the adhesive at all locations except for an initial decrease occurring at the locations of z equal to 0.018 in, 0.006 in, and 0.0 in. This increase is not necessarily monotonic and has slight local variations. For all cases, the distributions of longitudinal strain within the joint region

show a region of negative gradient leading to a local minimum value of longitudinal strain, followed by a region of positive gradient leading to a local maximum value of longitudinal strain near the adhesive. This occurs at all locations through the thickness, except for z greater than 0.054 in. These local minima in longitudinal strain occur within the joint region between x_a^* values of -0.5 and -0.7. In this region, at z equal to 0.054 in, there is a noticeable change in the gradient in longitudinal strain, but a local minimum in longitudinal strain does not occur. At the location of z equal to 0.066 in, adherend 2 does not extend within the joint region to span this region. However, for all cases, a local minimum in longitudinal strain occurs at this location of z prior to the joint region within a normalized distance of approximately 0.1 along x_a^*. At the location of z equal to 0.072 in, the gradient in longitudinal strain is only negative and results in a minimum value of longitudinal strain at x_a^* equal to 0.0. The maximum values of longitudinal strain at any location in z occur near the adhesive in all cases, with the greatest overall values occurring farthest from the centerline. This is illustrated through the normalized values of local peaks in longitudinal strain of 1.32, 1.18, 0.92, 1.13, 1.67, and 2.86 occurring at locations in z of 0.066 in, 0.054 in, 0.042 in, 0.030 in, 0.018 in, and 0.0 in, respectively, for the case of $[\pm 45_2/0_2]_S$. Similarly, for the corresponding homogenized 45° case, the normalized peak values of longitudinal strain at the corresponding locations in z are 1.31, 1.30, 1.18, 1.12, 1.15, and 2.86. It is also noted that the corresponding values for the homogenized 15° case are very close to those for the homogenized 45° case. For all cases, the values of normalized longitudinal strain always remain between 1.1 and 1.35 near the adhesive, except at the bottom of the adherend. At this location in z, there exists a region of steep positive gradient in longitudinal strain spanning a normalized distance of 0.5 from the adhesive.

The distributions of longitudinal strains for the laminated case of $[\pm 45_2/0_2]_S$ also indicate that the lower ±45° plies show higher values of longitudinal strain near the adhesive compared to those in the upper ±45° plies, with normalized values near the adhesive at the top and bottom locations of the adherend being 0.68 and 2.86, respectively. A similar trend is exhibited at the top and bottom of the adherend

for the homogenized cases with the normalized values of longitudinal strain for the cases of homogenized $[\pm 15_2/0_2]_S$ and homogenized $[\pm 45_2/0_2]_S$ being 0.44 and 0.56, respectively, at the top, and 3.18 and 3.14, respectively, at the bottom. The values of longitudinal strain for the laminated case of $[\pm 45_2/0_2]_S$ also decrease at locations in z of 0.054 in, 0.042 in, 0.018 in, and 0.006 in, just prior to the adhesive within a normalized distance of 1.0 from the adhesive. The distributions of longitudinal strain for the laminated case of $[\pm 45_2/0_2]_S$ exhibit the local effects of increases or decreases in longitudinal strain occurring at ply tips located at the various locations through the thickness of the adherend, in addition to the features characteristic of the distribution for the corresponding homogenized case.

The distributions of normalized shear strain, ϵ_{13}, for the cases of $[\pm\theta_2/0_2]_S$ and homogenized $[\pm\theta_2/0_2]_S$ along x_a^*-axes at various locations through the thickness of the adherend are presented in Figures 5.25 through 5.32. The distributions of normalized shear strain for the cases of $[\pm\theta/0]_{2S}$ are presented in Figures 5.33 and 5.34.

The distributions of shear strain share several characteristic trends with the distributions of longitudinal strain, and in general exhibit magnification of the effects occurring in the distributions of longitudinal strain. This is particularly true with the increases and decreases in the values of shear strain along x_a^* caused by the presence of ply tips at various locations through the thickness, particularly the decrease occurring near the edge of the joint region, where x_a^* equal to 0.0. Gradients in shear strain that arise for x_a^* values greater than 0.0 have positive values for locations of z equal to 0.072 in, 0.066 in, and 0.054 in, and negative values for all other locations of z. However, at the location of z equal to 0.054 in, the distributions of shear strain for all cases experience a local minimum at x_a^* equal to approximately -0.28, resulting from localized negative gradients in shear strain. Distributions of shear strain show positive and negative values in the adherend for all cases, with values being negative at x_a^* equal to 0.0 for all locations in z lower than and including z equal to 0.042 in, and near the adhesive within the $-45°$ plies at the locations of z equal to 0.018 in and 0.054 in for the laminated case of $[\pm 45_2/0_2]_S$. The magnitude of normalized shear strain is also higher for the cases of $[\pm 15_2/0_2]_S$ and homogenized $[\pm 15_2/0_2]_S$ in all

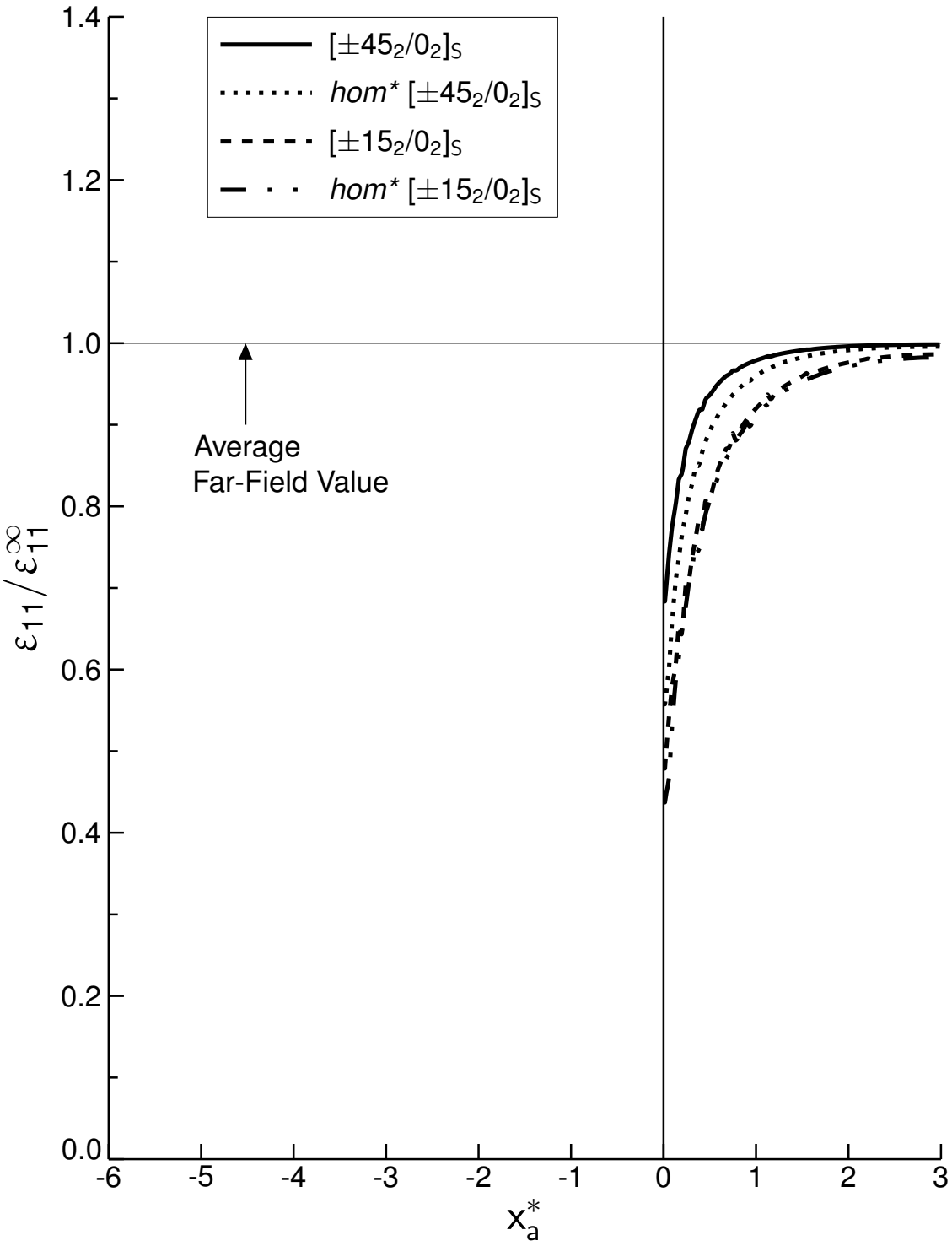

Figure 5.15 Plot of normalized ϵ_{11} versus x_a^* located at z equal to 0.072 in for the cases of laminate configurations of $[\pm 45_2/0_2]_S$, *homogenized* $[\pm 45_2/0_2]_S$, $[\pm 15_2/0_2]_S$, and *homogenized* $[\pm 15_2/0_2]_S$.

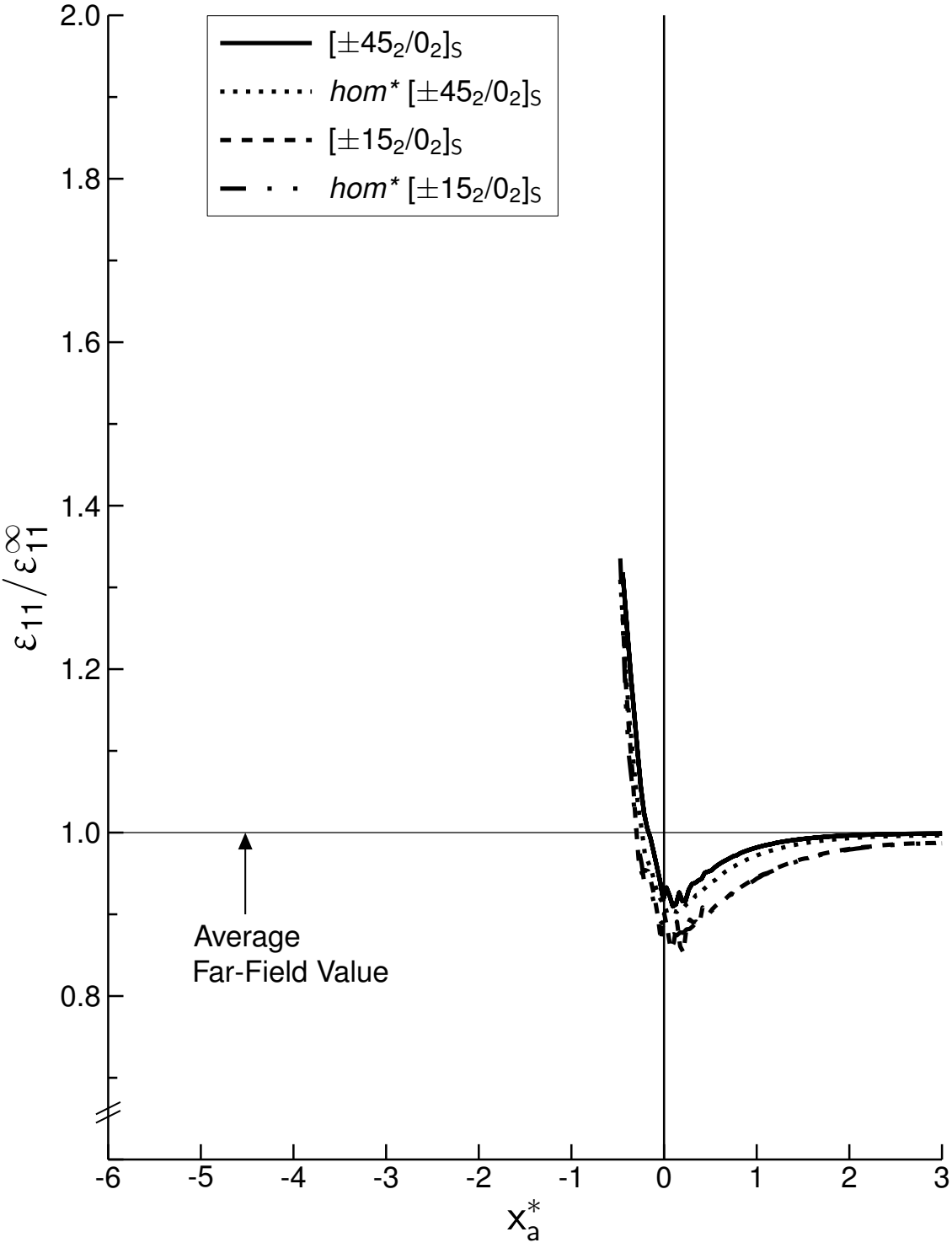

Figure 5.16 Plot of normalized ϵ_{11} versus x_a^* located at z equal to 0.066 in for the cases of laminate configurations of $[\pm 45_2/0_2]_S$, *homogenized* $[\pm 45_2/0_2]_S$, $[\pm 15_2/0_2]_S$, and *homogenized* $[\pm 15_2/0_2]_S$.

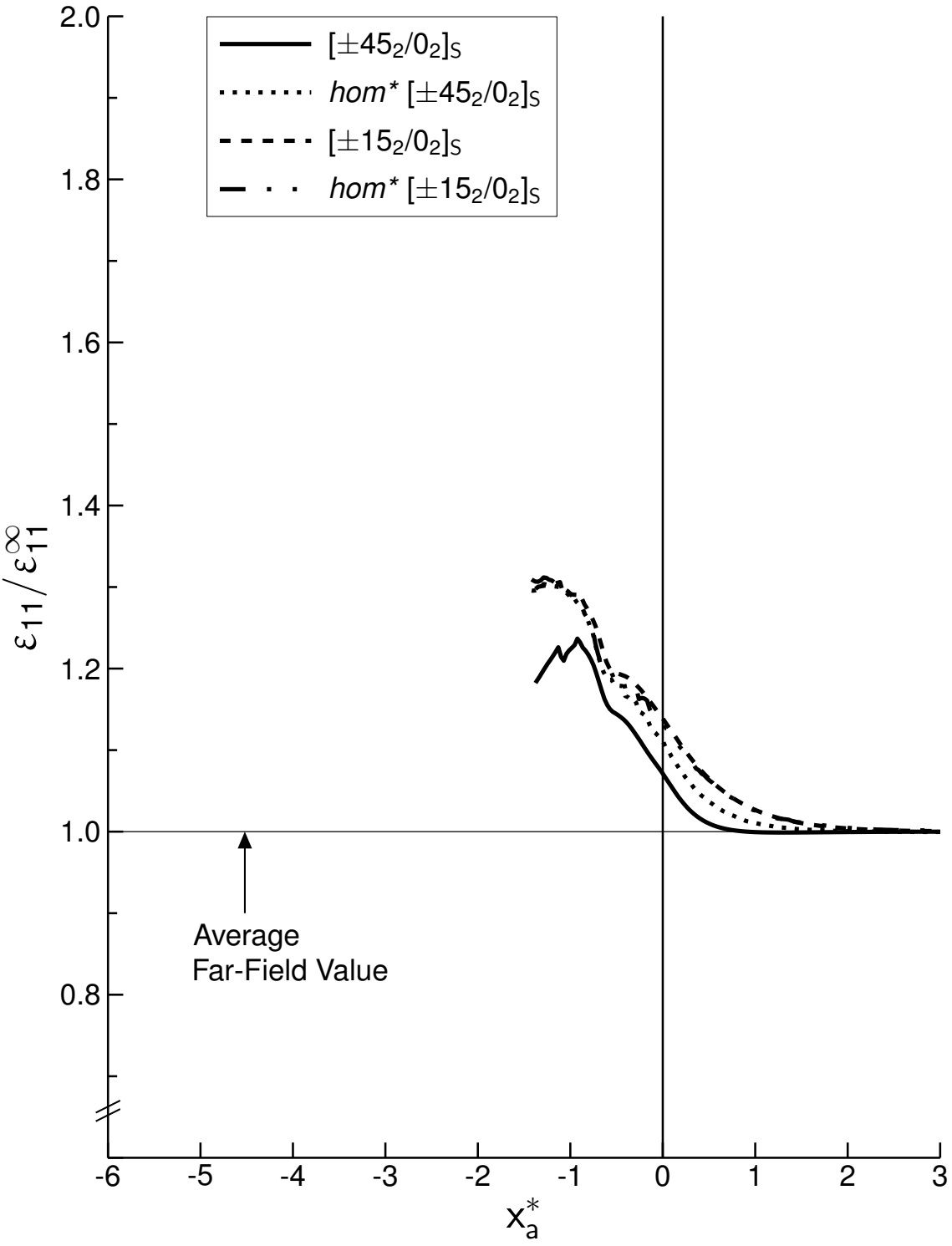

Figure 5.17 Plot of normalized ϵ_{11} versus x_a^* located at z equal to 0.054 in for the cases of laminate configurations of $[\pm 45_2/0_2]_S$, *homogenized* $[\pm 45_2/0_2]_S$, $[\pm 15_2/0_2]_S$, and *homogenized* $[\pm 15_2/0_2]_S$.

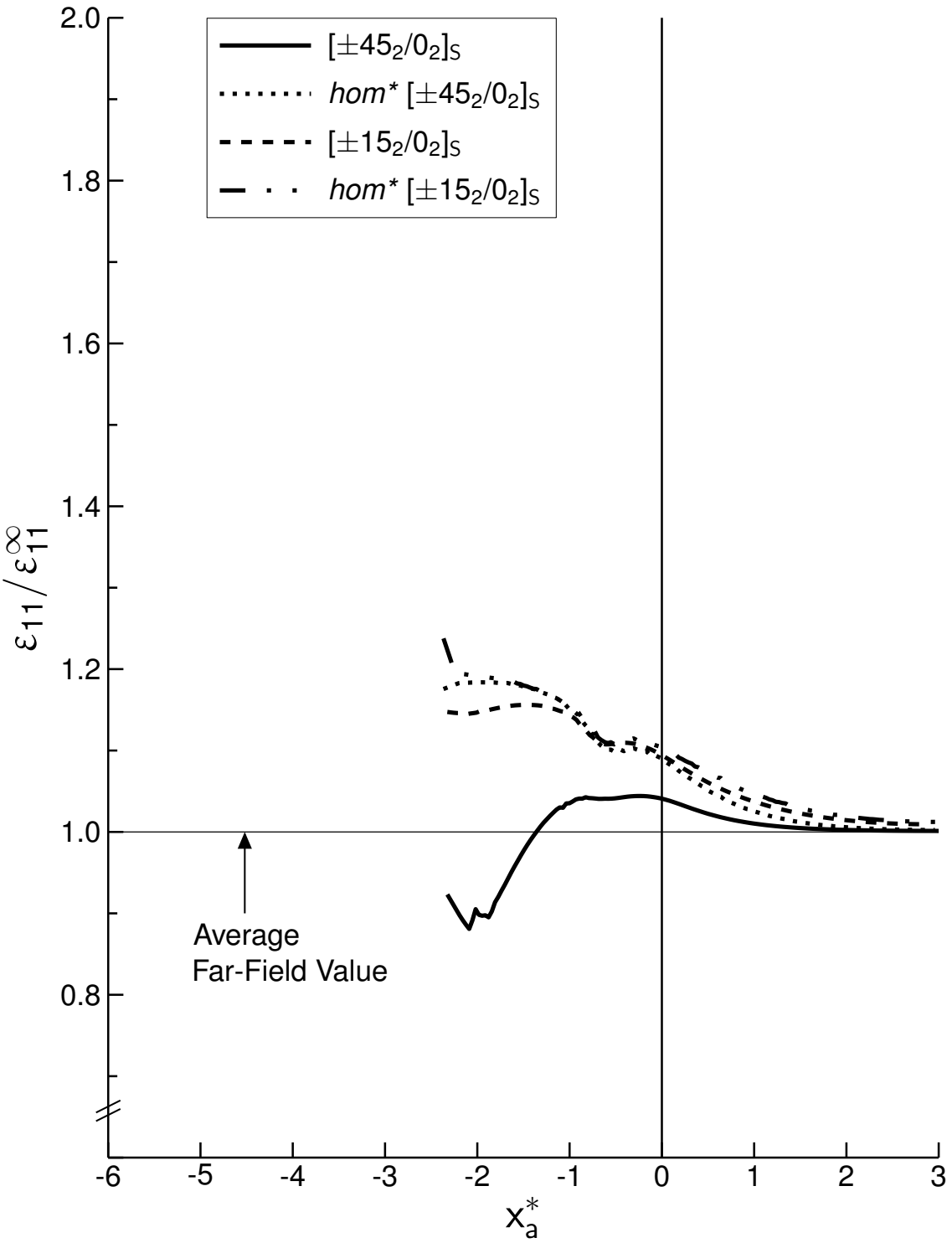

Figure 5.18 Plot of normalized ϵ_{11} versus x_a^* located at z equal to 0.042 in for the cases of laminate configurations of $[\pm 45_2/0_2]_S$, *homogenized* $[\pm 45_2/0_2]_S$, $[\pm 15_2/0_2]_S$, and *homogenized* $[\pm 15_2/0_2]_S$.

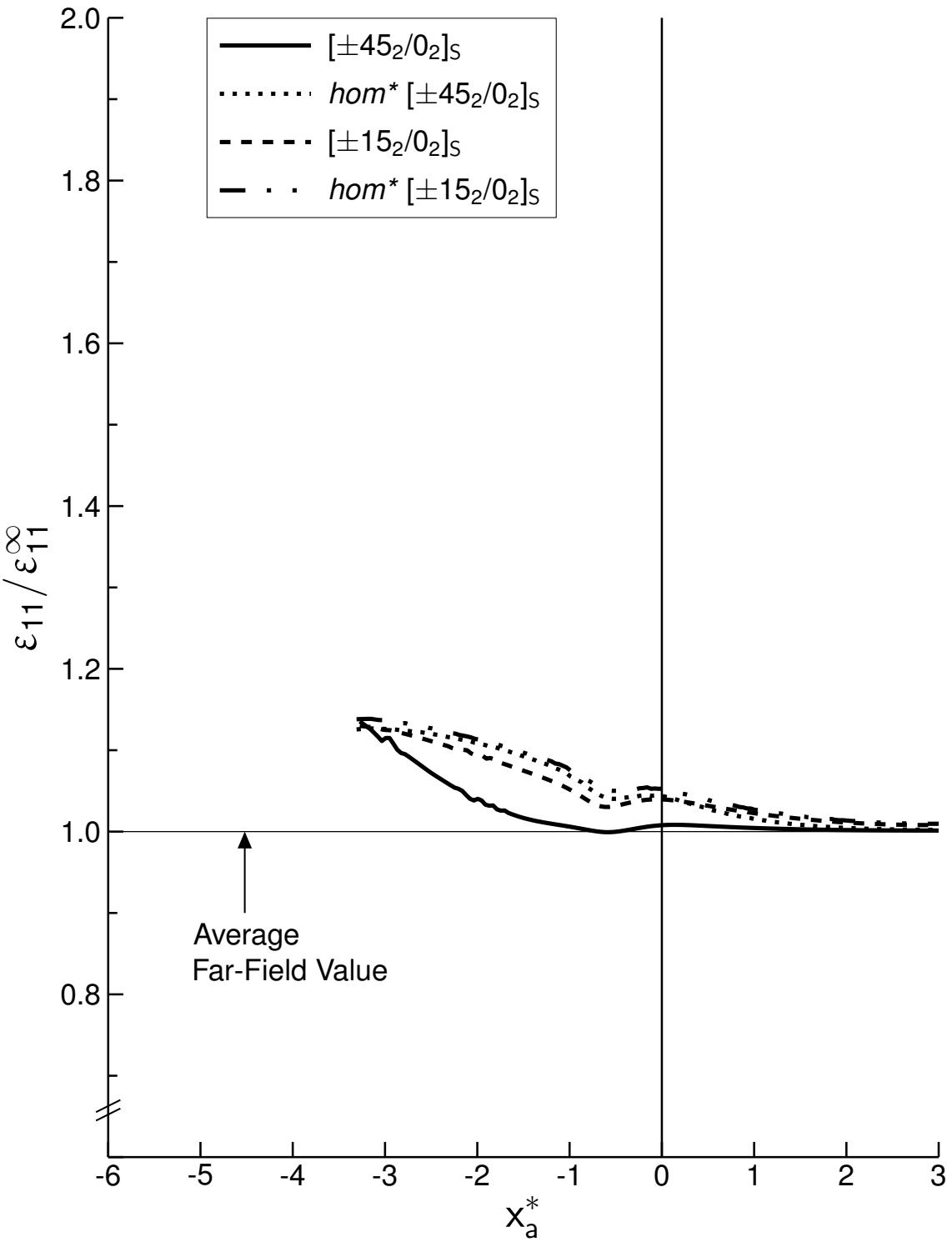

Figure 5.19 Plot of normalized ϵ_{11} versus x_a^* located at z equal to 0.030 in for the cases of laminate configurations of $[\pm 45_2/0_2]_S$, *homogenized* $[\pm 45_2/0_2]_S$, $[\pm 15_2/0_2]_S$, and *homogenized* $[\pm 15_2/0_2]_S$.

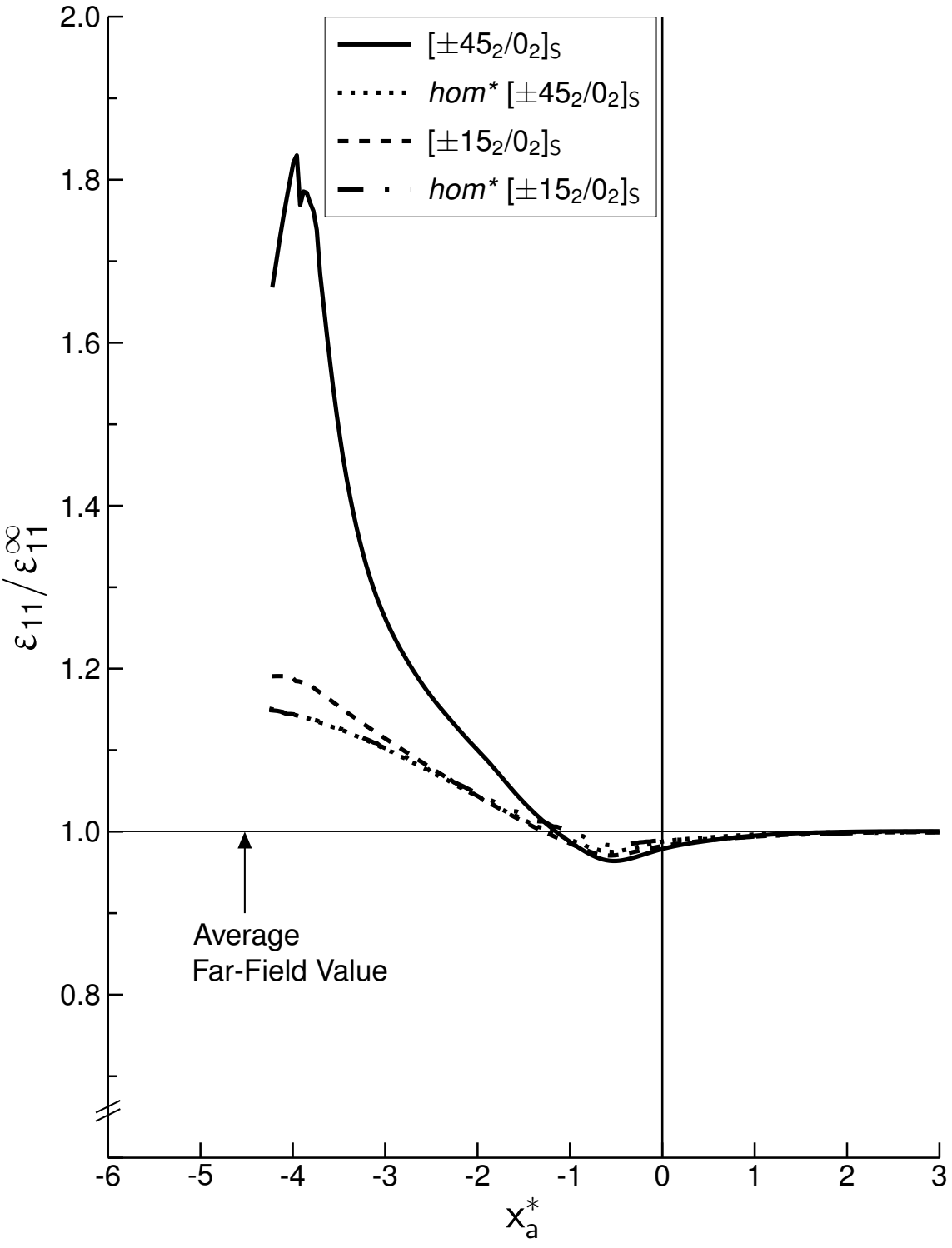

Figure 5.20 Plot of normalized ϵ_{11} versus x_a^* located at z equal to 0.018 in for the cases of laminate configurations of $[\pm 45_2/0_2]_S$, *homogenized* $[\pm 45_2/0_2]_S$, $[\pm 15_2/0_2]_S$, and *homogenized* $[\pm 15_2/0_2]_S$.

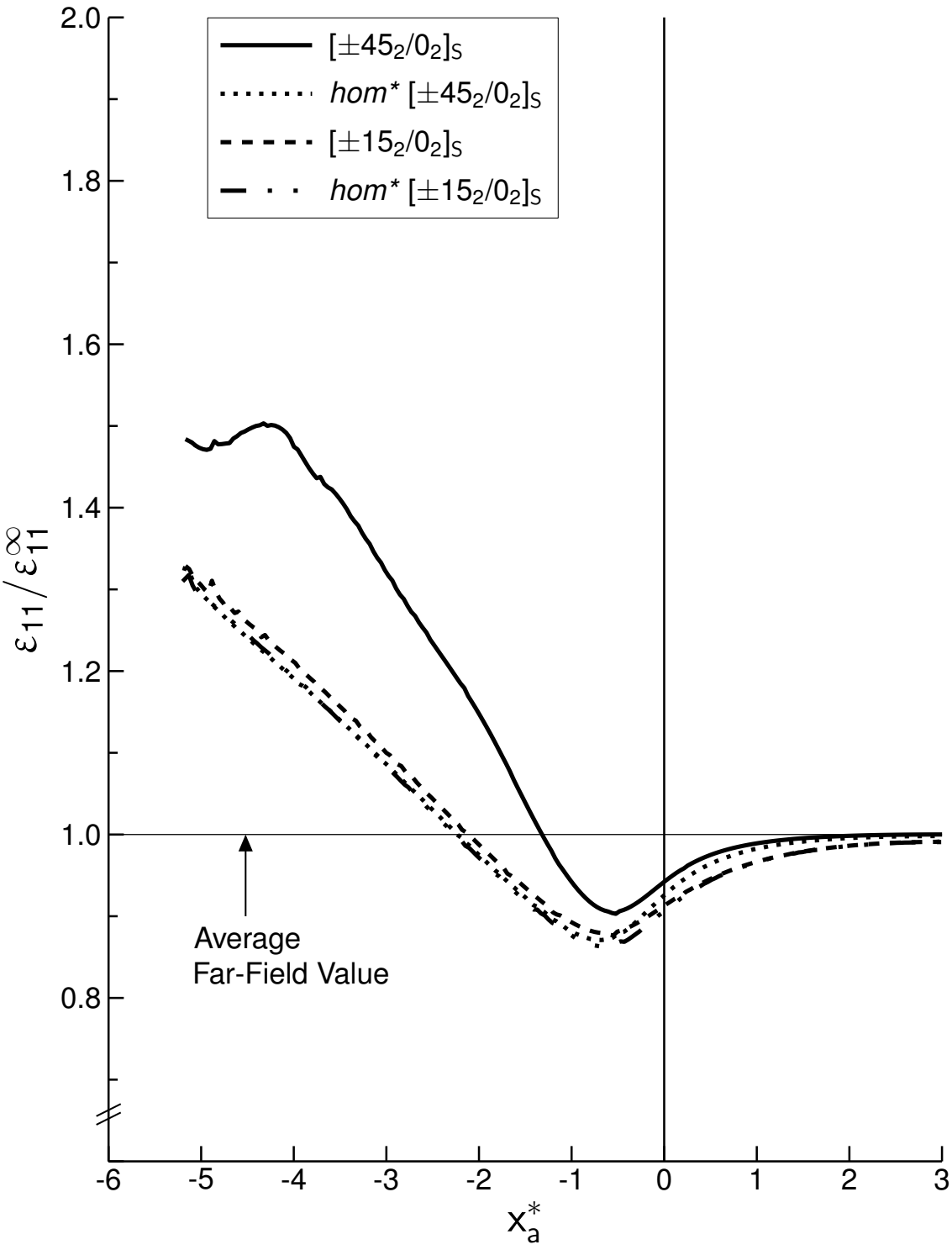

Figure 5.21 Plot of normalized ϵ_{11} versus x_a^* located at z equal to 0.006 in for the cases of laminate configurations of $[\pm 45_2/0_2]_S$, *homogenized* $[\pm 45_2/0_2]_S$, $[\pm 15_2/0_2]_S$, and *homogenized* $[\pm 15_2/0_2]_S$.

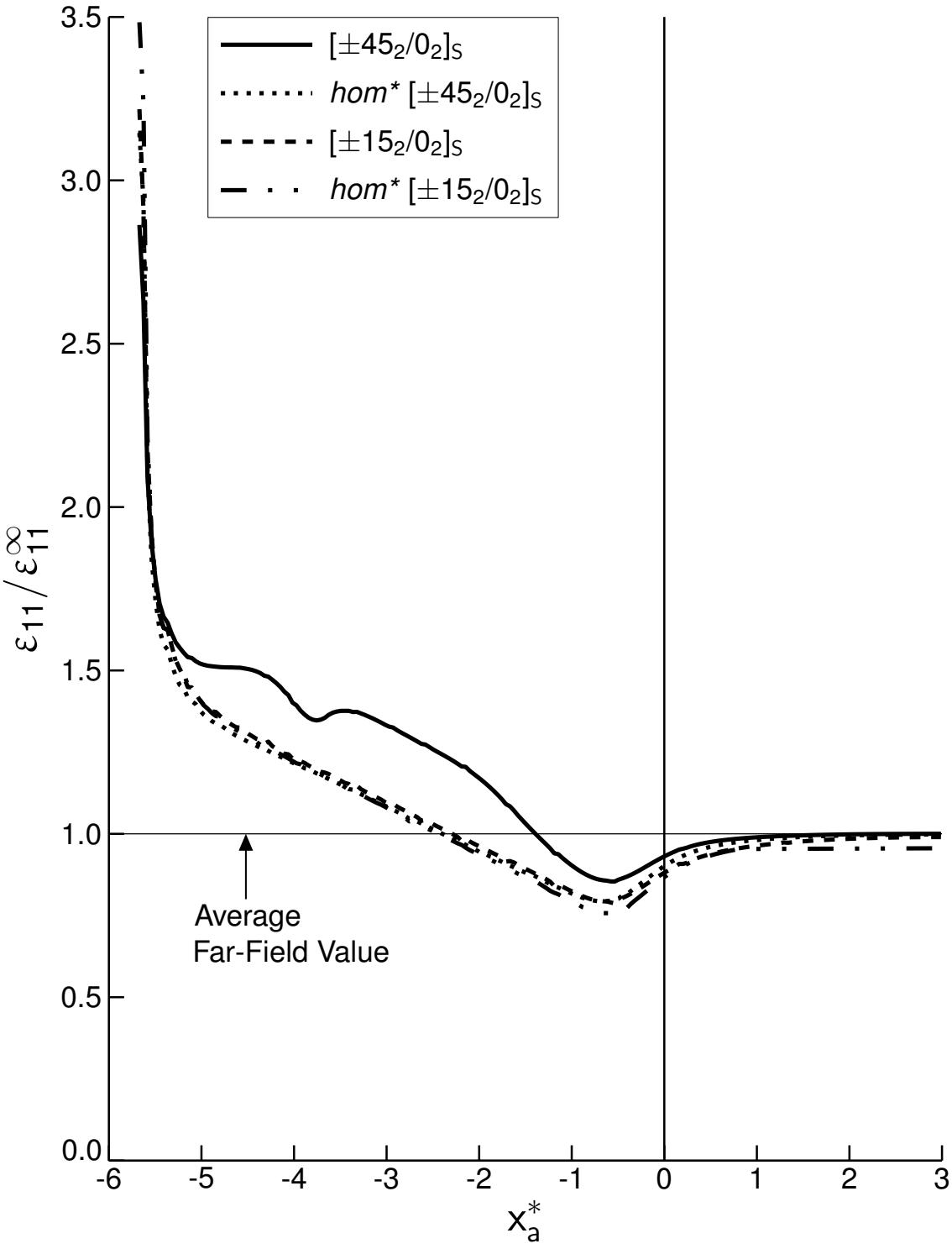

Figure 5.22 Plot of normalized ϵ_{11} versus x_a^* located at z equal to 0.0 in for the cases of laminate configurations of $[\pm 45_2/0_2]_S$, *homogenized* $[\pm 45_2/0_2]_S$, $[\pm 15_2/0_2]_S$, and *homogenized* $[\pm 15_2/0_2]_S$.

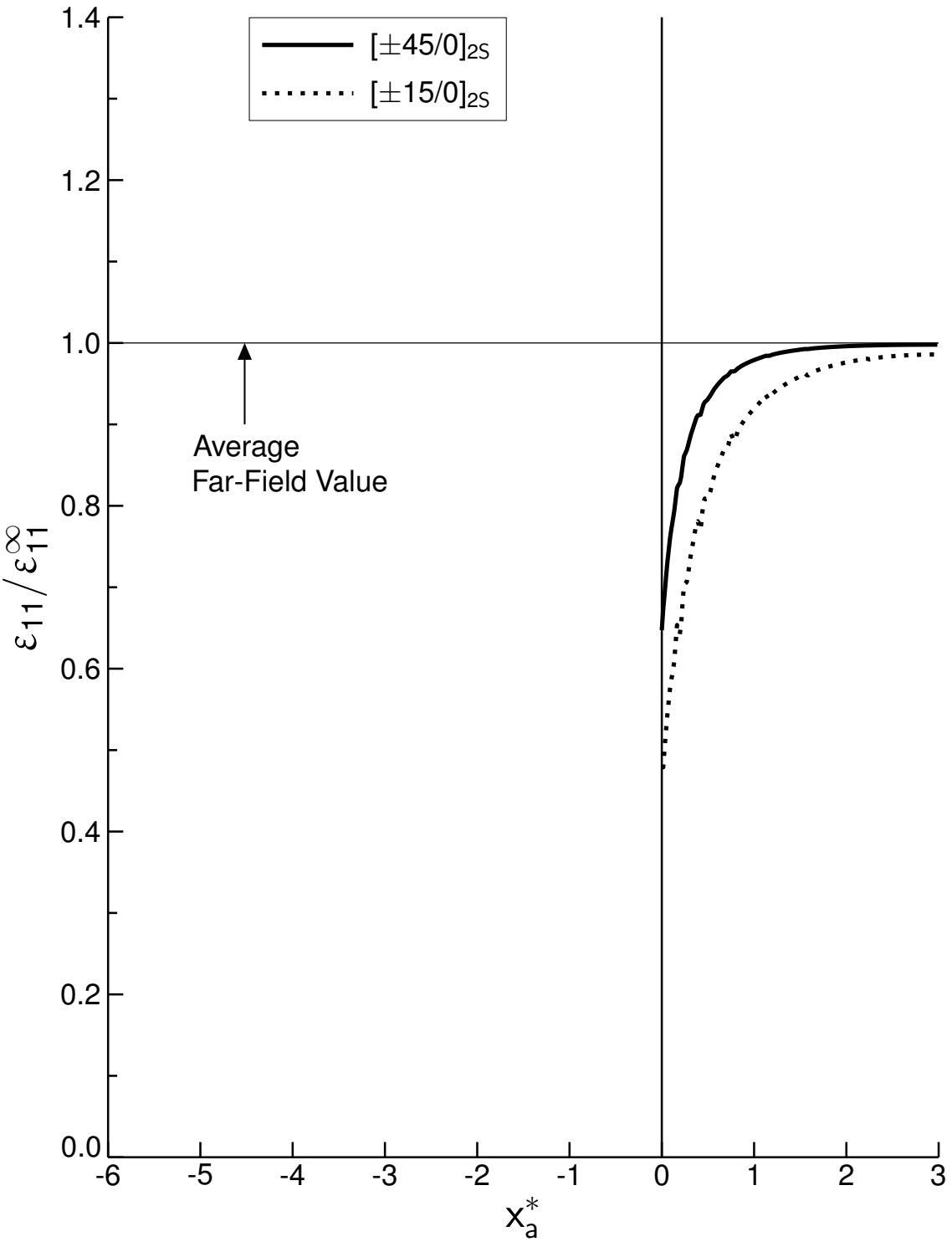

Figure 5.23 Plot of normalized ϵ_{11} versus x_a^* located at z equal to 0.072 in for the cases of laminate configurations of $[\pm 45/0]_{2S}$ and $[\pm 15/0]_{2S}$.

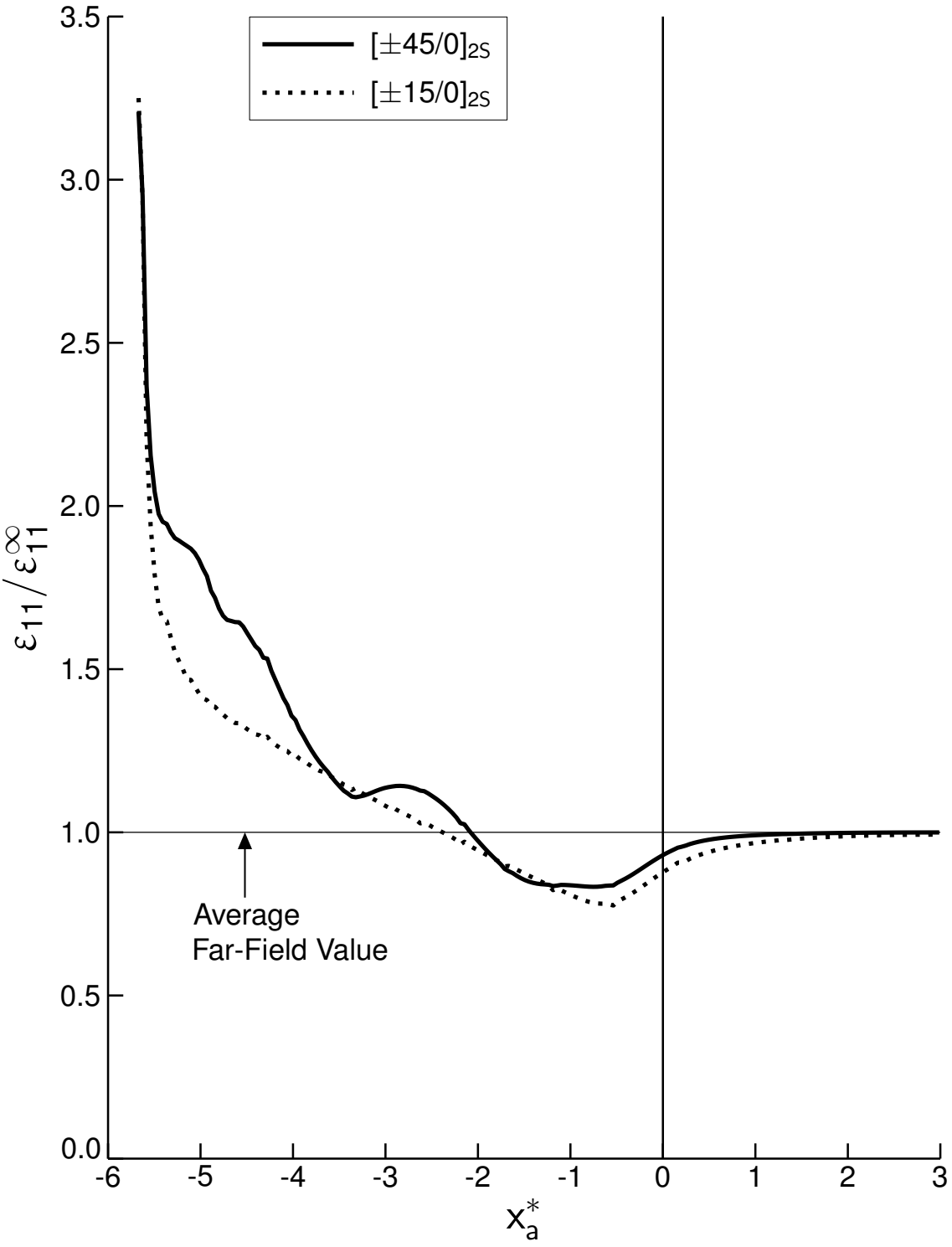

Figure 5.24 Plot of normalized ϵ_{11} versus x_a^* located at z equal to 0.0 in for the cases of laminate configurations of $[\pm 45/0]_{2S}$ and $[\pm 15/0]_{2S}$.

distributions compared to the corresponding distributions of cases having 45° plies. This is due to the stiffer in-plane properties. This is indicated through the values of normalized shear strain of 4.25, 5.46, 1.03, and 2.58 occurring at the acute tip of the adherend for the cases of $[\pm 15_2/0_2]_S$, homogenized $[\pm 15_2/0_2]_S$, $[\pm 45_2/0_2]_S$, and homogenized $[\pm 45_2/0_2]_S$, respectively. In addition, it is also noted that the ratio of the magnitudes of normalized shear strain for the case of homogenized $[\pm 15_2/0_2]_S$ to those for the case of homogenized $[\pm 45_2/0_2]_S$ is approximately 2.0 near the bondline in the joint region at the locations of z equal to 0.054 in, 0.042 in, 0.030 in, and 0.018 in.

The distributions of normalized strain along the x_a^*-axes for the laminated cases of $[\pm\theta/0]_{2S}$ exhibit similar trends to those occurring for the cases of $[\pm\theta_2/0_2]_S$, but with additional local strain variations due to the increased stiffness variation generated from a more variable $\pm\theta$ ply distribution. These effects are evident, particularly in the distributions of normalized longitudinal strain and normalized shear strain at z equal to 0.0 in, as shown in Figures 5.24 and 5.34, respectively, compared to those in Figures 5.22 and 5.32.

5.2 Effects of Scarf Angle (Equal Values)

The strain results for the scarf angle cases of 5°, 10°, and 15°, with equal values for both adherends, for the two-dimensional composite scarf joint configurations with the laminate of $[\pm 45_2/0_2]_S$ and adhesive thickness of 0.008 in are presented in this section. The distributions of strains for the scarf angle case of 10° are the same as those for the case in Section 5.1 with the laminated adherend configuration of $[\pm 45_2/0_2]_S$, representing the baseline configuration. Most importantly, the strains for the cases of the three scarf angles are generally very similar in terms of the characteristics of the distributions, as described in Section 5.1.

The distributions of normalized longitudinal strain, ϵ_{11}, for the cases of 5°, 10°, and 15°, at bondline 2 in adherend 2, at bondline 2 in the adhesive, and at the adhesive midline are presented in Figures 5.35, 5.36, and 5.37, respectively. These distribu-

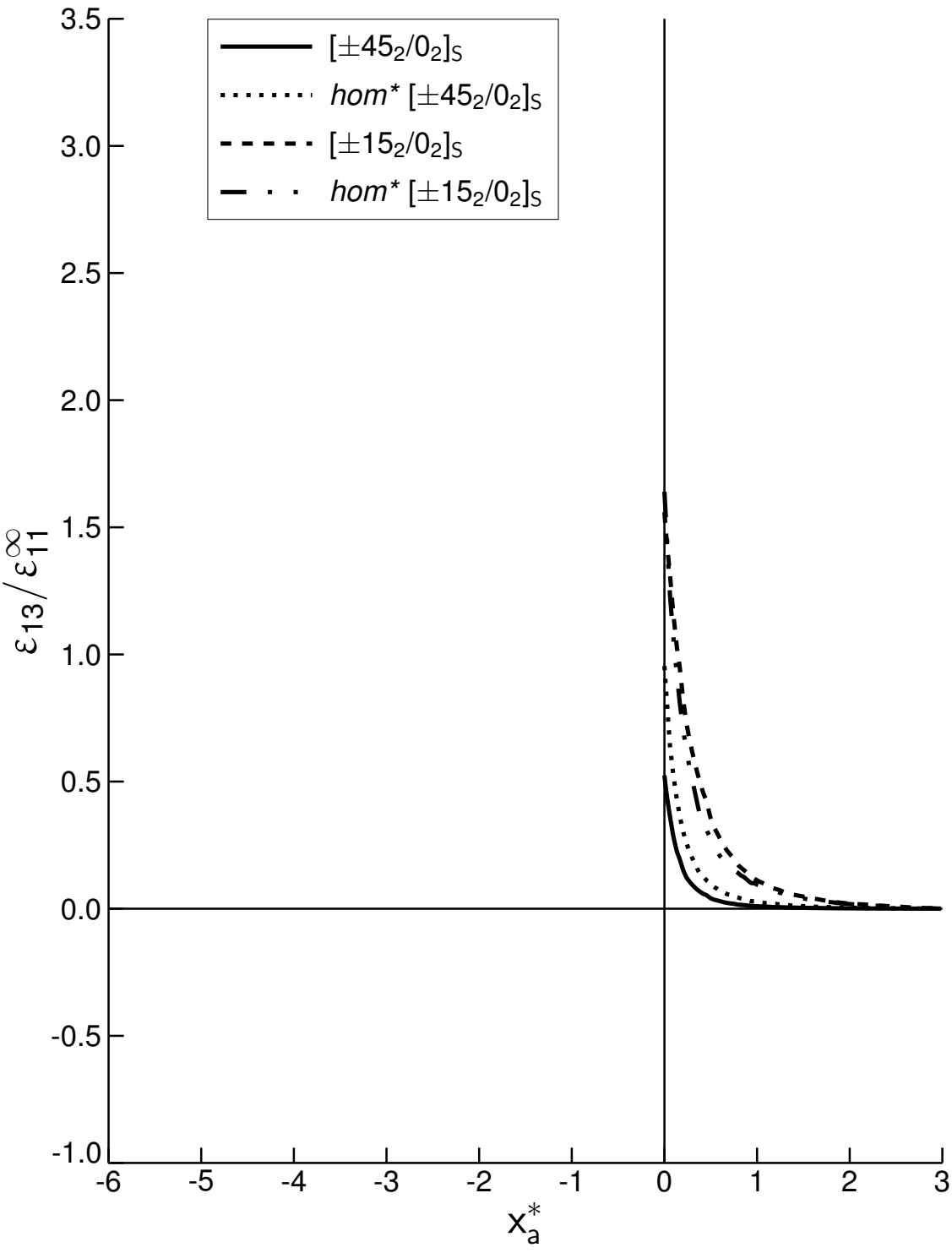

Figure 5.25 Plot of normalized ϵ_{13} versus x_a^* located at z equal to 0.072 in for the cases of laminate configurations of $[\pm 45_2/0_2]_S$, *homogenized* $[\pm 45_2/0_2]_S$, $[\pm 15_2/0_2]_S$, and *homogenized* $[\pm 15_2/0_2]_S$.

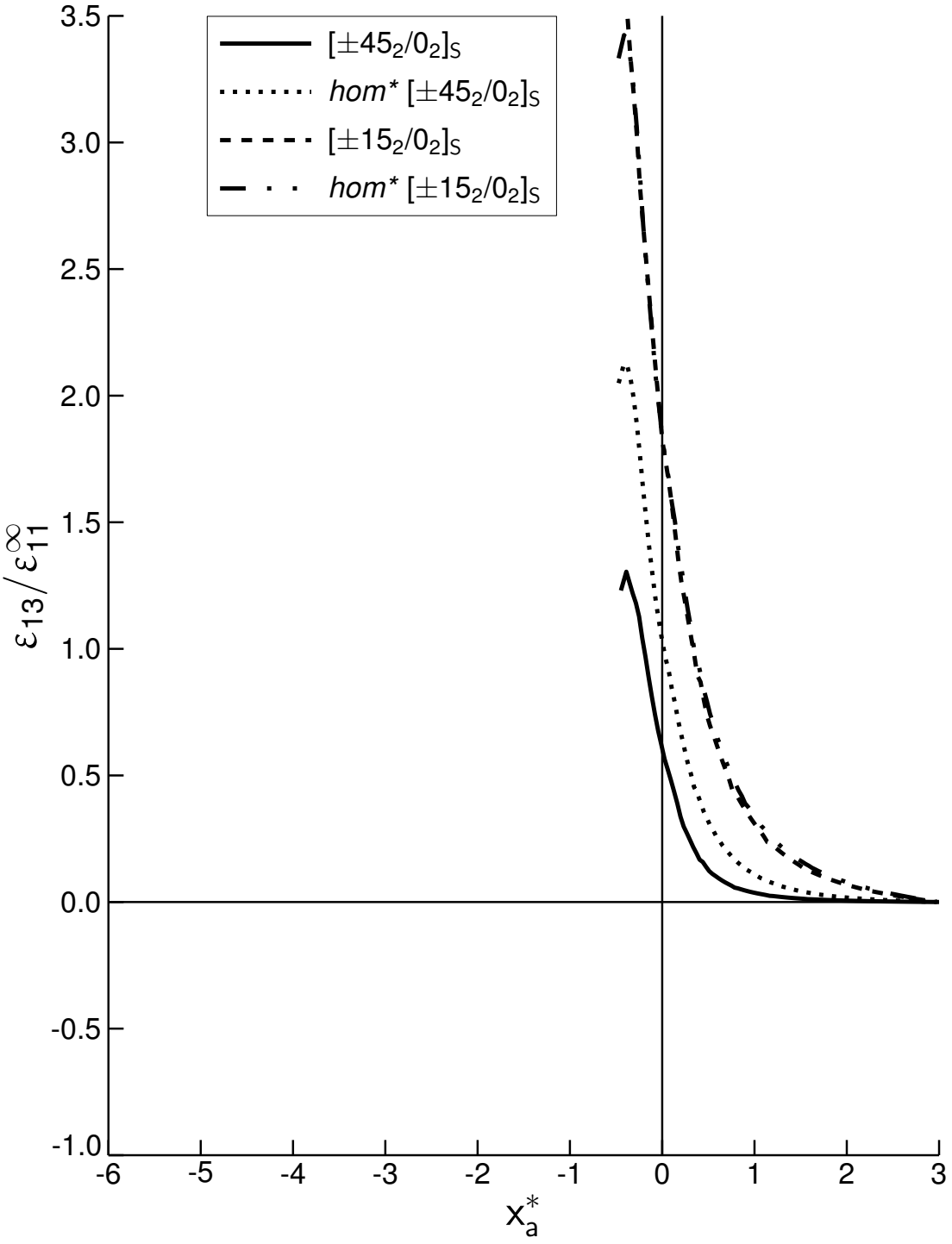

Figure 5.26 Plot of normalized ϵ_{13} versus x_a^* located at z equal to 0.066 in for the cases of laminate configurations of $[\pm 45_2/0_2]_S$, *homogenized* $[\pm 45_2/0_2]_S$, $[\pm 15_2/0_2]_S$, and *homogenized* $[\pm 15_2/0_2]_S$.

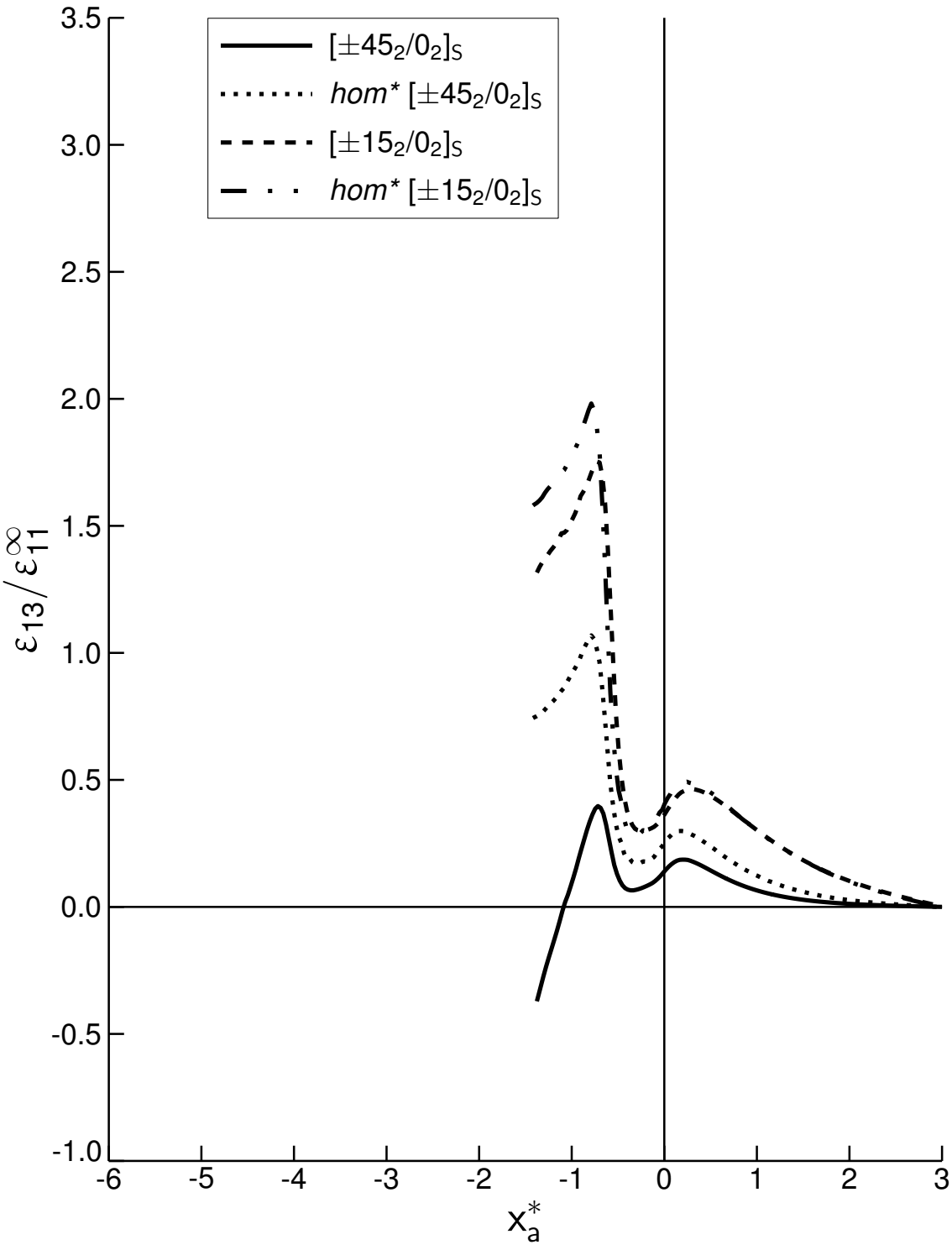

Figure 5.27 Plot of normalized ϵ_{13} versus x_a^* located at z equal to 0.054 in for the cases of laminate configurations of $[\pm 45_2/0_2]_S$, *homogenized* $[\pm 45_2/0_2]_S$, $[\pm 15_2/0_2]_S$, and *homogenized* $[\pm 15_2/0_2]_S$.

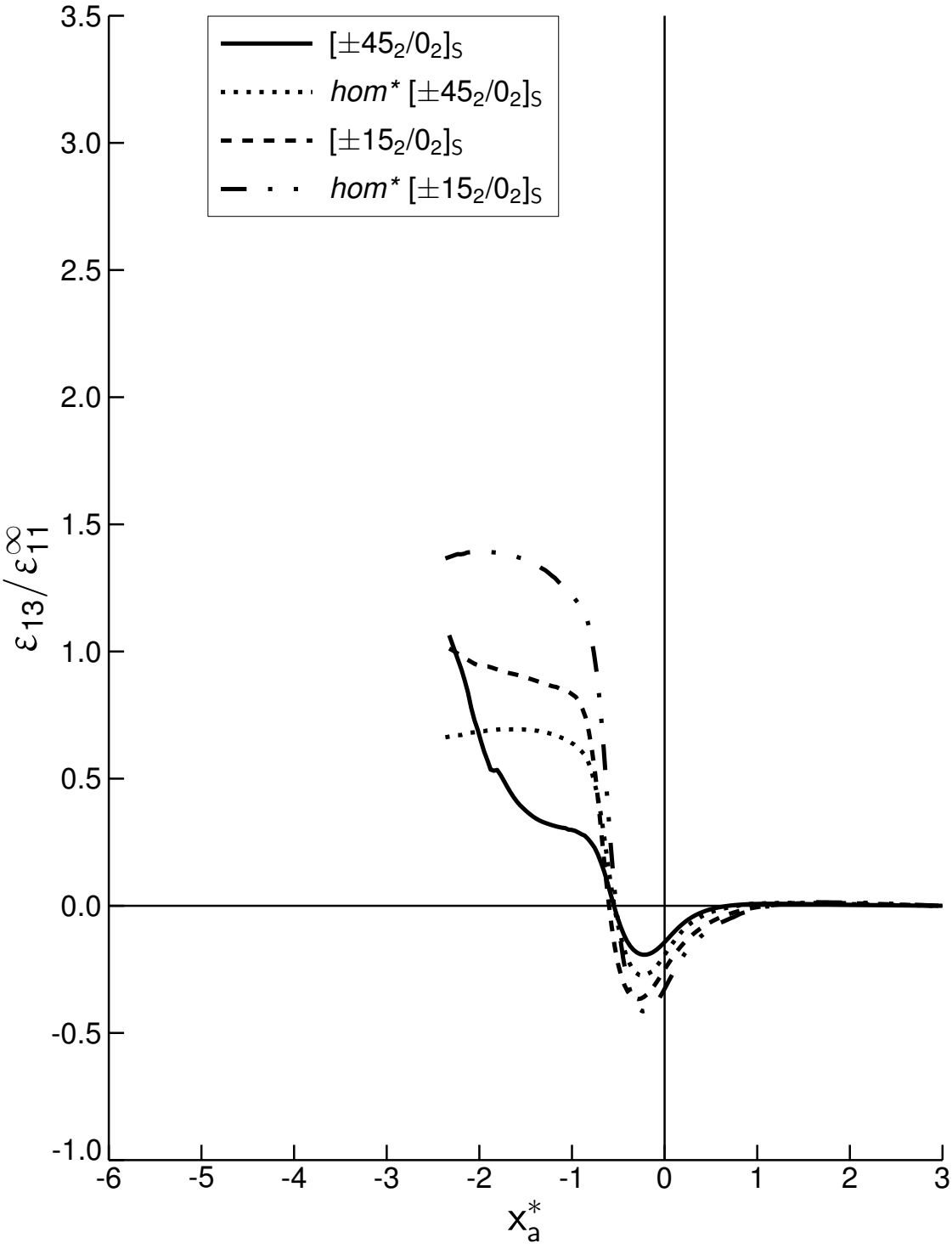

Figure 5.28 Plot of normalized ϵ_{13} versus x_a^* located at z equal to 0.042 in for the cases of laminate configurations of $[\pm 45_2/0_2]_S$, *homogenized* $[\pm 45_2/0_2]_S$, $[\pm 15_2/0_2]_S$, and *homogenized* $[\pm 15_2/0_2]_S$.

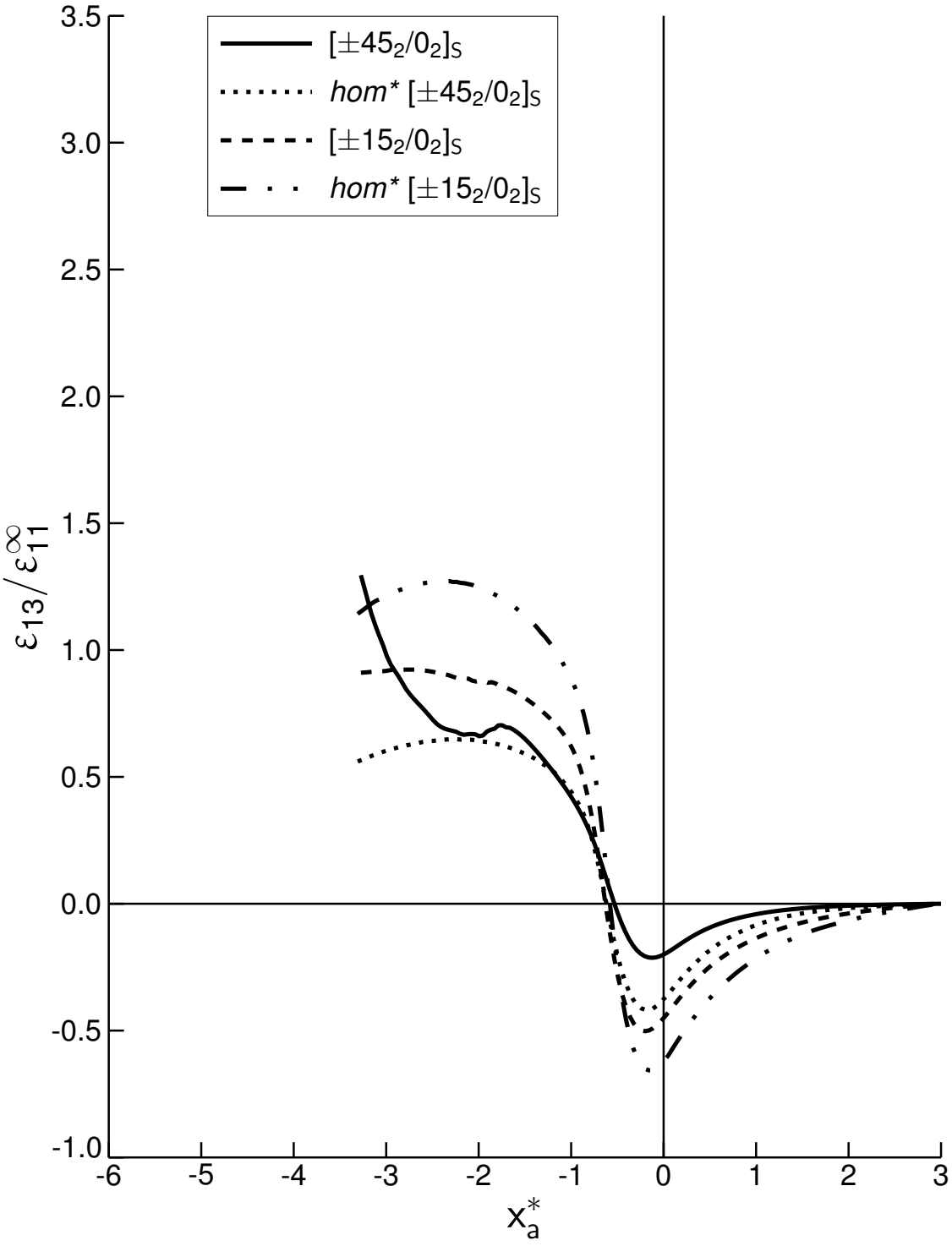

Figure 5.29 Plot of normalized ϵ_{13} versus x_a^* located at z equal to 0.030 in for the cases of laminate configurations of $[\pm 45_2/0_2]_S$, *homogenized* $[\pm 45_2/0_2]_S$, $[\pm 15_2/0_2]_S$, and *homogenized* $[\pm 15_2/0_2]_S$.

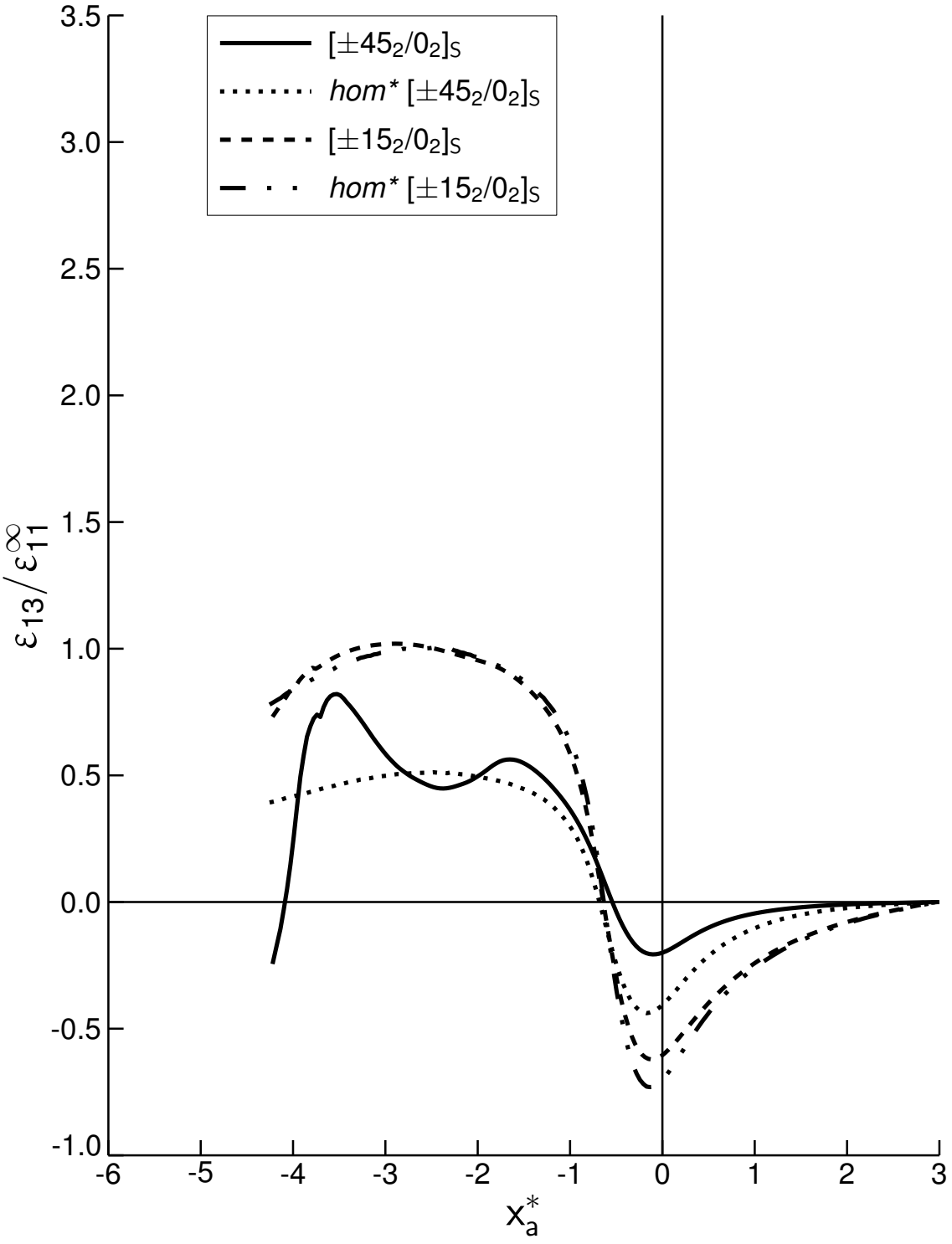

Figure 5.30 Plot of normalized ϵ_{13} versus x_a^* located at z equal to 0.018 in for the cases of laminate configurations of $[\pm 45_2/0_2]_S$, *homogenized* $[\pm 45_2/0_2]_S$, $[\pm 15_2/0_2]_S$, and *homogenized* $[\pm 15_2/0_2]_S$.

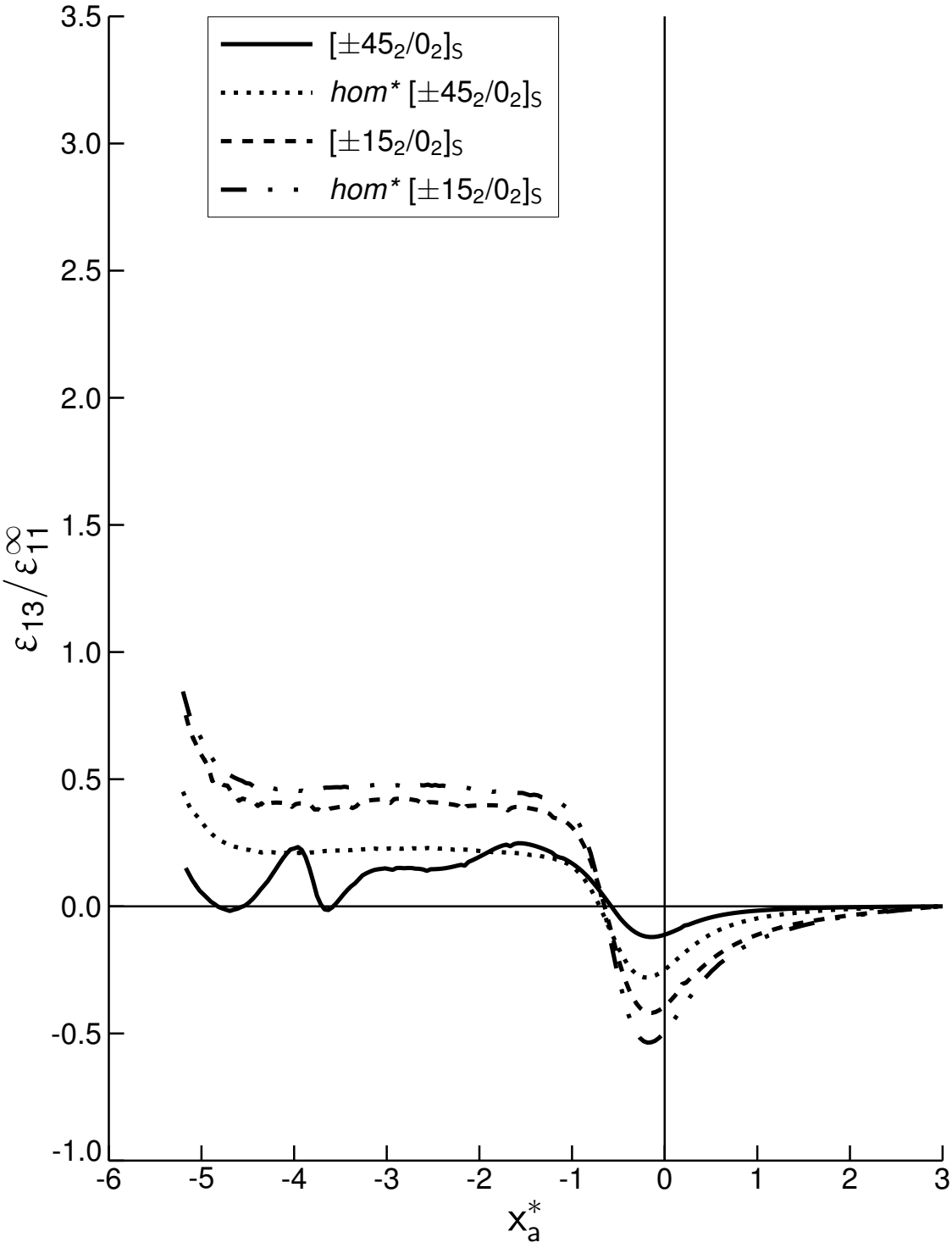

Figure 5.31 Plot of normalized ϵ_{13} versus x_a^* located at z equal to 0.006 in for the cases of laminate configurations of $[\pm 45_2/0_2]_S$, *homogenized* $[\pm 45_2/0_2]_S$, $[\pm 15_2/0_2]_S$, and *homogenized* $[\pm 15_2/0_2]_S$.

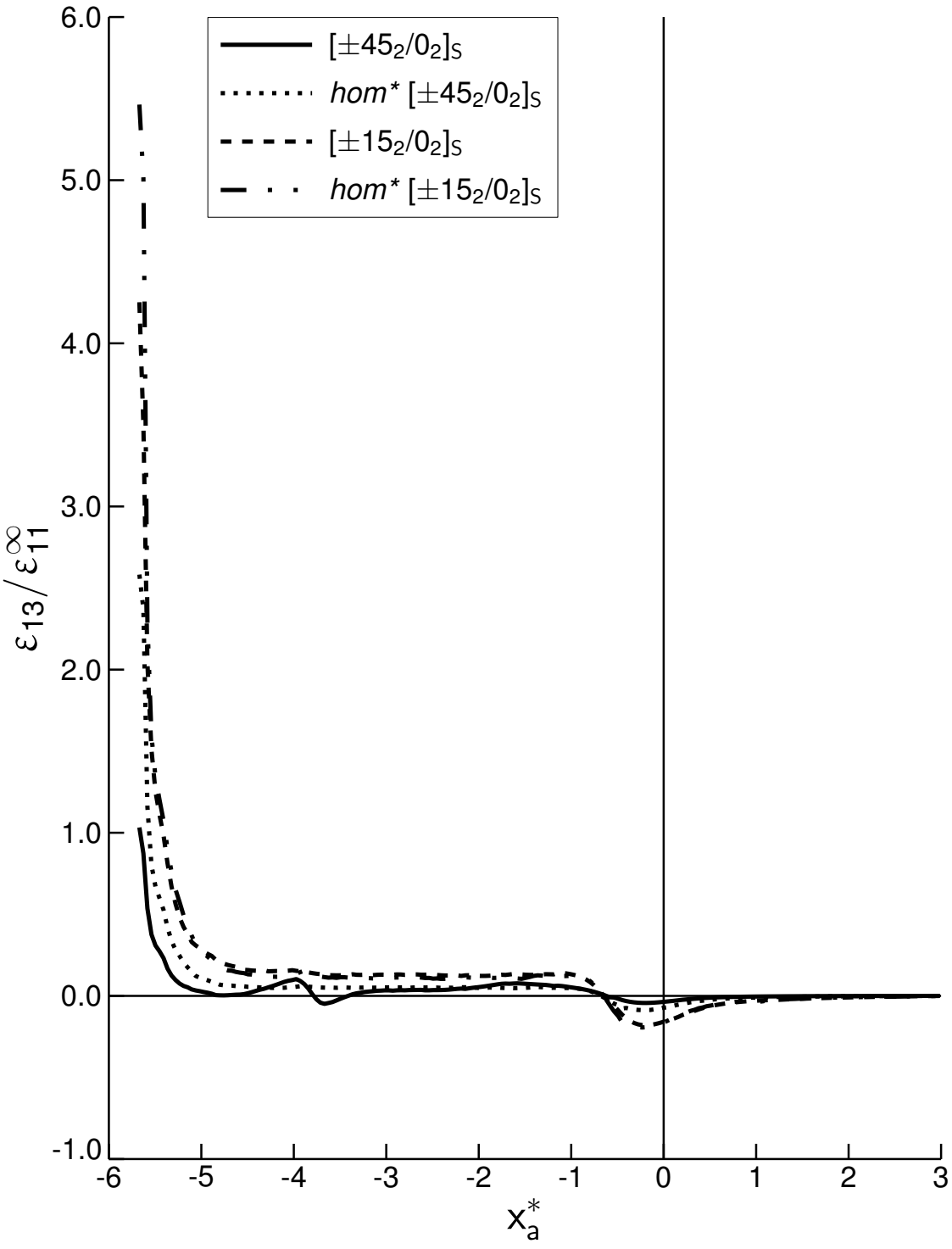

Figure 5.32 Plot of normalized ϵ_{13} versus x_a^* located at z equal to 0.0 in for the cases of laminate configurations of $[\pm 45_2/0_2]_S$, *homogenized* $[\pm 45_2/0_2]_S$, $[\pm 15_2/0_2]_S$, and *homogenized* $[\pm 15_2/0_2]_S$.

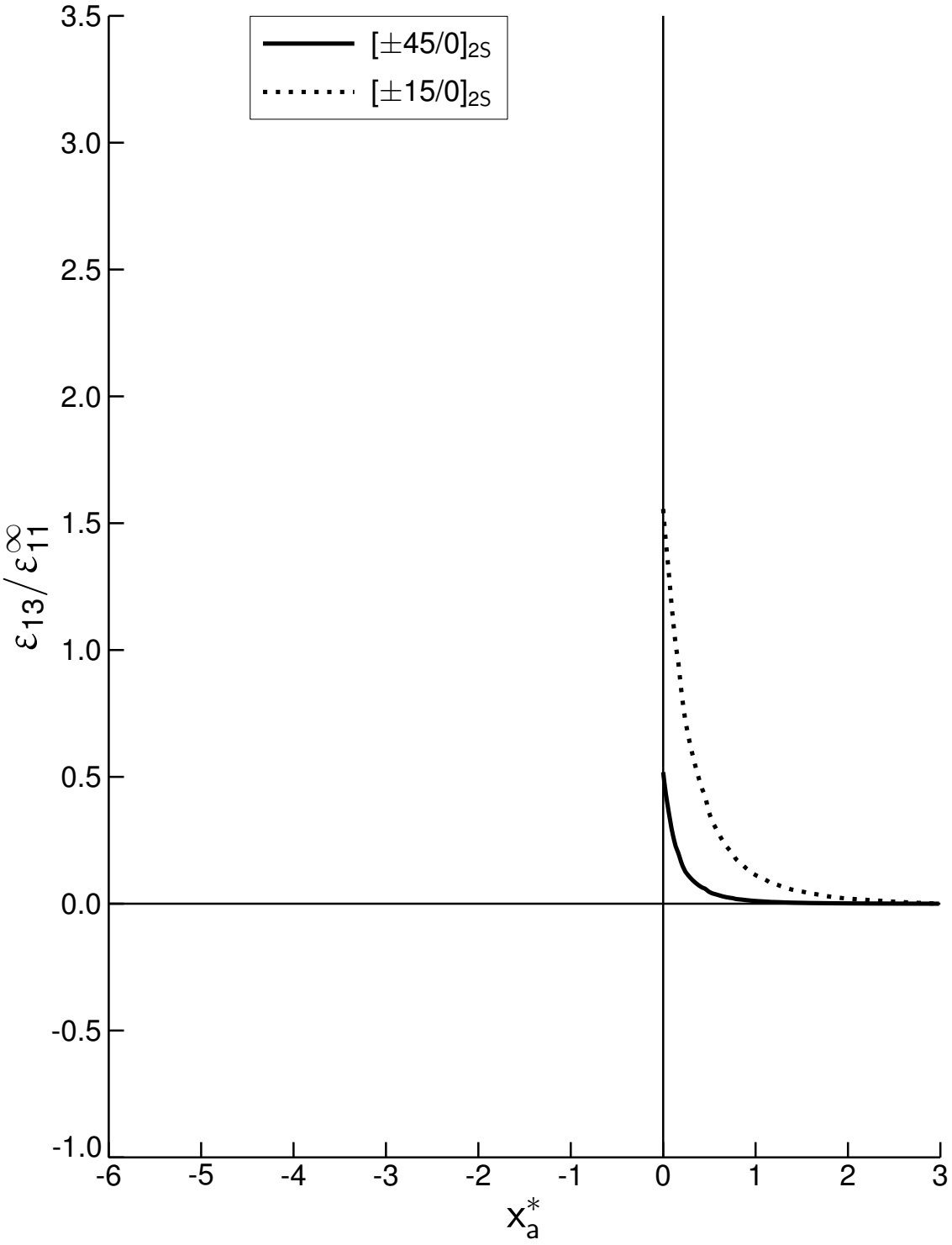

Figure 5.33 Plot of normalized ϵ_{13} versus x_a^* located at z equal to 0.072 in for the cases of laminate configurations of $[\pm 45/0]_{2S}$ and $[\pm 15/0]_{2S}$.

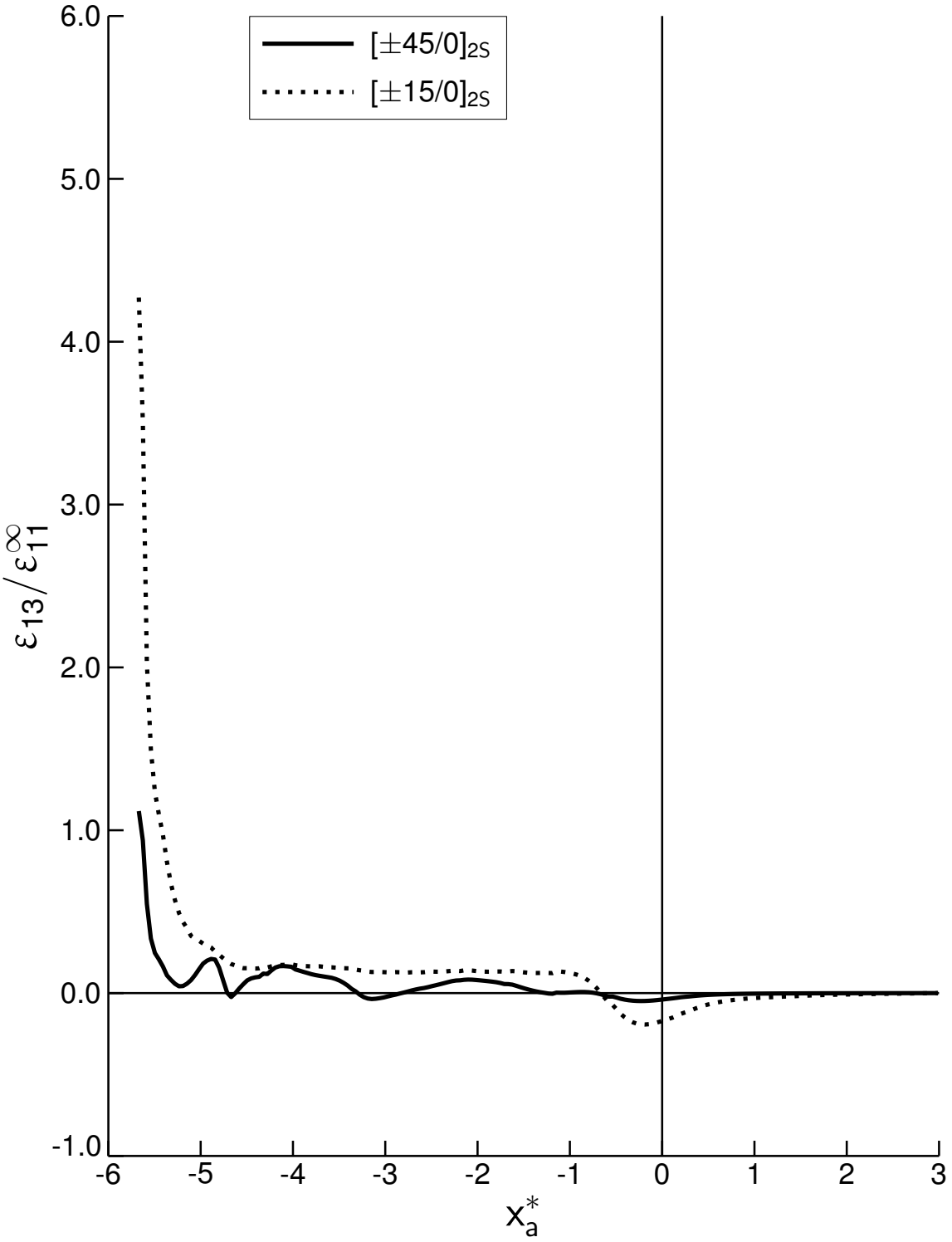

Figure 5.34 Plot of normalized ϵ_{13} versus x_a^* located at z equal to 0.0 in for the cases of laminate configurations of $[\pm 45/0]_{2S}$ and $[\pm 15/0]_{2S}$.

tions manifest the sensitivities in the response of longitudinal strain to changes in scarf angle by primarily exhibiting changes in the magnitudes of longitudinal strain. The shapes of the distributions, however, basically remain similar. The magnitudes of longitudinal strain increase progressively with increasing scarf angle in the adhesive. The magnitudes of longitudinal strain along the bondline in the adherend show much less variability than in the adhesive, wherein the differences in magnitude are magnified, among the different cases. The distributions of normalized longitudinal strain in the adherend show a relatively uniform ratio among the three cases within the lower $\pm 45^\circ$ and 0° plies, except near regions of steep gradients in longitudinal strain. The magnitudes of longitudinal strain increase with increasing scarf angle in the lower $\pm 45^\circ$ plies, but decrease with increasing scarf angle in the 0° plies. The ratios of normalized strain magnitudes for the case of 5° to the case of 10°, and for the case of 10° to the case of 15°, are both equal to 0.9 at the middle of the lower $\pm 45^\circ$ plies. In the middle of the 0° plies, these ratios are both equal to 1.1. The distributions of normalized longitudinal strain overlap each other in the upper $\pm 45^\circ$ plies in the adherend along the bondline. The distributions of normalized longitudinal strain within the adhesive at the bondline and at the midline also show relatively uniform ratios among the three cases, except near the end regions of steep gradients in longitudinal strain that occur within a normalized distance of 0.1 from each end. Thus, the normalized longitudinal strains in the adhesive at the bondline show approximate ratios of 0.51 between the strain magnitudes for the case of 5° to the case of 10°, and of 0.56 for the case of 10° to the case of 15°. In addition, the corresponding ratios of magnitudes of normalized longitudinal strain at the adhesive midline are 0.47 and 0.58. The longitudinal strain magnitudes for all three cases converge to within 25% of the normalized values at the end of the bondline in the adhesive, at the obtuse tip of the adherend.

The distributions of normalized shear strain, ϵ_{13}, for the cases of the various equal scarf angles at bondline 2 in adherend 2, at bondline 2 in the adhesive, and at the adhesive midline are presented in Figures 5.38, 5.39, and 5.40, respectively. The variations in the distributions of shear strain exhibit similar trends to those occurring

in the distributions of longitudinal strain. The distributions of shear strain generally exhibit magnification of the effects manifested in the distributions of longitudinal strain. The sharp gradients in shear strain occur at the same locations as in the longitudinal strains, in the adherend and the adhesive. For the distributions of shear strain in the adherend along the bondline, the magnitudes of shear strain increase with increasing scarf angle. The values of normalized shear strain for the cases of 5°, 10°, and 15° are 1.7, 3.6, and 4.1 at the acute tip of the 0° plies located at x'^{*}_{jb2} equal to 0.33, respectively, and are -0.6, -1.6, and -2.3 at the obtuse tip of the 0° plies located at x'^{*}_{jb2} equal to 0.67, respectively. The magnitudes of normalized shear strain in the adhesive along the bondline and along the midline also increase with increasing scarf angle. In addition, similar to the distributions of longitudinal strain, the distributions of shear strain in the adhesive for the cases of the various scarf angles also show relatively uniform ratios among each other, except near the end regions over a normalized distance of 0.1 from the ends. These ratios of normalized shear strain values for the 5° case to the 10° case, and for the 10° case to the 15° case in the adhesive at the bondline are approximately 0.6 and 0.8, respectively, except within regions of steep gradients in shear strain. The corresponding ratios of normalized shear strain values at the midline of the adhesive are the same. Another important observation in the distributions of shear strain in the adherend is the slight local decrease in shear strain occurring at the normalized distance of 0.89 along the bondline for the case of 10°, as previously observed in Section 5.1. The location of this local decrease in shear strain in the adherend shifts along the bondline for the cases of 5° and 15°, and occurs at the normalized distances of 0.88 and 0.90 along the bondline, respectively. This effect is also observed in the distributions of normalized shear strain along the bondline in the adhesive, although less magnified, and is manifested through slight kinks in the distributions of normalized shear strain for all the three cases at the same locations. Additional kinks are also observed in the distributions of normalized shear strain in the adhesive near the beginning of the bondline, all occurring within the normalized distance of 0.03 from the beginning of the bondline.

The distributions of normalized strains along x^{*}_{a}-axes in adherend 2 for the various

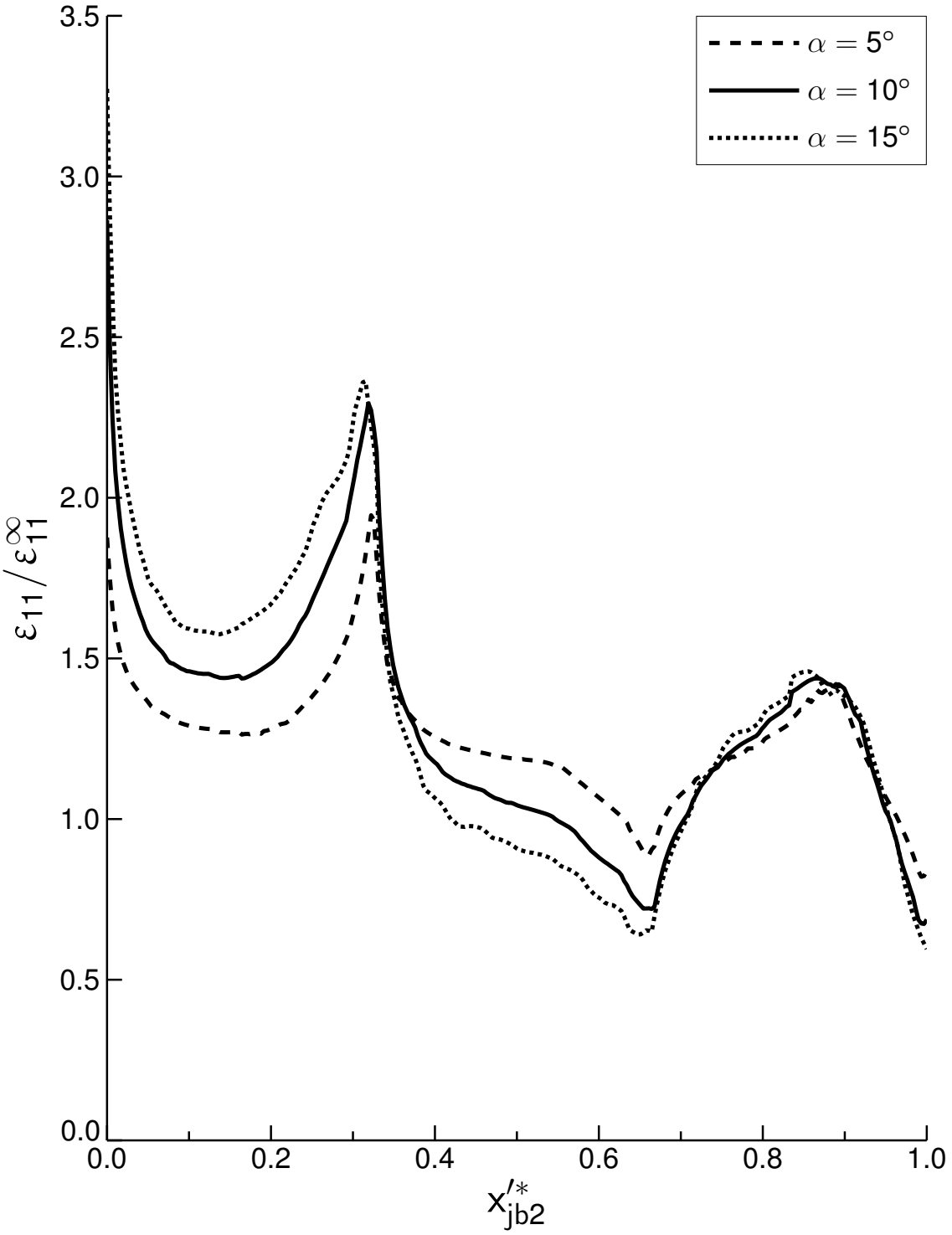

Figure 5.35 Plot of normalized ϵ_{11} versus x'^{*}_{jb2} at bondline 2 in adherend for the cases of scarf angles of 5°, 10°, and 15°.

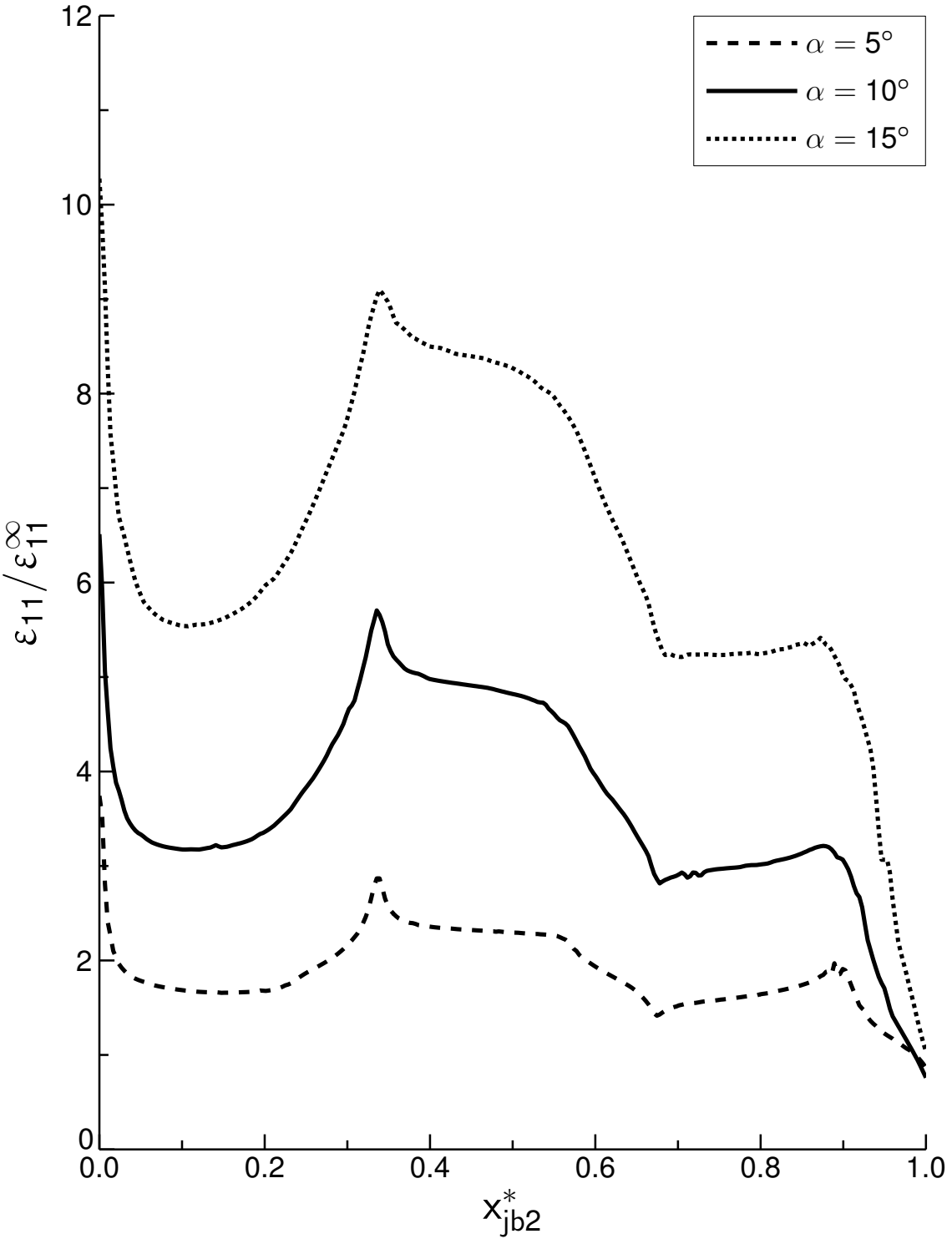

Figure 5.36 Plot of normalized ϵ_{11} versus x^*_{jb2} at bondline 2 in adhesive for the cases of scarf angles of 5°, 10°, and 15°.

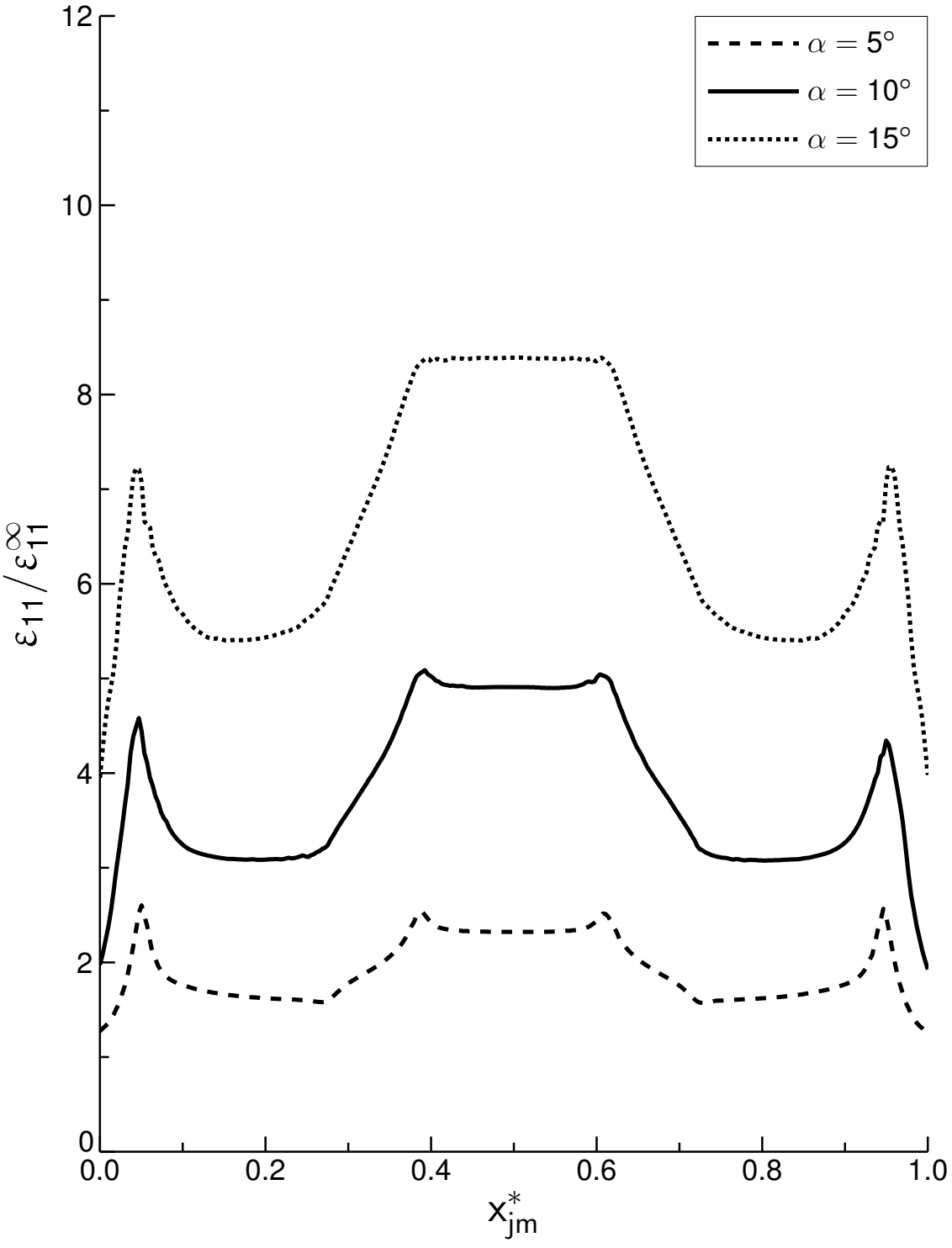

Figure 5.37 Plot of normalized ϵ_{11} versus x_{jm}^{*} at midline in adhesive for the cases of scarf angles of 5°, 10°, and 15°.

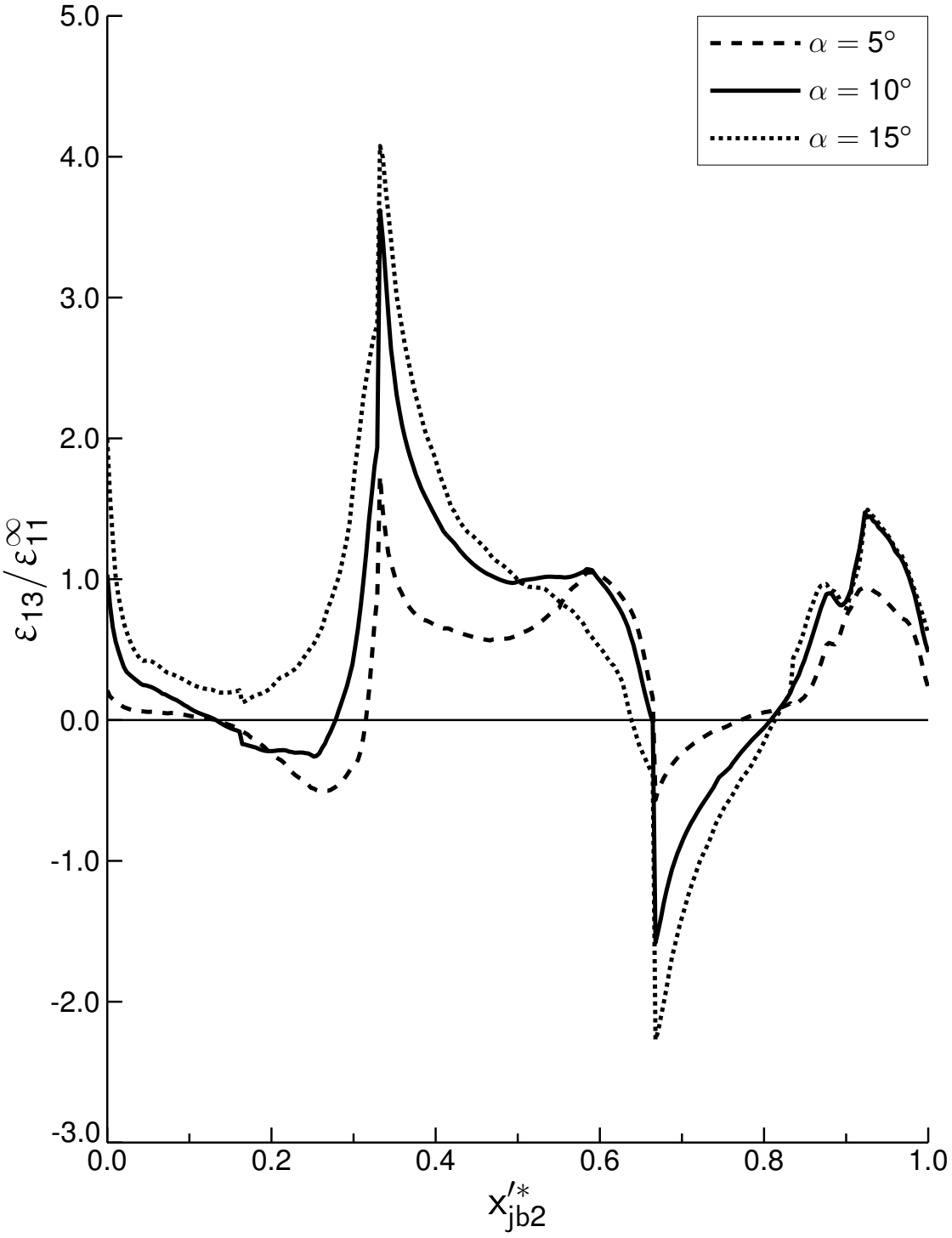

Figure 5.38 Plot of normalized ϵ_{13} versus x'^{*}_{jb2} at bondline 2 in adherend for the cases of scarf angles of 5°, 10°, and 15°.

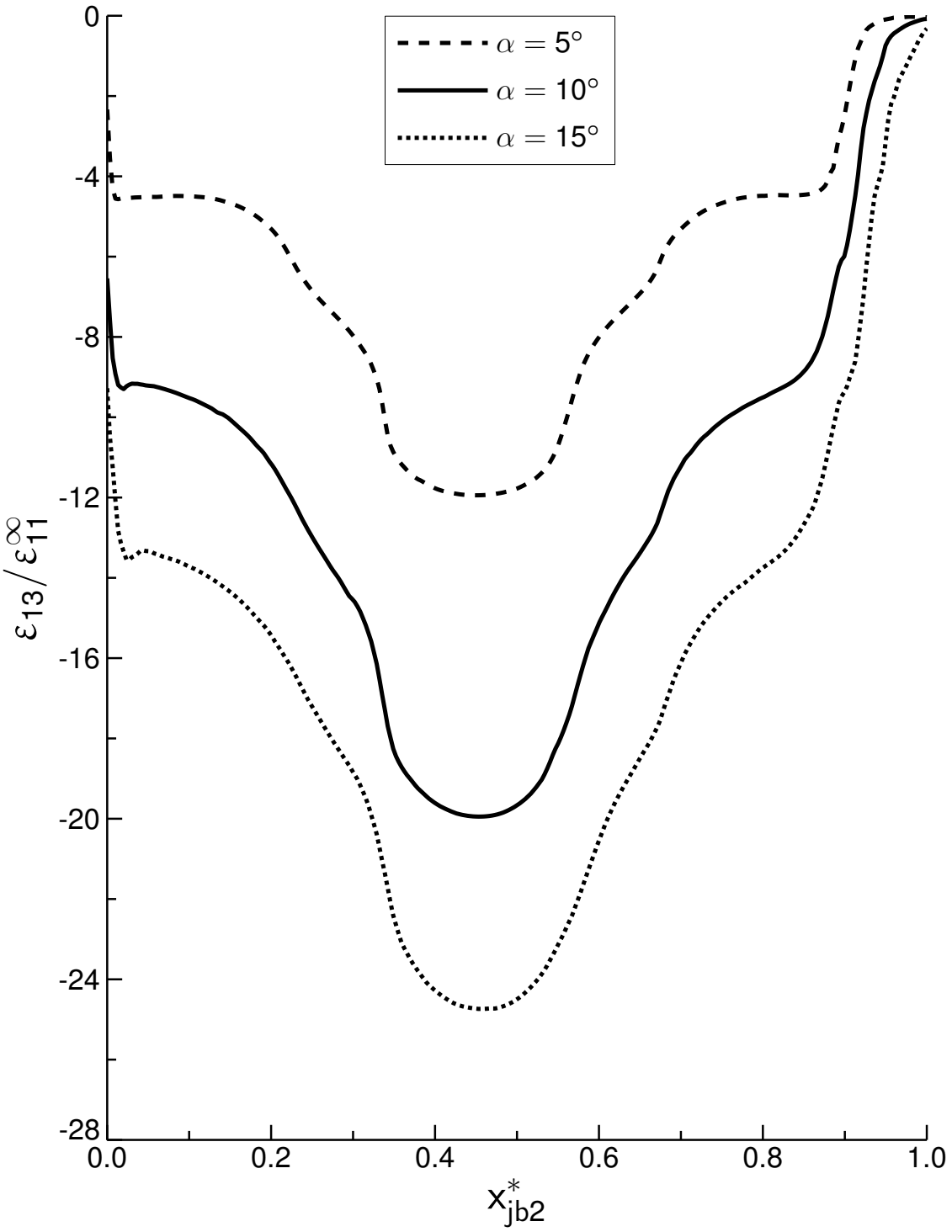

Figure 5.39 Plot of normalized ϵ_{13} versus x^*_{jb2} at bondline 2 in adhesive for the cases of scarf angles of 5°, 10°, and 15°.

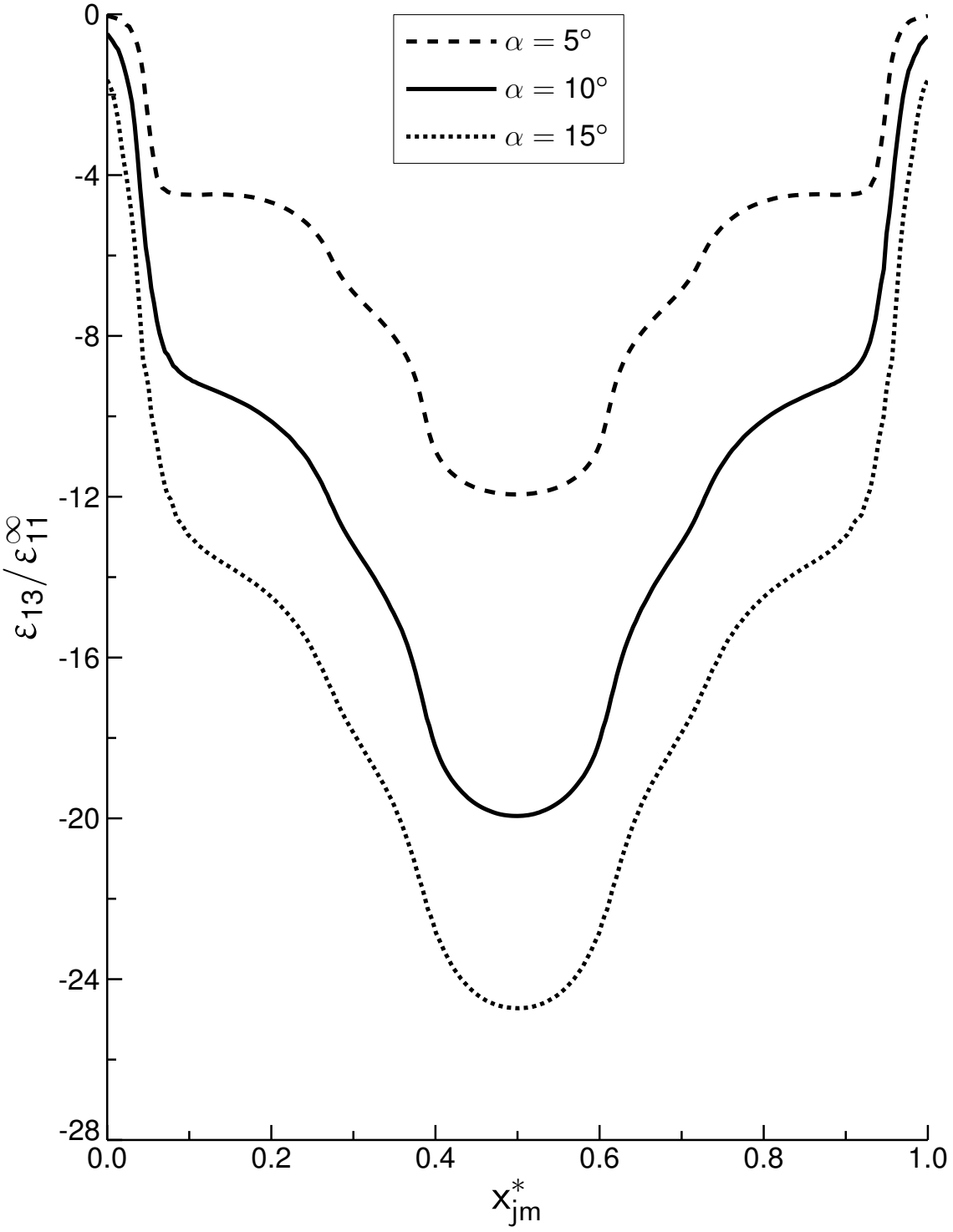

Figure 5.40 Plot of normalized ϵ_{13} versus x_{jm}^{*} at midline in adhesive for the cases of scarf angles of 5°, 10°, and 15°.

scarf angle cases are also essentially similar to each other. These are shown in Figures 5.41 and 5.42 for longitudinal strain, and in Figures 5.43 and 5.44 for shear strain. These are shown at the top (z = 0.072 in) and bottom (z = 0.0 in) of the adherend. The strain distributions are not presented for intermediate locations through the adherend thickness because they show similar characteristic trends for all the scarf angle cases. Thus, consideration of these results shows the effects of variation in scarf angle, and these can be used with the results for the distributions of strains at various locations through the adherend thickness, as presented in Section 5.1 for the case of 10°. Gradients in strains occur near both tips of the adherend, and their magnitudes increase with increasing scarf angle. The distributions of longitudinal strain show a monotonic reduction at the top of the adherend (z = 0.072 in), in approaching the location of the obtuse tip of the adherend, with normalized magnitudes of 0.84, 0.69, and 0.60 for the scarf angle cases of 5°, 10°, and 15°, respectively, at the obtuse tip of the adherend. The distributions of longitudinal strain at the bottom of the adherend (z = 0.0 in) experience sharp increases in strain values near the adhesive in approaching the location of the acute tip of the adherend. The magnitudes of normalized longitudinal strain for the cases of 5°, 10°, and 15° at the acute tip of the adherend are 1.88, 2.86, and 3.27, respectively. In addition, local decreases in longitudinal strain occur for each case near the beginning of the joint region. These local minima of normalized longitudinal strain for the cases of 5°, 10°, and 15° have values of 0.79, 0.85, and 0.93, respectively, and occur at x_a^* values of -1.3, -0.54, and -0.13, respectively. The local variations in longitudinal strain are spread over greater distances within the joint region for configurations with decreasing scarf angle, as indicated by the previous values of the locations at which they occur.

The distributions of shear strain along x_a^* at the top of the adherend (z = 0.072 in) show monotonic increase, in contrast to the corresponding decrease occurring in the distributions of longitudinal strain. Apart from this, the distributions of shear strain are similar to the corresponding distributions of longitudinal strain, showing wider spread of the distributions for negative values of x_a^* (joint region), and lower magnitudes of local maxima and minima with decreasing value of scarf angle. The

normalized value of local minimum in shear strain for the case of 10° occurring at the normalized distance of -3.67 is -0.051. Similar local minima in shear strain occur for the cases of 5° and 15°, having normalized values of -0.02 and -0.08, respectively, at the normalized distances of -7.51 and -2.20, respectively. For the cases of 5°, 10°, and 15°, the magnitudes of normalized shear strain at the obtuse tip of the adherend at the top of the adherend are 0.23, 0.48, and 0.61, respectively. The corresponding magnitudes of normalized shear strain at the acute tip of the adherend at the bottom of the adherend are 0.21, 1.03, and 2.0.

5.3 Effects of Adhesive Thickness

The strain results for the adhesive thickness cases of 0.004 in, 0.006 in, 0.008 in, 0.010 in, and 0.012 for the two-dimensional composite scarf joint configurations with the laminate of $[\pm 45_2/0_2]_S$, and equal scarf angles of 10° are presented in this section. The distributions of strains for the adhesive thickness case of 0.008 in are the same as those for the baseline case with equal scarf angles of 10° and laminate configuration of $[\pm 45_2/0_2]_S$, as presented in Section 5.1. The primary focus of this section is on documenting and establishing the sensitivities of the strain response to varying adhesive thickness for the two-dimensional composite scarf joint cases investigated.

The distributions of normalized longitudinal strain for the various adhesive thickness cases at bondline 2 in the adherend, at bondline 2 in the adhesive, and at the adhesive midline are presented in Figures 5.45, 5.46, and 5.47, respectively. For the distributions of normalized longitudinal strain along the bondline in the adherend, the magnitudes of longitudinal strain increase with increasing adhesive thickness in the lower ±45° plies, and the region of the upper ±45° plies with positive strain gradients occurring between the acute tip of the ±45° plies (x'^{*}_{jb2} equal to 0.67) and the locations of the local maxima of longitudinal strain. The distributions of normalized longitudinal strain are in relatively uniform ratios for all cases in the lower ±45° plies over a normalized distance of approximately 0.1 centered along the middle of

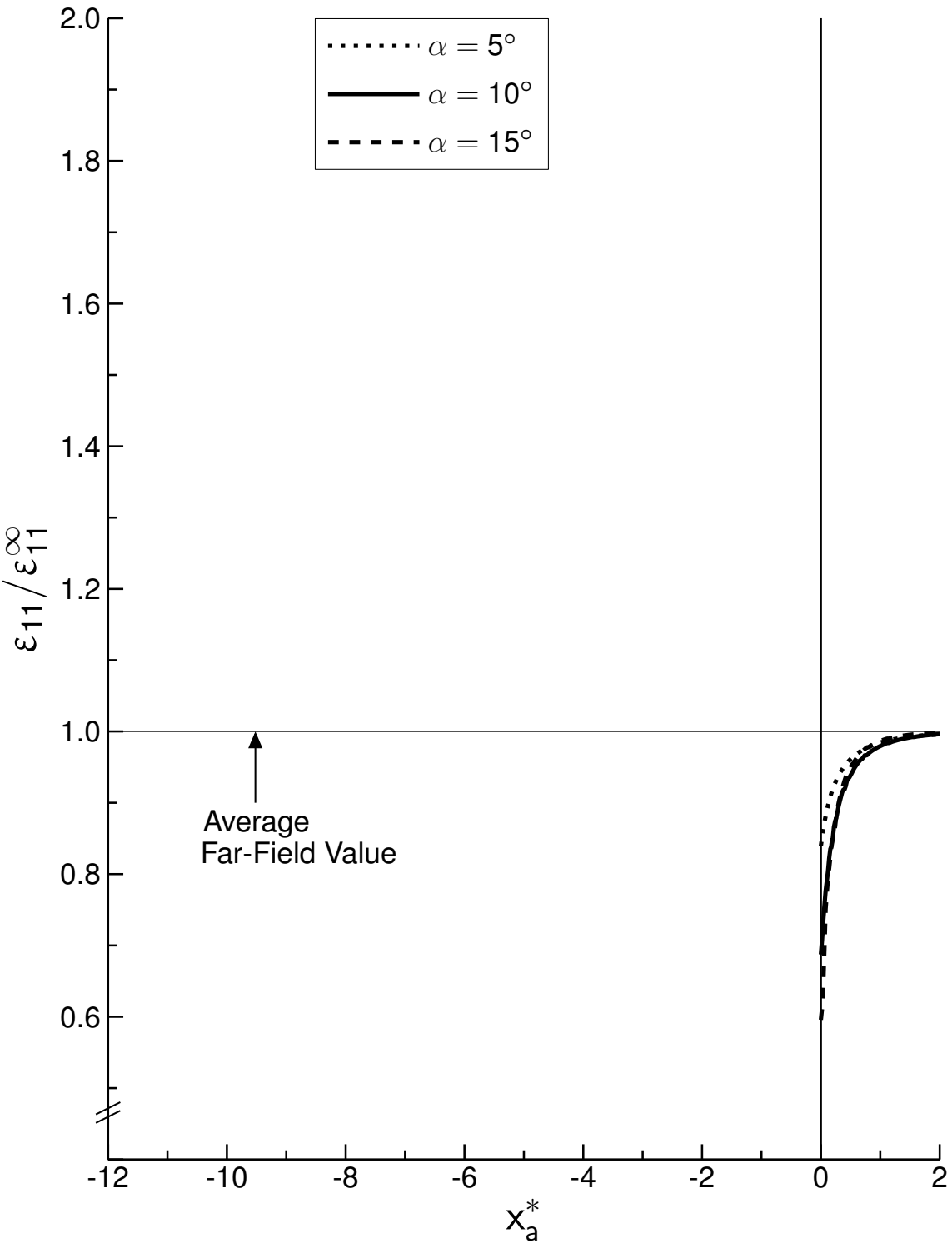

Figure 5.41 Plot of normalized ϵ_{11} versus x_a^* located at z equal to 0.072 in for the cases of scarf angles of 5°, 10°, and 15°.

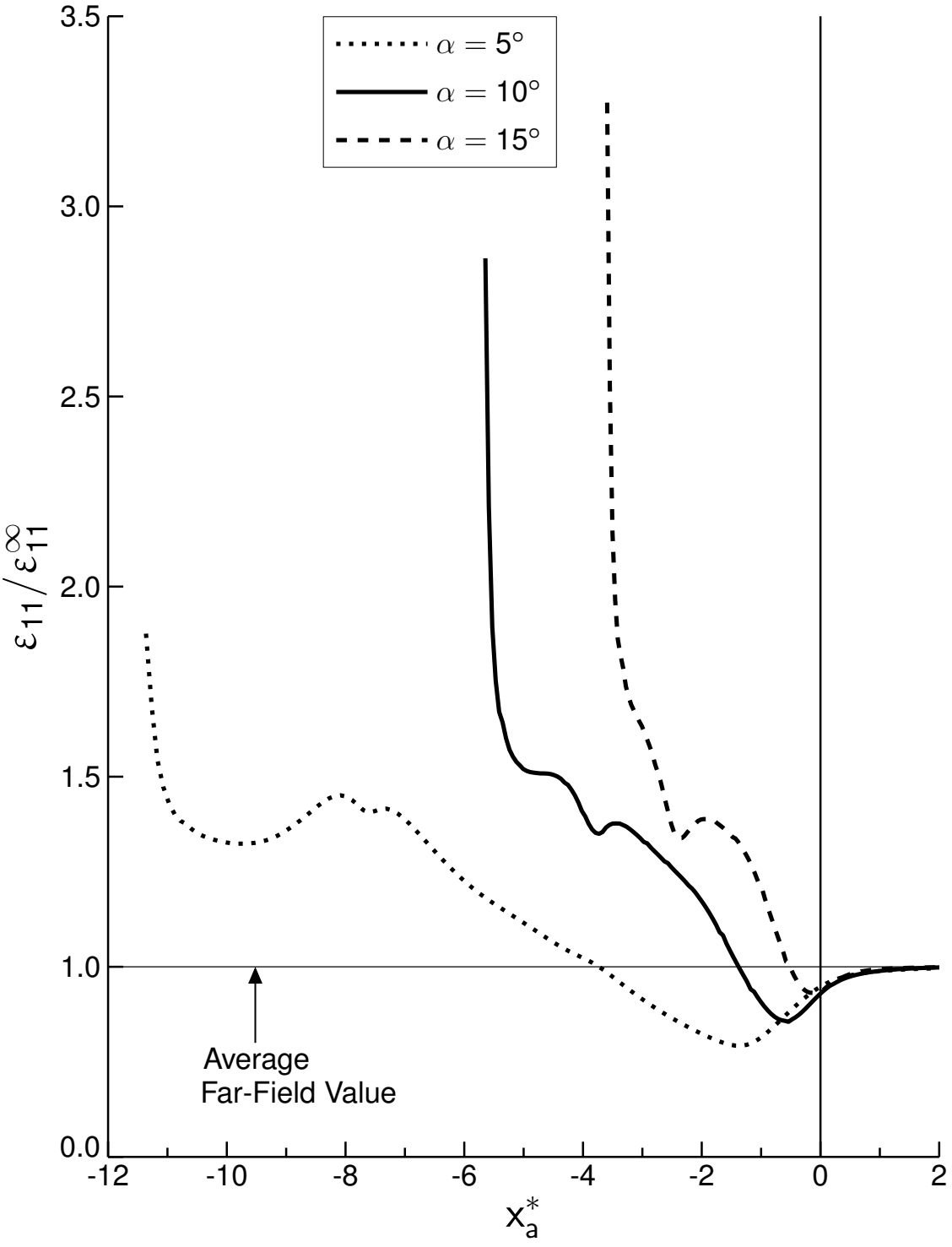

Figure 5.42 Plot of normalized ϵ_{11} versus x_a^* located at z equal to 0.0 in for the cases of scarf angles of 5°, 10°, and 15°.

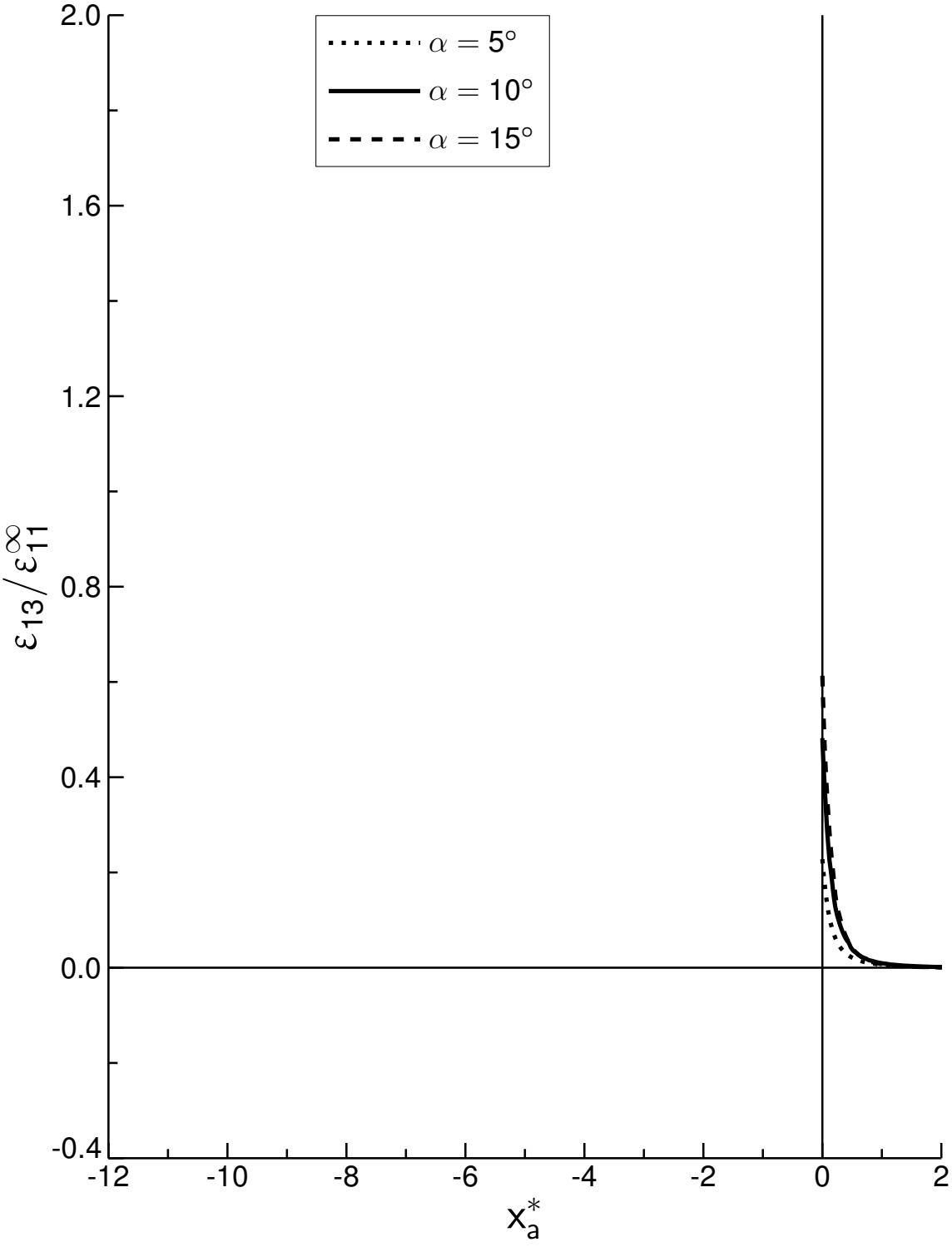

Figure 5.43 Plot of normalized ϵ_{13} versus x_a^* located at z equal to 0.072 in for the cases of scarf angles of 5°, 10°, and 15°.

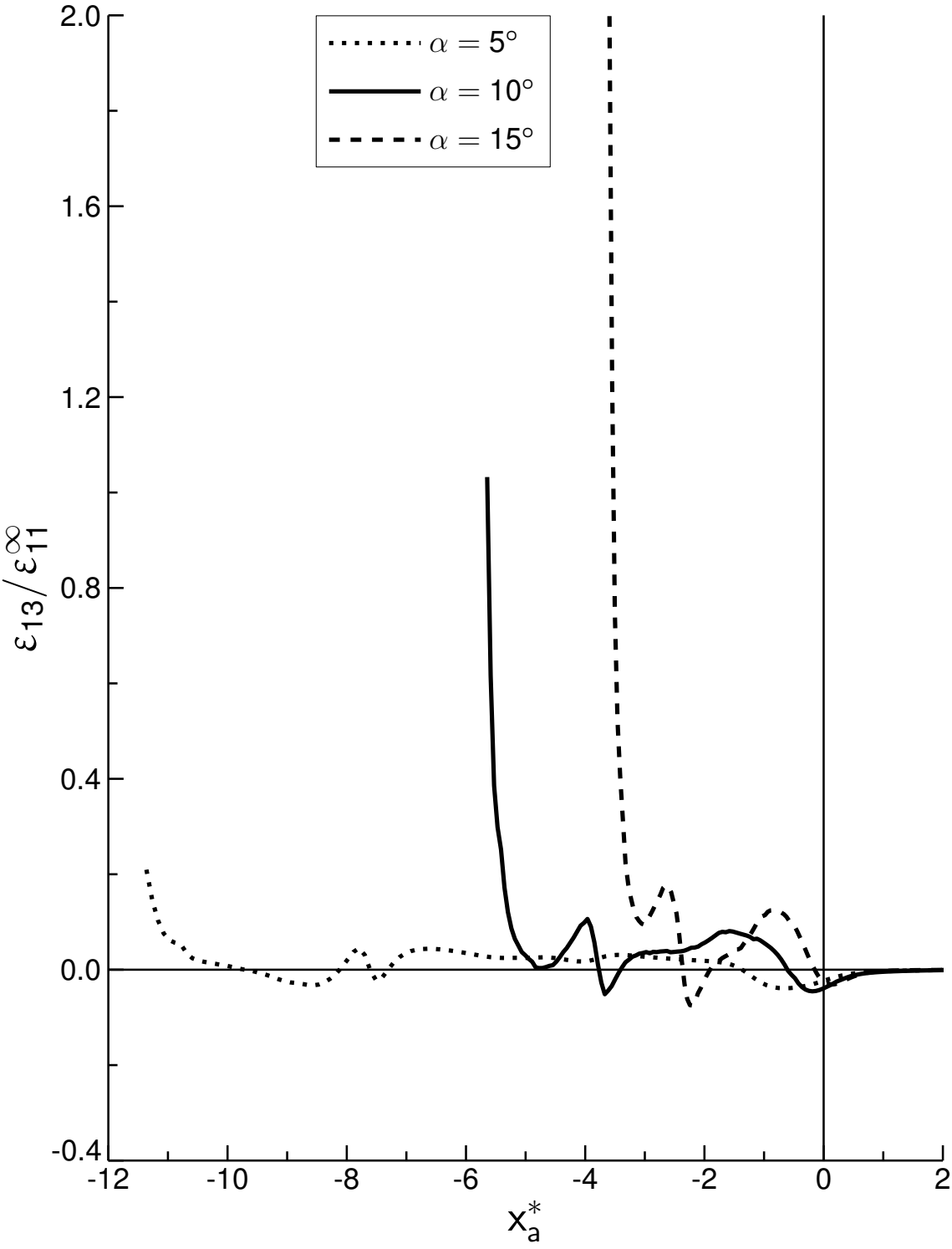

Figure 5.44 Plot of normalized ϵ_{13} versus x_a^* located at z equal to 0.0 in for the cases of scarf angles of 5°, 10°, and 15°.

the $\pm 45^\circ$ plies. These ratios can be determined by assessing the magnitudes of the normalized longitudinal strain at the interface of the lower $+45^\circ$ and -45° plies, at the normalized distance of 0.167. These ratios have values of 1.21, 1.32, 1.44, 1.56, and 1.69 corresponding to cases with increasing adhesive thickness. In the 0° plies, the distributions of longitudinal strain show little variation for the various cases and all show values of normalized longitudinal strain approximately equal to 1.0 at the normalized distance of 0.54, with the distributions almost overlapping each other between this location and the location of the obtuse tip of the 0° plies (x'^{*}_{jb2} equal to 0.67). The region over which negative gradients in longitudinal strain occur near the end of the bondline increases with increasing adhesive thickness. The local peaks in longitudinal strain in this region occur at the normalized distances of 0.84, 0.84, 0.87, 0.93, and 0.94 corresponding to the cases with decreasing adhesive thickness. The corresponding normalized values of the local peaks in longitudinal strain occurring at these locations for each case are 1.58, 1.55, 1.44, 1.47, and 1.33.

The distributions of longitudinal strain in the adhesive at the bondline follow similar trends to those in the adherend. An important observation for the distributions of longitudinal strain in the adhesive along the bondline is that the normalized value of longitudinal strain for all cases is approximately 5.0 at the normalized distance of 0.40. This location is in contrast to the location having normalized distance of 0.54 in the adherend, where the normalized value of longitudinal strain for all cases is approximately 1.0. Between this normalized distance of 0.40 along the bondline and the location adjacent to the obtuse tip of the 0° plies in the adhesive, the magnitudes of longitudinal strain decrease with increasing adhesive thickness, showing steeper gradients in longitudinal strain with decreasing adhesive thickness. The local peaks in normalized longitudinal strain in this region in the adhesive occur at the normalized distances of 0.82, 0.85, 0.88, 0.92, and 0.95, having values of 3.47, 3.38, 3.21, 3.13, and 3.33 corresponding to cases with decreasing adhesive thickness. The distributions of normalized longitudinal strain at the adhesive midline adjacent to the 0° plies show close overlap with values of approximately 5.0 for all cases. The distributions of longitudinal strain at the adhesive midline adjacent to the $\pm 45^\circ$ plies

show increasing magnitude of longitudinal strain with increasing adhesive thickness. The values of normalized longitudinal strain adjacent to the interface locations of the $+45^\circ$ and -45° plies (x^*_{jm} equal to 0.17 and 0.83) are 2.68, 2.88, 3.09, 3.29, and 3.51 corresponding to cases with increasing adhesive thickness. In addition, extended regions of negative gradients in longitudinal strain occur near the end of the adhesive midline for increasing adhesive thickness. The normalized values of local peaks near the upper end of the adhesive midline are 5.06, 4.68, 4.34, 4.32, and 4.11 corresponding to cases with decreasing adhesive thickness, occurring at the normalized distances of 0.93, 0.94, 0.95, 0.96, and 0.98. These peaks occur symmetrically about the midpoint near the beginning of the midline as well.

The distributions of normalized shear strain for the various cases of adhesive thickness at bondline 2 in the adherend, at bondline 2 in the adhesive, and at the midline of the adhesive are presented in Figures 5.48, 5.49, and 5.50. For the normalized shear strain in the adherend, the distributions for the various cases show little variability in the lower $\pm 45^\circ$ plies and basically overlap each other between the normalized distances of approximately 0.1 and 0.25. In the 0° plies and upper $\pm 45^\circ$ plies, the magnitudes of the normalized shear strain increase with increasing adhesive thickness. This effect is most amplified within the 0° plies, where the normalized magnitudes of shear strain at the middle of the 0° plies are 0.50, 0.73, 0.98, 1.32, and 1.62 for the increasing adhesive thickness cases. The value of normalized shear strain for all cases reduces to approximately -1.6 at the obtuse tip of the 0° plies (x'^*_{jb2} equal to 0.67). An important observation for the distributions of shear strain in the adherend along the bondline, as in the preceding cases, is the slight local decrease in the magnitudes of shear strain occurring near the end of the bondline before the terminal region of negative gradients in shear strain. For the cases of increasing adhesive thickness, this effect occurs at the normalized distances of 0.95, 0.92, 0.89, 0.88, and 0.86 along the bondline in the adherend.

The distributions of normalized shear strain along the bondline in the adhesive show increasing magnitudes of shear strain with increasing adhesive thickness adjacent to the lower $\pm 45^\circ$ plies, but decreasing magnitudes of shear strain with increasing

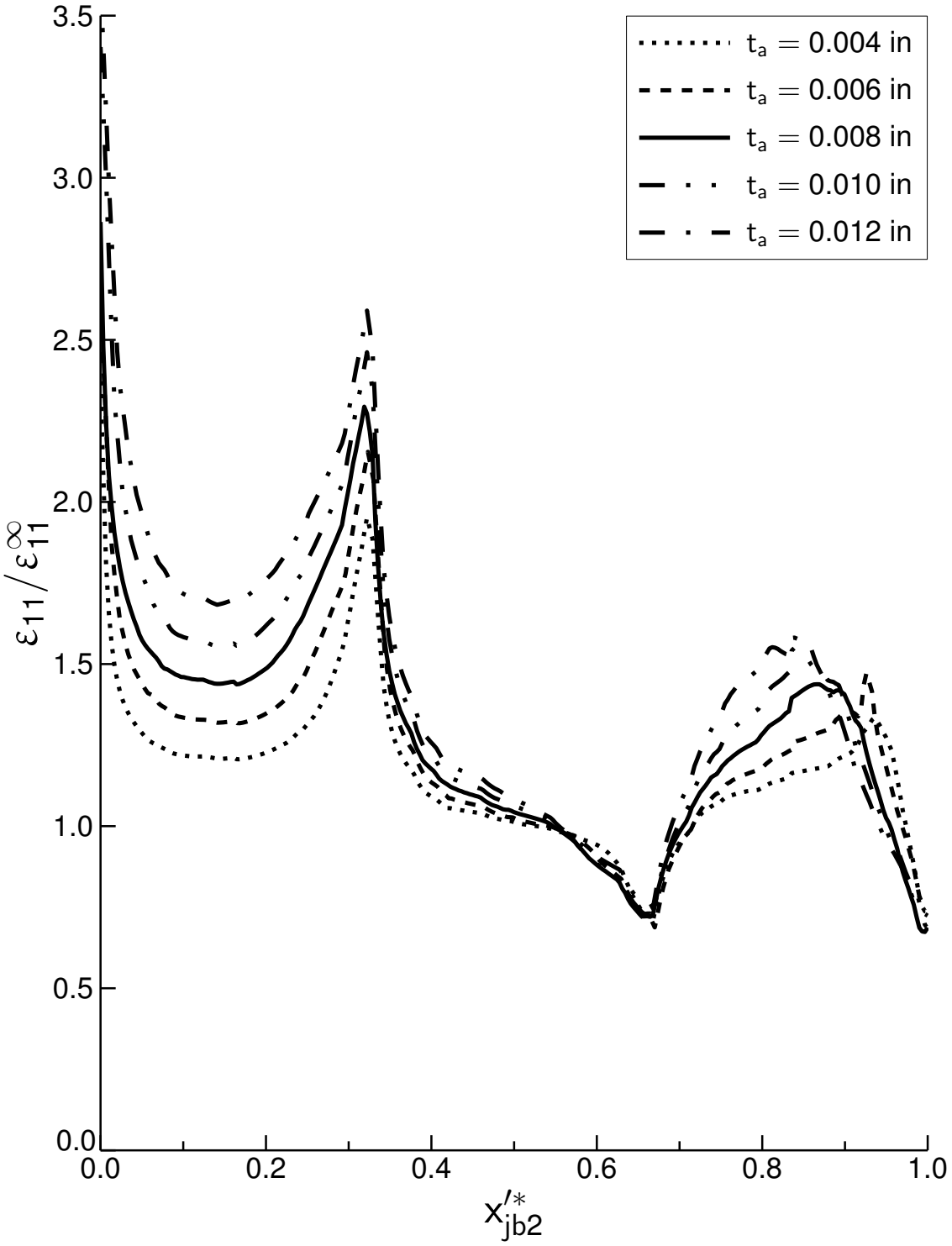

Figure 5.45 Plot of normalized ϵ_{11} versus x'^{*}_{jb2} at bondline 2 in adherend for the cases of adhesive thicknesses of 0.004 in, 0.006 in, 0.008 in, 0.010 in, and 0.012 in.

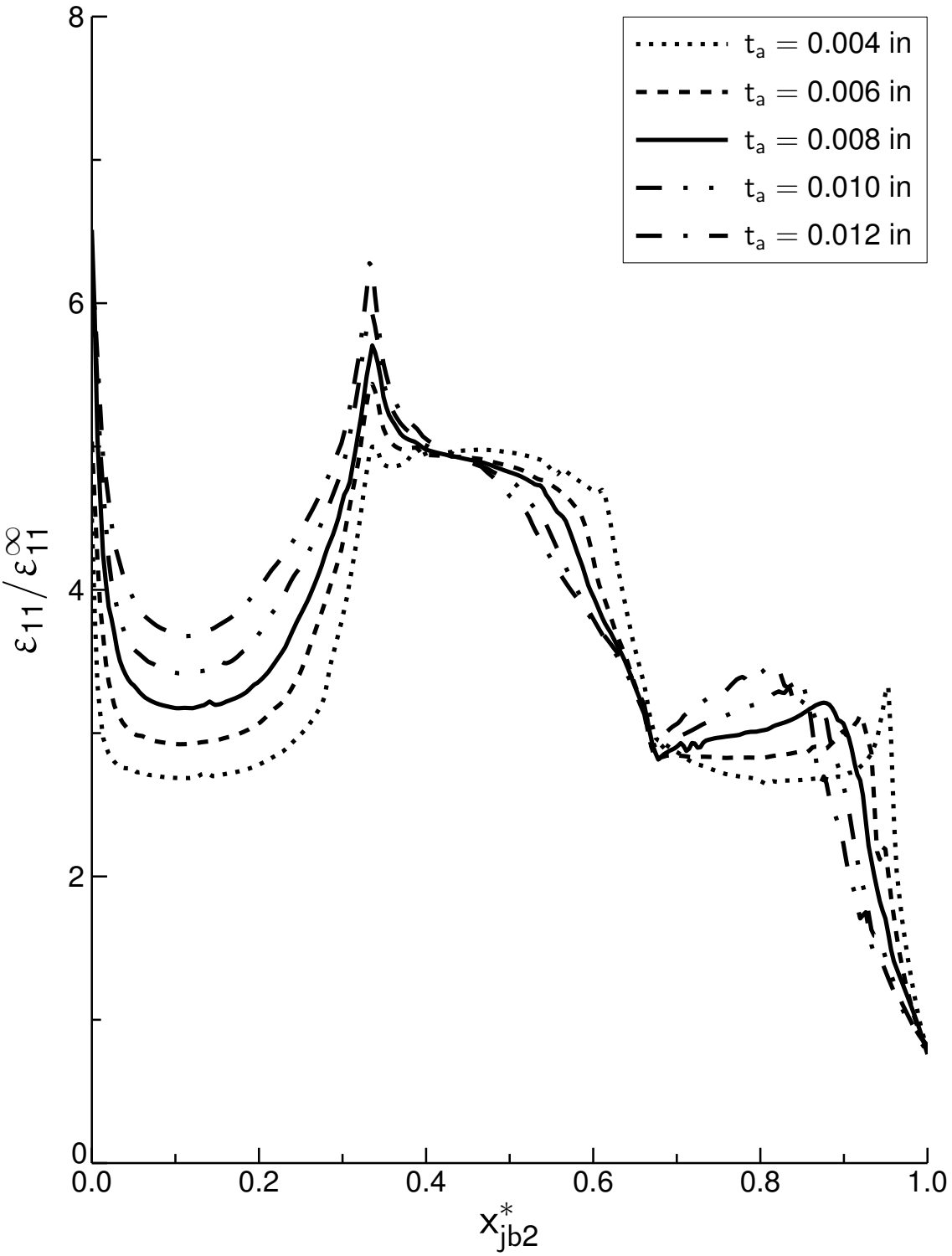

Figure 5.46 Plot of normalized ϵ_{11} versus x^*_{jb2} at bondline 2 in adhesive for the cases of adhesive thicknesses of 0.004 in, 0.006 in, 0.008 in, 0.010 in, and 0.012 in.

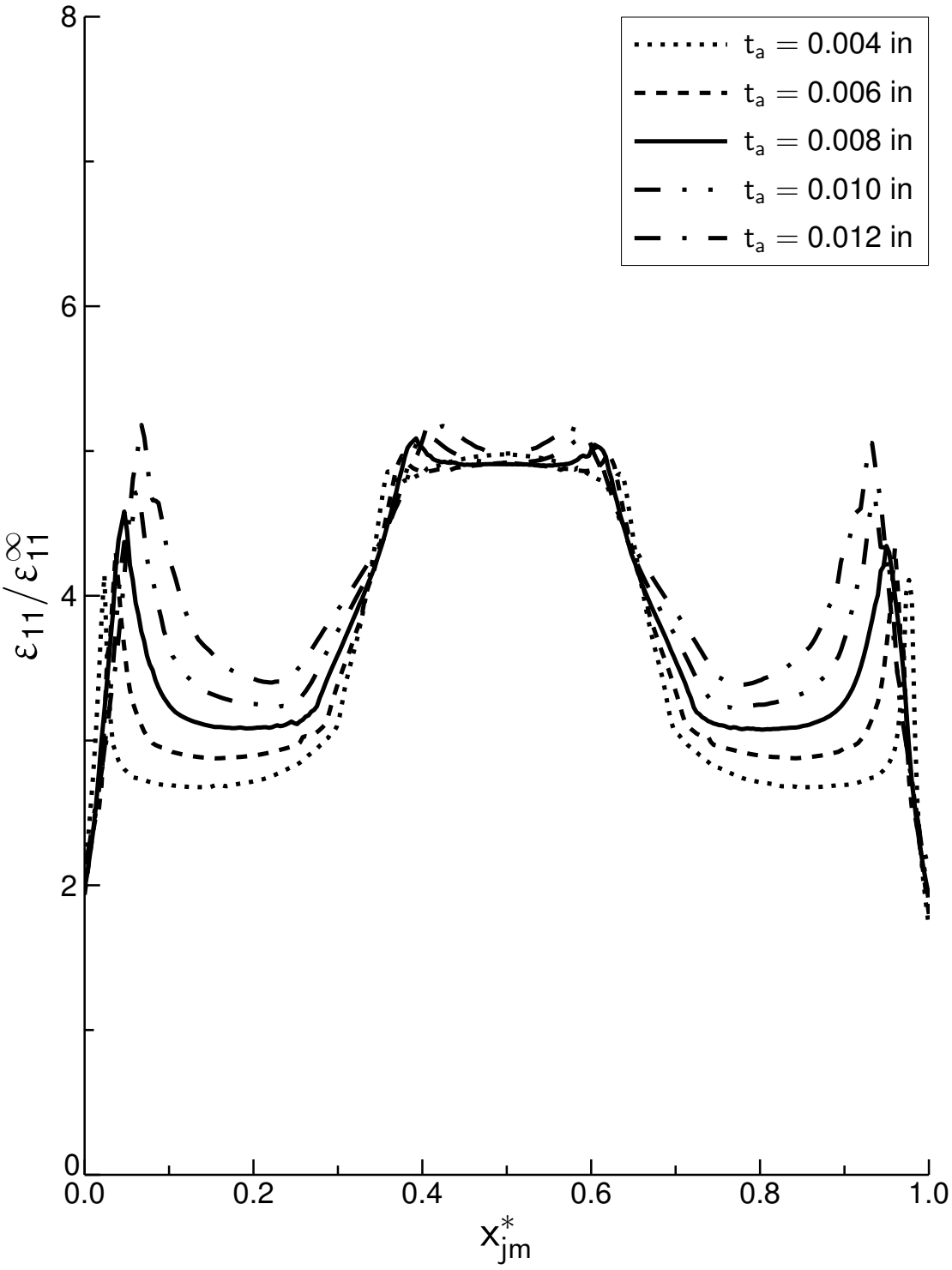

Figure 5.47 Plot of normalized ϵ_{11} versus x_{jm}^{*} at midline in adhesive for the cases of adhesive thicknesses of 0.004 in, 0.006 in, 0.008 in, 0.010 in, and 0.012 in.

adhesive thickness adjacent to the 0° plies. The location of the maximum in the magnitudes of normalized shear strain shifts lower on the bondline with increasing adhesive thickness. This has values of -21.3, -20.5, -19.9, -19.5, and -17.5, and occurs at the corresponding normalized distances of 0.48, 0.46, 0.45, 0.44, and 0.41 for the cases of increasing adhesive thickness. In addition, the locations near the end of the bondline at which a sharp change in the gradients in shear strain occurs change for the various cases, occurring at the normalized distances 0.84, 0.87, 0.89, 0.92, and 0.95 for the cases of decreasing adhesive thickness. The distributions of normalized shear strain in the adhesive at the midline show similar characteristics to those at the bondline in the adhesive. The magnitudes of normalized shear strain in the region adjacent to the ±45° plies increase with increasing adhesive thickness, but decrease in the region adjacent to the 0° plies. In addition, the regions of sharp change in the gradients in shear strain occurring near both ends of the midline shift inwards from the ends for the various cases of adhesive thicknesses. Near the upper end of the midline, these changes occur at the normalized distances of 0.89, 0.91, 0.92, 0.93, and 0.95 for the cases of decreasing adhesive thickness. Finally, these distributions exhibit symmetry as must occur as previously described.

The distributions of normalized longitudinal and shear strain along the x_a^*-axes at the top and bottom of adherend 2 for the various adhesive thickness cases are presented in Figures 5.51 through 5.54. The distributions for all cases show similar characteristics to those for the baseline case of 0.008 in. The distributions at the top of the adherend (z = 0.072 in) have similar shapes across all cases. For the distributions of normalized longitudinal strain at this location, the values of normalized longitudinal strain at x_a^* equal to 0.5 are 0.96, 0.95, 0.94, 0.93, and 0.92 corresponding to cases with increasing adhesive thickness. The main difference among the distributions of strains for the various cases is manifested in the distributions of longitudinal strain along x_a^* at the bottom of adherend 2, in which the magnitudes of normalized longitudinal strain relative to 1.0 increase with increasing adhesive thickness, and reach peak values of 2.37, 2.59, 2.86, 3.40, and 3.61 corresponding to cases with increasing adhesive thickness, at the corresponding locations of the acute tip of the adherend where

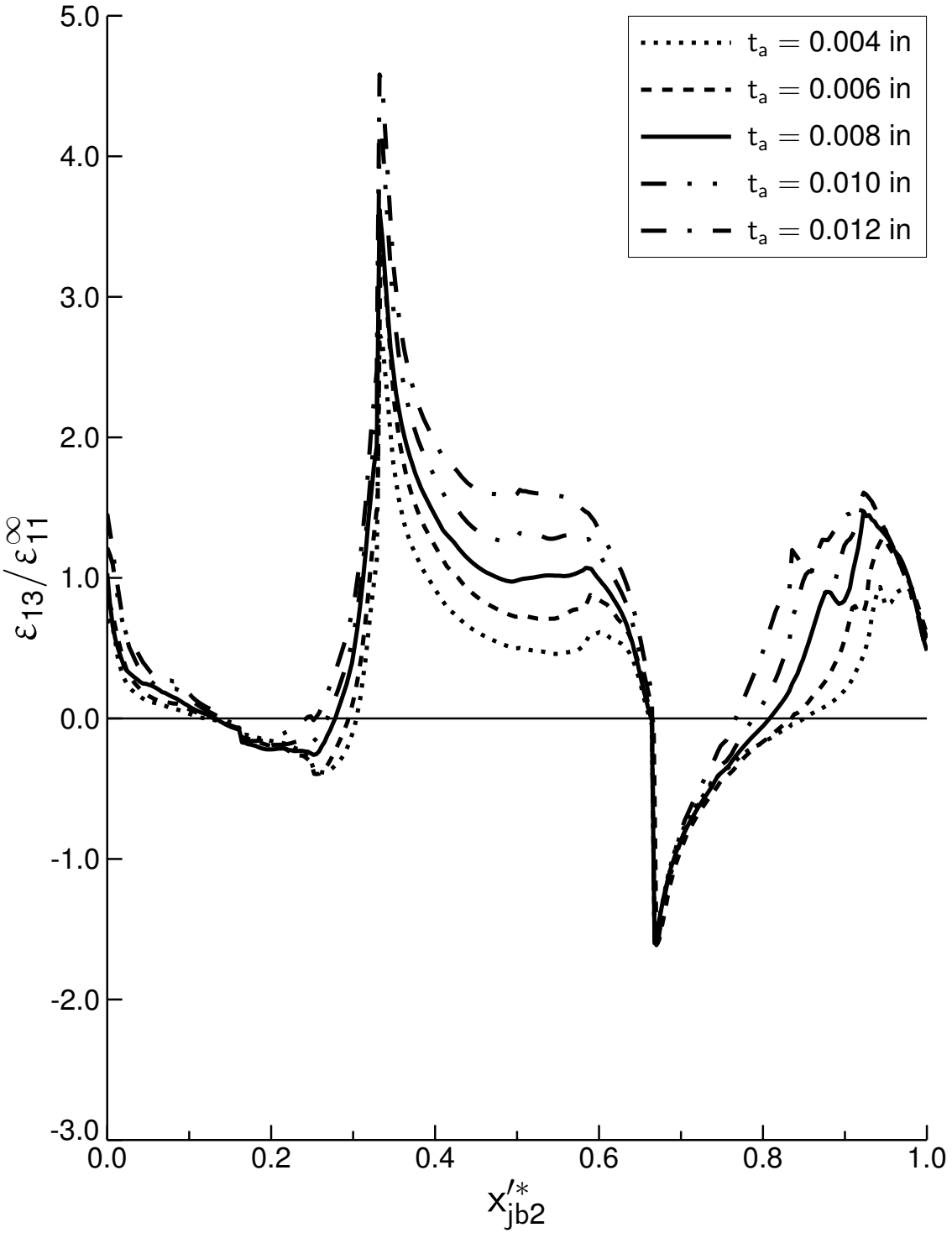

Figure 5.48 Plot of normalized ϵ_{13} versus x'^{*}_{jb2} at bondline 2 in adherend for the cases of adhesive thicknesses of 0.004 in, 0.006 in, 0.008 in, 0.010 in, and 0.012 in.

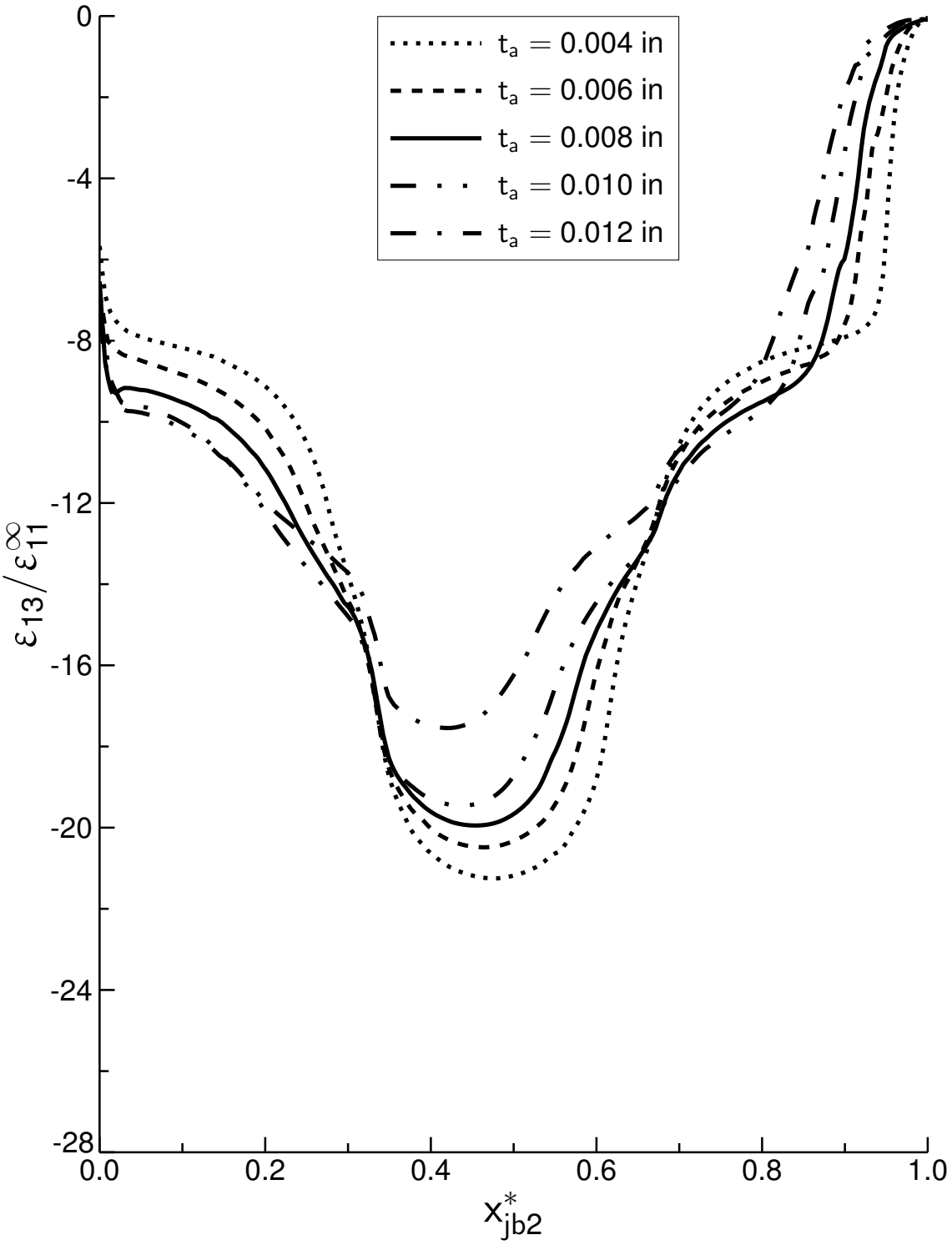

Figure 5.49 Plot of normalized ϵ_{13} versus x^*_{jb2} at bondline 2 in adhesive for the cases of adhesive thicknesses of 0.004 in, 0.006 in, 0.008 in, 0.010 in, and 0.012 in.

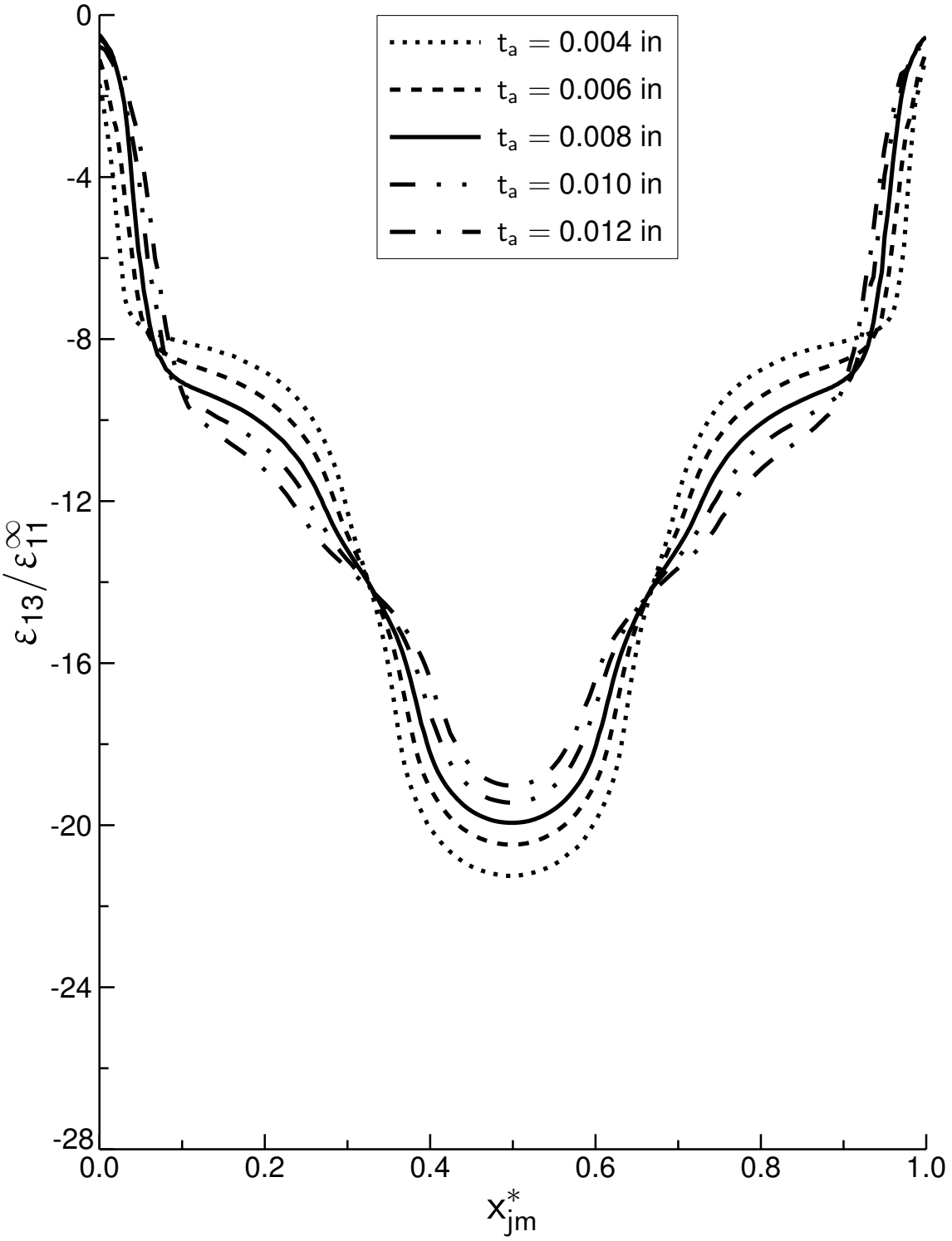

Figure 5.50 Plot of normalized ϵ_{13} versus x_{jm}^{*} at midline in adhesive for the cases of adhesive thicknesses of 0.004 in, 0.006 in, 0.008 in, 0.010 in, and 0.012 in.

x_a^* equal to -5.64. It can also be noted that the locations of the local minima in longitudinal strain, below the far-field value, shift inwards of the joint region with increasing adhesive thickness, and occur at x_a^* values of -0.35, -0.44, -0.54, -0.70, and -0.87 corresponding to cases with increasing adhesive thickness. The corresponding distributions of normalized shear strain exhibit similar behavior. In addition, the distributions of normalized shear strain show a region of maximum variation in the magnitudes of shear strain among the various cases, occurring between x_a^* values of 0 and -3.5. In this region, the maximum difference in the magnitudes of normalized shear strain for the various cases remains within 100% of the values for the baseline case of 0.008 in, but magnitudes of normalized shear strain for all cases remain below 0.13.

5.4 Effects of Unequal Scarf Angles

The strain results for the unequal scarf angle cases of (10°, 8°), (10°, 9°), (10°, 11°), and (10°, 12°) for the two-dimensional composite scarf joint configurations with the laminate of $[\pm 45_2/0_2]_S$ and minimum adhesive thickness of 0.008 in are presented in this section. The results for the case of (10°, 10°) with equal scarf angles are reproduced as those for the baseline case, and shown for comparison with the results for all other cases of unequal scarf angles. Additional results are included for all cases along the x_{jb1}^*-axis at bondline 1, as defined in Figure 5.1. These results specifically capture the effects incurred due to the asymmetry of the configurations with unequal scarf angles. The strains in adherend 2 along the x_a^*-axes are included for locations at the top and bottom of the adherend, and at the mid-ply locations of the upper and lower 0° plies. The additional mid-ply locations for the 0° plies were chosen in order to illustrate the asymmetric distributions of longitudinal strain in the far-field region occurring through the adherend thickness for the cases of unequal scarf angles.

The distributions of normalized strains for all cases along both bondlines and the adhesive midline are affected by the combination of the changing adhesive thickness within each case, introduced through the dissimilarity in scarf angles, and the chang-

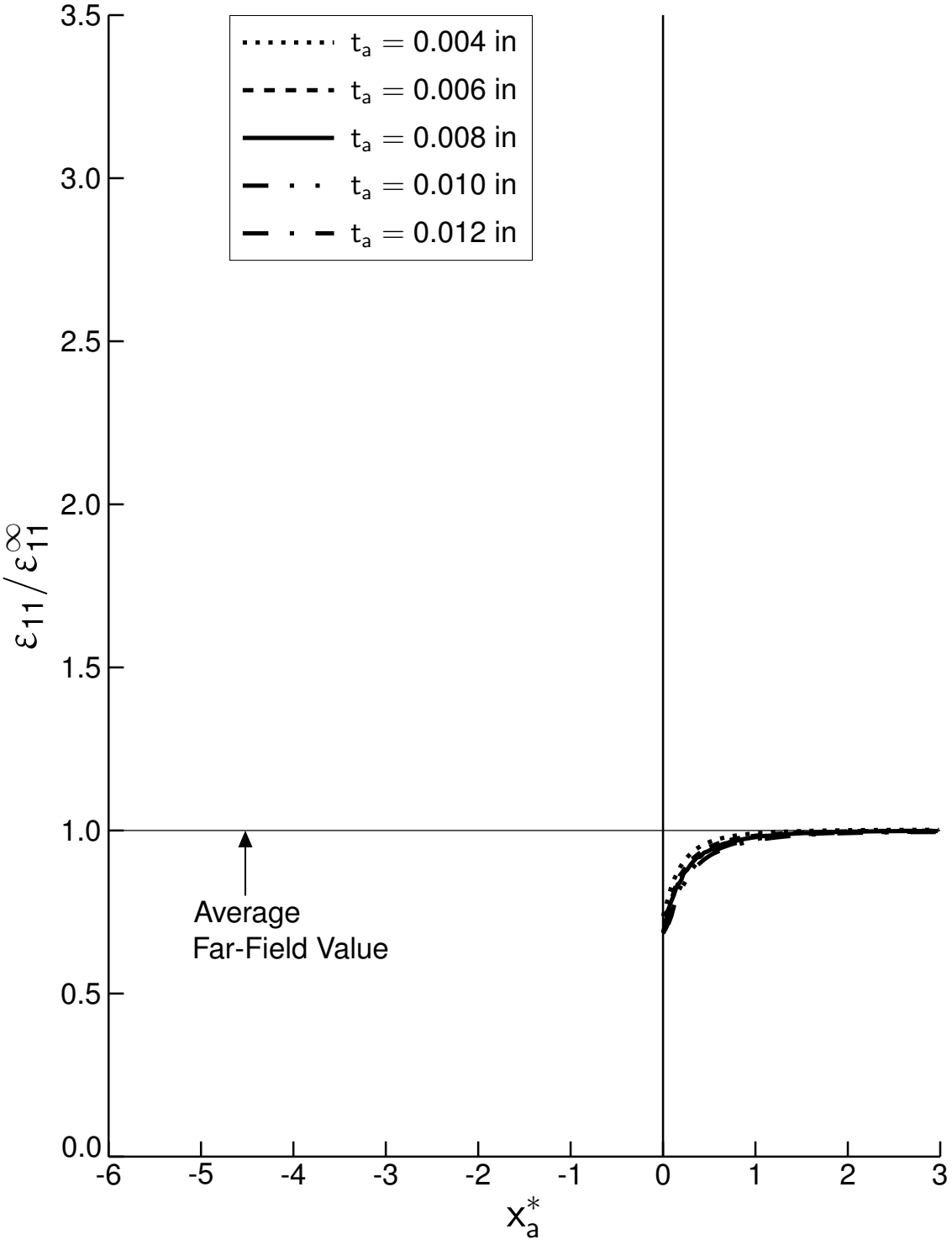

Figure 5.51 Plot of normalized ϵ_{11} versus x_a^* located at z equal to 0.072 in for the cases of adhesive thicknesses of 0.004 in, 0.006 in, 0.008 in, 0.010 in, and 0.012 in.

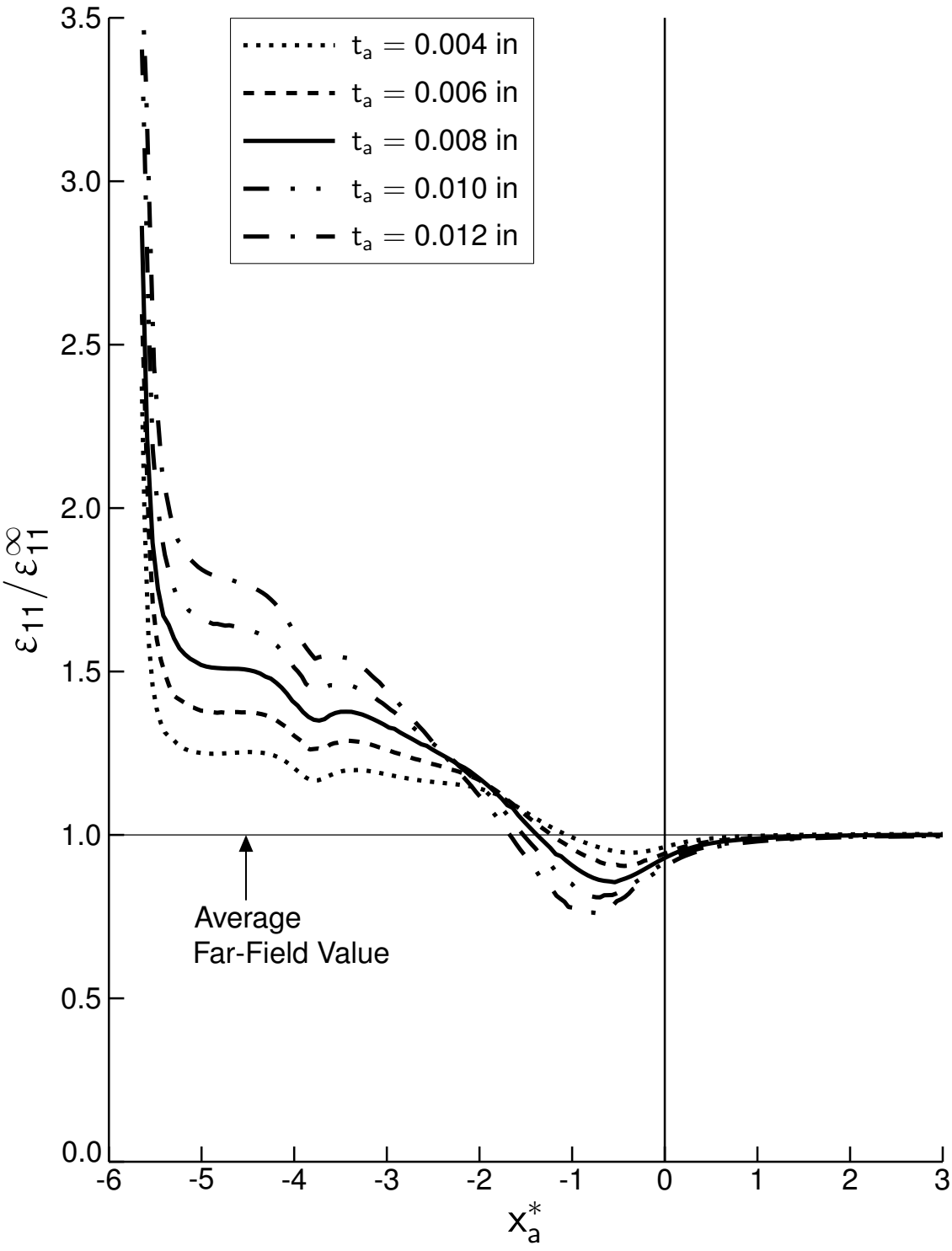

Figure 5.52 Plot of normalized ϵ_{11} versus x_a^* located at z equal to 0.0 in for the cases of adhesive thicknesses of 0.004 in, 0.006 in, 0.008 in, 0.010 in, and 0.012 in.

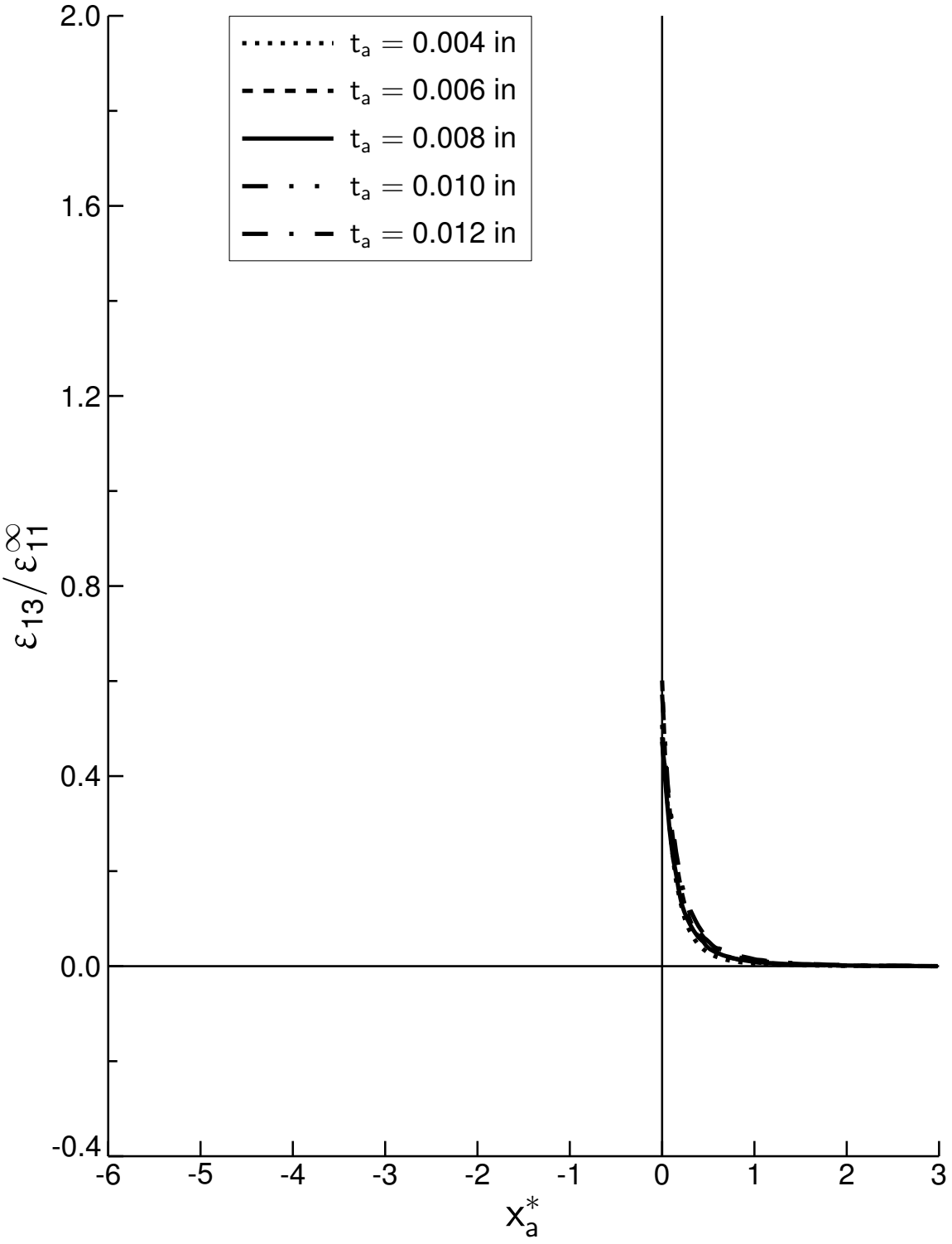

Figure 5.53 Plot of normalized ϵ_{13} versus x_a^* located at z equal to 0.072 in for the cases of adhesive thicknesses of 0.004 in, 0.006 in, 0.008 in, 0.010 in, and 0.012 in.

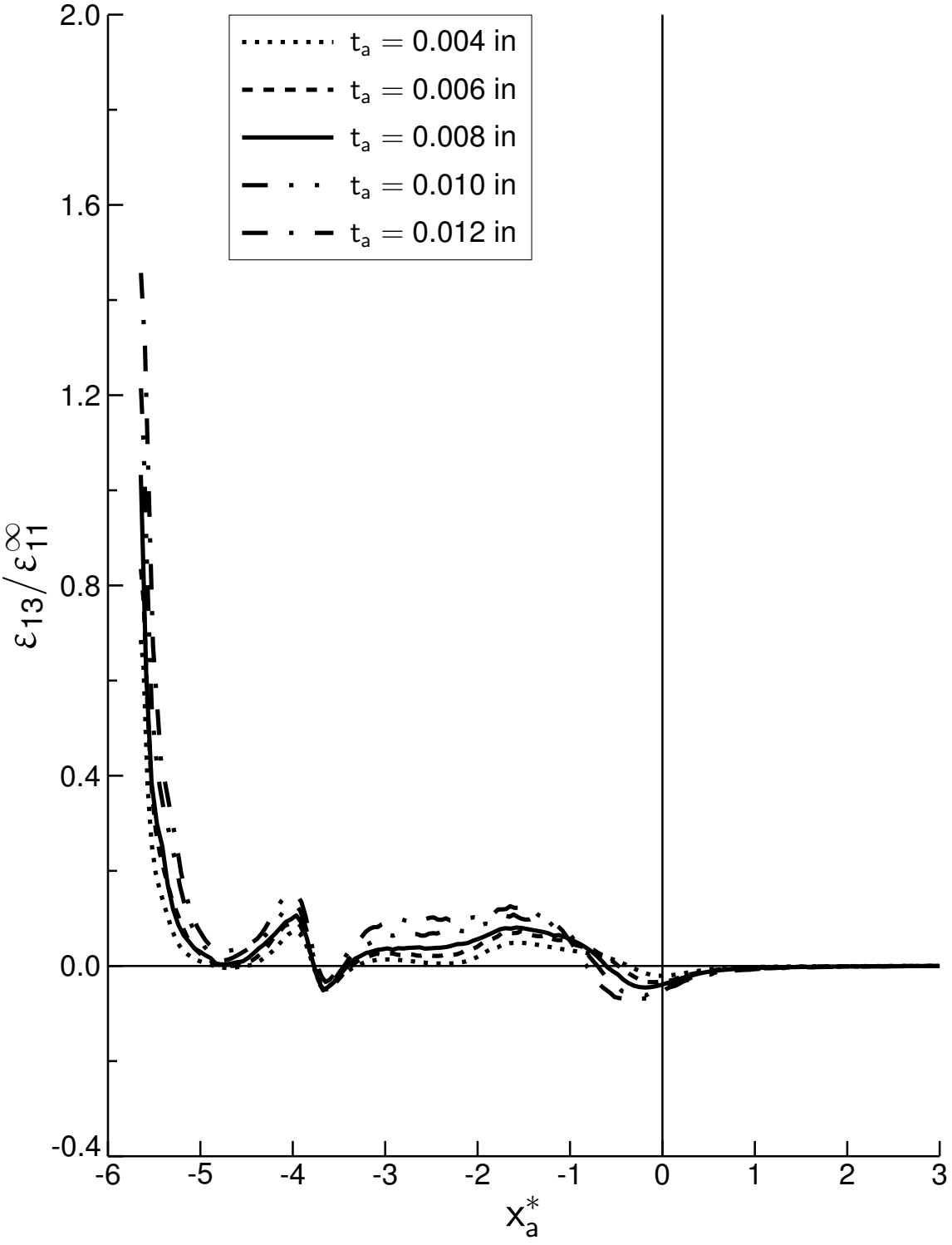

Figure 5.54 Plot of normalized ϵ_{13} versus x_a^* located at z equal to 0.0 in for the cases of adhesive thicknesses of 0.004 in, 0.006 in, 0.008 in, 0.010 in, and 0.012 in.

ing magnitude of the scarf angle for adherend 2 across all cases. The scarf angle for adherend 1 remains constant at 10°. Thus, the adhesive thickness decreases along bondline 1 for the cases of (10°, 8°) and (10°, 9°), but increases for the cases of (10°, 11°) and (10°, 12°). Conversely, the adhesive thickness increases along bondline 2 for the cases of (10°, 8°) and (10°, 9°), but decreases for the cases of (10°, 11°) and (10°, 12°). For all cases, the adhesive thickness varies linearly along the bondline. The maximum values of adhesive thickness corresponding to the cases with increasing scarf angle for adherend 2 are 0.020 in, 0.014 in, 0.008 in, 0.014 in, and 0.020 in. The distributions of normalized longitudinal strain along bondline 1 in adherend 1 and the adhesive are presented in Figures 5.55 and 5.57, respectively. The distributions of normalized longitudinal strain along bondline 2 in adherend 2 and the adhesive are presented in Figures 5.56 and 5.58, respectively. The distributions of normalized longitudinal strain along the adhesive midline are presented in Figure 5.59.

The distributions of normalized longitudinal strain in the adherend along both bondlines are the same for the baseline case, as they must be due to symmetry. In addition, the shapes of the distributions remain the same for all cases. For the distributions of longitudinal strain in the adherend along bondlines 1 and 2, the magnitudes of longitudinal strain in the ±45° plies near the acute tip of each adherend increase with increasing dissimilarity in scarf angles and increasing magnitude of the scarf angle for adherend 2. Thus, for longitudinal strain along bondline 1 in the adherend, the case of (10°, 12°) has the highest magnitudes with a local normalized peak of 4.81 at the acute tip of adherend 1, and 3.07 at the acute tip of 0° plies. The baseline case of (10°, 10°) has the lowest magnitudes of longitudinal strain with corresponding normalized peaks of 2.86 and 2.29 at the acute tip of adherend 1 and the acute tip of the 0° plies, respectively. In the ±45° plies, the magnitudes of longitudinal strain are increasingly ordered corresponding to the cases of (10°, 9°), (10°, 11°), and (10°, 8°) along bondline 1. The distributions of normalized longitudinal strain in the 0° plies for the cases of (10°, 8°), (10°, 9°), and (10°, 10°) overlap each other along bondline 1, while the magnitudes of longitudinal strain are increasingly ordered corresponding to the cases of (10°, 10°), (10°, 11°), and (10°, 12°), with normalized

values of 0.72, 0.77, and 0.94, occurring at the obtuse tip of the 0° plies, respectively. In contrast, the distributions in the 0° plies overlap each other for the cases of (10°, 10°), (10°, 11°), and (10°, 12°) along bondline 2, while for the cases of (10°, 8°) and (10°, 9°), the magnitudes of longitudinal strain remain higher than those for the case of (10°, 10°), with normalized magnitudes of 2.96, 2.63, and 1.94 at the acute tip of the 0° plies, and 1.02, 0.82, and 0.72 at the obtuse tip of the 0° plies, respectively. It is also noted that the magnitudes of negative gradients in longitudinal strain occurring near the end of bondline 1 decrease in order from the case of (10°, 8°) through to the case of (10°, 12°). In this region, local peaks in the magnitudes of longitudinal strain occur. The normalized values for these peaks along bondline 1 are 1.60, 1.52, 1.40 for the cases of (10°, 8°), (10°, 9°), and (10°, 10°), respectively, occurring at the normalized distance of 0.90. For the cases of (10°, 11°) and (10°, 12°), these values are 1.54 and 1.60, respectively, occurring at the normalized distances of 0.84 and 0.77, respectively. Similar trends are also exhibited in the distributions of longitudinal strain in the adherend in the corresponding region of bondline 2, with the magnitudes of negative gradients in longitudinal strain decreasing with decreasing scarf angle for adherend 2. For these distributions, the local peaks in longitudinal strain occur at the normalized distances of 0.76 and 0.81 for the cases of (10°, 8°) and (10°, 9°), respectively, with corresponding normalized values of 1.59 and 1.54, and at 0.90 for the cases of (10°, 10°), (10°, 11°), and (10°, 12°), with corresponding normalized values of 1.42, 1.54, and 1.65.

In the adhesive, the distributions of longitudinal strain along bondline 1 are similar to those in adherend 1. The most notable difference in the strain distributions occurs adjacent to the 0° plies. In this interval, the distributions of longitudinal strain for the cases of (10°, 8°) and (10°, 9°) have lower magnitudes than those for the baseline case, instead of any overlap in the distributions. For the distributions of longitudinal strain in the adhesive along bondline 2, the primary differences are exhibited through the increase in the magnitudes of normalized longitudinal strain for increasing magnitude of the scarf angle for adherend 2. Thus, the cases of (10°, 12°) and (10°, 11°) show higher magnitudes of longitudinal strain than those for the other cases along the

entire length of bondline 2. In addition, the distributions of normalized longitudinal strain for the cases of (10°, 8°) and (10°, 9°) show higher magnitudes than those for the baseline case adjacent to the lower ±45° plies, but lower magnitudes adjacent to the 0° and upper ±45° plies.

The distributions of normalized longitudinal strain at the adhesive midline also show similar characteristics to those at the bondlines in the adhesive. The magnitudes of longitudinal strain increase with increasing dissimilarity in scarf angles and the magnitude of scarf angle for adherend 2 adjacent to the ±45° plies, with the effect of increase in the magnitude of the scarf angle for adherend 2 being more amplified. This is indicated through the normalized magnitude of local peaks in longitudinal strain near the beginning and end of the adhesive midline. The local peaks in normalized longitudinal strain near the upper end of the midline have values of 4.27, 4.38, 4.34, 5.35, and 6.72 for the cases of (10°, 8°) through (10°, 12°), respectively. In the region adjacent to the 0° plies, the magnitudes of longitudinal strain increase simply with increase in magnitude of the scarf angle for adherend 2. In addition, due to asymmetry, the peaks in the magnitudes of longitudinal strain occurring near the beginning and end of the midline are shifted in location for all the cases. This is illustrated near the end of the midline, where local peaks in longitudinal strain occur at the normalized distance of 0.95 for the cases of (10°, 10°), (10°, 11°), and (10°, 12°), and at the normalized distances of 0.87 and 0.91 for the cases of (10°, 8°) and (10°, 9°), respectively. Similar shifts in location occur near the beginning of the adhesive midline as well, where the local peaks occur at the normalized distance of 0.05 for the cases of (10°, 8°), (10°, 9°), and (10°, 10°), and at 0.08, and 0.12 for the cases of (10°, 11°) and (10°, 12°), respectively.

The distributions of normalized shear strain along bondline 1 in adherend 1 and the adhesive are presented in Figures 5.60 and 5.62, respectively. The distributions of normalized shear strains along bondline 2 in adherend 2 and the adhesive are presented in Figures 5.61 and 5.63, respectively. The distributions of normalized shear strain along the adhesive midline are presented in Figure 5.64. As in the case of the distributions for longitudinal strain, the distributions for shear strain along

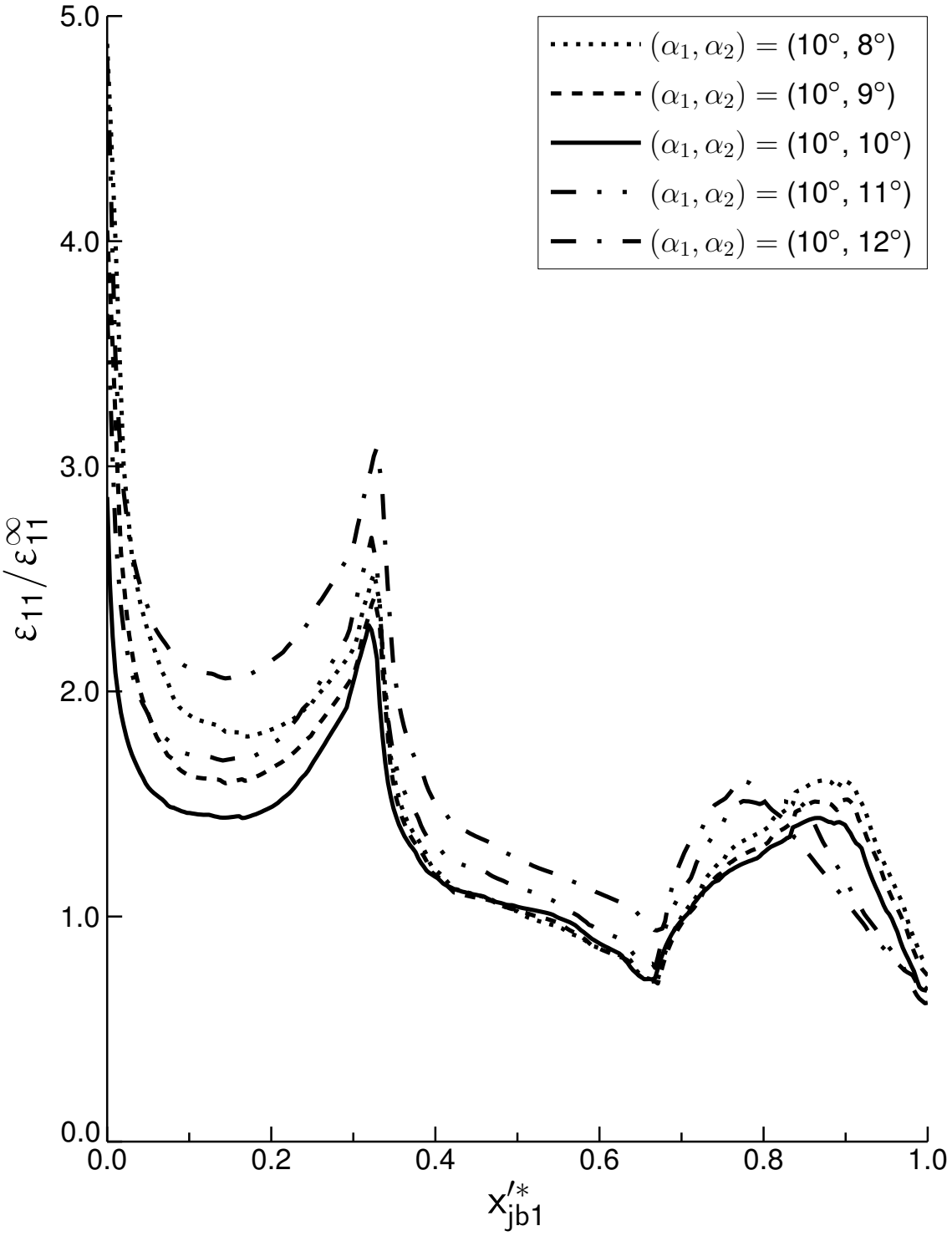

Figure 5.55 Plot of normalized ϵ_{11} versus $x_{jb1}^{\prime *}$ at bondline 1 in adherend for the cases of unequal scarf angles of (10°, 8°), (10°, 9°), (10°, 10°), (10°, 11°), and (10°, 12°).

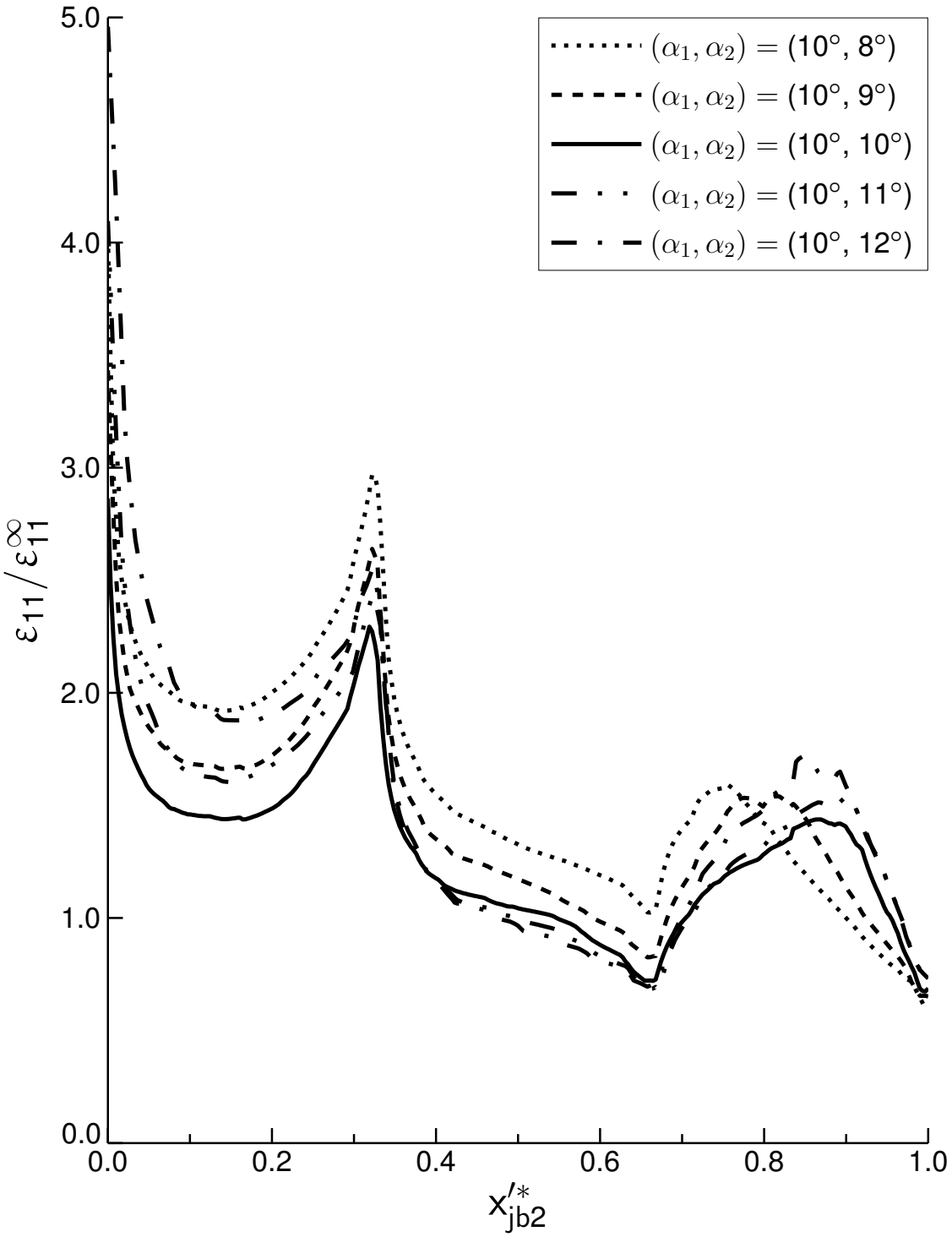

Figure 5.56 Plot of normalized ϵ_{11} versus x'^{*}_{jb2} at bondline 2 in adherend for the cases of unequal scarf angles of (10°, 8°), (10°, 9°), (10°, 10°), (10°, 11°), and (10°, 12°).

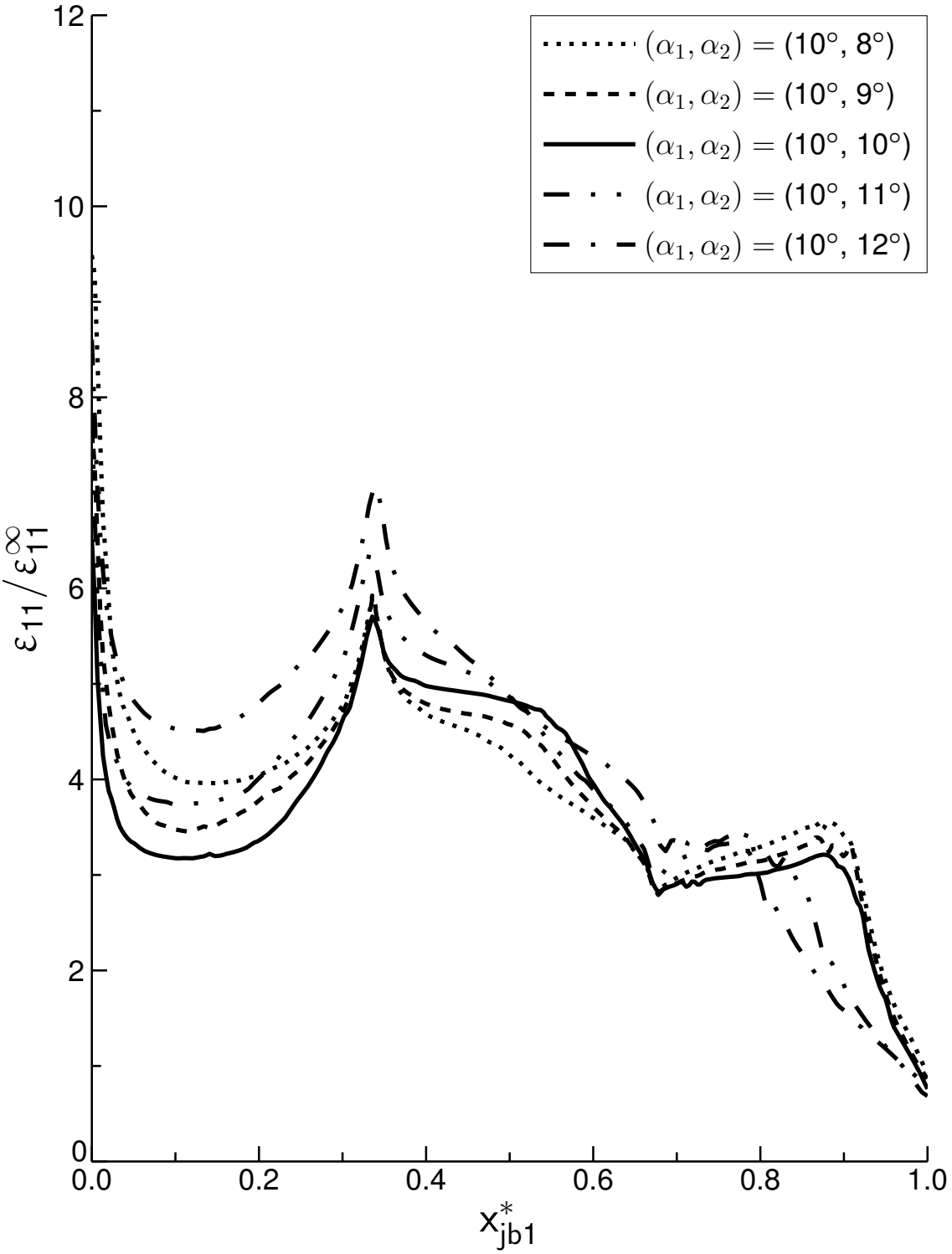

Figure 5.57 Plot of normalized ϵ_{11} versus x^*_{jb1} at bondline 1 in adhesive for the cases of unequal scarf angles of (10°, 8°), (10°, 9°), (10°, 10°), (10°, 11°), and (10°, 12°).

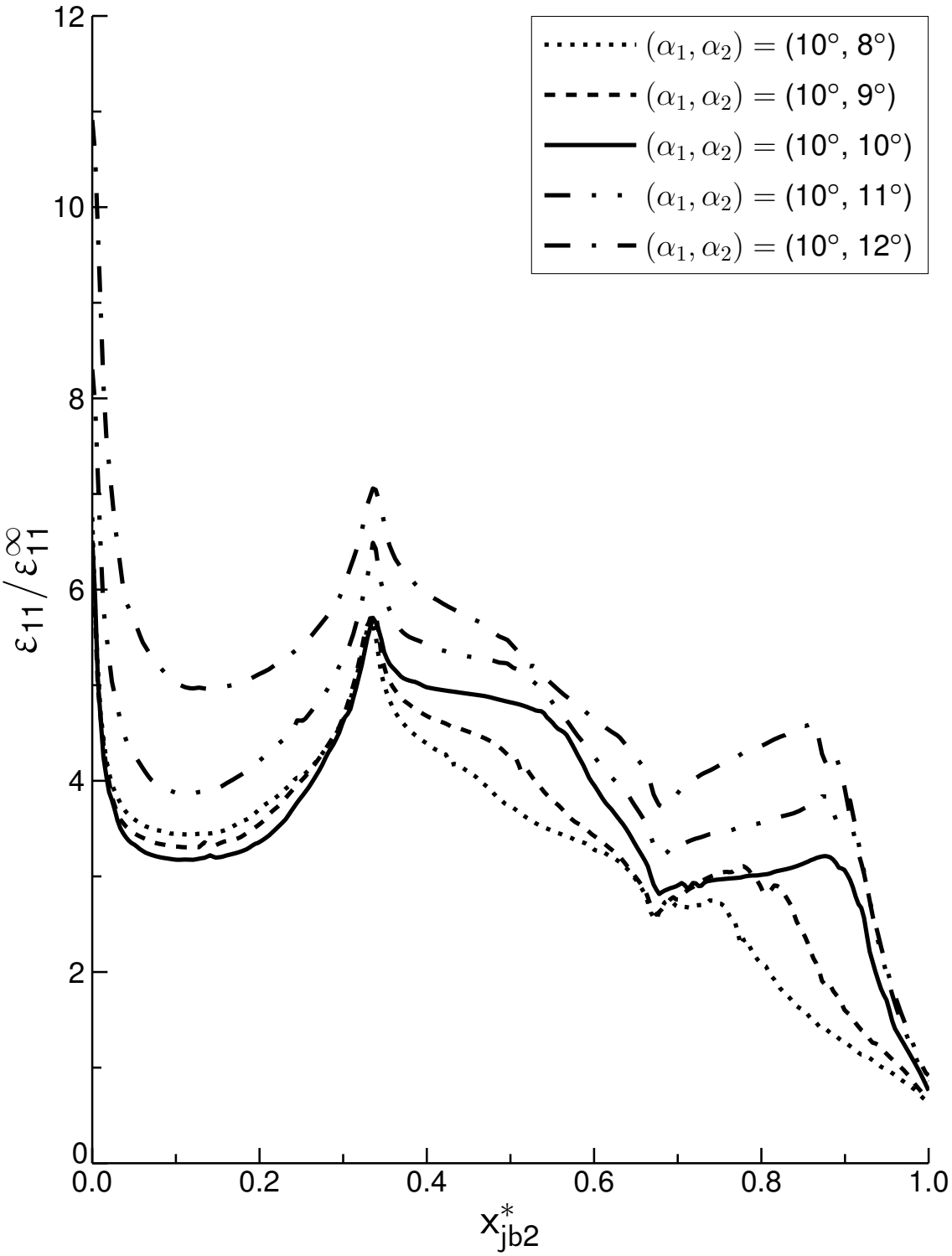

Figure 5.58 Plot of normalized ϵ_{11} versus x_{jb2}^{*} at bondline 2 in adhesive for the cases of unequal scarf angles of (10°, 8°), (10°, 9°), (10°, 10°), (10°, 11°), and (10°, 12°).

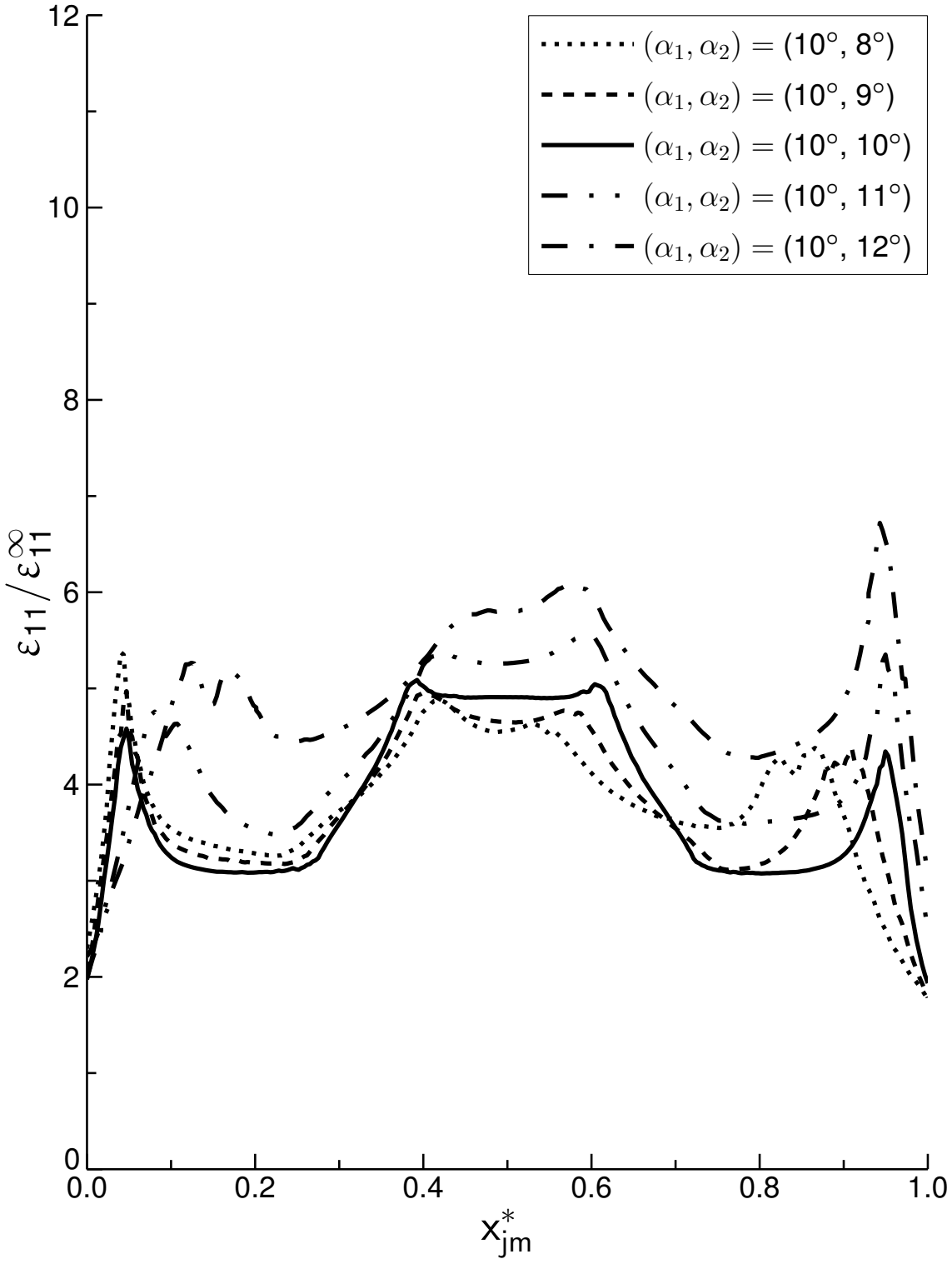

Figure 5.59 Plot of normalized ϵ_{11} versus x_{jm}^{*} at midline in adhesive for the cases of unequal scarf angles of (10°, 8°), (10°, 9°), (10°, 10°), (10°, 11°), and (10°, 12°).

both bondlines show similar characteristics in the adherends and in the adhesive. However, unlike for longitudinal strains, there also are significant differences between the distributions in the adherend and the adhesive. Along bondlines 1 and 2, for the distributions of normalized shear strain in the adherend in the ±45° plies near the acute tip of the adherend, the magnitudes of shear strain increase with increasing dissimilarity in scarf angles and increasing magnitude of the scarf angle for adherend 2, as in the case of distributions for longitudinal strain in this region. The greatest variation in the magnitudes of shear strain occurs within the 0° plies and the ±45° plies near the obtuse tip of the adherend for the various cases of unequal scarf angles. In the 0° plies along bondline 1, the magnitudes of shear strain increase in order corresponding to the cases of (10°, 10°), (10°, 9°), (10°, 8°), (10°, 11°), and (10°, 12°), thus indicating increase in magnitudes with both increasing dissimilarity in scarf angles as well as magnitude of the scarf angle for adherend 2. The distributions for the cases of (10°, 8°) and (10°, 11°) in this region overlap. Along bondline 2, the magnitudes of shear strain in the 0° plies increase in order corresponding to the cases of (10°, 10°), (10°, 11°), (10°, 9°), (10°, 12°), and (10°, 8°), thus indicating increase in magnitudes with increasing dissimilarity in scarf angles but decreasing scarf angle for adherend 2. In the ±45° plies near the obtuse tip of the adherend along bondline 1, the distributions of normalized shear strain for the cases of (10°, 10°), (10°, 9°), and (10°, 8°) almost entirely overlap, and the magnitudes increase with increasing scarf angle of adherend 2 greater than 10°. Along bondline 2, the distributions of normalized shear strain for the cases of (10°, 10°), (10°, 11°), and (10°, 12°) show overlap in this region, while the magnitudes increase with decreasing scarf angle of adherend 2 less than 10°. The values of local peaks in normalized shear strain in the adherend along bondline 1 near the obtuse tip of the adherend are 1.78, 1.56, 1.45 for the cases of (10°, 8°), (10°, 9°) and (10°, 10°), respectively, and occur at the normalized distance of 0.93. For the cases of (10°, 11°), and (10°, 12°), the corresponding peak values are 1.54 and 1.40, occurring at the normalized distances of 0.92 and 0.94, respectively. Similarly, along bondline 2 in the adherend, the corresponding values of local peaks in normalized shear strain are 1.22 and 1.43 for the cases of (10°, 8°) and (10°, 9°),

respectively, occurring at the normalized distance of 0.92, and are 1.45, 1.56, and 1.91 for the cases of (10°, 10°), (10°, 11°), and (10°, 12°), respectively, occurring at the normalized distance of 0.93.

The distributions of normalized shear strain in the adhesive along both bondlines show similar characteristics. In the region adjacent to the ±45° plies near the acute tip of the adherend along both bondlines, the magnitudes of normalized shear strain increase with increasing dissimilarity in scarf angles and increasing scarf angle for adherend 2, with the baseline case having the lowest magnitudes. Conversely, in the region adjacent to the 0° plies, the baseline case has the highest magnitudes of normalized shear strain, and the magnitudes of normalized shear strain decrease with decreasing scarf angle for adherend 2. In addition, the locations of the local peaks in shear strain shift along the bondlines for the various cases. Thus, along bondline 1, the local peaks in normalized shear strain in this region have values of -17.2, -18.6, -20.0, -19.9, and -19.7 corresponding to cases with increasing scarf angle for adherend 2, respectively, and occur at the normalized distances of 0.41, 0.45, 0.45, 0.41, and 0.37, respectively. Similarly, along bondline 2, the local peaks in normalized shear strain in the region adjacent to the 0° plies have values of -17.4, -18.6, -20.0, -19.8, and -19.3 for the cases of increasing scarf angle for adherend 2, respectively, and occur at the normalized distances of 0.37, 0.41, 0.45, 0.45, and 0.41, respectively. In the region adjacent to the ±45° plies near the obtuse tip of the adherend, the magnitudes of normalized shear strain increase with decreasing scarf angle for adherend 2, with the distributions for the cases of (10°, 8°), (10°, 9°), and (10°, 10°) almost overlapping. In this region along bondline 2, however, the magnitudes of longitudinal strain increase with increasing scarf angle for adherend 2, as in the region adjacent to the ±45° plies near the acute tip of the adherend. It is also noted, as for previous parametric cases, that sharp gradients in shear strain occur near the ends of both bondlines in the adhesive, and these changes occur at varying locations for the different cases. Along bondline 1, these changes occur at the normalized distance of 0.86 for the cases of (10°, 8°), (10°, 9°), and (10°, 10°), and at 0.78 and 0.74 for the cases of (10°, 11°) and (10°, 12°), respectively. Similarly, along bondline 2, similar changes occur at the

normalized distances 0.73 for the case of (10°, 8°), at 0.81 for the case of (10°, 9°), at 0.86 for the cases of (10°, 10°) and (10°, 11°), and 0.84 for the case of (10°, 12°).

The distributions of normalized shear strain at the adhesive midline generally show similar characteristics as those in the adhesive at the bondlines. There are, however, some differences. The magnitudes of normalized shear strain in the region adjacent to the 0° plies again are highest for the baseline case and decrease with decreasing scarf angle for adherend 2. In addition, there are accompanying shifts in the locations of the local peak values in the region. The local peaks in normalized shear strain occur at 0.46, 0.47, 0.50, 0.52, and 0.53 corresponding to cases with increasing scarf angle for adherend 2, respectively, and have corresponding values of -17.2, -18.6, -19.9, -19.9, and -19.4. In the region adjacent to the ±45° plies near the acute tip of each adherend, the magnitudes of normalized shear strain decrease with increasing scarf angle for adherend 2, except in the transition region adjacent to the 0° plies. However, in the corresponding region adjacent to the ±45° plies near the obtuse tip of each adherend, except within the transition region adjacent to the 0° plies, the magnitudes of normalized shear strain increase with increasing scarf angle for adherend 2, and show greater variation among the various cases. Finally, the locations of sharp changes in gradients in shear strain occurring near the end of the adhesive midline vary for the different cases, as for the distributions along the bondlines. They occur at the normalized distance of 0.80 for the case of (10°, 8°), at 0.87 for the case of (10°, 9°), and at 0.92 for the cases of (10°, 10°), (10°, 11°), and (10°, 12°).

The distributions of normalized strains along the x_a^*-axes at the top and bottom of adherend 2, and at the mid-ply locations of the top and bottom 0° plies at z equal to 0.042 in and 0.030 in, respectively, are presented in Figures 5.65 through 5.72. The strain behavior for the cases of unequal scarf angles exhibits similar characteristics in the joint region as exhibited for the equal scarf angle cases, and for the adhesive thickness cases as presented in Sections 5.2 and 5.3.

The main difference for the cases of unequal scarf angles is exhibited outside the joint region in the far-field values of normalized longitudinal strain at different loca-

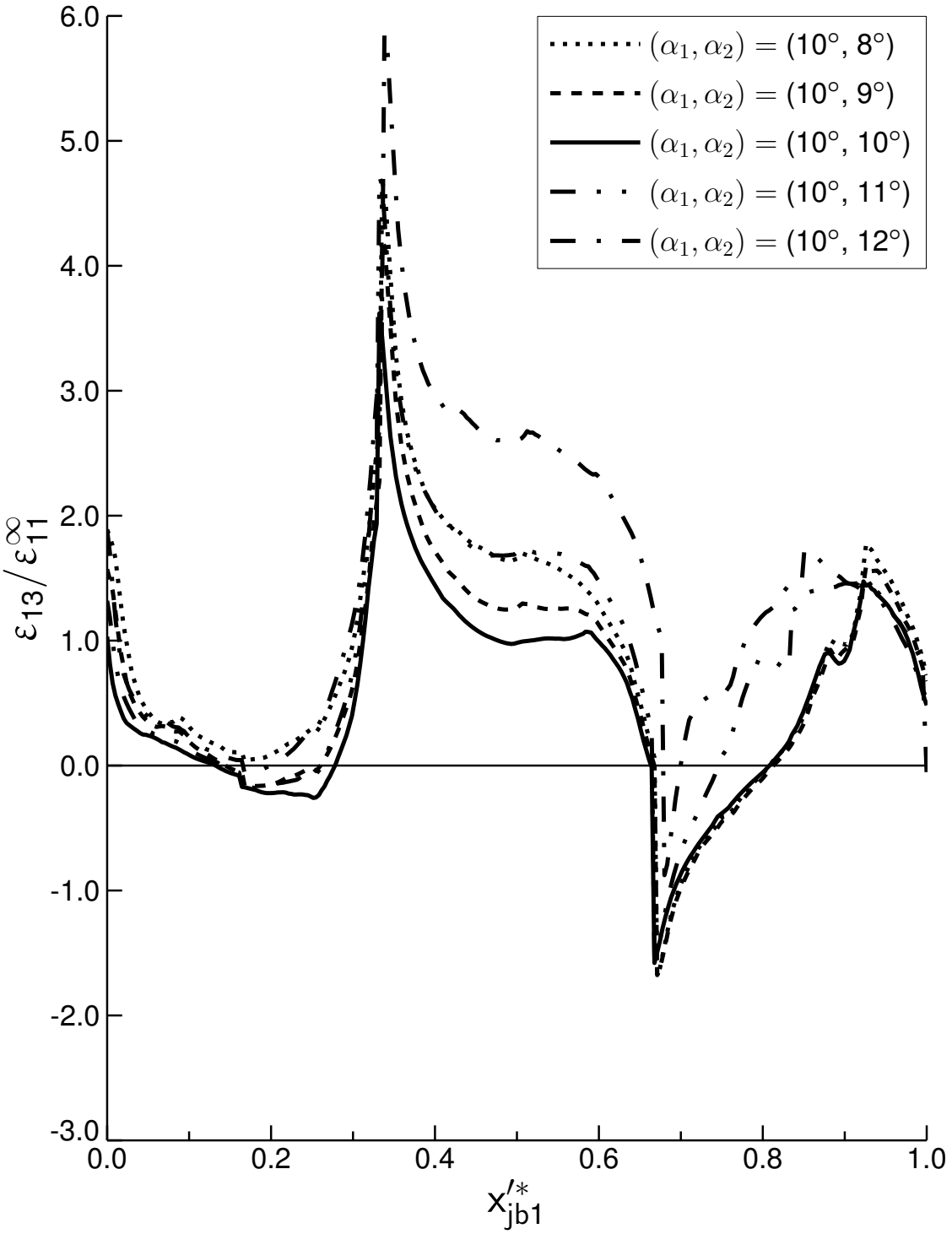

Figure 5.60 Plot of normalized ϵ_{13} versus x'^{*}_{jb1} at bondline 1 in adherend for the cases of unequal scarf angles of (10°, 8°), (10°, 9°), (10°, 10°), (10°, 11°), and (10°, 12°).

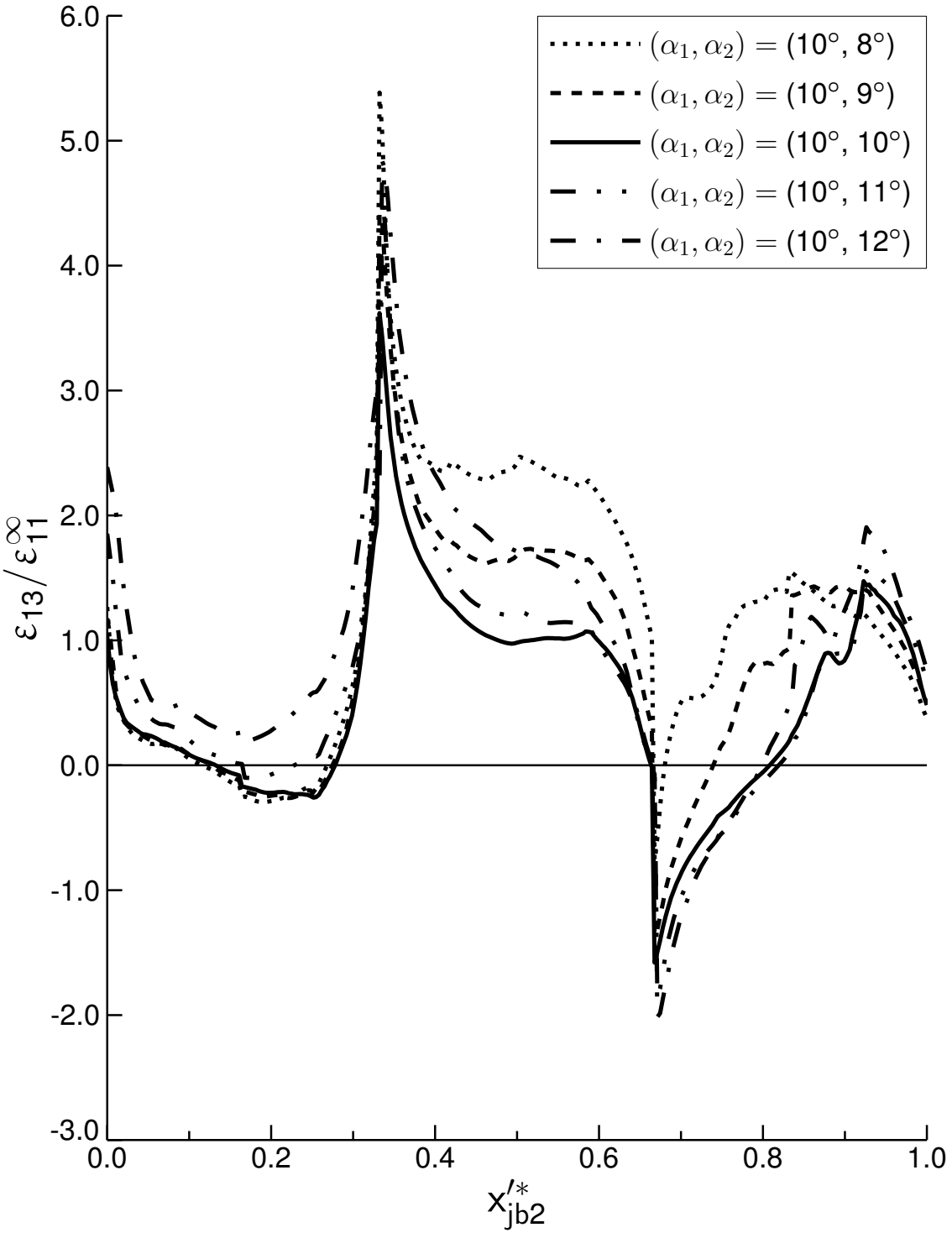

Figure 5.61 Plot of normalized ϵ_{13} versus x'^{*}_{jb2} at bondline 2 in adherend for the cases of unequal scarf angles of (10°, 8°), (10°, 9°), (10°, 10°), (10°, 11°), and (10°, 12°).

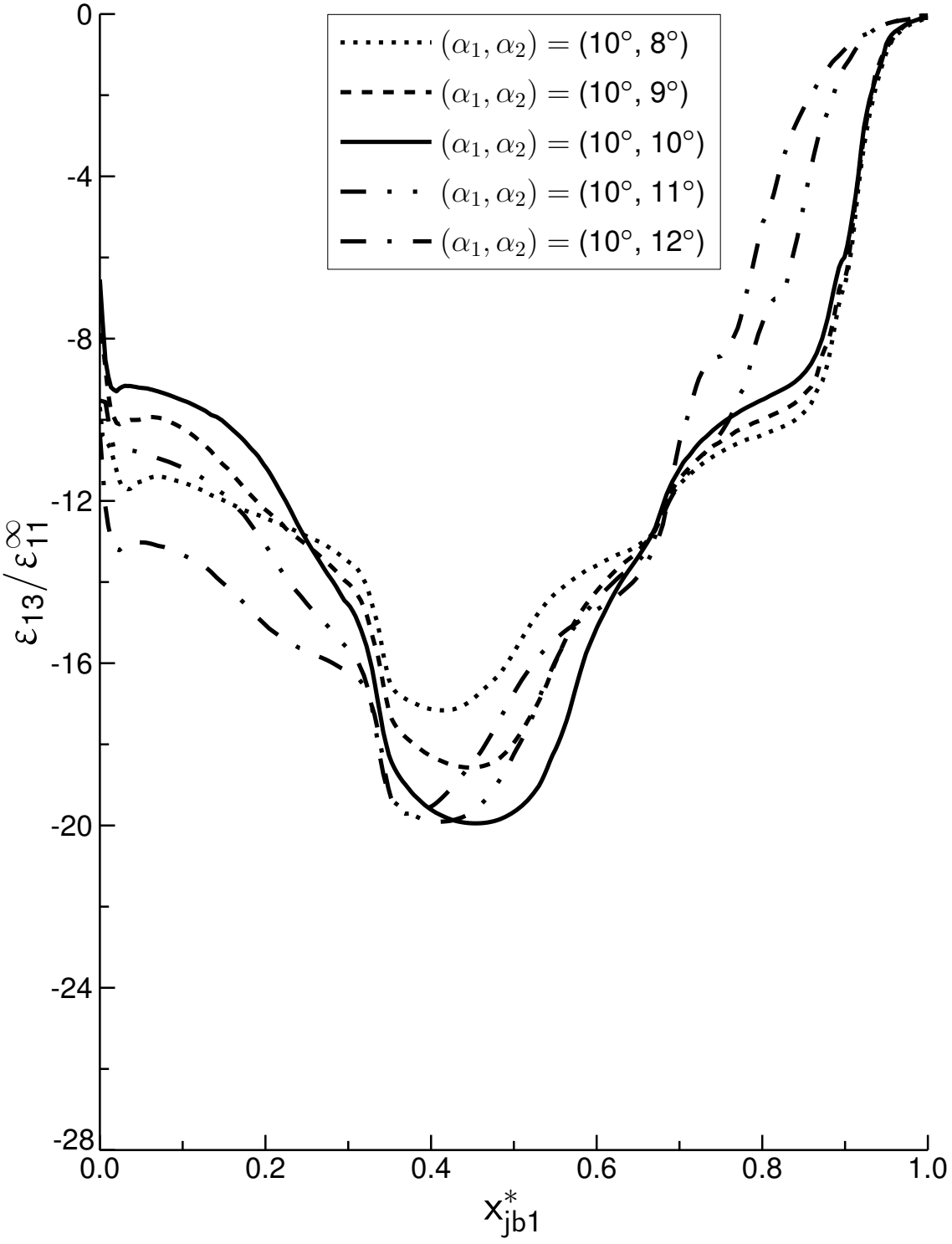

Figure 5.62 Plot of normalized ϵ_{13} versus x_{jb1}^{*} at bondline 1 in adhesive for the cases of unequal scarf angles of (10°, 8°), (10°, 9°), (10°, 10°), (10°, 11°), and (10°, 12°).

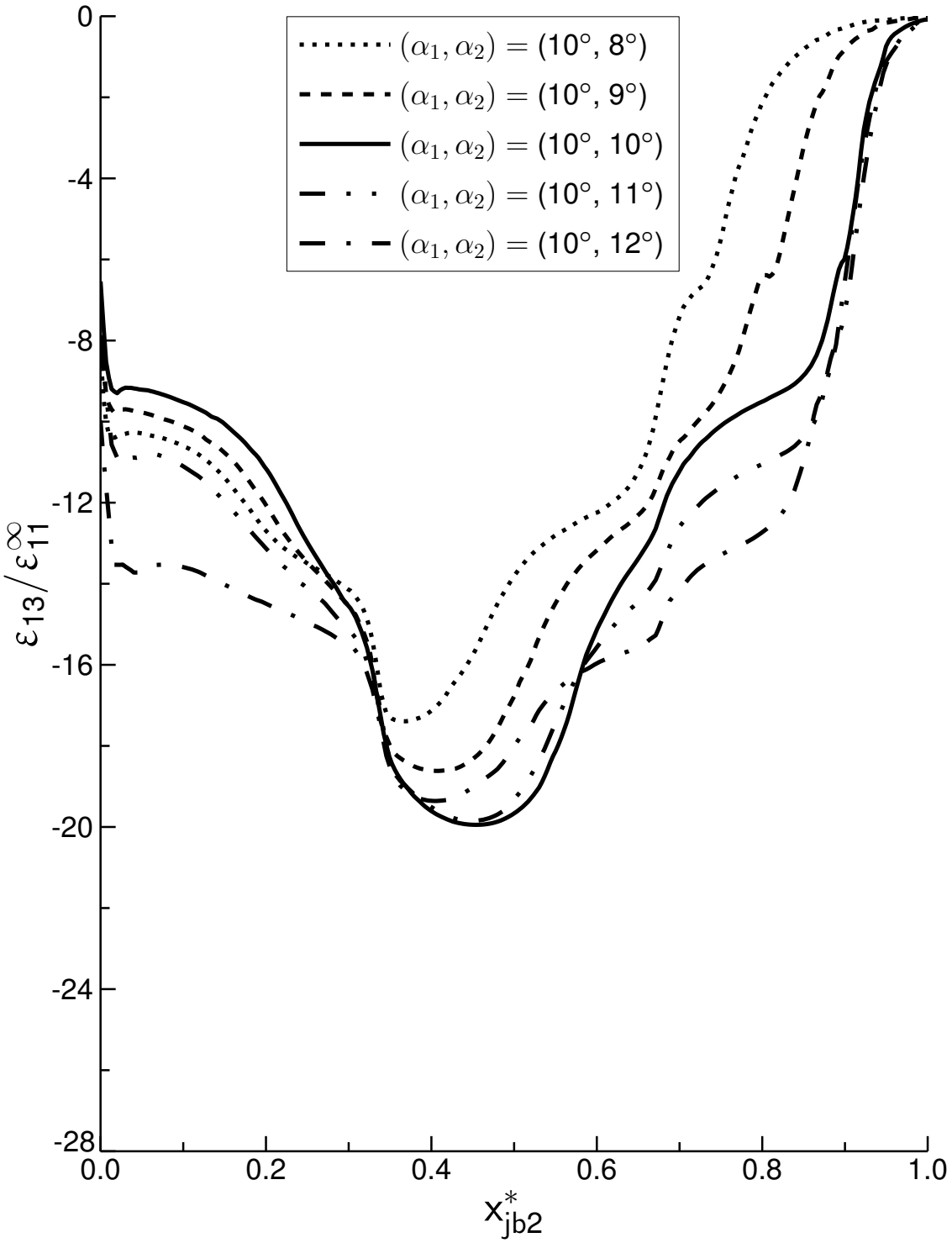

Figure 5.63 Plot of normalized ϵ_{13} versus x^*_{jb2} at bondline 2 in adhesive for the cases of unequal scarf angles of (10°, 8°), (10°, 9°), (10°, 10°), (10°, 11°), and (10°, 12°).

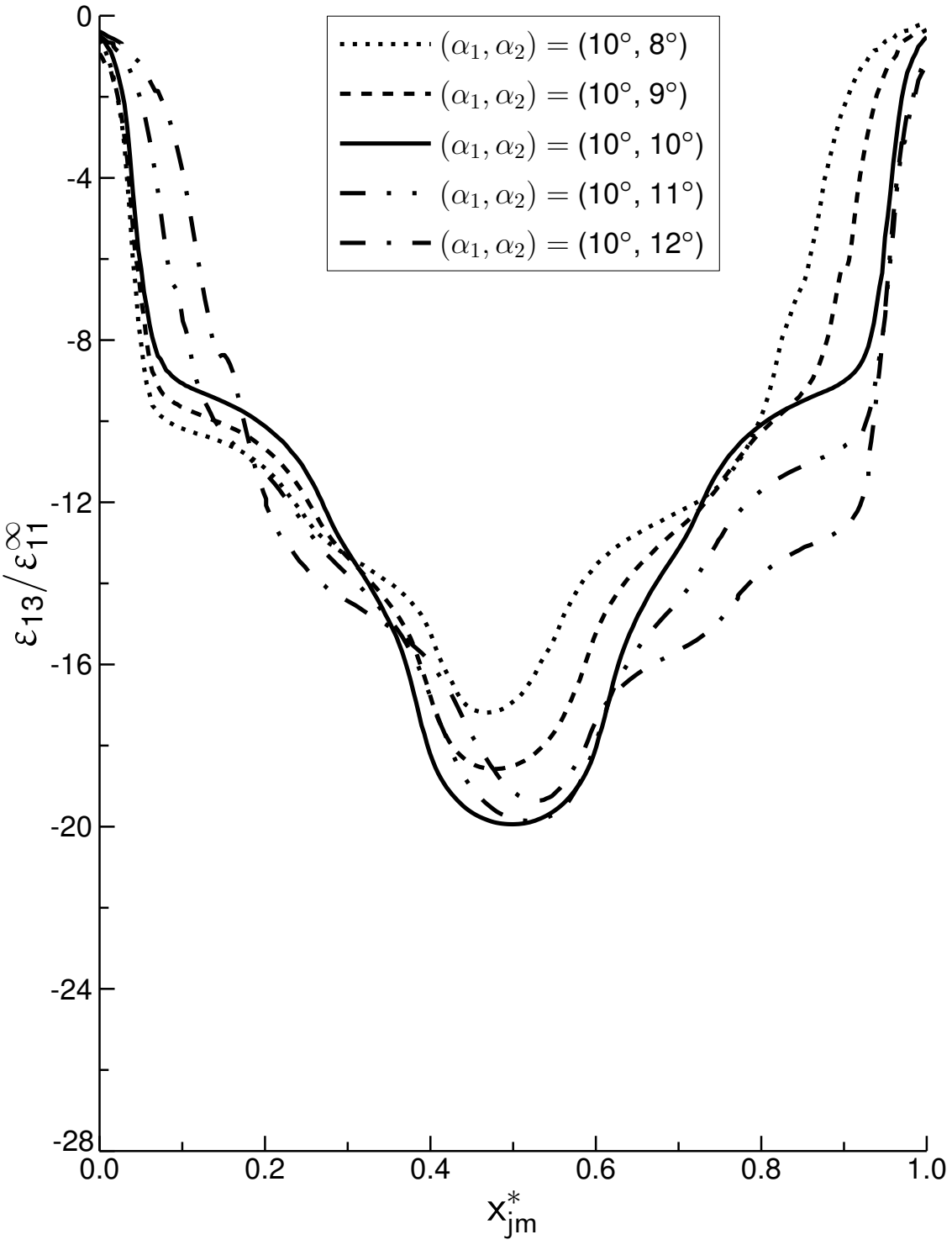

Figure 5.64 Plot of normalized ϵ_{13} versus x_{jm}^{*} at midline in adhesive for the cases of unequal scarf angles of (10°, 8°), (10°, 9°), (10°, 10°), (10°, 11°), and (10°, 12°).

tions through the adherend thickness. The far-field values of normalized longitudinal strain vary from 1.0 for the various cases, and the difference in values increases with increasing dissimilarity in scarf angles and the distance of the through-thickness location from the centerline of the adherend at z equal to 0.036 in. It is noted that for the cases of (10°, 8°) and (10°, 12°), the values of normalized far-field longitudinal strains reach 0.85 and 1.15 at the top and bottom of the adherend, respectively, for both cases. Similarly, for the cases of (10°, 9°) and (10°, 11°), the values of normalized far-field longitudinal strains reach 0.93 and 1.07 at the top and bottom of the adherend, respectively, for both cases. The far-field values of normalized longitudinal strain at the mid-ply location of the upper 0° plies are 0.97 for the case of (10°, 8°), 0.99 for the cases of (10°, 9°) and (10°, 11°), and 0.98 for the case of (10°, 12°). Similarly, at the mid-ply location of the lower 0° plies, the far-field values of normalized longitudinal strain are 1.01 for the cases of (10°, 9°) and (10°, 11°), and 1.02 for the cases of (10°, 8°) and (10°, 12°). The magnitude of the mismatch in the values of longitudinal strain from the value of the average far-field longitudinal strain at different through-thickness locations in the adherend in the far-field region thus depends linearly on the magnitude of mismatch between the scarf angles and the distance of the location from the centerline of the adherend. The far-field value of normalized shear strain for all cases at all through-thickness locations is 0.0.

In general, the magnitudes of normalized longitudinal strain in the joint region increase near the adhesive, except at the top of adherend 2. At this location, there is only negative strain gradient, leading to normalized values of longitudinal strain at the obtuse tip of the adherend of 0.59, 0.65, 0.69, 0.72, and 0.73 corresponding to cases with increasing scarf angle for adherend 2, respectively. The sharpest increase for all cases is observed at the bottom of adherend 2, near the acute tip of the adherend, where the normalized values of longitudinal strain are 4.03, 3.43, 2.86, 4.10, and 4.96 corresponding to cases with increasing scarf angle for adherend 2, respectively. Thus, the magnitudes of longitudinal strain increase with increasing dissimilarity in scarf angles, and with increasing scarf angle for adherend 2. In addition, the location of the local minimum occurring near the beginning of the joint region shifts

towards the adhesive along x_a^* for all cases. This is exhibited in the distributions of longitudinal strain at the bottom of the adherend, where the local minimum in longitudinal strain near the beginning of the joint region occurs at x_a^* values of -1.85, -1.14, -0.54, -0.94, and -1.33 corresponding to cases with increasing scarf angle for adherend 2, respectively. This indicates the greater spread of the distributions of longitudinal strain within the joint region for the various cases. The distributions of normalized shear strain are different than those for normalized longitudinal strain, but do show some similar trends for all cases, with increasing magnitude of shear strain with increasing dissimilarity between scarf angles as well as increasing scarf angle for adherend 2. This is indicated through the values of normalized shear strain near the acute tip of the adherend, which are 1.27, 1.18, 1.03, 1.85, and 2.35 corresponding to cases with increasing scarf angle for adherend 2, respectively.

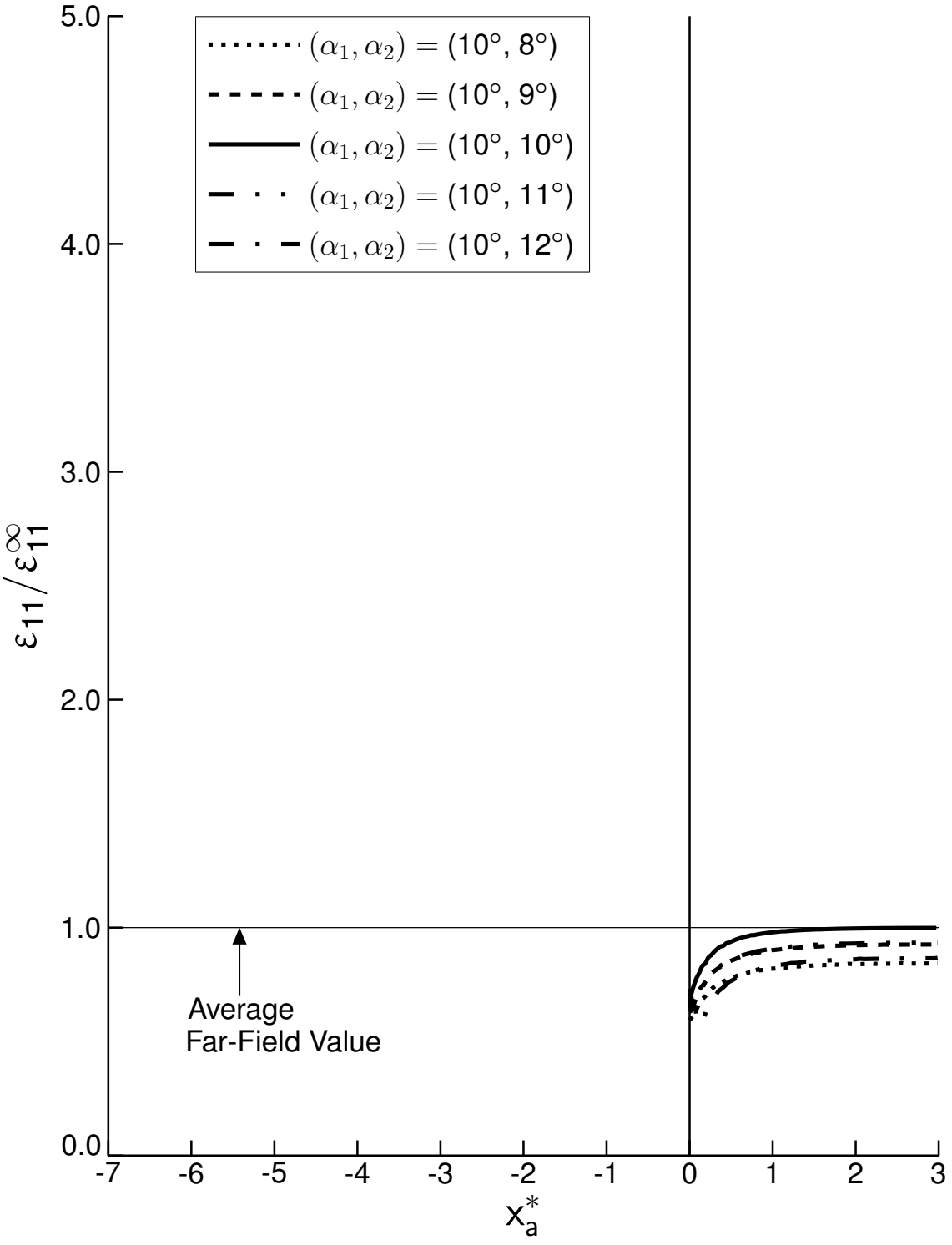

Figure 5.65 Plot of normalized ϵ_{11} versus x_a^* located at z equal to 0.072 in for the cases of unequal scarf angles of (10°, 8°), (10°, 9°), (10°, 10°), (10°, 11°), and (10°, 12°).

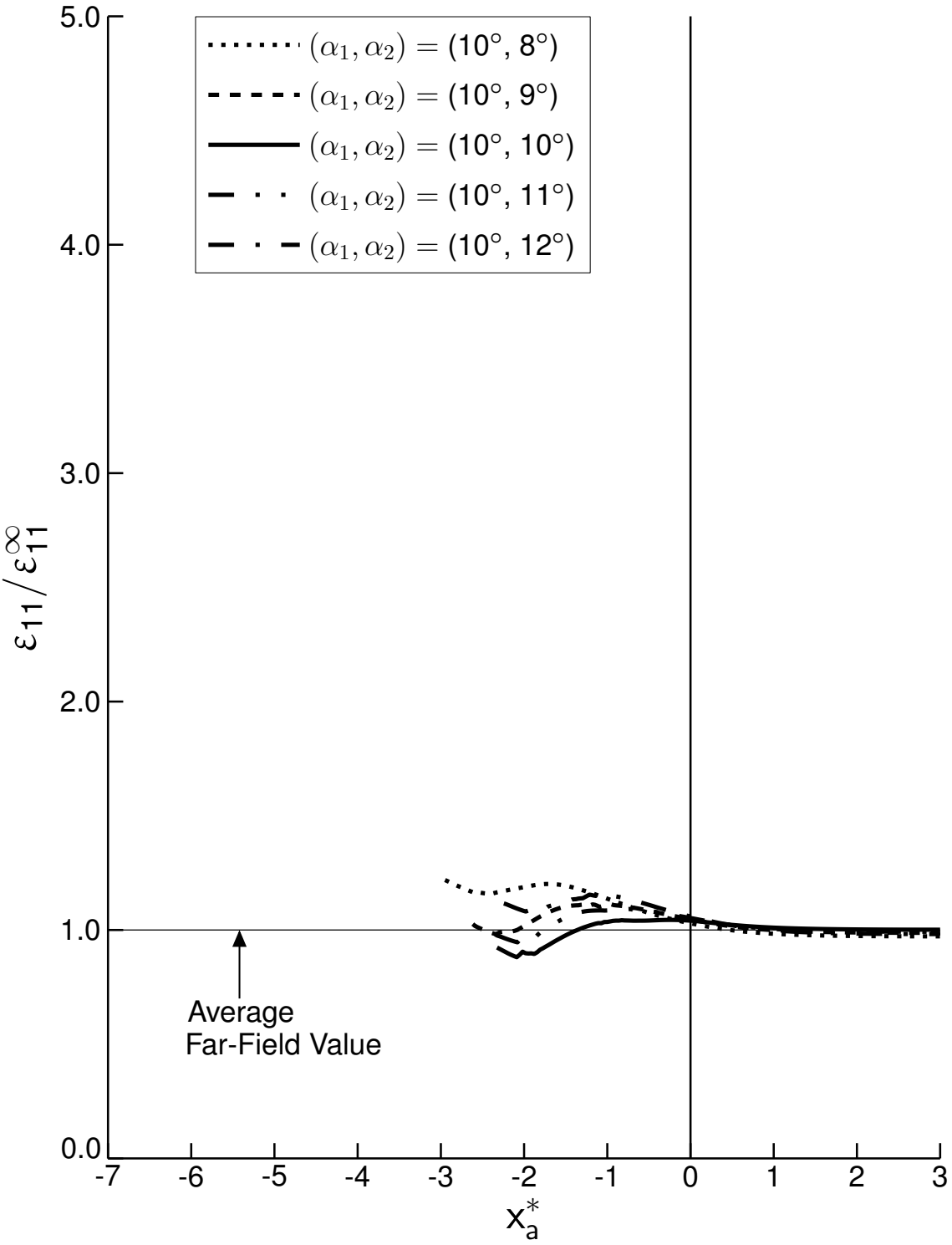

Figure 5.66 Plot of normalized ϵ_{11} versus x_a^* located at z equal to 0.042 in for the cases of unequal scarf angles of (10°, 8°), (10°, 9°), (10°, 10°), (10°, 11°), and (10°, 12°).

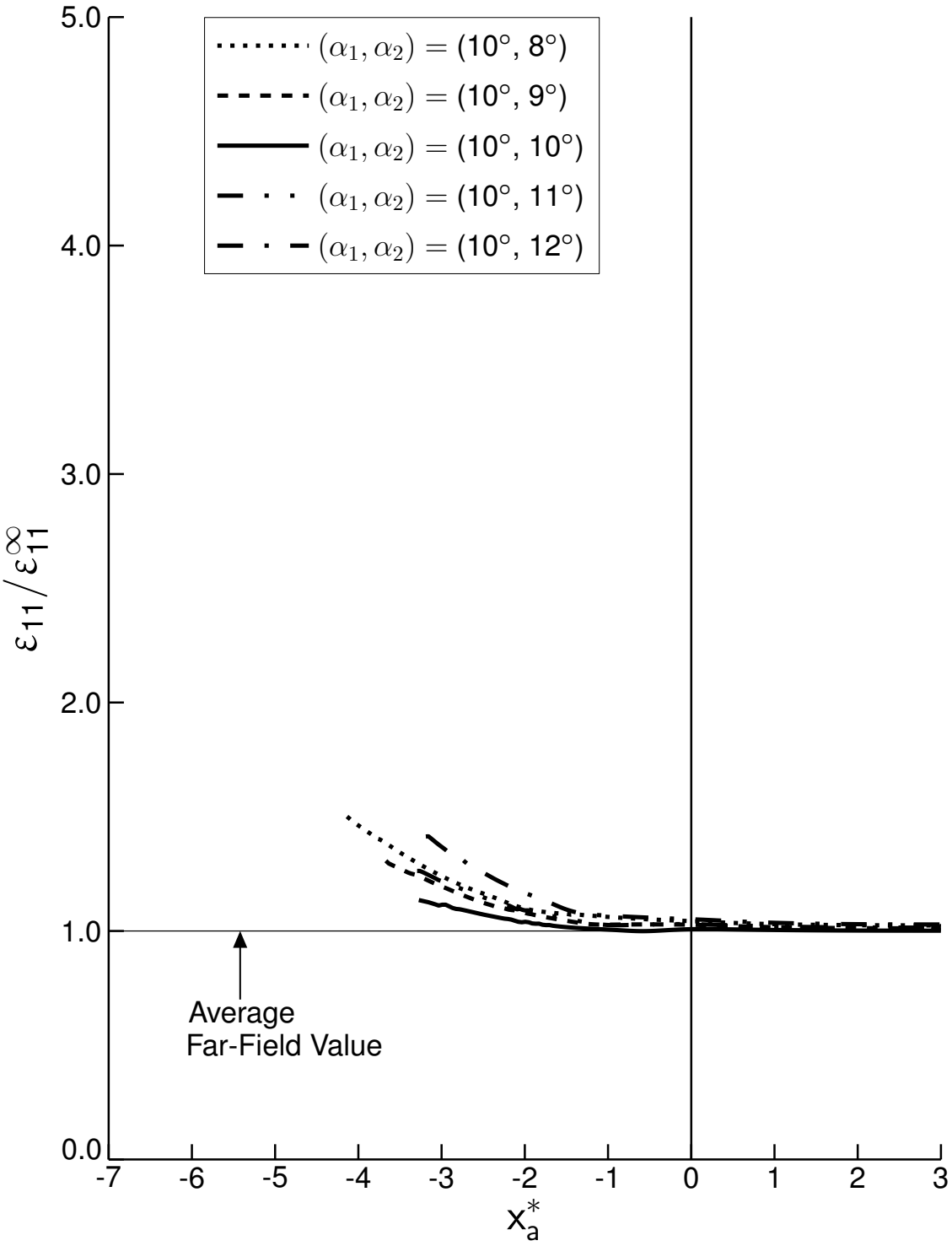

Figure 5.67 Plot of normalized ϵ_{11} versus x_a^* located at z equal to 0.030 in for the cases of unequal scarf angles of (10°, 8°), (10°, 9°), (10°, 10°), (10°, 11°), and (10°, 12°).

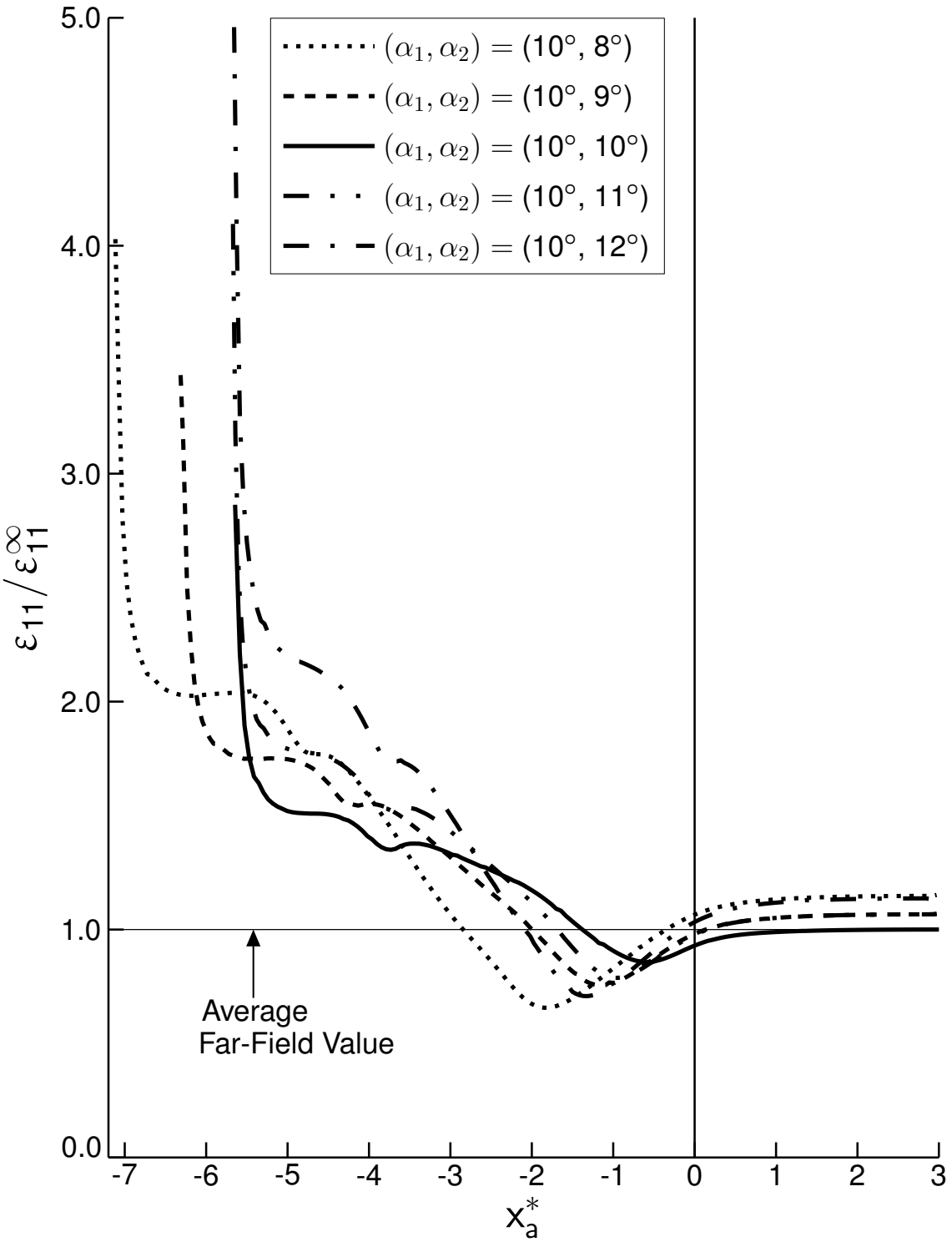

Figure 5.68 Plot of normalized ϵ_{11} versus x_a^* located at z equal to 0.0 in for the cases of unequal scarf angles of (10°, 8°), (10°, 9°), (10°, 10°), (10°, 11°), and (10°, 12°).

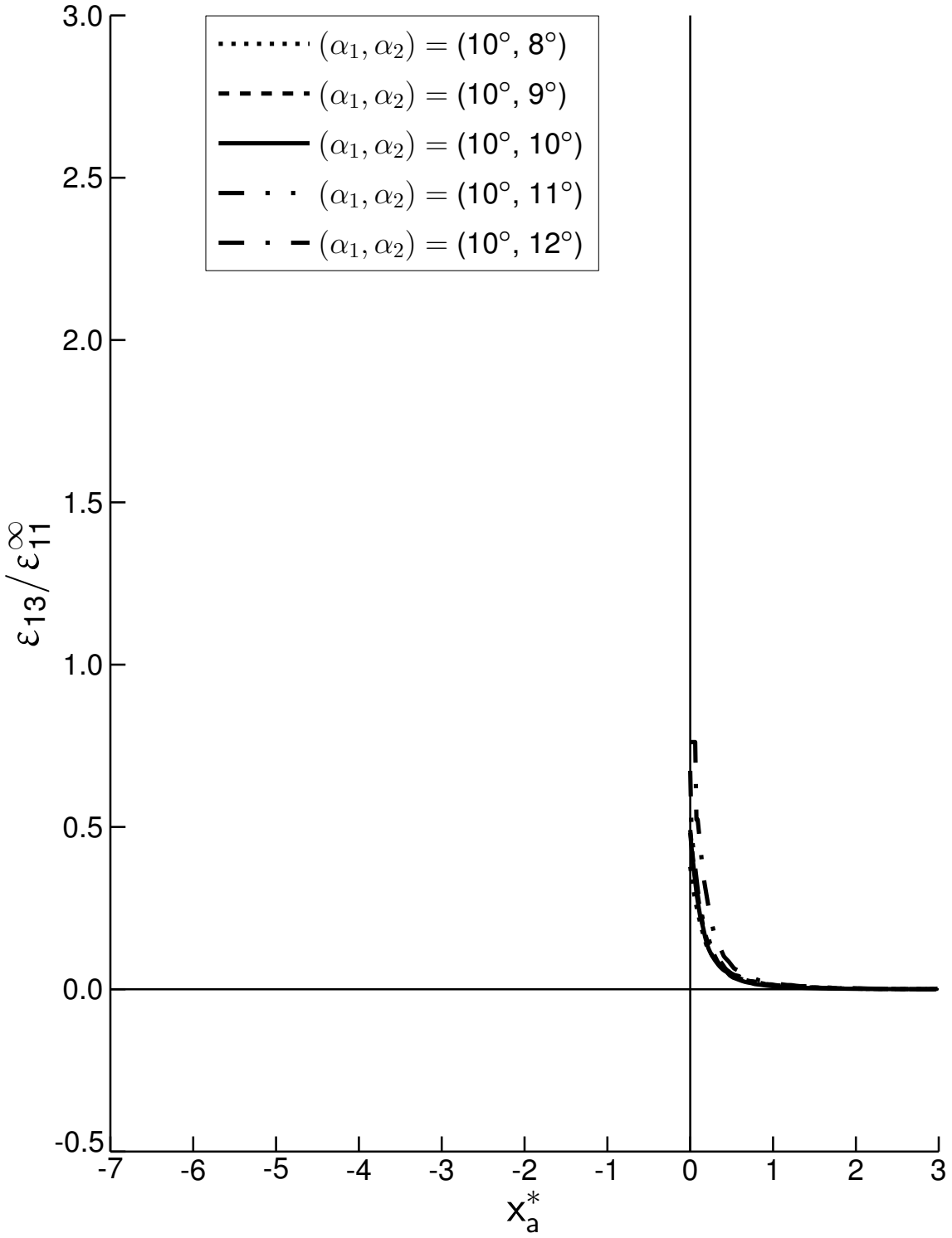

Figure 5.69 Plot of normalized ϵ_{13} versus x_a^* located at z equal to 0.072 in for the cases of unequal scarf angles of (10°, 8°), (10°, 9°), (10°, 10°), (10°, 11°), and (10°, 12°).

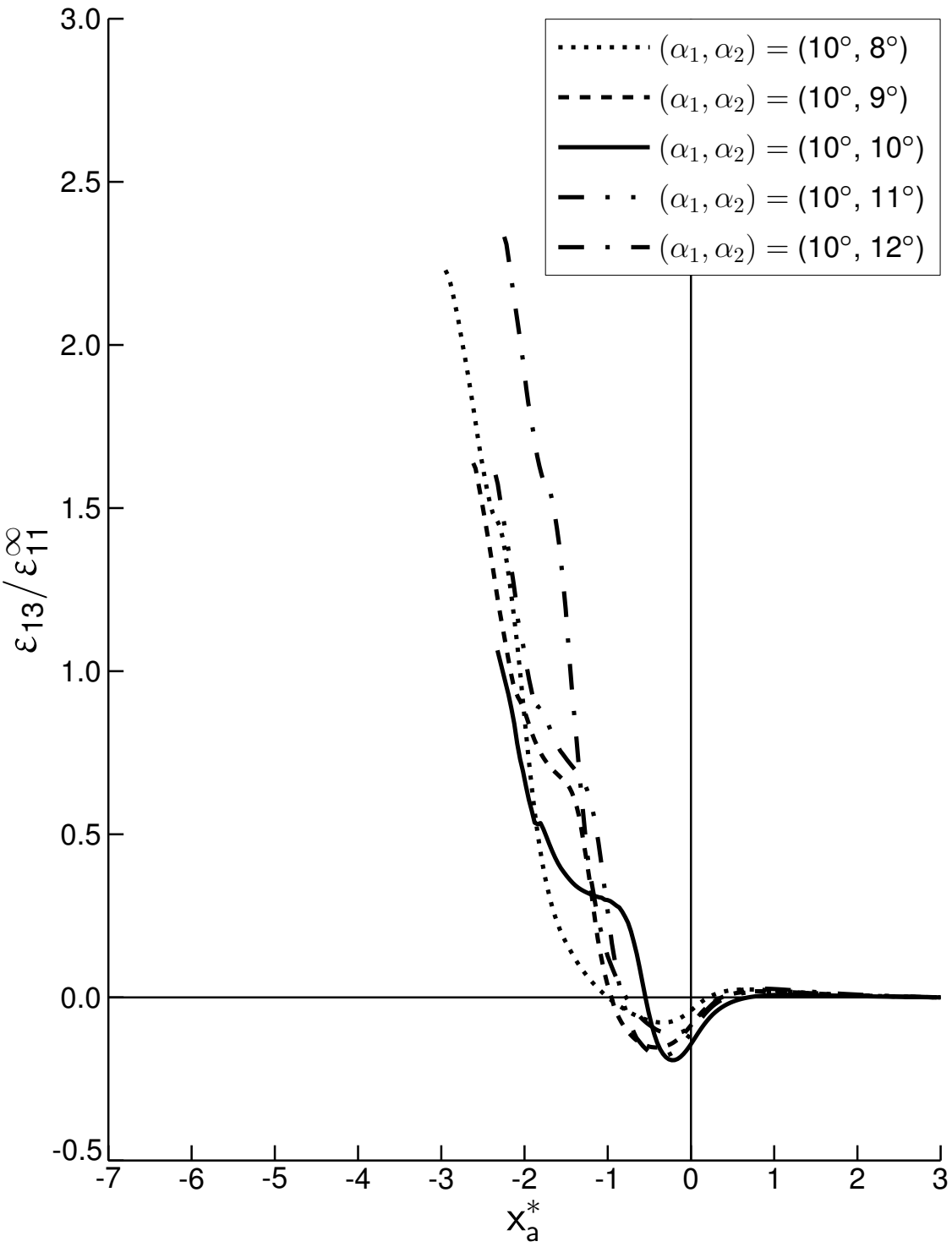

Figure 5.70 Plot of normalized ϵ_{13} versus x_a^* located at z equal to 0.042 in for the cases of unequal scarf angles of (10°, 8°), (10°, 9°), (10°, 10°), (10°, 11°), and (10°, 12°).

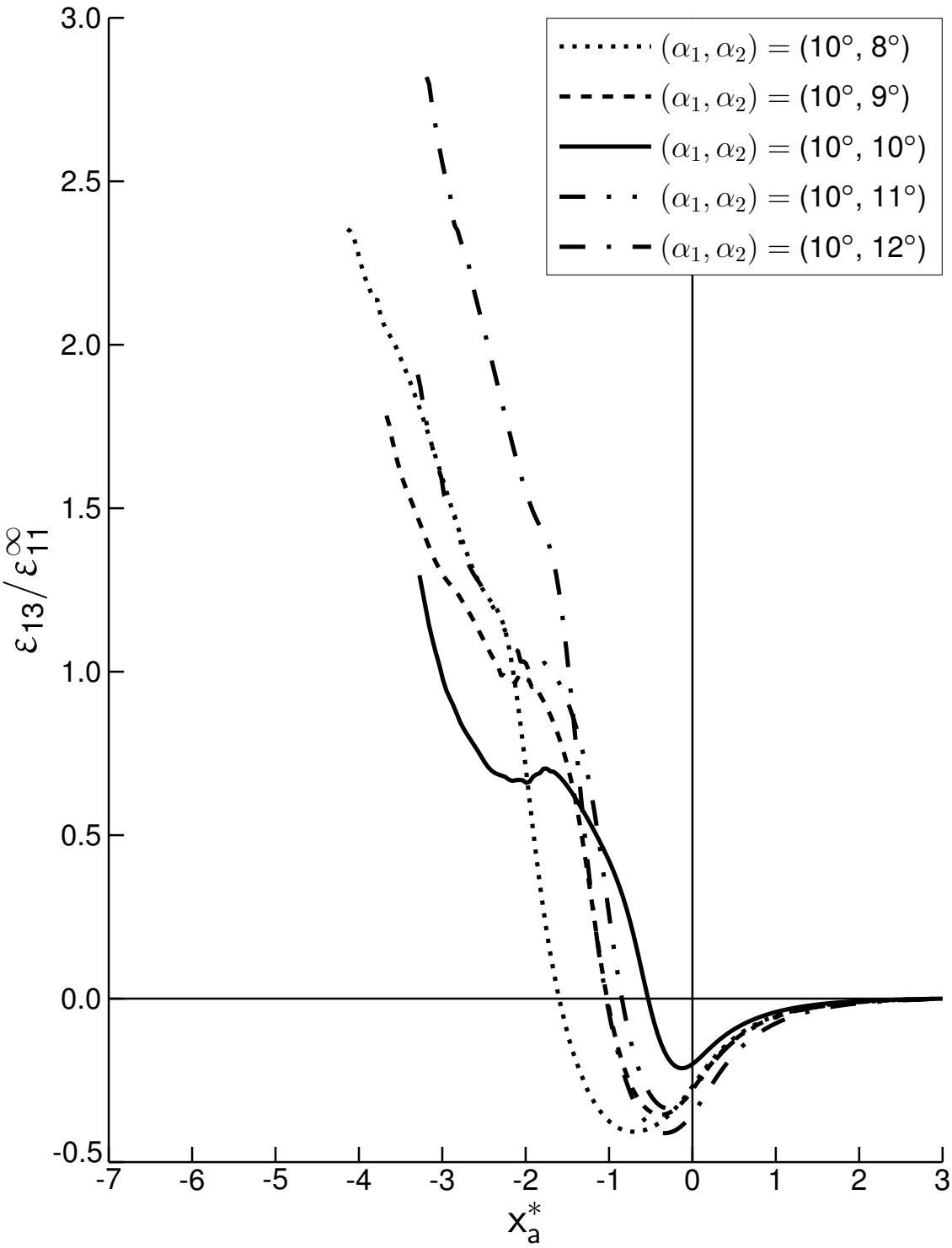

Figure 5.71 Plot of normalized ϵ_{13} versus x_a^* located at z equal to 0.030 in for the cases of unequal scarf angles of (10°, 8°), (10°, 9°), (10°, 10°), (10°, 11°), and (10°, 12°).

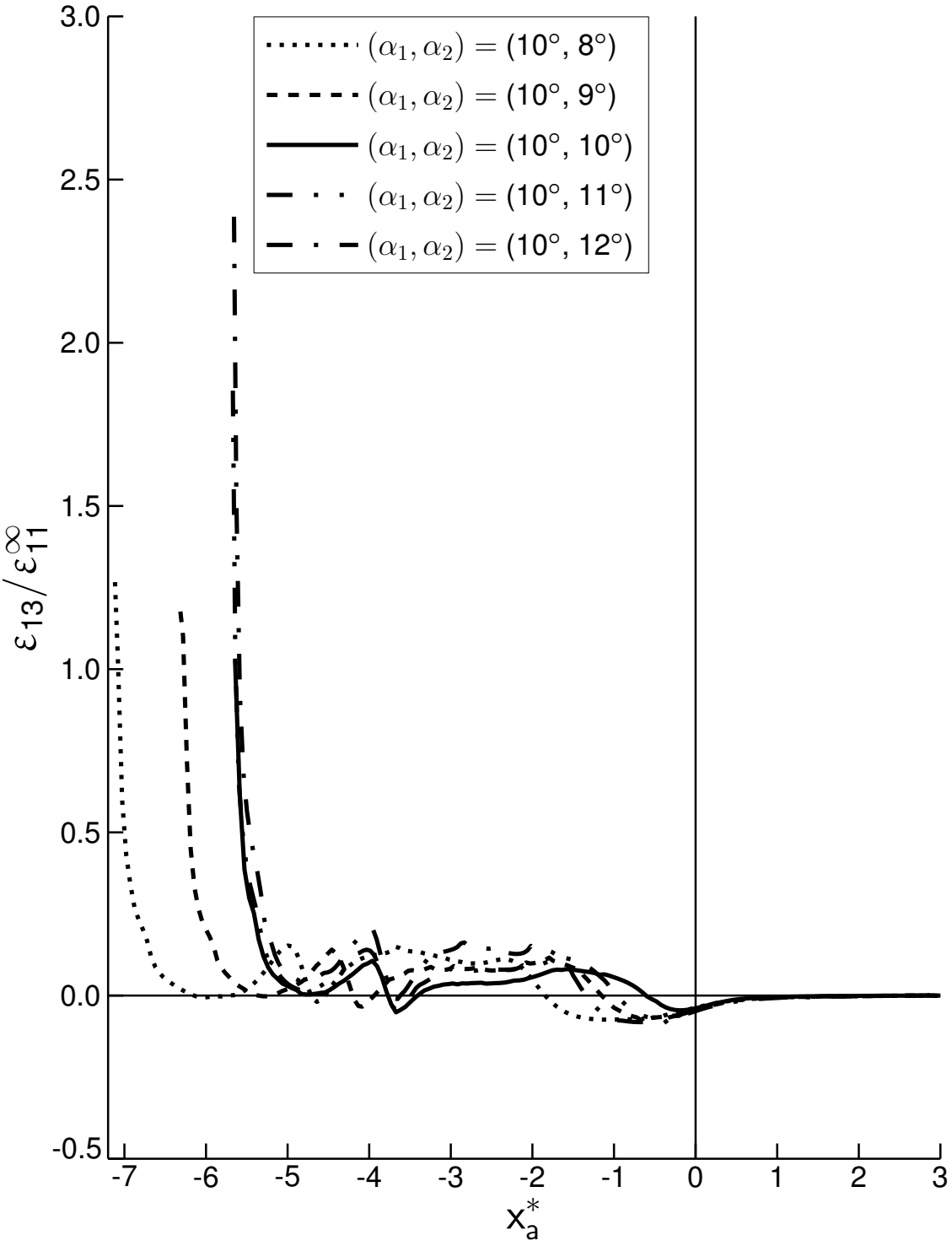

Figure 5.72 Plot of normalized ϵ_{13} versus x_a^* located at z equal to 0.0 in for the cases of unequal scarf angles of (10°, 8°), (10°, 9°), (10°, 10°), (10°, 11°), and (10°, 12°).

Chapter 6

Discussions

The discussions of the results based on the distributions of normalized strains presented in Chapter 5 are the focus of this chapter. The mechanics of the characteristic response and the fundamental mechanisms of load transfer for a two-dimensional composite scarf joint are discussed in Section 6.1. In Section 6.2, the sensitivities in mechanical response related to the joint parameters investigated in this work are discussed.

6.1 Mechanics of the Characteristic Response

The mechanics of the characteristic response of a two-dimensional composite scarf joint are discussed in this section. These are determined from the distributions of the strains presented in Chapter 5, and are thus discussed in relation to the features exhibited in them. In addition, aspects of mechanisms of load transfer specific to the scarf joint configuration are discussed.

The basic mechanics of the characteristic response of a two-dimensional composite scarf joint can be established by first considering the results for the cases with homogenized adherends. For the region of normalized distances between 0.2 and 0.8 along the bondline, both in the adhesive and in the adherend, the distributions of longitudinal and shear strains are relatively uniform. However, sharp gradients in strains occur near the acute and obtuse tips of the adherend. The gradients in longitudinal

strain are positive near the acute tip of the adherend and negative near the obtuse tip. Conversely, the gradients in shear strain are negative near the acute tip of the adherend and positive near the obtuse tip. For both longitudinal and shear strains, however, the gradients near the acute tip of the adherend result in a large increase in the magnitudes of strains, whereas those near the obtuse tip of the adherend result in a large decrease in the magnitudes of strains. These effects are noticeable by considering the distribution of normalized longitudinal strain in the adherend along the bondline for the case of homogenized $[\pm 45_2/0_2]_S$, which has the normalized value of 3.14 at the acute tip of the adherend, and of 0.56 at the obtuse tip, compared to the normalized value of 1.22 in the region where the longitudinal strain remains relatively uniform. Such local effects near the tips of the adherend also occur in the cases with laminated adherends, and are thus characteristic of the configuration of the scarf joint rather than of the specific laminate configurations of the adherend.

The distributions of strains along the x_a^*-axes in the adherend provide additional information for an understanding of the underlying mechanics of the adherend response in transferring load from the prescribed far-field boundary condition to the adhesive at the bondline for a two-dimensional scarf joint. These are also consistent with the previous discussion concerning the basic mechanics. First, the distributions of longitudinal and shear strains generally remain uniform for all cases outside the joint region for x_a^* values greater than 1.0. This indicates the existence of uniform through-thickness distributions of strains in this region, as is expected for balanced and symmetric laminates (including homogenized adherends) subjected to symmetric longitudinal loading, in accordance with Classical Laminated Plate Theory. In the joint region for the homogenized adherends, the magnitudes of strains generally increase in approaching the bondline for the locations associated with the region along the bondline having normalized distances between 0.2 and 0.8. The normalized magnitudes of longitudinal strain for all cases of adherend configurations remain between 1.1 and 1.35, as noted in Section 5.1. Additionally, the magnitudes of gradients in strains near the bondline increase with distance from the centerline of the adherend, such as at the top and bottom of the adherend. These features are in consistency with

those exhibited in the distributions of strains along the bondline in the adherend. Due to the lower stiffness of the adhesive compared to the adherend, there must be larger magnitudes of strains in the adhesive than those in the adherend in order to transfer the same load from one adherend to the other through the adhesive, and thus for mechanical equilibrium to be satisfied. Moreover, the displacement continuity at the bondline causes the magnitudes of strains to increase in the adherend in approaching the bondline. This behavior is different from that for the case of a laminated configuration with an intermediate region similar to the adherend in the joint region, which has gradual ply drop-offs of upper plies from the top of the configuration, and the drop-off region is not adhered to an adhesive or secondary structure. In this case, the values of strains near the ending region of ply drop-offs (the region comparative to the bondline in the adherend for a scarf joint) must gradually decay to zero as they end as this is a boundary condition on stress [32].

In the cases with homogenized adherends, the magnitudes of longitudinal strain in the adhesive are related to the corresponding longitudinal stiffness moduli of the adherends. This can particularly be seen in the region where the distributions of longitudinal strain remain relatively uniform, between the normalized distances of 0.2 and 0.8. The difference in the values of normalized longitudinal strain for the two cases reflects the mismatch in stiffness properties of the adherends for the two cases. For the cases of homogenized $[\pm 45_2/0_2]_S$ and homogenized $[\pm 15_2/0_2]_S$ adherends, the ratio of normalized longitudinal strain for the homogenized $[\pm 45_2/0_2]_S$ case to the homogenized $[\pm 15_2/0_2]_S$ case is approximately 0.61. This compares well with the corresponding ratio of the longitudinal stiffness moduli for the two adherends, which is 0.65. In addition, the distributions of strains in the adhesive along the bondline and the midline show similar characteristics for similar laminate configurations of the adherend, and do not exhibit any variations in trends with changes in scarf angle or adhesive thickness of the configuration.

The strain response along the bondline in the adherend generally depends on the stiffness distribution through the adherend thickness, and hence along the bondline. The stiffness variation in the adherend is introduced by the varied orientation of

plies through the adherend thickness. The dependence of the strain response on the stiffness distribution in the adherend is indicated by comparison of the distributions of strains for the cases with laminated adherends to those for the cases with homogenized adherends. For the cases with laminated adherends, sharp increases and decreases in the magnitudes of strains occur along the bondline in the adherend at locations of ply interfaces, in addition to those occurring near the end regions. These effects are caused by the mismatch in stiffness properties occurring at these interfaces. Thus, sharp increases in the magnitudes of both longitudinal and shear strains occur at the acute tip of the 0° plies, and conversely, sharp decreases occur at the obtuse tip of the 0° plies for all laminated cases. The variations in the magnitudes of strains between the laminated and homogenized cases having 15° plies do exist, but are much smaller compared to those occurring between the corresponding cases having 45° plies. This is a consequence of the reduced mismatch between the stiffness properties of the 15° and 0° plies compared to that between the 45° and 0° plies. This is indicated by considering the ratio of the magnitudes of normalized longitudinal strain at the acute tip of the 0° plies along the bondline for the case of $[\pm 45_2/0_2]_S$ to those for the case of $[\pm 15_2/0_2]_S$, which is 1.88. This compares well with the inverse of the ratio of the corresponding longitudinal moduli, which is 1.66. The differences in the magnitudes of normalized shear strain for the two cases are greater than those in normalized longitudinal strain near regions of ply interfaces, indicating greater mismatch in the in-plane shear stiffness properties as compared to longitudinal stiffness properties between plies oriented at θ and at 0° for each case.

In addition to magnitudes of strains being affected by the variation in stiffness properties between dissimilarly oriented plies, there is evidence of the role of effective ply thickness as a key lengthscale involved in the strain response. In the region between the ends along the bondline in the adherend within normalized distances of 0.2 and 0.8, the intervals of strain gradients occurring between the maxima and minima in the magnitudes of strains vary for the cases of $[\pm\theta_2/0_2]_S$ and $[\pm\theta/0]_{2S}$. As these maxima and minima in the magnitudes of strains occur at the acute and obtuse tips of the 0° plies, respectively, the length intervals along the bondline corresponding to

the span of the 0° plies (i.e. the effective ply thickness) for the two cases indicate the lengthscales over which the steep strain gradients occur. These normalized lengthscales are 0.083 for the case of $[\pm\theta/0]_{2S}$, and 0.333 for the case of $[\pm\theta_2/0_2]_S$, with the effective ply thickness of the 0° plies changing by a factor of 4 (from four single 0° plies distributed through the thickness of the laminate to four 0° plies all stacked at the center of the laminate). However, the magnitudes of the associated peaks in strains remain relatively unaffected among the cases of different effective ply thicknesses in the laminate configurations of the adherend.

The regions over which the steep strain gradients occur near the ends of the bondline, both in the adherend and in the adhesive, are also limited by lengthscales associated with the specifics of each configuration. In the cases with laminated adherends having single effective ply thickness, $[\pm\theta/0]_{2S}$, this lengthscale is associated with the normalized length interval of 0.083 along the bondline spanning the unit ply thickness of 0.006 in for these cases. This lengthscale is not apparent in the distributions of strains for the cases of $[\pm\theta_2/0_2]_S$, having twice the effective ply thickness (0.012 in), and this is specifically exhibited in the results for the case of $[\pm45/0]_{2S}$. For these cases, the normalized length interval over which the steep strain gradients occur near the end regions is the same as the corresponding normalized length interval for the homogenized cases. The absence of this lengthscale associated with the effective ply thickness near the end regions of the bondline is thus established for the cases of $[\pm\theta_2/0_2]_S$, as the distributions for these cases have similar length intervals over which steep strain gradients occur near the end regions as for the homogenized cases, which essentially comprise homogeneously orthotropic plate adherends with no ply-by-ply delimitation through the adherend thickness. Thus, the lengthscale associated with the overall dimensions of the configurations is dominant in these cases.

The mechanics of stiffness variation on a ply-by-ply basis are also exhibited in the distributions of strains along the x_a^*-axes in the adherend for the cases with laminated adherends. Local variations in the magnitudes of strains occur at different locations along x_a^* in the joint region. These local variations are well reflected in the distributions of longitudinal strain through the adherend thickness for the case of $[\pm45_2/0_2]_S$.

The distributions of longitudinal strain for this case show increasing deviation from the distributions of longitudinal strain for the corresponding homogenized case at locations below z equal to 0.054 in within the adherend. These deviations essentially result from the mismatch in stiffness properties between the $\pm 45^\circ$ plies and the 0° plies. The magnitudes of longitudinal strain decrease near the bondline at the location of z equal to 0.042 in, but increase at the location of z equal to 0.018 in. These effects are essentially local manifestations of the sharp decreases and increases in the magnitudes of longitudinal strain occurring at the obtuse and acute tips of the 0° plies, respectively, as exhibited in the distribution of longitudinal strain along the bondline in the adherend for the case of $[\pm 45_2/0_2]_S$.

The macroscopic response of the effective laminate configuration through the thickness at any location in x remains the same. Thus, as per mechanical equilibrium, the net longitudinal stress resultant for any given cross-section in the joint region equals that outside the joint region. In the region outside the joint, the laminate composition through the thickness remains invariable. However, in the joint region, the cross-sectional composition of the 'effective' laminate is different at every location in x due to the presence of the adhesive region. This is illustrated in Figure 6.1. The net longitudinal stress resultant at any given location in x can be approximated to first order as the integral along the z-direction of the product of the longitudinal strain and the local value of the longitudinal modulus. The value of this net resultant for all locations in x should equal the average far-field longitudinal stress in order for mechanical equilibrium to hold. Thus, the difference in the cross-sectional composition at each location in the joint region mainly leads to the variations in the distributions of strains along the z-direction from those for a simple laminate. Considering the cases of homogenized adherends, the effective longitudinal stiffness of the configuration in the joint region, accounting for the presence of the adhesive region, is given by Equation 6.1, where E_{eff} denotes the effective longitudinal stiffness of the configuration in the joint region, E_{xx} denotes the effective longitudinal stiffness of the homogenized adherend, and E denotes the extensional modulus of the

adhesive:

$$E_{eff} = E_{xx} \frac{\left(t_{adherend} - \frac{t_a}{\cos\alpha} \right) + \frac{E}{E_{xx}} \left(\frac{t_a}{\cos\alpha} \right)}{t_{adherend}} \tag{6.1}$$

The cross-sectional extent of the adhesive region through the thickness of the scarf joint configuration is given by the term $[t_a/\cos\alpha]$, as illustrated in Figure 6.2.

An important feature in the distributions of longitudinal and shear strains is the sharp reduction in the magnitudes of longitudinal and shear strains, but particularly evident in the distributions of shear strain, occurring at the normalized distance of 0.89 for the cases with baseline geometry, and at corresponding locations for all other parametric cases. This point along bondline 2 is precisely aligned with the acute tip of adherend 1, both having the same location in x, and consequently in x^*_{jb2}. The region between the normalized distances of 0.89 and 1.0 represents the region wherein the adhesive region begins to reduce at 0.89, until the entire original configuration of the laminate for the adherend is recovered at 1.0. These reductions in the magnitudes of strains are also essentially a macroscopic feature characteristic of the configuration of a scarf joint rather than being specific to any parameter, as per the issue of the macroscopic response through the thickness. However, since the location of the acute tip of the adherend varies with the geometric parameters of the scarf joint, such as scarf angle and adhesive thickness, the locations of associated reductions in the magnitudes of strains do vary accordingly.

The local effects of the varying stiffness distribution in the adherend on the distributions of strains were discussed previously. Additionally, a macroscopic effect of the varying cross-sectional composition of the 'effective' laminate in the joint region is also exhibited in the distributions of strains in the adherend along the x^*_a-axes. This is most noticeable by considering the cases with homogenized adherends, wherein the cross-sectional composition of the 'effective' laminate remains constant between the acute tips of both adherends in the joint region. For these cases, at locations of z in the adherend except at the top and the bottom, the magnitudes of strains along the x^*_a-axes monotonically increase towards the bondline without showing any variation in trend, thus indicating invariance in the 'effective' stiffness of the cross-section in

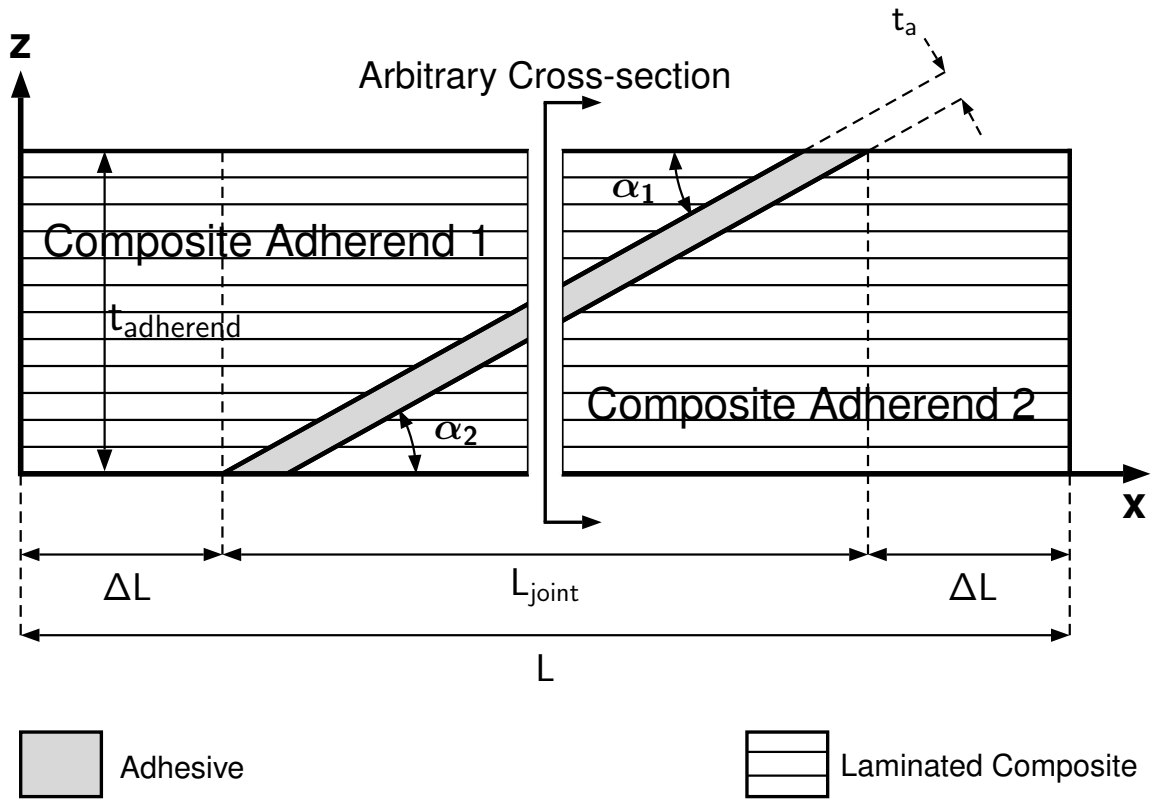

Figure 6.1 Illustration of a cross-section through the z-direction in the joint region at an arbitrary location in x for a two-dimensional composite scarf joint.

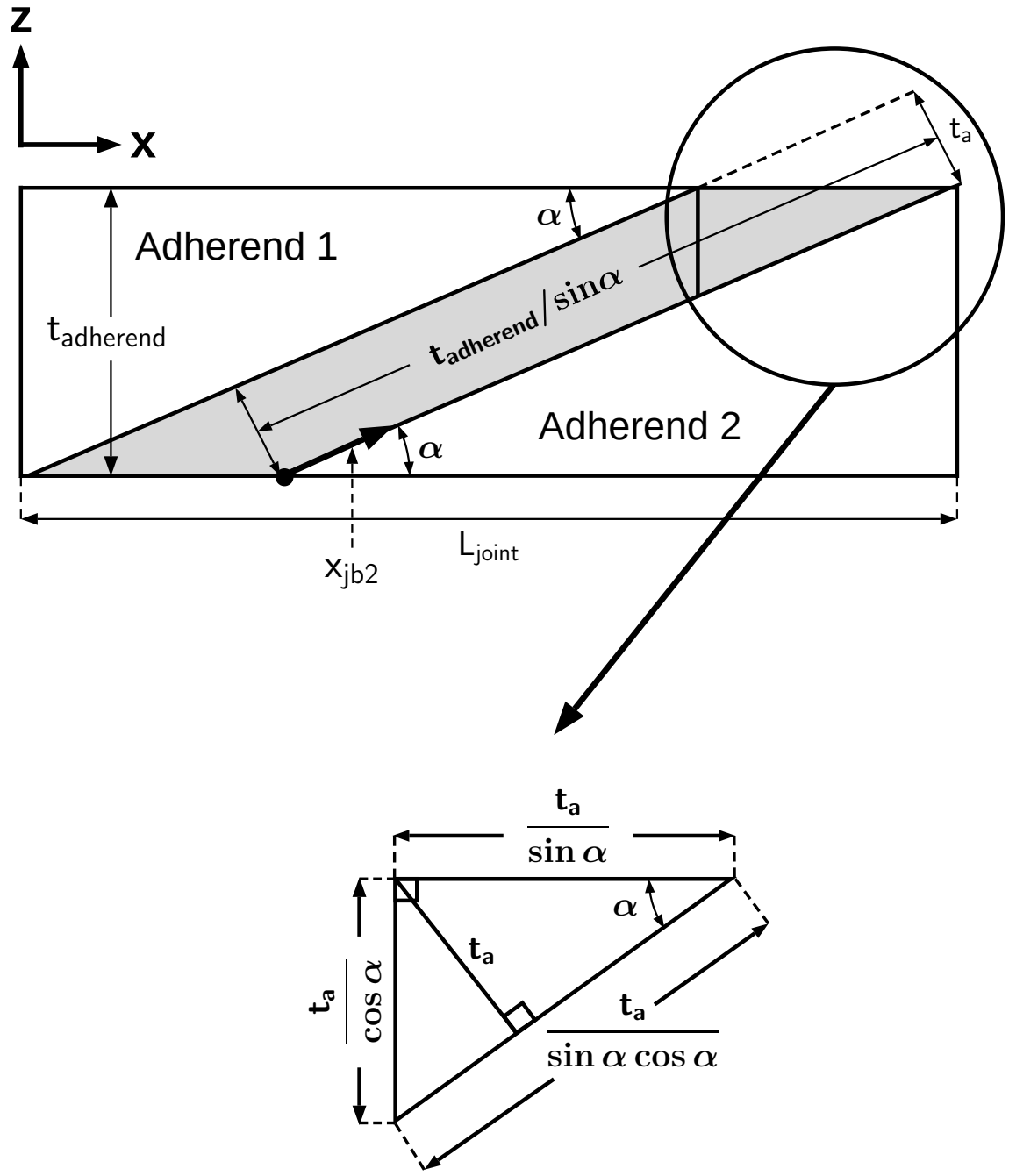

Figure 6.2 Physical dimensions identifying the location of the acute tip of adherend 1 along various axes in a two-dimensional composite scarf joint.

this region.

These macroscopic effects are also exhibited for the cases with adherend configurations of $[\pm\theta_2/0_2]_S$, and are particularly noticeable in the distributions of strains for the case of $[\pm 45_2/0_2]_S$. Near the beginning of the joint region, local reductions in the magnitudes of strains occur near the same location in x, or x_a^*, as that identifying the acute tip of adherend 1 at x_a^* equal to -0.64 for the baseline geometric configuration. These reductions in the magnitudes of strains manifest the effect of varying 'effective' cross-sectional composition of the adherend through the z-direction, as discussed previously. These are more discernible in the distributions of shear strain, and at lower locations in z, farther from the centerline of the adherend at z equal to 0.036 in. These variations are also in consistency with those occurring in the distributions of strains along the associated bondline region, in the adherend and in the adhesive. In addition, this feature is also a characteristic of the configuration of a scarf joint, and occurs for all cases, reflecting the effect of the acute tip of adherend 1.

Considering the equilibrium of a differential triangular element in the adhesive at the bondline allows better characterization of the geometric effects of the configuration, such as scarf angle, on the general state of stress near the bondline. These considerations are formulated in Appendix C, and can be used in conjunction with the results of the distributions of strains to indicate key controlling mechanisms. The equilibrium of a single differential triangular element is considered first in terms of the differential stresses and differential forces acting on it. Next, the overall macroscopic equilibrium formulation along any x_j-y plane in the adhesive is considered by integrating the differential forces of these infinitesimal differential triangular elements along the length of the bondline (or any x_j-axis) and relating these to the resultant longitudinal and through-thickness far-field loading conditions. Thus, at any virtual cut along the x_j-direction through the adhesive, or anywhere in the joint, the net force in the longitudinal direction must equate to that at the far-field application of load, and the net force in the through-thickness direction must equal to zero.

A two-dimensional scarf joint must transfer the entire load from one adherend to the other via the adhesive. The adhesive experiences strains with distributions that

depend on the distributions of strains occurring in the adherend at the interface of the adherend and the adhesive, as the deformation must be continuous at the bondline. This is indicated by the similarities in the distributions of strains in the adherend and the adhesive at the bondline. The increases and decreases in the magnitudes of strains occurring at the bondline in the adherend cause corresponding increases and decreases in the magnitudes of strains in the adjacent adhesive region, at the bondline and at the midline. It is noted that the associated shear strain is positive in the adherend, but negative in the adhesive, as must occur. This is indicated from the schematic of the equilibrium considerations of a differential triangular element in the adhesive in Appendix C, as negative shear stress (and thus negative shear strain) must act on the horizontal edge of a triangular element, along with positive longitudinal stress acting on the vertical edge, in order to equilibrate a positive net longitudinal load.

The adhesive region, which is less stiff compared to the adherends, has much higher magnitudes of strains. This is driven by the significant mismatch in stiffness properties between the adherend and the adhesive. In addition, the magnitudes of the shear strain in the adhesive are significantly larger compared to those of the longitudinal strain. This indicates that the response is shear dominant in the adhesive, and that the bulk of the extensional load is transferred from one adherend to the other via the adhesive undergoing significant shear deformation. This is exhibited by comparing the distributions of normalized longitudinal and shear strain for the case of homogenized $[\pm 45_2/0_2]_S$. At the center of the adhesive midline, the magnitude of shear strain is 3.5 times that of longitudinal strain. This effect is also indicated from equilibrium considerations in terms of the in-plane components of stress along the bondline for a differential triangular element. These indicate higher magnitudes of shear stress and strain in proportion to longitudinal stress and strain, as the value of the scarf angle decreases, in order to maintain equilibrium of the differential triangular element, and thus of any x_j-y plane of unit width in the y-direction when subjected to extensional load.

One of the key aspects of the equilibrium considerations along x_j-axes in the adhe-

sive, as formulated in Appendix C, is the area bounded by the distributions of strains along these x_j-axes. Considering equal load-carrying capability across all cases investigated in this work, the areas bounded by the (normalized) distributions of strains, $\epsilon_{ij}(x_j)$, for two different x_j-axes in the adhesive, x_{jb2} and x_{jm}, must be approximately equal for all configurations having similar effective longitudinal adherend stiffness, and thus similar average far-field longitudinal strain, ϵ_{11}^{∞}, in order for macroscopic equilibrium to be satisfied. In addition, for the distributions of strains in the adhesive along the bondline and along the midline, the ratio of the area bounded by the distributions adjacent to the 0° plies to that bounded by the distributions adjacent to the $\pm\theta$° plies indicates the proportion of load transmitted across the 0° plies versus that transmitted across the $\pm\theta$° plies by the adhesive. This is particularly noticeable for the cases of laminated adherends having ±45° plies. For these cases, the distributions of normalized longitudinal and shear strains indicate that the greatest load-carrying capability in the adherend is always provided by the 0° plies which experience the highest magnitudes of stresses, because the adjacent length interval in the adhesive region along the bondline or the midline has the greatest bounded area for the distributions of both longitudinal and shear strains. This is also indicated by comparing the differences in the normalized values of longitudinal strain adjacent to the middle of the 0° plies at the adhesive midline for the cases of $[\pm 45_2/0_2]_S$ and $[\pm 15_2/0_2]_S$, which are 4.9 and 5.34, respectively, to those adjacent to the middle of the ±45° plies, which are 3.09 and 5.75, respectively. For the cases with homogenized adherends, the area bounded by the distributions of normalized strains along corresponding intervals remains relatively uniform, indicating uniform load-carrying capability through the adherend thickness, except near the top and bottom of the adherend at its tips.

The distributions of strains at the adhesive midline exhibit an averaged effect of the distributions occurring at both bondlines. Thus, at every location along the adhesive midline, the distributions of strains are affected by the adjacent distributions along both bondlines. The distributions remain symmetric about the center of the adhesive midline, in addition to the macroscopic equilibrium for the x_{jm}-y plane of

unit width in the y-direction, as formulated along the bondline in the adhesive in Appendix C. Considering the ends of the midline, the distributions of strains capture the net effect of the sharp increase in the magnitudes of strains at the obtuse tip of the adhesive, as well as the sharp decrease in the magnitudes of strains at the corresponding acute tip of the adhesive. This causes local peaks in strains to occur slightly inwards of the ends of the midline, in comparison to those occurring precisely at the obtuse tip of the adhesive in the distributions of strains in the adhesive along the bondline. However, the magnitudes of strains at the adhesive midline remain similar to those at the bondline, as in the case of homogenized $[\pm 45_2/0_2]_S$, where the magnitudes of normalized longitudinal strain in the adhesive at the middle of the midline and the bondline are 3.41 and 3.43, respectively. The regions of sharp strain gradients do exhibit variation through the distribution over larger length intervals and with reduced associated magnitudes occurring at the midline than at the bondline in the adhesive. In addition, for the laminated cases, the ratios of magnitudes of longitudinal strain adjacent to the $\pm\theta$ plies to those adjacent to the 0° plies at the adhesive midline generally remain similar to those at the bondline in the adhesive, but again show broader spread of distributions and associated reductions in magnitudes.

The overall behavior of a two-dimensional composite scarf joint therefore can be characterized with local features as well as macroscopic features, as shown by the results of the distributions of strains, and as discussed in this section. The local effects can be grouped into those occurring due to ply-by-ply stiffness variation in the adherend and governing lengthscales associated with these ply-by-ply stiffness variations, and with regions of steep strain gradients near the ends of the bondline. The macroscopic effects can be categorized into those related to variations in the cross-sectional composition of the 'effective' laminate in the joint region and issues of mechanical equilibrium and load transfer along x_j-axes, as exhibited by the distributions of strains along these axes.

6.2 Sensitivities of Response to Parameters

The sensitivities of the response, as shown in the distributions of strains, to the parametric variations in the configurations of two-dimensional composite scarf joints are discussed in this section. The results show that the greatest sensitivity in response among all parameters is to the variations in scarf angle.

The sensitivities to variations in the laminate configuration of the adherends are discussed first. The sensitivities in response are generally controlled by two primary factors. The first involves the overall macroscopic stiffness properties of the adherend. The distributions of strains in the adhesive are higher in magnitude compared to those in the adherend, which is essentially due to the mismatch in stiffness properties between the adherend and the adhesive. In addition, the case of homogenized $[\pm 15_2/0_2]_S$ shows higher normalized magnitudes of strains in the adhesive than those occurring for the case of homogenized $[\pm 45_2/0_2]_S$. For increasing effective longitudinal stiffness of the adherend, the resulting magnitude of average far-field longitudinal strain must decrease, and so must the magnitudes of strains in the configuration. This therefore indicates the macroscopic difference in the stiffness properties between the adherends for the two cases. For the cases with laminated adherends, considering macroscopic equilibrium along any x_j-axis and the associated x_j-y plane in the adhesive, as formulated in Appendix C, the local magnitudes of normalized strains along any x_j-axis depend on the stiffness properties of the adjacent plies. In addition to these local variations, as in the distributions of normalized longitudinal strain, the total bounded area of these distributions along any x_j-axis is preserved among the cases of laminated adherends having similar effective longitudinal stiffness, reflecting equal load-carrying capability as indicated by the equilibrium of resultant longitudinal force in Equation C.7. Thus, the distributions of strains show local variations along any x_j-axis in correspondence to the adjacent variation in the distribution of stiffness in the adherend along the axis, which includes local increases and decreases in strains at the acute and obtuse tips of the 0° plies, respectively, while preserving the area bounded by the distributions among the cases with adherends of similar

effective longitudinal stiffness.

The second factor pertains to the variation of stiffness properties through the adherend thickness. The main sensitivities of the distributions of strains along the x_j-axes in the adherend and in the adhesive are manifested through the sharp increases and decreases in strains corresponding to the location of stiffness variations through the adherend thickness. Thus, the configurations with homogenized adherends exhibit relatively uniform distributions of strains along the x_j-axes, except near the end regions, manifesting the absence of stiffness variation through the adherend thickness. In comparison, the laminated adherend cases of $[\pm\theta_2/0_2]_S$ and $[\pm\theta/0]_{2S}$ show localized increases and decreases in the magnitudes of strains at and adjacent to the acute and obtuse tips of the 0° plies in all configurations, respectively, along the x_j-axes in the adherend and in the adhesive. The magnitudes of these local variations (magnitudes of local increases and decreases) show particular sensitivities to the change in the value of the ply angle, θ, in the laminate configurations, but are relatively insensitive to lay-up sequence, such as those occurring for the cases of $[\pm\theta_2/0_2]_S$ and $[\pm\theta/0]_{2S}$ for each of the two values of θ. The increased sensitivities exhibited between the corresponding configurations of different ply angle θ essentially reflect the stiffness mismatch between the 0° plies and θ plies for the respective cases.

Similar sensitivities in the strain response to adherend configurations are observed in the distributions of strains in the adherend along the x_a-axes. The distributions of normalized longitudinal strain are essentially insensitive to the ply angle, θ, between the homogenized cases and the laminated case of $[\pm15_2/0_2]_S$. However, the response of normalized longitudinal strain for the laminated case of $[\pm45_2/0_2]_S$ exhibits greater magnitudes as well as more local variations along the x_a-axes in the adherend compared to the response for the homogenized cases and the laminated case of $[\pm15_2/0_2]_S$. For the distributions of normalized shear strain along the x_a-axes, the response is sensitive to both variations in ply angle, θ, of the configurations, as well as specific laminate configurations of the adherend. In these cases, the response of normalized shear strain shows the highest normalized magnitudes for the case of homogenized $[\pm15_2/0_2]_S$. The normalized magnitudes of shear strain for the cases

having $\pm 45^\circ$ plies are lower than those for the cases having $\pm 15^\circ$ plies, resulting from greater mismatch in the in-plane shear stiffness properties between the $\pm 45^\circ$ plies and the 0° plies compared to that between the $\pm 15^\circ$ plies and the 0° plies. The distributions for the laminated case of $[\pm 45_2/0_2]_S$ show greater sensitivity in terms of local variations in magnitudes from its corresponding homogenized case. Near the tips of the adherend, the normalized magnitudes of both longitudinal and shear strains exhibit similar trends in sensitivities in terms of the increases in the magnitudes of strains. In these regions, these magnitudes increase with respect to the far-field value for the cases of laminated $[\pm 45_2/0_2]_S$, homogenized $[\pm 45_2/0_2]_S$, laminated $[\pm 15_2/0_2]_S$, and homogenized $[\pm 15_2/0_2]_S$, progressively. This is indicated specifically by the normalized magnitudes of shear strain of 1.03, 2.58, 4.25, and 5.46 occurring at the acute tip of the adherend for these cases, as noted in Section 5.1. These variations in magnitudes indicate the sensitivity in the response of shear strain to the differences in in-plane shear stiffness properties of the different cases in two different manners. One aspect of the response sensitivities is manifested through the overall stiffness variation of the adherend, as clearly exhibited in the homogenized cases of homogenized $[\pm\theta_2/0_2]_S$. Another aspect is manifested through local ply-to-ply variation within each adherend, as exhibited in the laminated cases of $[\pm\theta_2/0_2]_S$, where the $+\theta$ ply is at the acute tip of the adherend. Similar trends are also exhibited in the distributions of shear strain for the cases of $[\pm 45/0]_{2S}$ and $[\pm 15/0]_{2S}$, having corresponding normalized values of 1.12 and 4.27, respectively.

The distributions of strains for the cases of equal scarf angles exhibit explicit trends in sensitivity to variation in scarf angle. One of the primary trends is the amplification in the normalized magnitudes of both longitudinal and shear strains along the x_j-axes, particularly in the adhesive, for cases of increasing values of scarf angle. The distributions of normalized strains along the x_j-axes show relatively uniform ratios of magnitudes among the different cases of equal scarf angles, except near the end regions, where similar behavior is also exhibited but the specific values of the ratios do not remain uniform. These effects are illustrated in the distributions of normalized longitudinal strain along the bondline in the adhesive, as noted in Section 5.2, with the

approximate ratios of normalized magnitudes of longitudinal strain taking values of 0.51 for the case of 5° to the case of 10°, and 0.56 for the case of 10° to the case of 15°. Corresponding ratios of 0.47 and 0.58 are noted for the distributions of normalized longitudinal strain along the adhesive midline. Similarly, for the distributions of normalized shear strain along the bondline and the adhesive midline, the approximate ratios of normalized magnitudes of shear strain take values of 0.6 for the case of 5° to the case of 10°, and 0.8 for the case of 10° to the case of 15°, as noted in Section 5.2. The magnitudes of strains thus increase with increasing values of equal scarf angles, as indicated by corresponding normalized values of longitudinal strain of 1.88, 2.86, and 3.27 at the acute tip of the adherend. Such increase in the magnitudes of strains are exhibited for increasing values of scarf angle over the entire joint region.

The increase in magnitudes of strains with increasing values of scarf angle can also be related to equilibrium considerations in the adhesive, as formulated in Appendix C. The equilibrium equations resulting from these considerations indicate that in the process of load transfer from the adherend to the adhesive, the state of stress (and strain) must decompose into all of its in-plane components in contrast to the longitudinal state of stress occurring in the far-field region. This decomposition is directly related to the scarf angle of the configuration, as indicated by Equations C.3 and C.4. Thus, the strains in the adhesive along the bondline resulting from the deformation induced by the adherend in the process of load transfer are particularly sensitive to the scarf angle of the configuration. The dependence of the length of the bondline on the scarf angle of the configuration is given by $[t_{adherend}/\sin\alpha]$, as illustrated in Figure 6.2, and has values of 0.826, 0.415, and 0.278 for the cases of increasing values of scarf angle. Therefore, for increasing values of scarf angle, the local magnitudes of both longitudinal and shear strains must increase along the bondline as the length of the bondline reduces correspondingly, because the stresses maintaining equilibrium act upon increasingly shorter regions for equivalent resultant longitudinal load, as per Equation C.7. The ratios of these numbers from equilibrium considerations also compare well with the corresponding ratios of the magnitudes of strains for the cases of equal scarf angles reported previously. Furthermore, this

effect is expected for scarf angles of less than 90°. In the limiting case of 90°, that corresponding to a butt-joint, the load transfer process is expected to induce a state of stress in the adhesive that is dominantly in extension.

The magnitudes of the strains in the adherend for the cases of equal scarf angles are also related to the 'effective' stiffness properties of each configuration in the joint region. These properties depend upon the local cross-sectional stiffness contribution of the adhesive region through the thickness of the configuration, at any location in x in the joint region, through the term $[E\, t_a/(E_{xx} \cos\alpha)]$ in Equation 6.1, in addition to the cross-sectional stiffness contributions from both adherends. The 'effective' cross-sectional contributions from the adhesive and the adherend regions thus depend on the variable parameter of scarf angle in these cases, which affects the overall macroscopic strain behavior in the adherend. For the distributions of strains along the bondline in the adherend, particularly those of normalized shear strain, the location of local decrease in the magnitude of strain occurring near the upper end of the bondline shifts slightly downwards along the bondline in the upper ±45° plies for the cases with decreasing value of scarf angle. The locations for these decreases in the values of normalized shear strain are noted to be 0.88, 0.89, and 0.90 for the cases of increasing value of scarf angle in Section 5.2. The occurrence of these local variations can be attributed to be effects associated with the change in the 'effective' cross-sectional stiffness properties of the configuration due to the changing stiffness contribution from adherend 1 and the adhesive, in addition to the increasing stiffness contribution from adherend 2 in this region. Along the bondline, the location of the acute tip of adherend 1 from the end of the bondline is given by $[t_a/(\sin\alpha \cos\alpha)]$, as illustrated in Figure 6.2. This denotes the location along the bondline at which the cross-sectional stiffness contribution from adherend 1 begins. Using this expression, the normalized values along the bondline for the location of the acute tip of adherend 1 are 0.888, 0.887, and 0.885 for the cases of increasing values of equal scarf angles. This shows similar trends as those from the strain results noted previously.

The distributions of strains for the various cases of equal scarf angles also indicate a larger spread of distributions across the normalized distances for decreasing values

of scarf angle. This is obviously due to the enlarged joint region for cases with smaller scarf angles. The length of the joint region, L_{joint}, is given by Equation 3.1, and the length of the bondline in the joint region is given by $[t_{adherend}/\sin\alpha]$, as illustrated in Figure 6.2. Thus, this increases in value for decreasing values of equal scarf angles as noted previously, just as L_{joint} does. The effects of increasing bondline length with decreasing values of equal scarf angles, and hence increasing span of the joint region, are indicated by the shifts in the locations of local variations in the magnitudes of strains. This feature is most noticeable in the distributions of normalized shear strain along the bondline in the adherend, and the distributions of normalized longitudinal and shear strains along the x_a^*-axis at the bottom of the adherend. At this location at the bottom of the adherend, the locations of local increases and decreases in strains along x_a^* for the different cases occur over larger distances for decreasing values of scarf angle. The local minima in normalized longitudinal strain near the beginning of the joint region are noted to occur at the normalized distances of -1.3, -0.54, and -0.13 for the cases of increasing values of equal scarf angles. These effects are associated with the change in the 'effective' cross-sectional stiffness properties of the configuration in the joint region due to the varying cross-sectional stiffness contributions from the adherends and the adhesive. The location of the acute tip of adherend 1 along the x_a^*-axes is given by $[-t_a/(\sin\alpha)]$, as illustrated in Figure 6.2. Using this expression, the normalized values for the location of the acute tip of adherend 1 along x_a^* are -1.27, -0.64, and -0.43 for the cases of increasing values of scarf angle. This location along x_a^* identifies the point beyond which the stiffness properties of adherend 1 have cross-sectional contribution, in addition to the cross-sectional stiffness contributions of adherend 2 and the adhesive. These locations correspond to regions near the beginning of the joint region along the x_a^*-axes where local minima in the magnitudes of strains occur, as previously reported.

The strain responses also exhibit explicit trends to variations in values of adhesive thickness. However, for changes in values of 50% in magnitude from the baseline value for this parameter, the distributions of strains along the x_j-axes in the adherend and in the adhesive show significantly reduced sensitivities in the magnitudes of strains

compared to those occurring for the changes in scarf angles. This can be related to equilibrium considerations at the bondline as well (as formulated in Appendix C), as the decomposition of the in-plane state of stress along an x_j-axis only depends on the scarf angle of the configuration, and not on the adhesive thickness. Thus, the sensitivities in the strain response for the cases of changing adhesive thickness result from the macroscopic variation in the 'effective' stiffness properties of the configuration in the joint region based on the changing cross-sectional stiffness contribution of the adhesive through the weighted term of $[E\,t_a/(E_{xx}\,t_{adherend}\cos\alpha)]$ in Equation 6.1. It is noted that the effective change in the cross-sectional stiffness of the configuration, E_{eff}, is approximately 3% from that of the baseline case for changes in adhesive thickness values of 25% from the baseline value. This compares well with the magnitudes of variations in normalized strains for the different cases of adhesive thickness, and is particularly manifested in the variations in the magnitudes of normalized shear strain at the center of the adhesive midline. At this location, the magnitudes of normalized shear strain for the cases of 0.006 in and 0.010 in (25% variation from the baseline value) also vary by approximately 3% from that of the baseline case of 0.008 in, and those for the cases of 0.004 in and 0.012 in by approximately 6%, accordingly.

The magnitudes of normalized longitudinal strain along the x_j-axes in the adherend and the adhesive generally increase with increasing values of adhesive thickness, particularly in and adjacent to the $\pm 45^\circ$ plies. This is indicated, as noted in Section 5.3, by the normalized values of longitudinal strain of 2.68, 2.88, 3.09, 3.29, and 3.51 for the cases of increasing values of adhesive thickness, occurring at the normalized distances of 0.17 and 0.83 (adjacent to the -45° and $+45^\circ$ ply interfaces) at the adhesive midline. The corresponding values of normalized longitudinal strain at the normalized distance of 0.83 (at the upper -45° and $+45^\circ$ ply interface) in the adherend at the bondline are 1.15, 1.23, 1.35, 1.47, and 1.53. Similarly, this trend is also exhibited at the acute tip of the adherend, where the values of normalized longitudinal strain for increasing values of adhesive thickness are 2.37, 2.59, 2.86, 3.40, and 3.61. For the distributions of normalized shear strain along the x_j-axes, greater sensitivities in the magnitudes of normalized shear strain occur in and adjacent to

the 0° plies compared to the ±45° plies. It is noted that along the x_j-axes in the adhesive, the distributions of normalized shear strain show increasing magnitudes with increasing adhesive thickness adjacent to the ±45 plies, but decreasing magnitudes with increasing adhesive thickness adjacent to the 0° plies. In addition, the location of the global peaks in shear strain occurring in the adhesive along the bondline shift lower along the bondline with increasing adhesive thickness, taking normalized values of -21.3, -20.5, -19.9, -19.5, and -17.5 at the corresponding normalized distances of 0.48, 0.46, 0.45, 0.44, and 0.41, as noted in Section 5.3.

The locations of local increases and decreases in the magnitudes of strains are also sensitive to the changes in the adhesive thickness of the configuration. This is noted particularly for distributions of normalized shear strain along the bondline in the adherend and for distributions of longitudinal strain along the x_a-axis at the bottom of the adherend. For the distributions of normalized shear strain along the bondline in the adherend, local decrease in the magnitudes of shear strain occurs near the upper end of the bondline at the normalized distances of 0.84, 0.87, 0.89, 0.92, and 0.95 for the cases of decreasing adhesive thickness, as noted in Section 5.3. These effects, as in the cases of variations in equal scarf angles, can be attributed to the variation in 'effective' cross-sectional stiffness contributions of the adhesive and the adherend regions near the end of the bondline, influenced by the changing locations of the acute tip of adherend 1 for each configuration. The location along the bondline of the acute tip of adherend 1 from the end of the bondline for each configuration is again given by $[t_a/(\sin\alpha\cos\alpha)]$, as previously noted for equal scarf angles, and varies with the parameter of adhesive thickness in these cases. Thus, for decreasing values of adhesive thickness, this results in normalized values for the location of the acute tip of adherend 1 of 0.83, 0.86, 0.89, 0.91, and 0.94 along the bondline. These locations also compare well with the region of local decrease in the magnitudes of shear strain, as reported previously.

The distributions of normalized longitudinal strain along the x_a-axis at the bottom of the adherend also indicate the slightly increased spread of the distributions of strains with increasing adhesive thickness. Although the length of the joint region

spanning the adherend for configurations with changing adhesive thickness remains the same, the local minima in longitudinal strain near the beginning of the joint region occur at the normalized distances of -0.35, -0.44, -0.54, -0.70, and -0.87 for the cases of increasing value of adhesive thickness, as also noted in Section 5.3. These shifts are associated with the corresponding shifts in the location of the acute tip of adherend 1 along x_a. As noted previously for the cases of equal scarf angles, this location is given by $[-t_a/(\sin\alpha)]$, and varies with the parameter of adhesive thickness in these cases. Using this expression, for the cases of increasing value of adhesive thickness, the normalized values of the location of the acute tip of adherend 1 along x_a are -0.32, -0.48, -0.64, -0.80, and -0.96. These effects are manifested in the distributions of normalized shear strains as well, as previously noted. The occurrence of local minima in both longitudinal and shear strains near the beginning of the joint region can also be attributed, as in the cases of equal scarf angles, to the variations in 'effective' cross-sectional stiffness contributions of the adhesive and adherend regions, which are affected by the geometric location of the acute tip of adherend 1.

The sensitivities exhibited in the distributions of strains for the cases of unequal scarf angles reflect the combined effects of sensitivities in the strain responses to variations in scarf angle for adherend 2 as well as the accompanying variation in adhesive thickness along the bondline. It is recalled here from Section 5.4 that the adhesive thickness decreases linearly along bondline 1 for the cases of (10°, 8°) and (10°, 9°), but increases linearly for the cases of (10°, 11°) and (10°, 12°). Conversely, the adhesive thickness increases linearly along bondline 2 for the cases of (10°, 8°) and (10°, 9°), but decreases linearly for the cases of (10°, 11°) and (10°, 12°). The increase in the maximum values of adhesive thickness from the minimum baseline value of 0.008 in along each bondline is 75% (to 0.014 in) for cases with a 1° mismatch in scarf angles, and 150% (to 0.020 in) for cases with a 2° mismatch in scarf angles. The magnitudes of normalized longitudinal strain overlap in the 0° plies for the cases of (10°, 8°), (10°, 9°), and (10°, 10°) along bondline 1, and for (10°, 10°), (10°, 11°), and (10°, 12°) along bondline 2. In addition, the magnitudes of normalized longitudinal strain increase along bondline 1 for the cases of (10°, 11°) and (10°, 12°), and along

bondline 2 for the cases of (10°, 8°), and (10°, 9°) relative to those for the baseline case. The general characteristics of the distributions of longitudinal and shear strains remain the same for these cases as those for cases of similar scarf angle and adhesive thickness values.

The magnitude of the gradient in longitudinal strain decreases near the obtuse tip of adherend 1 along bondline 1 for cases of increasing scarf angle for adherend 2. The normalized local peaks in longitudinal strain occur at the same normalized distance of 0.90 for the cases of (10°, 8°), (10°, 9°), and (10°, 10°), with values of 1.60, 1.52, and 1.40, and at 0.84 and 0.77 for the cases of (10°, 11°) and (10°, 12°), respectively, with values of 1.54 and 1.60, respectively, as noted in Section 5.4. Along bondline 2 in the adherend, the magnitude of the gradient in longitudinal strain decreases for cases with decreasing scarf angle for adherend 2. The normalized location of local peaks in the longitudinal strain has the same value of 0.90 for the cases of (10°, 10°), (10°, 11°), and (10°, 12°), with peak normalized values of 1.42, 1.54, and 1.65, respectively, and normalized locations of 0.76 and 0.81 for the cases of (10°, 8°) and (10°, 9°), respectively, with normalized peak values of 1.59 and 1.54, respectively, also noted in Section 5.4. The shifts in locations of these local effects can be attributed to the geometric shifts in locations of the acute tips of both adherends, which depend on the associated scarf angles as well as the local value of adhesive thickness, as illustrated in Figure 6.2 for the location of the acute tip of adherend 1 for configurations with equal scarf angles. Similar trends in sensitivities are also exhibited in the distributions of longitudinal strain along the x_j-axes in the adhesive, and those of normalized shear strain, with values of local peaks and relevant normalized locations recorded in Section 5.4. The magnitudes of strains for the different cases generally increase with increasing magnitude of scarf angle for adherend 2, increasing dissimilarity in scarf angles for each adherend, and the associated increase in adhesive thickness along the bondline. The distributions of strains also indicate greater spread along the x_a-axes, with variations in the scarf angle for adherend 2. This is indicated by the shifts in the locations of local minima in longitudinal strain occurring near the beginning of the adherend region at the bottom of the adherend, with values of x_a of -1.85, -1.14,

-0.54, -0.94, and -1.33 for the cases of increasing scarf angle for adherend 2. The shifts in these locations, as noted previously for other parameters, can also be attributed to the shifts in geometric locations of the acute tip of adherend 1 along x_a, which depend on the associated scarf angles as well as the local value of adhesive thickness.

An important feature of the strain response for the cases of unequal scarf angles is the asymmetric distribution of longitudinal strains occurring through the thickness of the adherend at the far-field location. This asymmetry results from the overall asymmetric configuration of the scarf joint caused by the asymmetric adhesive distribution along the scarf length. The prescribed displacements at the far-field location through the thickness of the adherend are uniform. However, as the effective adhesive thickness at any location in z is not the same, the resulting far-field longitudinal strain for that location in z also varies, in order to preserve the condition of uniform distribution of displacement through the thickness of the adherend. It is also noted that the magnitudes of longitudinal strain at the far-field location vary linearly with mismatch in scarf angles, and with distance from the centerline of the adherend at z equal to 0.036 in. Thus, at the top and bottom of the adherend, the values of normalized longitudinal strain vary by $\pm 7\%$ for the cases of (10°, 9°) and (10°, 11°), each with a 1° mismatch, and $\pm 15\%$ for the cases of (10°, 8°) and (10°, 12°), each with a 2° mismatch, as noted in Section 5.4.

Chapter 7

Conclusions and Recommendations

An investigation was performed in this work in order to explore the general characteristics of the mechanical response and mechanisms of load transfer in two-dimensional composite scarf joints. This includes consideration of the sensitivities of the mechanical response to variations in the geometric parameters of equal scarf angles, adhesive thickness, and unequal scarf angles, and variations in laminate configurations for both adherends of the types of $[\pm\theta_2/0_2]_S$, $[\pm\theta/0]_{2S}$, and homogenized $[\pm\theta_2/0_2]_S$ (equivalently homogeneously orthotropic) for values of θ of 45° and 15°. Linear elastic plane strain analyses were performed for all cases via finite element modeling. The configurations were subjected to uniform extensional loading corresponding to equal load-carrying capability across all cases, and the resulting strain fields were used to characterize the response.

The following conclusions are drawn from this work:

1. The strain fields are asymmetric about the center of the adhesive midline for all cases, except for those cases with unequal scarf angles, due to associated asymmetry in material constitution, geometric configuration, and loading conditions.

2. The overall response is influenced by global/macroscopic features and local features of the two-dimensional composite scarf joint configuration. The global/ma-

croscopic effects are manifested via the effective cross-sectional stiffness of the configuration in the joint region, E_{eff}, and equilibrium considerations along the bondline. The local effects are manifested at the ends of the joint region at the tips of the adherend, and through ply-by-ply level mismatch in stiffness properties within the adherend.

3. The macroscopic equilibrium holds at any arbitrary x_j-axis parallel to the bondline in the configuration, considering the fundamental principles of mechanics. Along such an axis, such as along the bondline in the adhesive, all three in-plane components of stress (and strain) are involved in equilibrating the resultant load. The magnitudes of strains in the adhesive are significantly greater than those in the adherend, and are driven by the extent of mismatch in stiffness properties between the adhesive and the adherend.

4. The magnitudes of strains within the joint region are generally controlled by the effective macroscopic through-thickness stiffness properties of the configuration, such as the effective longitudinal stiffness of the configuration, E_{eff}, which is controlled by the stiffness and thickness ratios of the adhesive to the adherends.

5. For all cases, slight kinks in the magnitudes of strains occur at locations corresponding to places where the cross-sectional stiffness contribution of adherend 1 through the z-direction ends along the bondline, thus illustrating the effect of overall cross-sectional stiffness properties of the configuration.

6. The distributions of strains in the adherend along the bondline reflect the distribution of stiffness properties of the adherend through the thickness, and the distributions of strains along the bondline and the adhesive midline essentially reflect the distributions of strains at the bondline in the adherend, which are governed by local effects of mismatch in stiffness properties between the θ and 0° plies.

7. For all cases, sharp increases in the magnitudes of longitudinal and shear strains occur near the acute tip of the adherend, whereas sharp decreases occur near

the obtuse tip. These effects are comparative in some aspects to those occurring in regions of ply drop-offs in associated laminated structures. The overall lengthscales of the gradient regions associated with these sharp changes in the magnitudes of strains are governed by the overall geometry of the configuration.

8. The effective ply thickness is a key lengthscale governing the local variations in strains along the x_j-axes, and this is shown particularly via the effective ply thickness of the 0° plies in determining the spans of the regions of sharp gradients in strains along these axes.

9. The global lengthscales controlling the regions of high gradients in strains near the tips of the adherend along the bondline can interact with lengthscales associated with the effective ply thicknesses, as the basic distributions of strains remain the same for the cases of $[\pm\theta_2/0_2]_S$ and homogenized $[\pm\theta_2/0_2]_S$, but change for the case of $[\pm\theta/0]_{2S}$.

10. Sensitivity to laminate configuration mainly occurs through variations in the overall stiffness properties of the configuration within the joint region through variations in the cross-sectional stiffness contributions of each laminate.

11. The magnitudes of strains show the greatest sensitivity to variations in the value of scarf angle of the scarf joint configuration. This is related to the specific decomposition of the state of stress into all three planar components near the bondline through the scarf angle of the configuration via equilibrium considerations along the bondline. This results in greater contribution of shear stress versus longitudinal stress in load transfer as the value of scarf angle decreases.

12. The length of the bondline increases significantly with decreasing value of scarf angle, thus allowing greater region for associated stresses to act and equilibrate the resultant load. This results in reduced magnitudes of stresses, and thus strains, for equal load-bearing capability across the cases, with decreasing value of scarf angle.

13. The magnitudes of strains show relatively little sensitivity to variation in the value of adhesive thickness of the scarf joint configuration, as the changes in the magnitudes of strains are comparable to the variation in the 'effective' cross-sectional stiffness of the configuration in the joint region, E_{eff}, occurring due to cross-sectional variations in the stiffness and thickness ratios of the adhesive to the adherends.

14. Magnitudes of strains are reduced at the adhesive midline compared to those at the bondline, and this effect increases with increasing adhesive thickness.

15. For the cases of unequal scarf angles, the distributions of strains show explicit asymmetry due to the asymmetric nature of the configurations, but the shapes and trends of the distributions exhibit a combination of common characteristics to those exhibited for the cases of equal scarf angles and adhesive thicknesses, independently, with scarf angle being the primary factor.

16. For the cases of unequal scarf angles, the distributions of longitudinal strain in the adherend exhibit increasing asymmetry through the adherend thickness in the far-field region with increasing mismatch between the values of scarf angles. This is attributed to increasing resulting asymmetry for these configurations.

Based on the results of this investigation, recommendations for further work include:

1. Finite element analyses should be performed for two-dimensional composite scarf joints with variations in global parameters, such as the ratio of the stiffness properties of the adherend to those of the adhesive, adherend thickness, and scarf angle, in order to characterize the effects on the lengthscales associated with these key parameters.

2. Finite element analyses should be performed to better characterize the local lengthscales associated with effective ply thickness by varying the effective stiffness mismatch between plies and the effective thickness of these plies.

3. Finite element analyses should be performed to more fully investigate the variations in the overall characteristics of the distributions of strains at the adhesive midline with changes in the adhesive thickness of the configuration.

4. Finite element analyses should be performed to investigate the mechanical response and associated sensitivities of full three-dimensional composite scarf joint configurations allowing by-pass load transmission pathways in the structure, and considering variations in joint parameters associated with the third dimension.

5. The mechanical response of composite scarf joints with nonlinear load-bearing capability of the adhesive should be investigated via finite element analyses, as design practices require considerations of much higher load-bearing capability for the adhesive in order to consider final failure of such configurations.

6. Mechanical response with modeled 'defects' in the scarf joint configuration should be investigated via finite element analyses, with appropriate failure criteria defined in the models to predict ultimate joint strength for both two- and three-dimensional composite scarf joint configurations.

7. Experiments should be conducted in order to test the ultimate strength of composite scarf joint specimens similar to the configurations modeled in this work, including observations of the failure modes of the specimens and their locations. Comparisons of such to the locations of global peaks in the magnitudes of strains and their locations, as identified in this work, should be made.

Appendix A

Transformation of Ply Stiffness Properties

The transformation relations used in transforming the ply stiffness components relative to the Ply Coordinate System for each ply orientation to their corresponding stiffness components relative to the Abaqus/FEM Coordinate System are detailed in this appendix. The coordinate systems used are defined in Section 4.2 and illustrated in Figure 4.1. The compliance matrix for the ply within the Ply Coordinate System is:

$$\mathrm{C} = \begin{pmatrix} \frac{1}{\mathrm{E}_1} & \frac{-\nu_{12}}{\mathrm{E}_1} & \frac{-\nu_{13}}{\mathrm{E}_1} & 0 & 0 & 0 \\ \frac{-\nu_{12}}{\mathrm{E}_1} & \frac{1}{\mathrm{E}_2} & \frac{-\nu_{23}}{\mathrm{E}_2} & 0 & 0 & 0 \\ \frac{-\nu_{13}}{\mathrm{E}_1} & \frac{-\nu_{23}}{\mathrm{E}_2} & \frac{1}{\mathrm{E}_3} & 0 & 0 & 0 \\ 0 & 0 & 0 & \frac{1}{\mathrm{G}_{23}} & 0 & 0 \\ 0 & 0 & 0 & 0 & \frac{1}{\mathrm{G}_{13}} & 0 \\ 0 & 0 & 0 & 0 & 0 & \frac{1}{\mathrm{G}_{12}} \end{pmatrix}. \tag{A.1}$$

The unidirectional ply material properties in Table 4.2 are used for the T700/2510 material. The compliance matrix is first transformed from the Ply Coordinate System to the Laminate/Joint Coordinate System via:

$$\hat{\mathrm{C}}(\theta) = \mathrm{T}_{1\sigma}^{-1}(\theta)\, \mathrm{C}\, \mathrm{T}_{1\varepsilon}(\theta), \tag{A.2}$$

where:

$$\mathrm{T}_{1\sigma}(\theta) = \begin{pmatrix} \cos^2\theta & \sin^2\theta & 0 & 0 & 0 & 2\cos\theta\sin\theta \\ \sin^2\theta & \cos^2\theta & 0 & 0 & 0 & -2\cos\theta\sin\theta \\ 0 & 0 & 1 & 0 & 0 & 0 \\ 0 & 0 & 0 & \cos\theta & -\sin\theta & 0 \\ 0 & 0 & 0 & \sin\theta & \cos\theta & 0 \\ -\cos\theta\sin\theta & \cos\theta\sin\theta & 0 & 0 & 0 & \cos^2\theta - \sin^2\theta \end{pmatrix}, \qquad \text{(A.3)}$$

and:

$$\mathrm{T}_{1\varepsilon}(\theta) = \begin{pmatrix} \cos^2\theta & \sin^2\theta & 0 & 0 & 0 & \cos\theta\sin\theta \\ \sin^2\theta & \cos^2\theta & 0 & 0 & 0 & -\cos\theta\sin\theta \\ 0 & 0 & 1 & 0 & 0 & 0 \\ 0 & 0 & 0 & \cos\theta & -\sin\theta & 0 \\ 0 & 0 & 0 & \sin\theta & \cos\theta & 0 \\ -2\cos\theta\sin\theta & 2\cos\theta\sin\theta & 0 & 0 & 0 & \cos^2\theta - \sin^2\theta \end{pmatrix}. \qquad \text{(A.4)}$$

In these equations, the angle, θ, is the ply orientation angle for each ply. The transformed compliance matrix for T700/2510 as a function of the ply orientation angle is given as $\hat{\mathrm{C}}(\theta)$.

Next, the T700/2510 compliance matrix, $\hat{\mathrm{C}}(\theta)$, is transformed relative to the Abaqus/FEM Coordinate System via:

$$\hat{\hat{\mathrm{C}}}(\theta) = \mathrm{T}_{2\sigma}(\phi)\,\hat{\mathrm{C}}(\theta)\,\mathrm{T}_{2\varepsilon}^{-1}(\phi), \qquad \text{(A.5)}$$

where:

$$T_{2\sigma}(\phi) = \begin{pmatrix} 1 & 0 & 0 & 0 & 0 & 0 \\ 0 & \cos^2\phi & \sin^2\phi & 2\cos\phi\sin\phi & 0 & 0 \\ 0 & \sin^2\phi & \cos^2\phi & -2\cos\phi\sin\phi & 0 & 0 \\ 0 & -\cos\phi\sin\phi & \cos\phi\sin\phi & \cos^2\phi - \sin^2\phi & 0 & 0 \\ 0 & 0 & 0 & 0 & \cos\phi & -\sin\phi \\ 0 & 0 & 0 & 0 & \sin\phi & \cos\phi \end{pmatrix}, \quad \text{(A.6)}$$

and:

$$T_{2\epsilon}(\phi) = \begin{pmatrix} 1 & 0 & 0 & 0 & 0 & 0 \\ 0 & \cos^2\phi & \sin^2\phi & \cos\phi\sin\phi & 0 & 0 \\ 0 & \sin^2\phi & \cos^2\phi & -\cos\phi\sin\phi & 0 & 0 \\ 0 & -2\cos\phi\sin\phi & 2\cos\phi\sin\phi & \cos^2\phi - \sin^2\phi & 0 & 0 \\ 0 & 0 & 0 & 0 & \cos\phi & -\sin\phi \\ 0 & 0 & 0 & 0 & \sin\phi & \cos\phi \end{pmatrix}. \quad \text{(A.7)}$$

The transformation angle, ϕ, is set to 90° in this case since the Abaqus/FEM Coordinate system is obtained by rotating the Laminate/Joint Coordinate System by +90° about the x-axis in the Laminate/Joint Coordinate System. The components of the transformed compliance matrix, $\hat{\hat{C}}(\theta)$, relative to the Abaqus/FEM Coordinate System for each ply orientation were directly inputted into Abaqus for material definitions of each ply region in the finite element models.

Appendix B

Isostrain Contour Field Plots

The normalized isostrain contour field plots for all two-dimensional composite scarf joint configurations investigated in this work are presented in this appendix. As discussed in the introduction to Chapter 5, the strain fields in the joint region are anti-symmetric about the rectangular coordinate system originating at the geometric center of the scarf joint at x equal to L/2 and z equal to $t_{adherend}/2$, with one axis being aligned with the adhesive midline, x_{jm}, as shown in Figure 5.1, for all cases except those with unequal scarf angles. The primary strain response is manifested in the joint region. These characteristics of the strain fields allow for convenient presentation of the isostrain contour field plots as it suffices to present the strain response in only one half of the joint region. All normalized isostrain contour fields in this appendix are therefore presented for regions spanning one half of the joint length, between x equal to L/2 and x equal to $(L + L_{joint})/2$.

The normalized isostrain contour field plots are presented for each scarf joint configuration for each of the three planar tensorial components of strain: longitudinal strain (ϵ_{11}), shear strain (ϵ_{13}), and transverse strain (ϵ_{33}). The magnitudes of strains in each isostrain contour field plot are normalized by the estimated far-field longitudinal strain of 182.5 μstrain for the cases with laminated adherends of $[\pm 45_2/0_2]_s$,

$[\pm 45/0]_{2s}$, and homogenized $[\pm 45/0]_{2s}$, and 86.8 μstrain for the cases with laminated adherends of $[\pm 15_2/0_2]_s$, $[\pm 15/0]_{2s}$, and homogenized $[\pm 15/0]_{2s}$. The normalized contour intervals are 0.5 for longitudinal and transverse strains, ϵ_{11} and ϵ_{33}, and 1.0 for shear strain, ϵ_{13}. The global peak magnitude of strain occurring in each scarf joint configuration is denoted by ϵ_{m}. The actual and scaled magnitudes of strains for other loading conditions can be determined from these normalized isostrain contour field plots as per the discussion in Section 4.3.

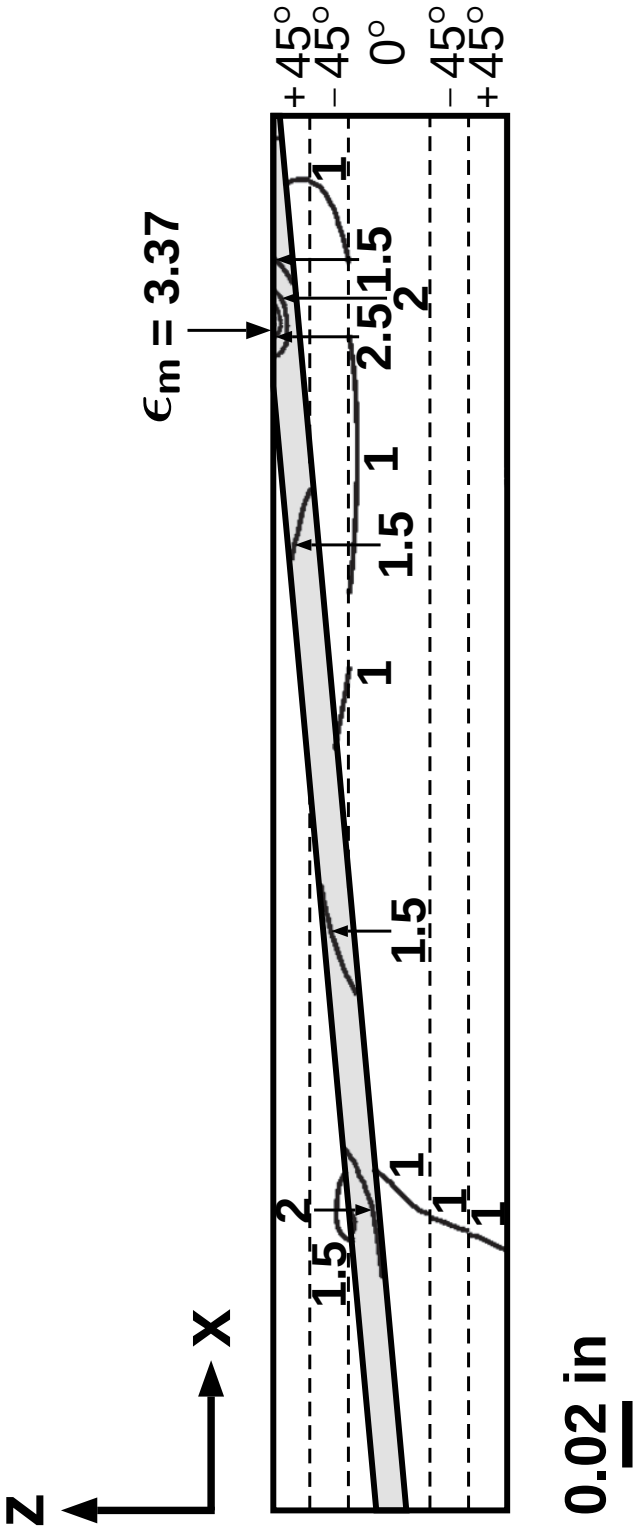

Figure B.1 Normalized isostrain contour field plot of ϵ_{11} for the two-dimensional composite scarf joint with equal scarf angles of 5°, adhesive thickness of 0.008 in, and laminate configuration of $[\pm 45_2/0_2]_S$.

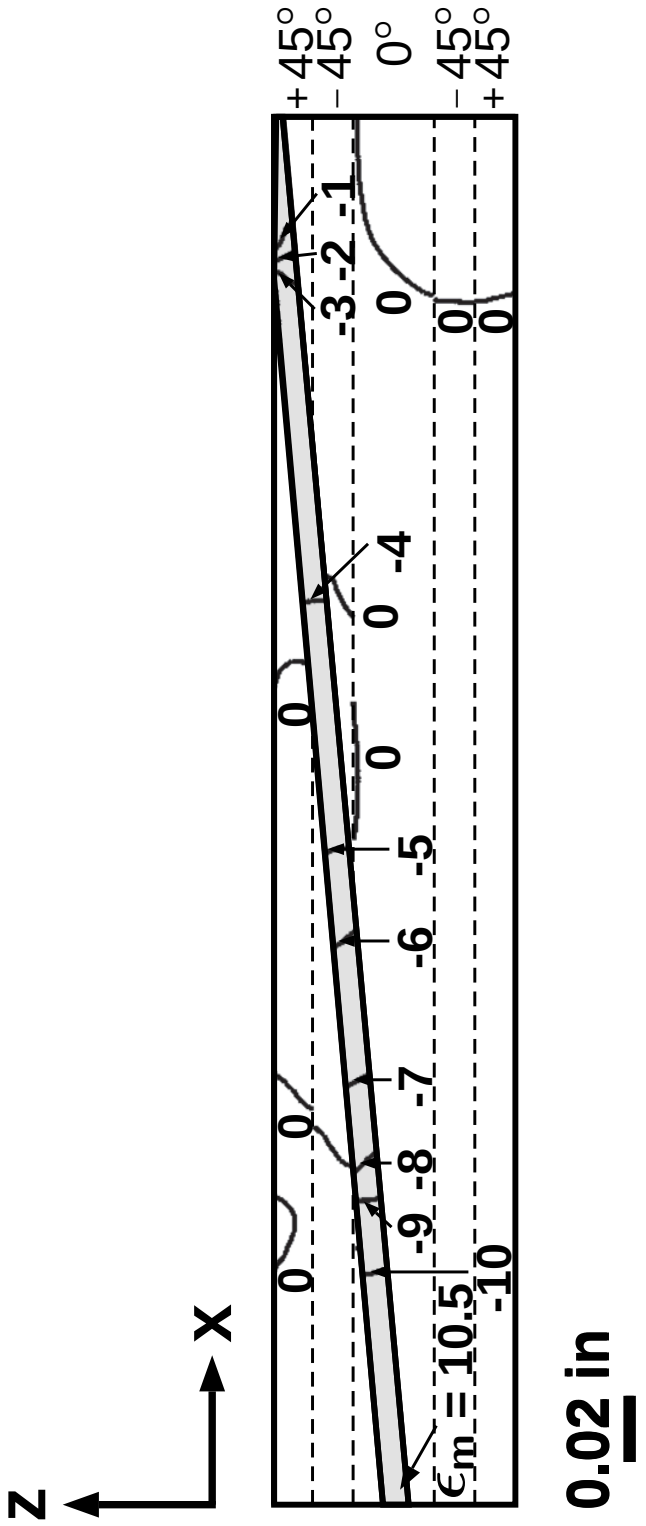

Figure B.2 Normalized isostrain contour field plot of ϵ_{13} for the two-dimensional composite scarf joint with equal scarf angles of 5°, adhesive thickness of 0.008 in, and laminate configuration of $[\pm 45_2/0_2]_S$.

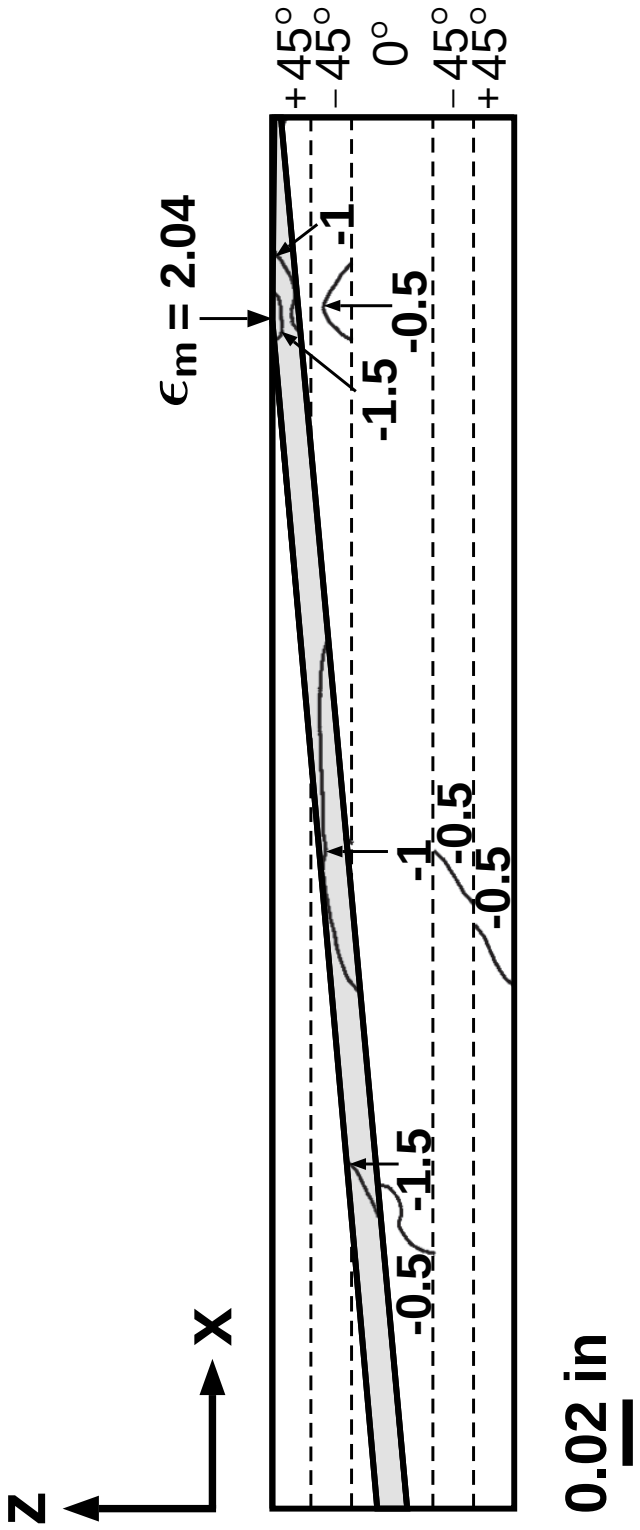

Figure B.3 Normalized isostrain contour field plot of ϵ_{33} for the two-dimensional composite scarf joint with equal scarf angles of 5°, adhesive thickness of 0.008 in, and laminate configuration of $[\pm 45_2/0_2]_S$.

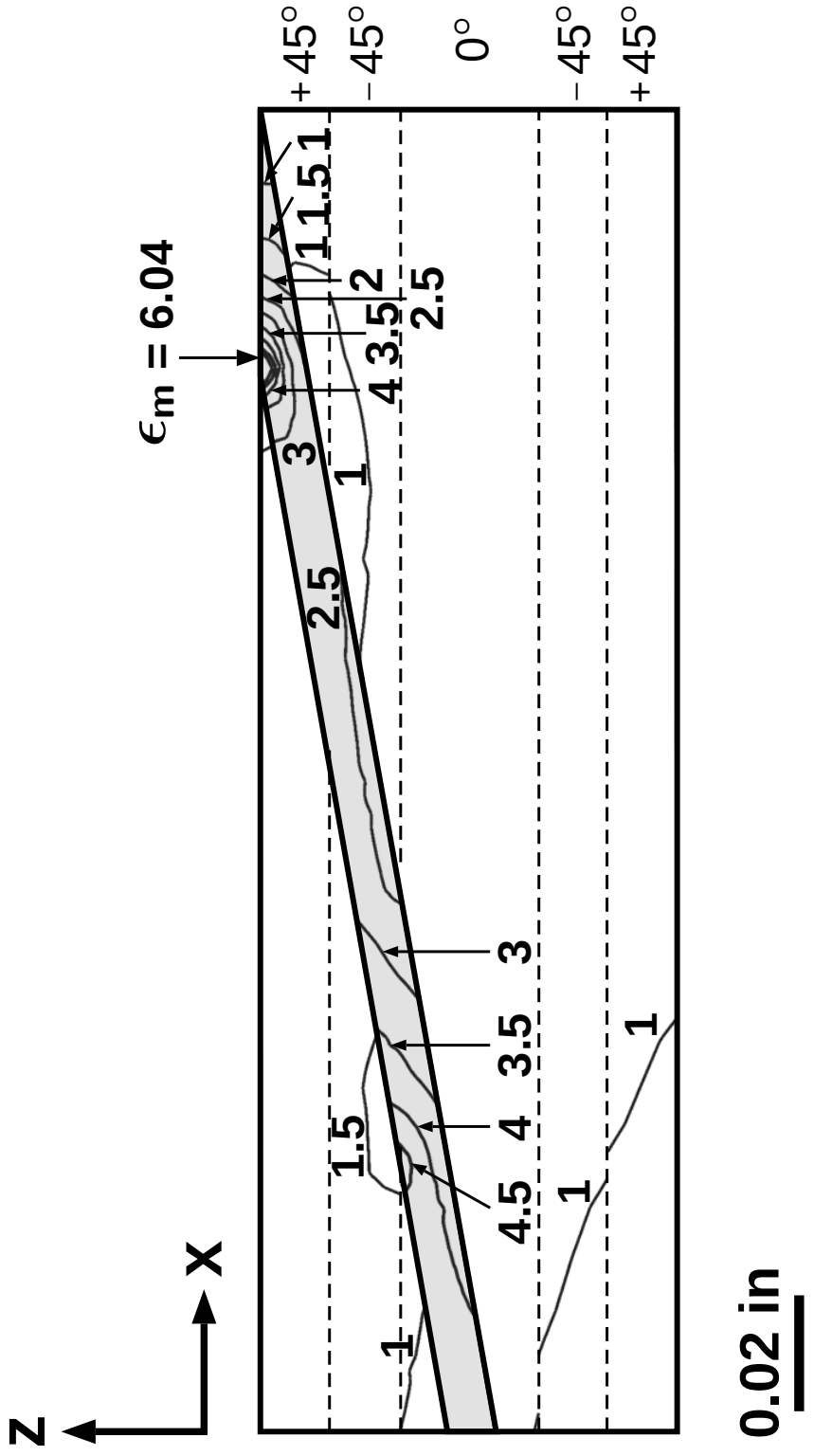

Figure B.4 Normalized isostrain contour field plot of ϵ_{11} for the two-dimensional composite scarf joint with equal scarf angles of 10°, adhesive thickness of 0.008 in, and laminate configuration of $[\pm 45_2/0_2]_S$.

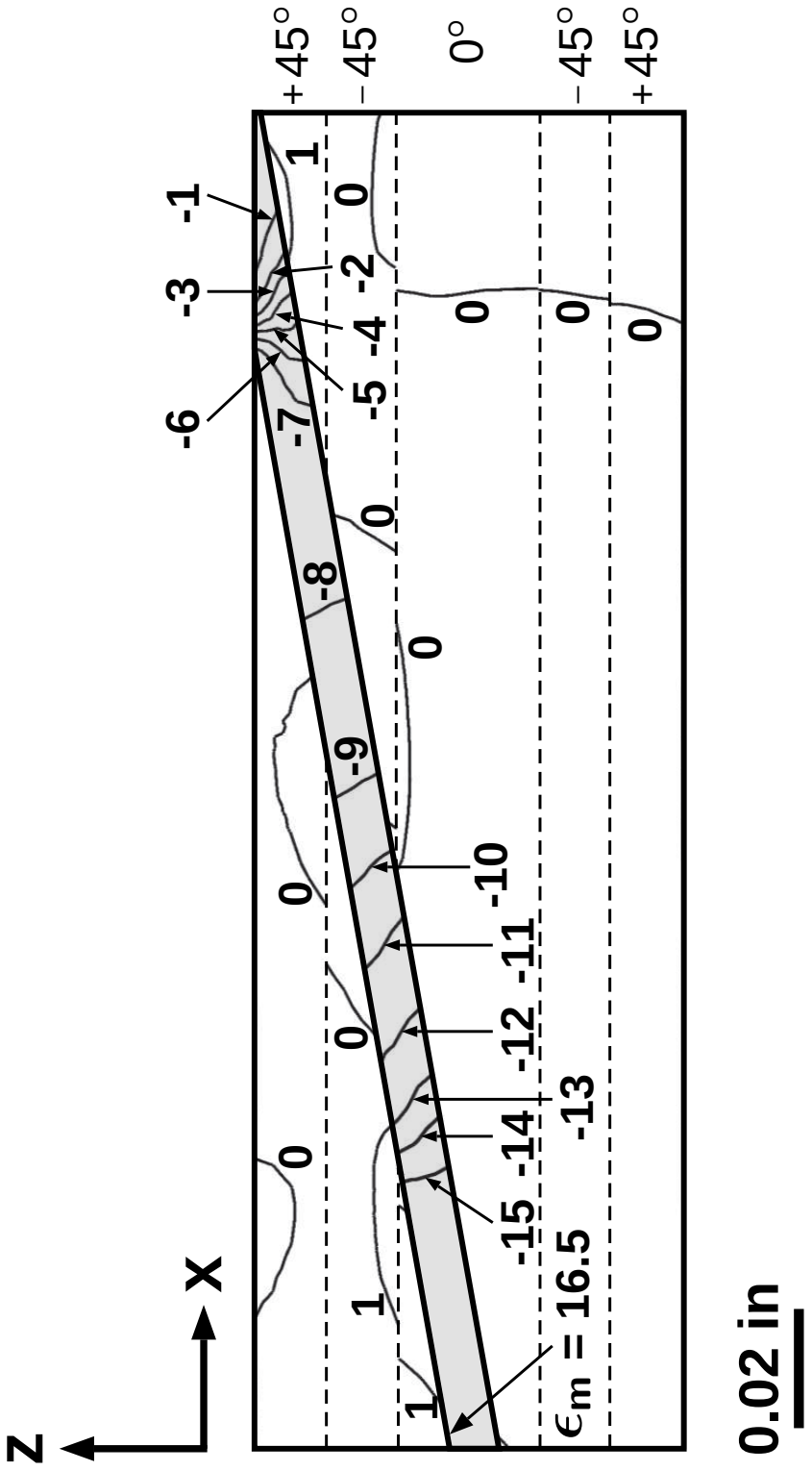

Figure B.5 Normalized isostrain contour field plot of ϵ_{13} for the two-dimensional composite scarf joint with equal scarf angles of 10°, adhesive thickness of 0.008 in, and laminate configuration of $[\pm 45_2/0_2]_S$.

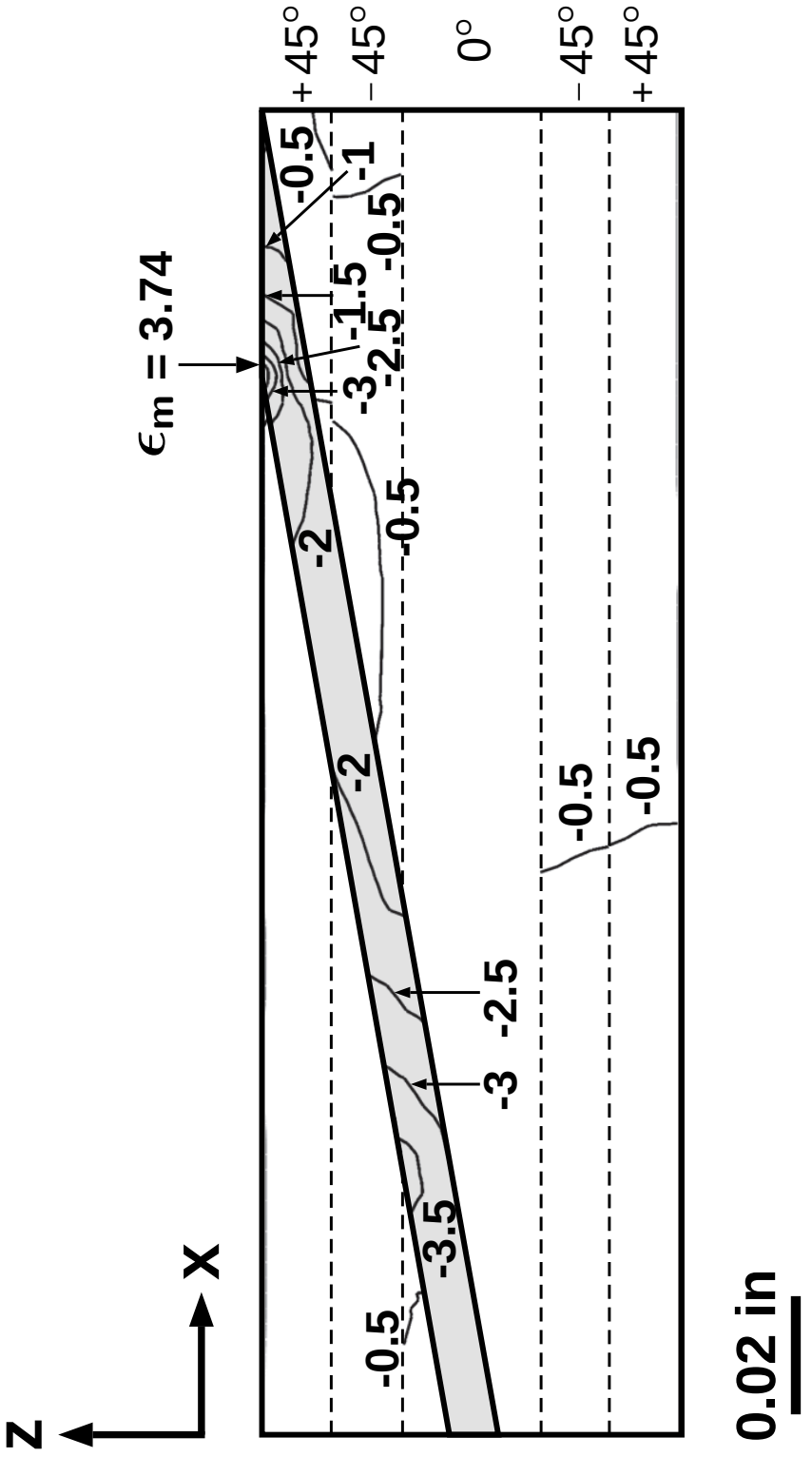

Figure B.6 Normalized isostrain contour field plot of ϵ_{33} for the two-dimensional composite scarf joint with equal scarf angles of 10°, adhesive thickness of 0.008 in, and laminate configuration of $[\pm 45_2/0_2]_S$.

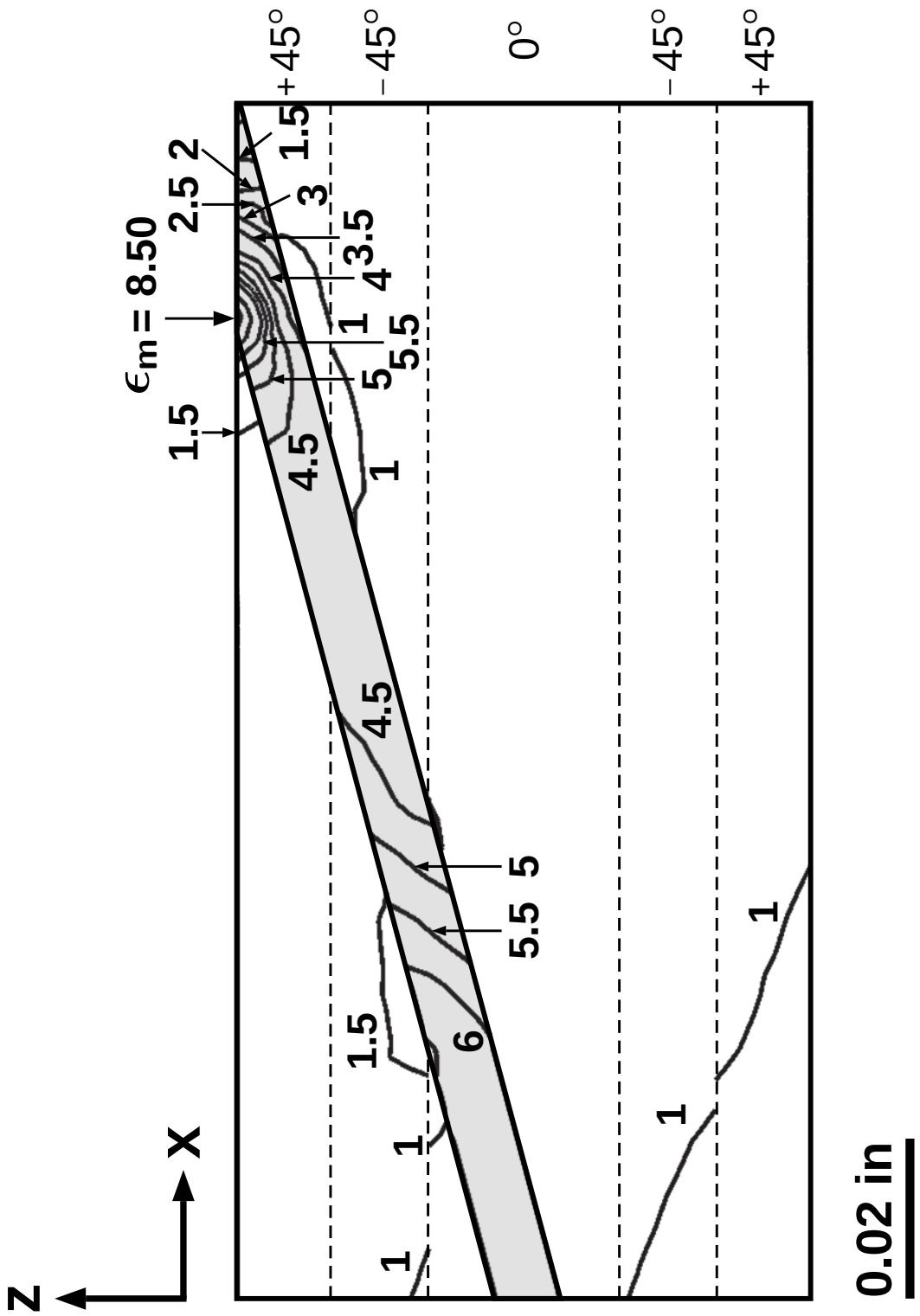

Figure B.7 Normalized isostrain contour field plot of ϵ_{11} for the two-dimensional composite scarf joint with equal scarf angles of 15°, adhesive thickness of 0.008 in, and laminate configuration of $[\pm 45_2/0_2]_S$.

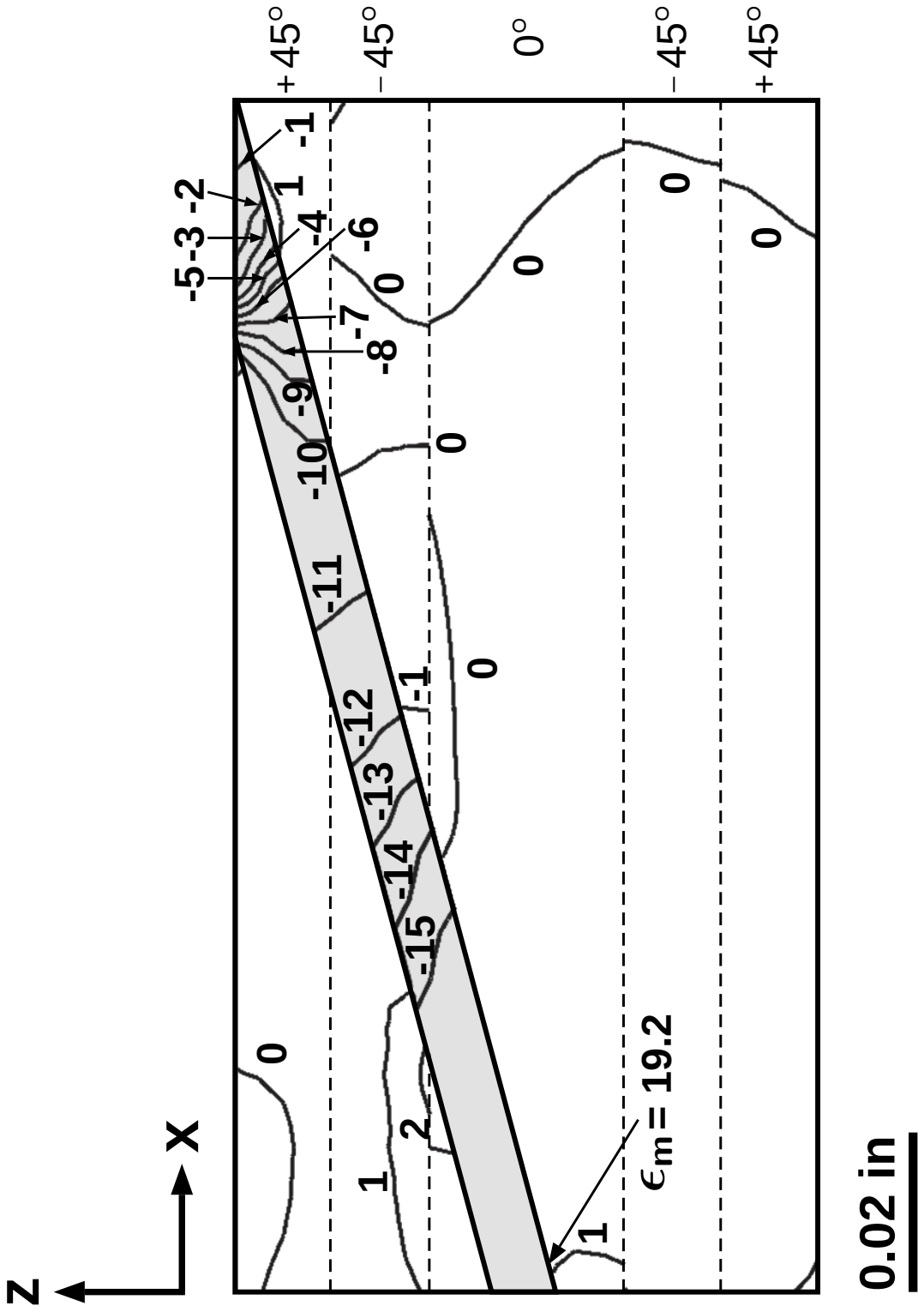

Figure B.8 Normalized isostrain contour field plot of ϵ_{13} for the two-dimensional composite scarf joint with equal scarf angles of 15°, adhesive thickness of 0.008 in, and laminate configuration of $[\pm 45_2/0_2]_S$.

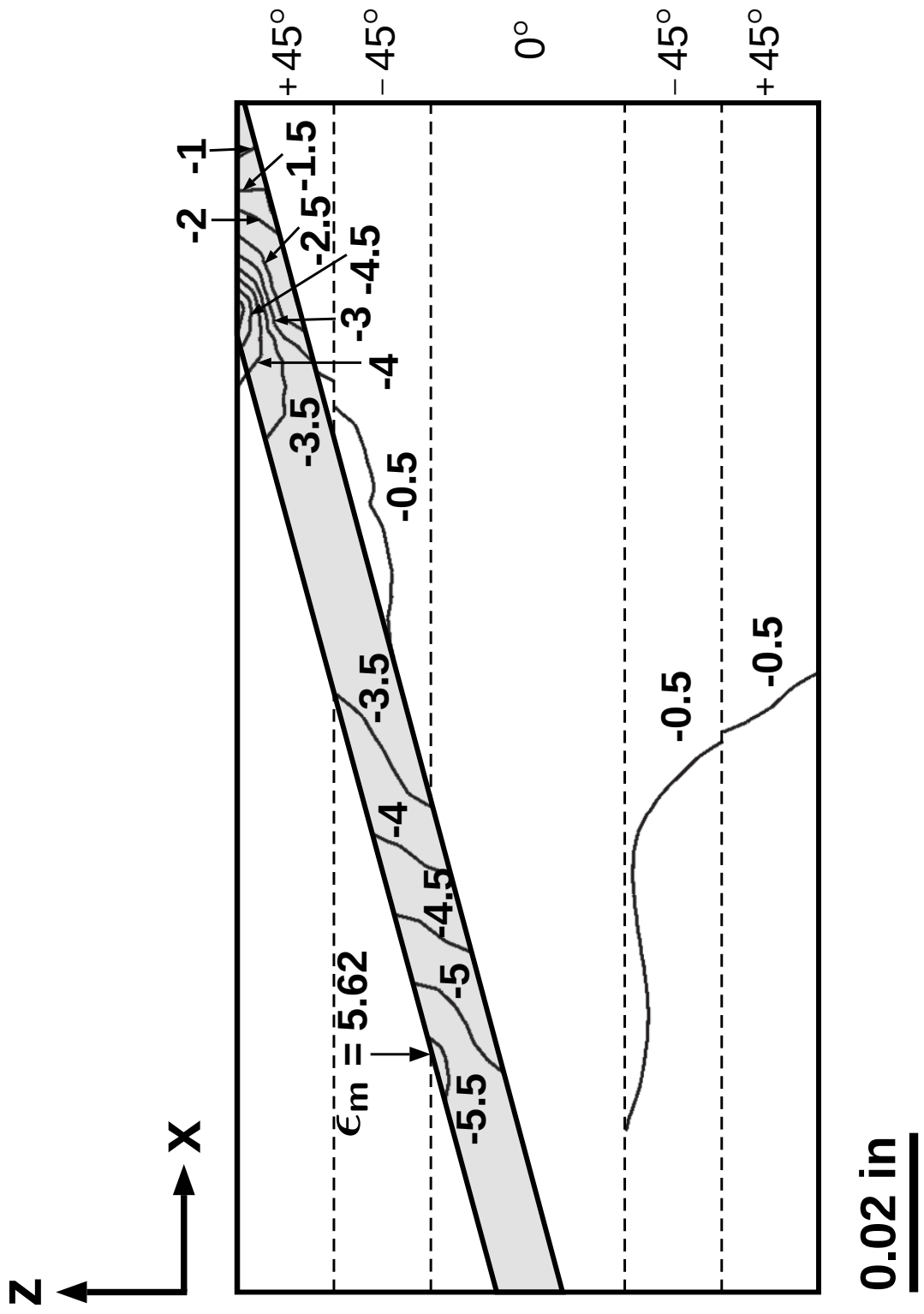

Figure B.9 Normalized isostrain contour field plot of ϵ_{33} for the two-dimensional composite scarf joint with equal scarf angles of 15°, adhesive thickness of 0.008 in, and laminate configuration of $[\pm 45_2/0_2]_S$.

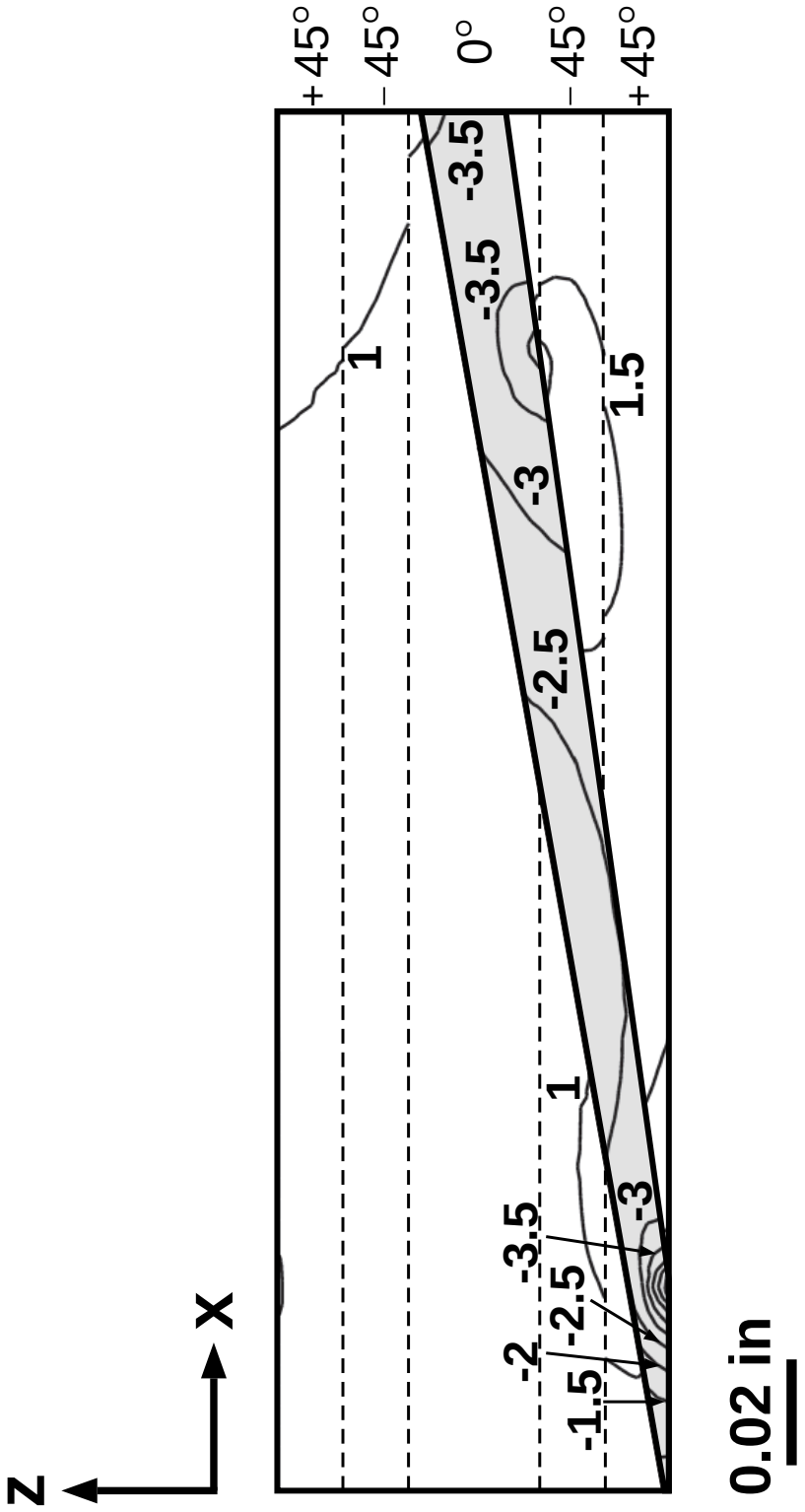

Figure B.10 Normalized isostrain contour field plot of ϵ_{11} for the two-dimensional composite scarf joint with unequal scarf angles of (10°, 8°), minimum adhesive thickness of 0.008 in, and laminate configuration of $[\pm 45_2/0_2]_S$.

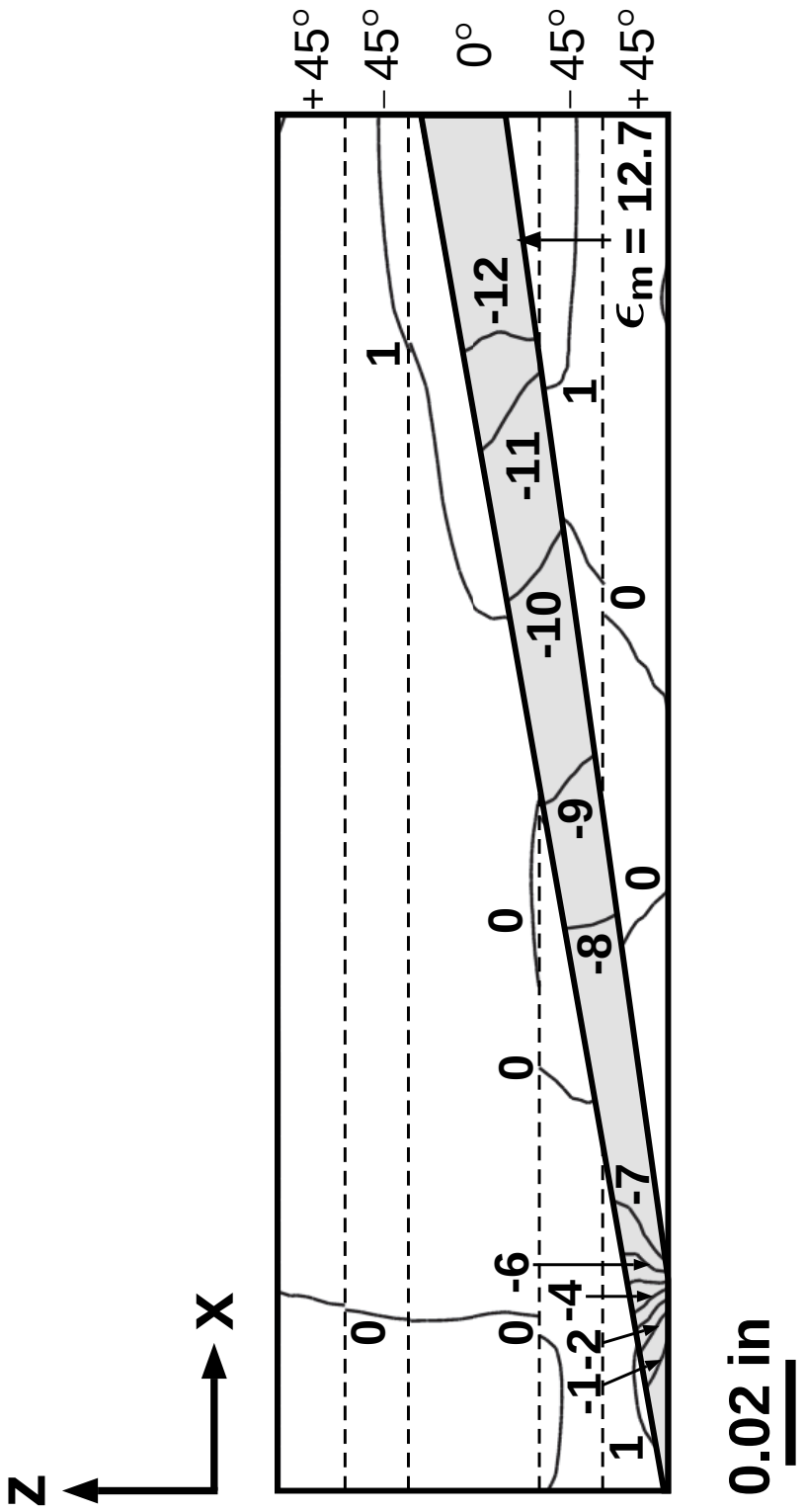

Figure B.11 Normalized isostrain contour field plot of ϵ_{13} for the two-dimensional composite scarf joint with unequal scarf angles of (10°, 8°), minimum adhesive thickness of 0.008 in, and laminate configuration of $[\pm 45_2/0_2]_S$.

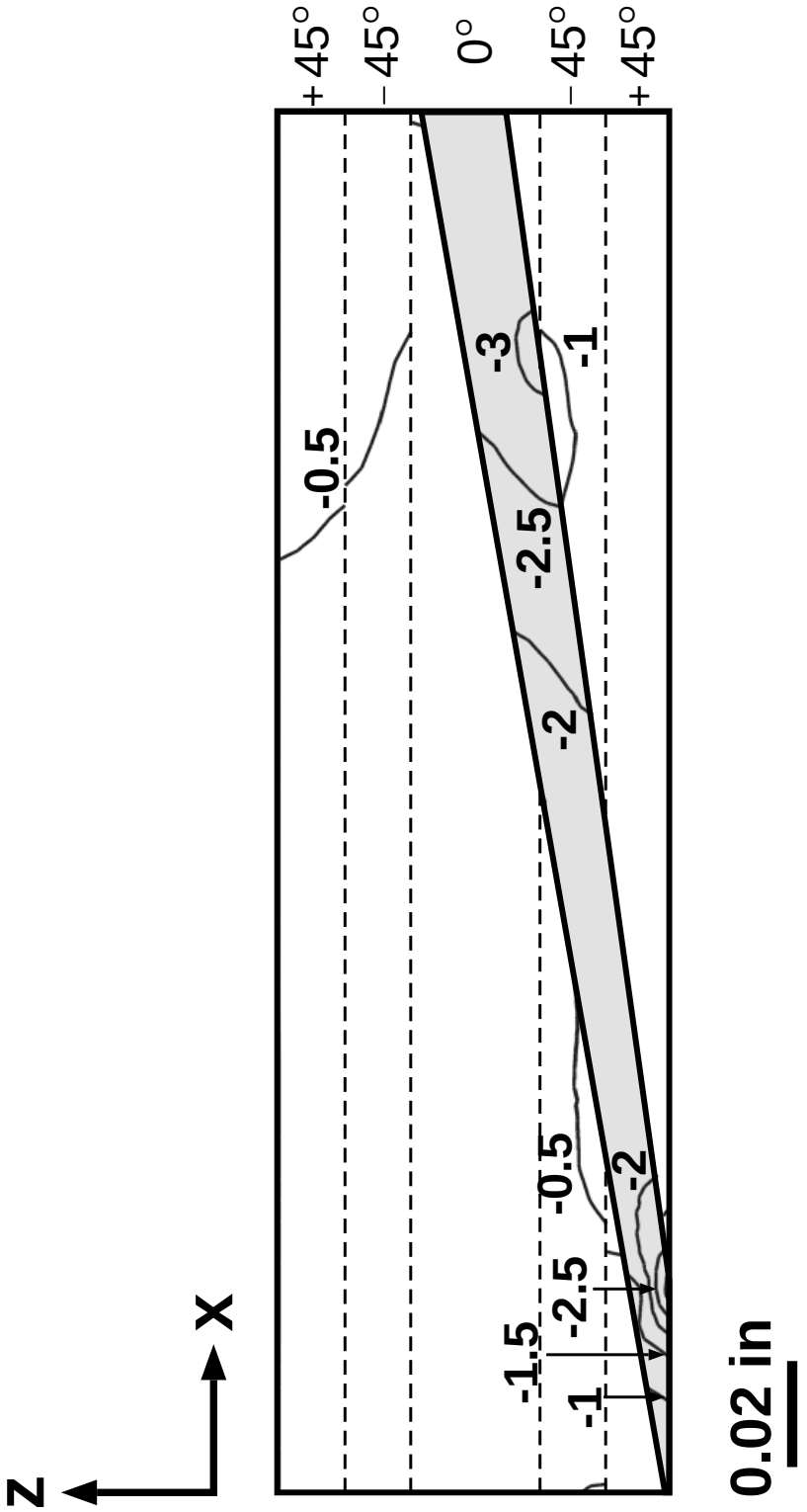

Figure B.12 Normalized isostrain contour field plot of ϵ_{33} for the two-dimensional composite scarf joint with unequal scarf angles of (10°, 8°), minimum adhesive thickness of 0.008 in, and laminate configuration of $[\pm 45_2/0_2]_S$.

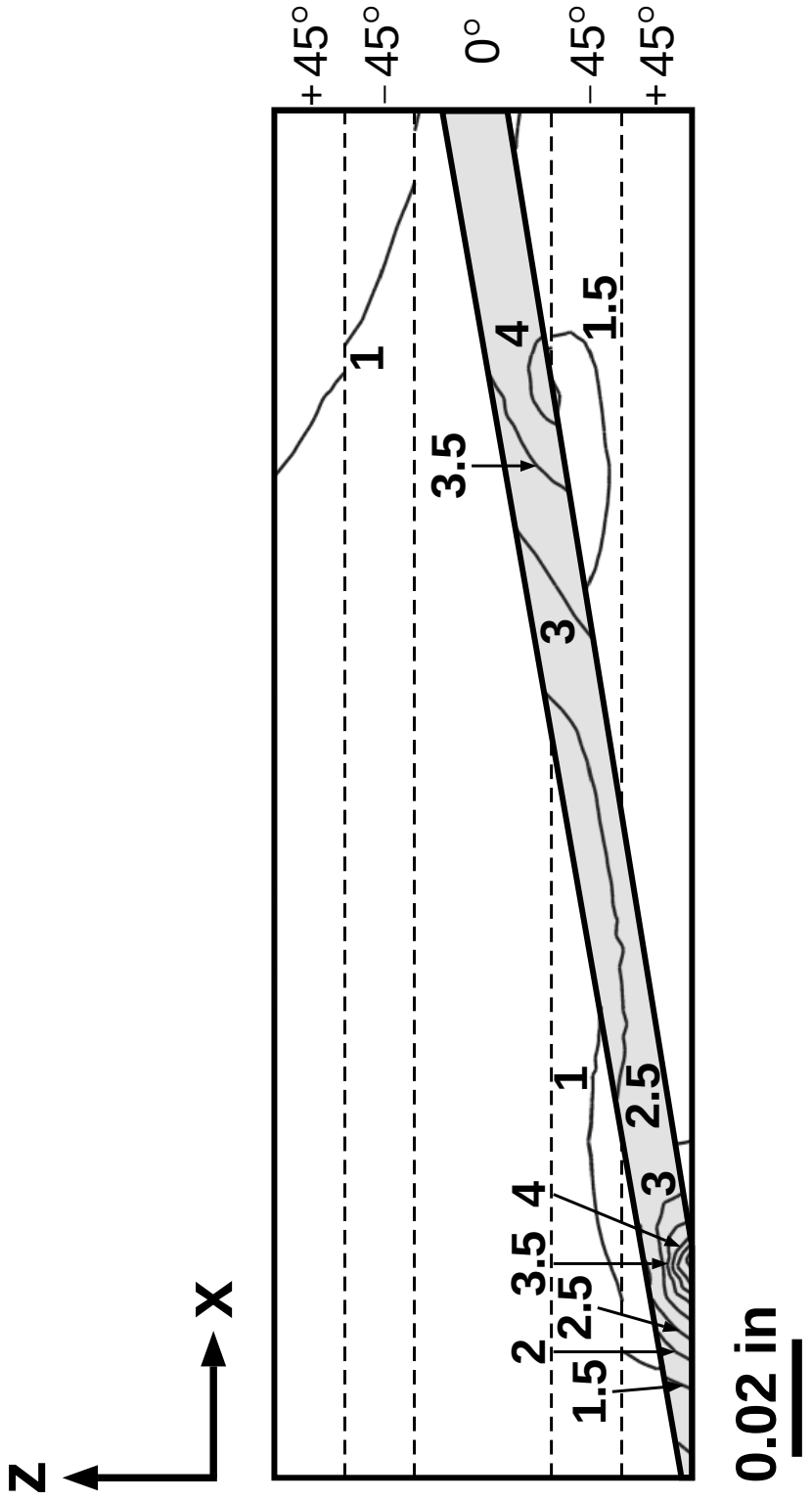

Figure B.13 Normalized isostrain contour field plot of ϵ_{11} for the two-dimensional composite scarf joint with unequal scarf angles of (10°, 9°), minimum adhesive thickness of 0.008 in, and laminate configuration of $[\pm 45_2/0_2]_S$.

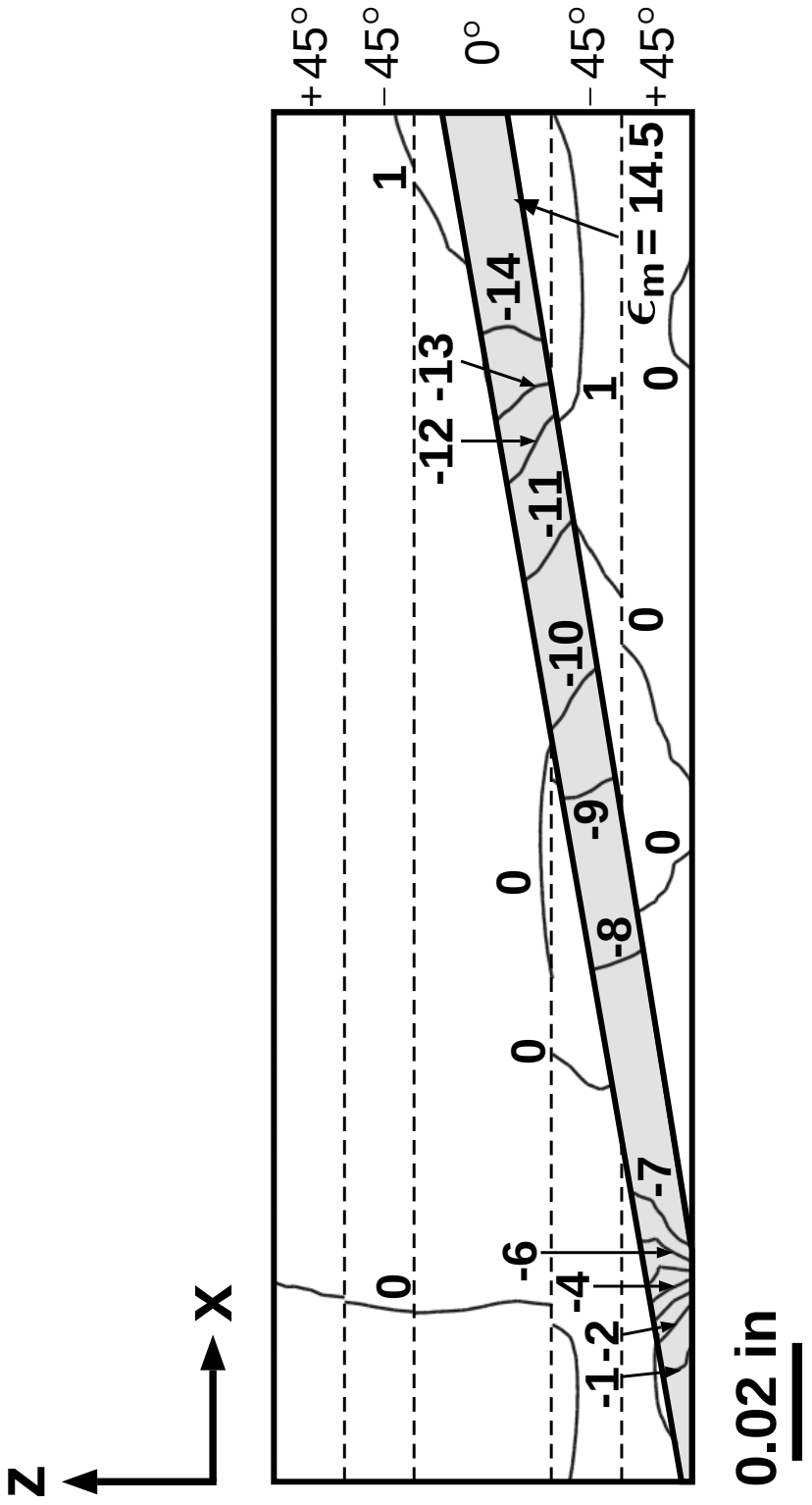

Figure B.14 Normalized isostrain contour field plot of ϵ_{13} for the two-dimensional composite scarf joint with unequal scarf angles of (10°, 9°), minimum adhesive thickness of 0.008 in, and laminate configuration of $[\pm 45_2/0_2]_S$.

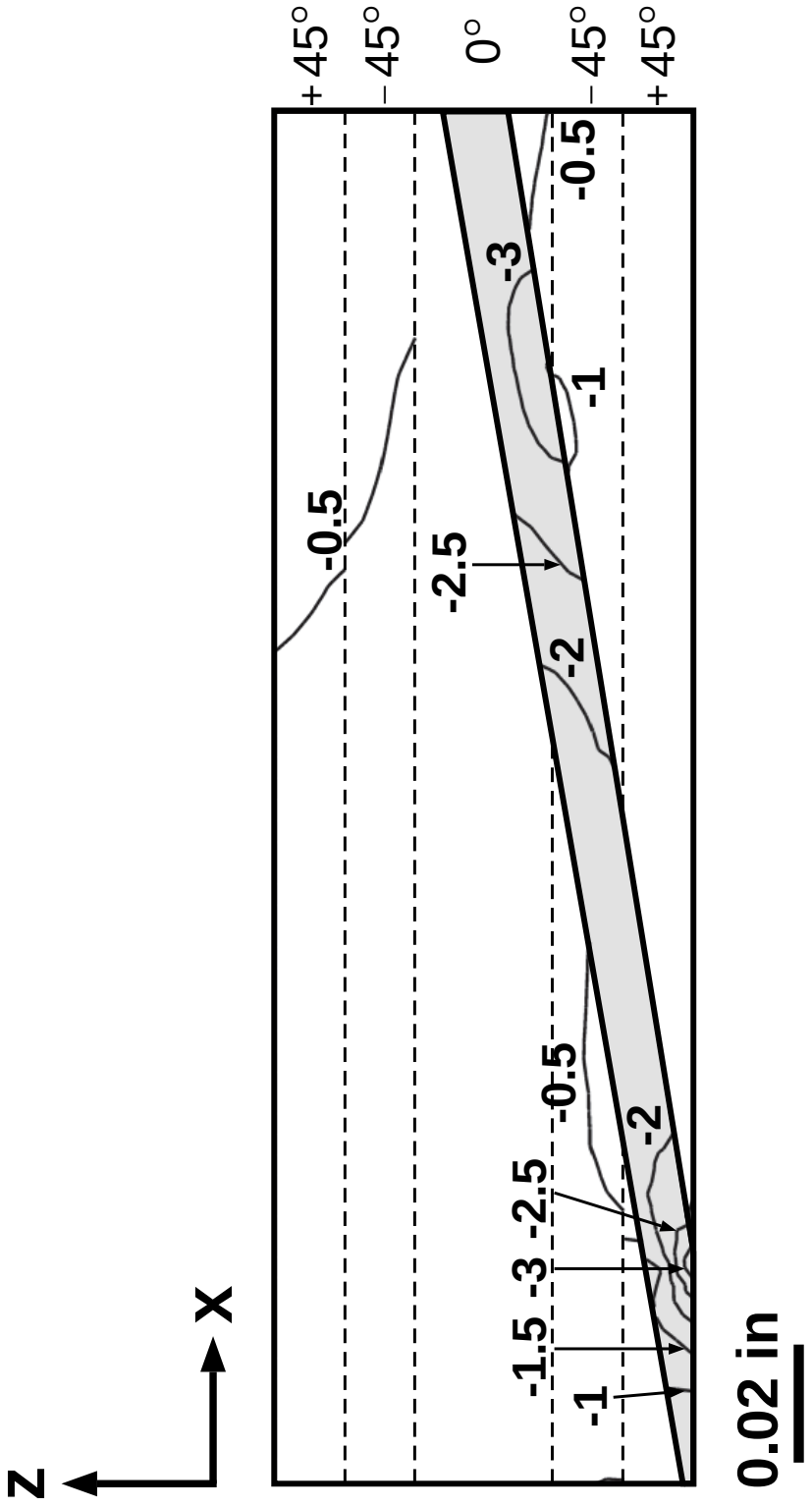

Figure B.15 Normalized isostrain contour field plot of ϵ_{33} for the two-dimensional composite scarf joint with unequal scarf angles of (10°, 9°), minimum adhesive thickness of 0.008 in, and laminate configuration of $[\pm 45_2/0_2]_S$.

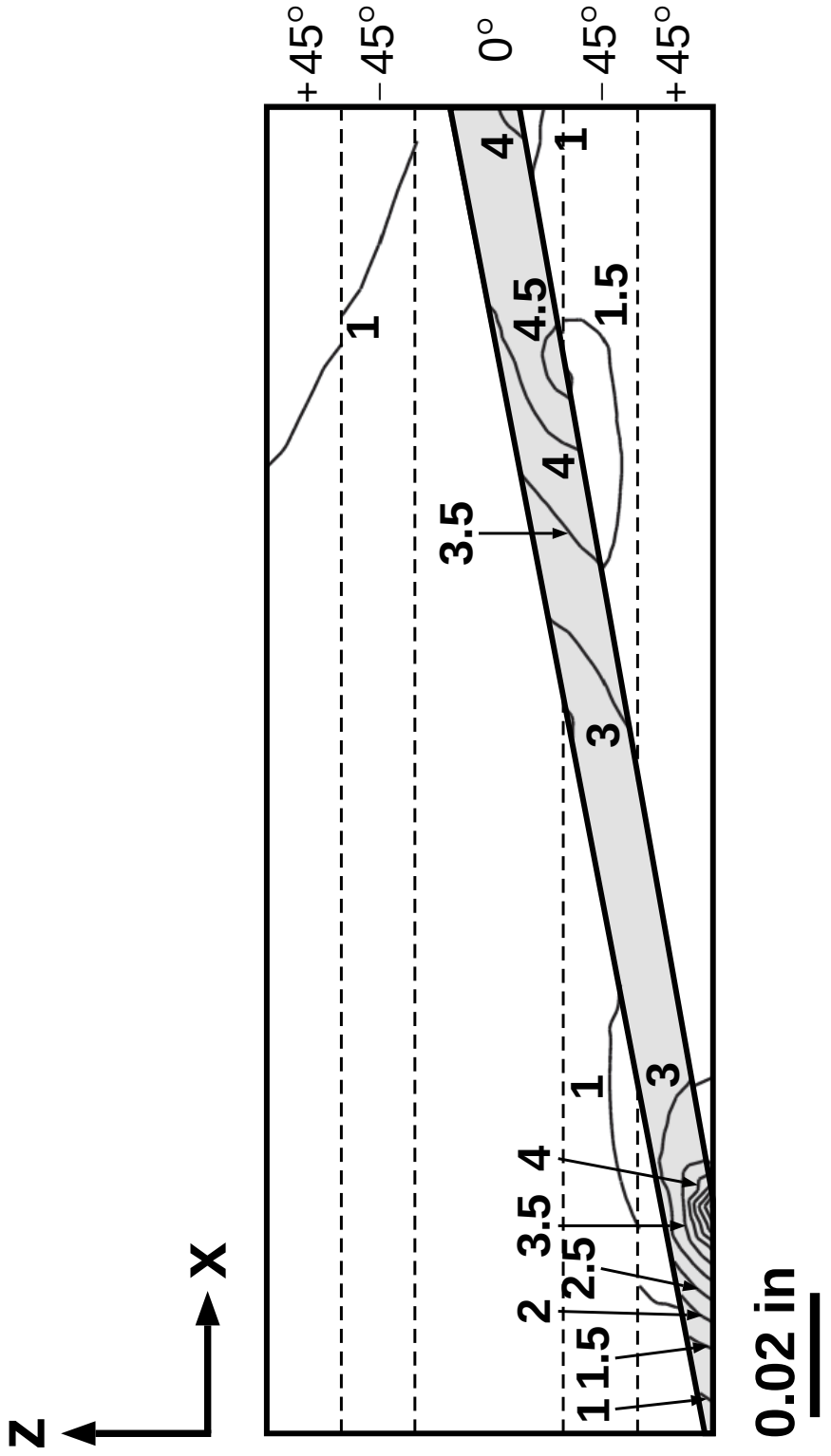

Figure B.16 Normalized isostrain contour field plot of ϵ_{11} for the two-dimensional composite scarf joint with unequal scarf angles of (10°, 11°), minimum adhesive thickness of 0.008 in, and laminate configuration of $[\pm 45_2/0_2]_S$.

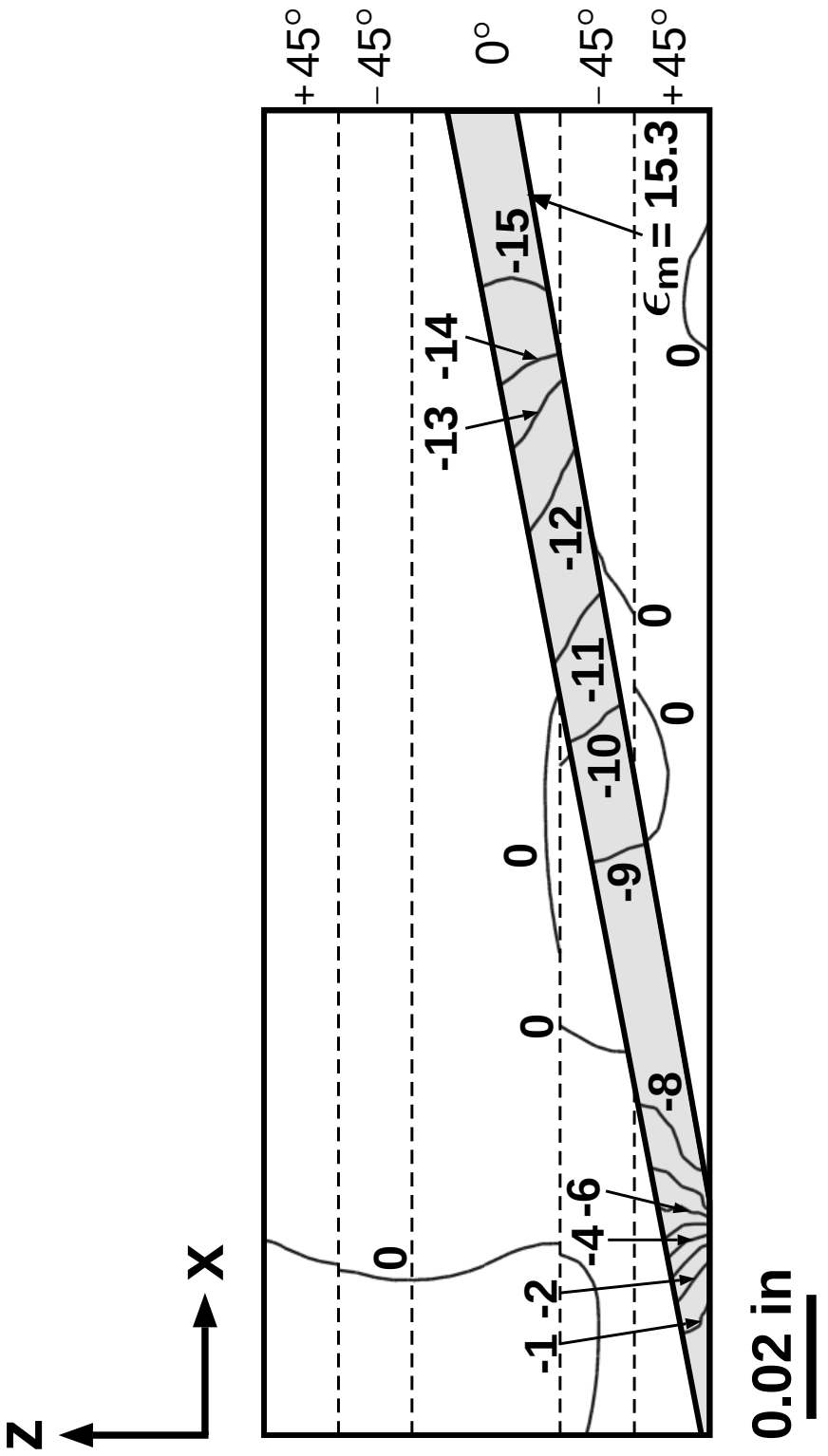

Figure B.17 Normalized isostrain contour field plot of ϵ_{13} for the two-dimensional composite scarf joint with unequal scarf angles of (10°, 11°), minimum adhesive thickness of 0.008 in, and laminate configuration of $[\pm 45_2/0_2]_S$.

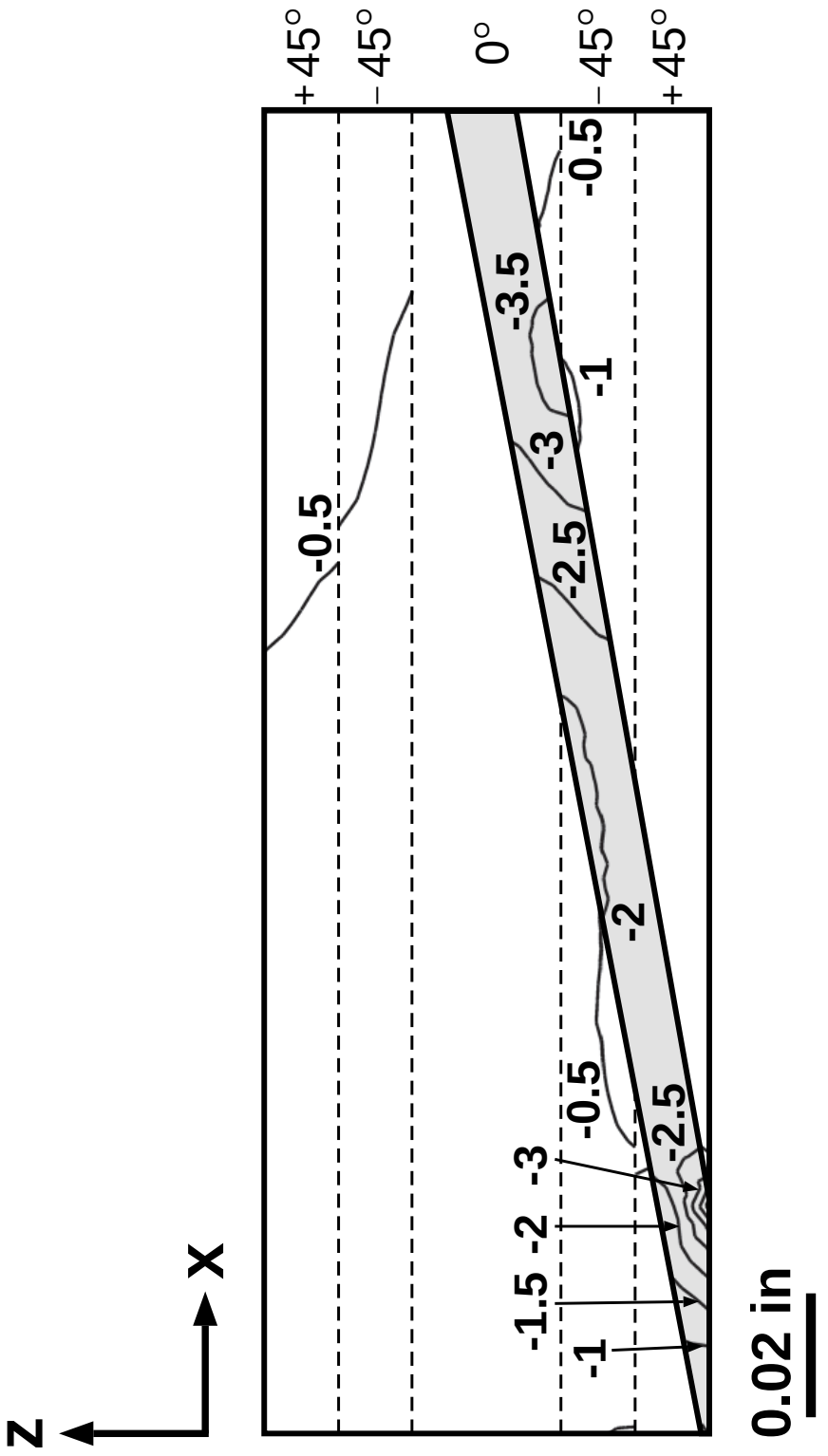

Figure B.18 Normalized isostrain contour field plot of ϵ_{33} for the two-dimensional composite scarf joint with unequal scarf angles of (10°, 11°), minimum adhesive thickness of 0.008 in, and laminate configuration of $[\pm 45_2/0_2]_S$.

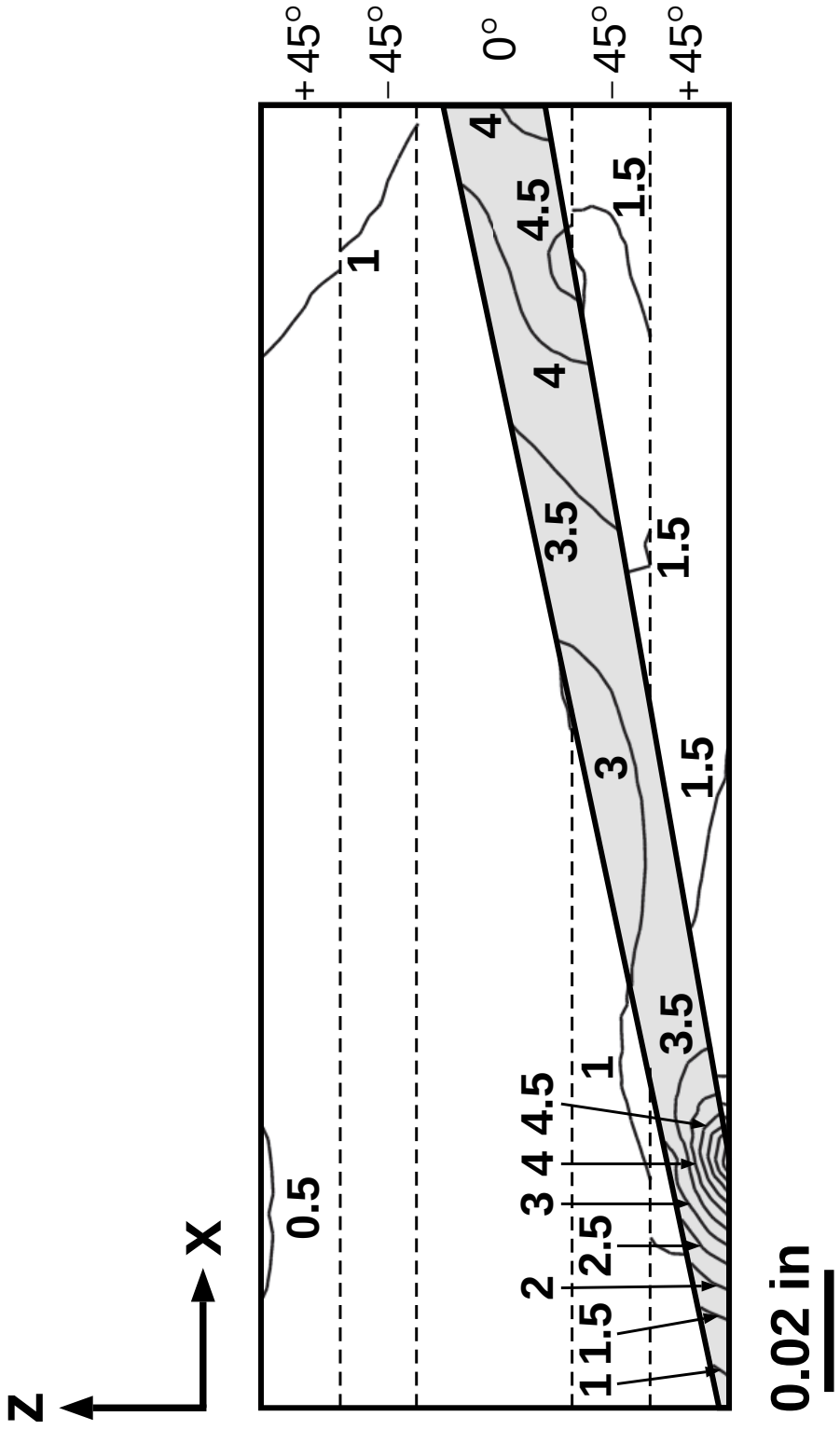

Figure B.19 Normalized isostrain contour field plot of ϵ_{11} for the two-dimensional composite scarf joint with unequal scarf angles of (10°, 12°), minimum adhesive thickness of 0.008 in, and laminate configuration of $[\pm 45_2/0_2]_S$.

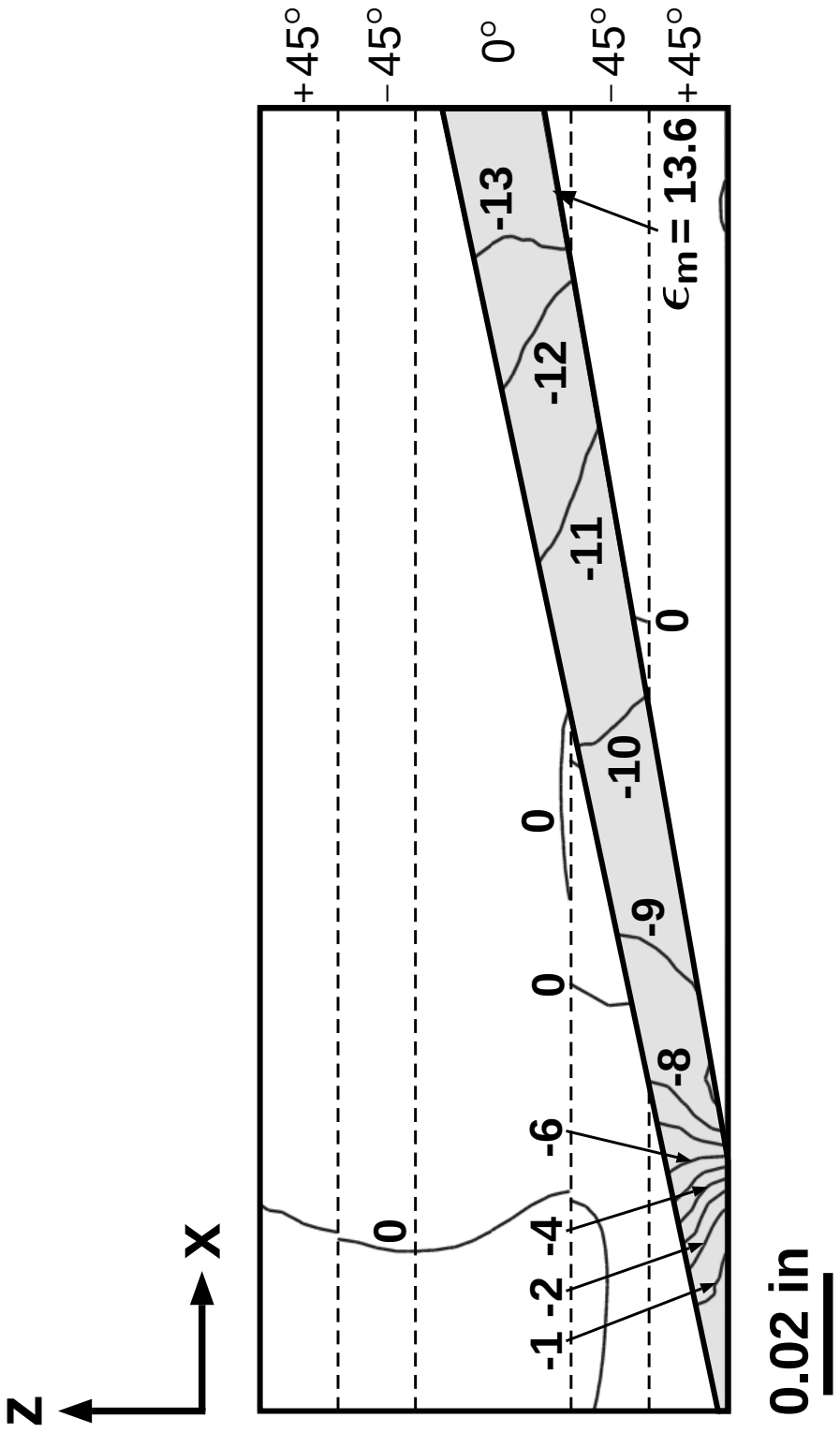

Figure B.20 Normalized isostrain contour field plot of ϵ_{13} for the two-dimensional composite scarf joint with unequal scarf angles of (10°, 12°), minimum adhesive thickness of 0.008 in, and laminate configuration of $[\pm 45_2/0_2]_S$.

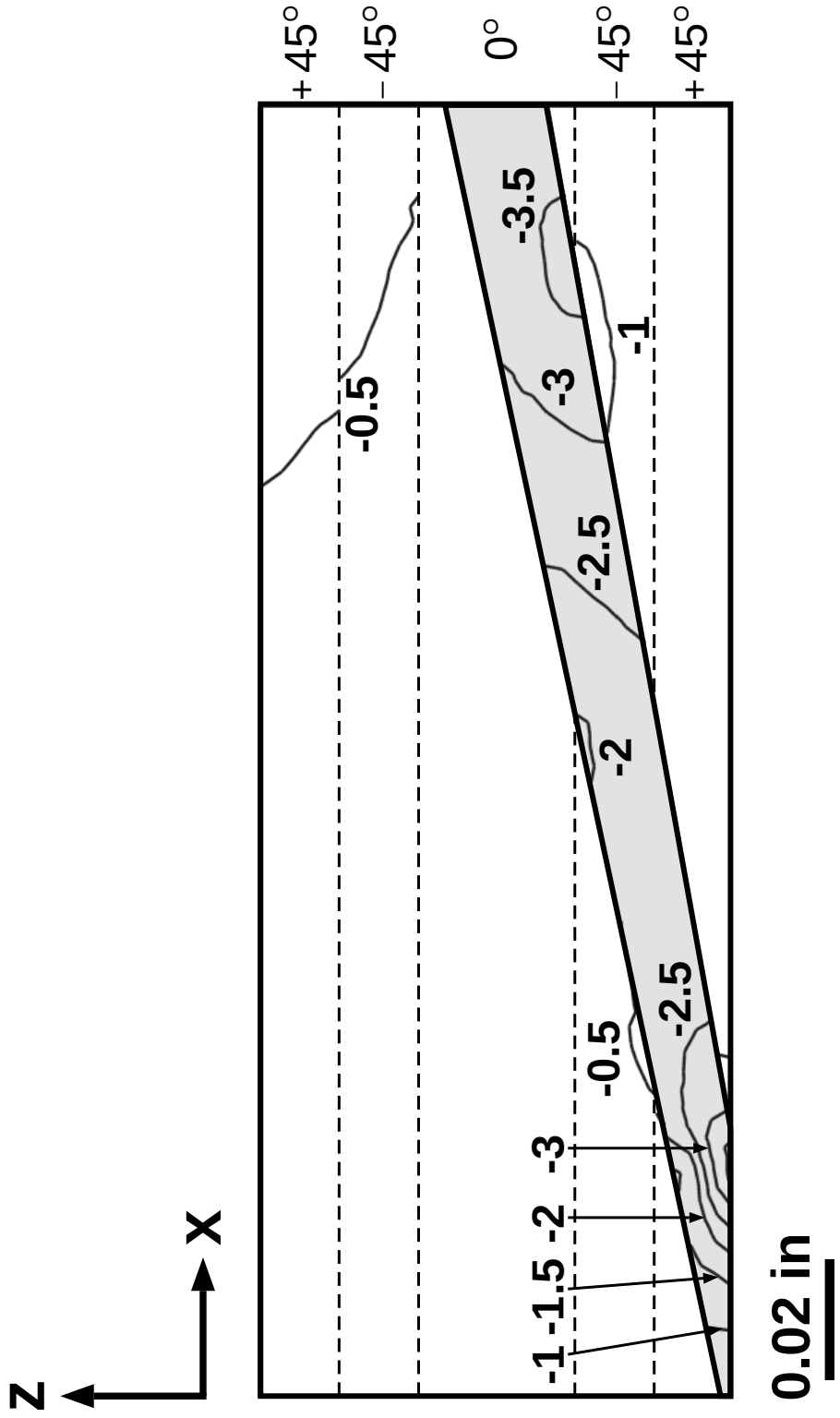

Figure B.21 Normalized isostrain contour field plot of ϵ_{33} for the two-dimensional composite scarf joint with unequal scarf angles of (10°, 12°), minimum adhesive thickness of 0.008 in, and laminate configuration of $[\pm 45_2/0_2]_S$.

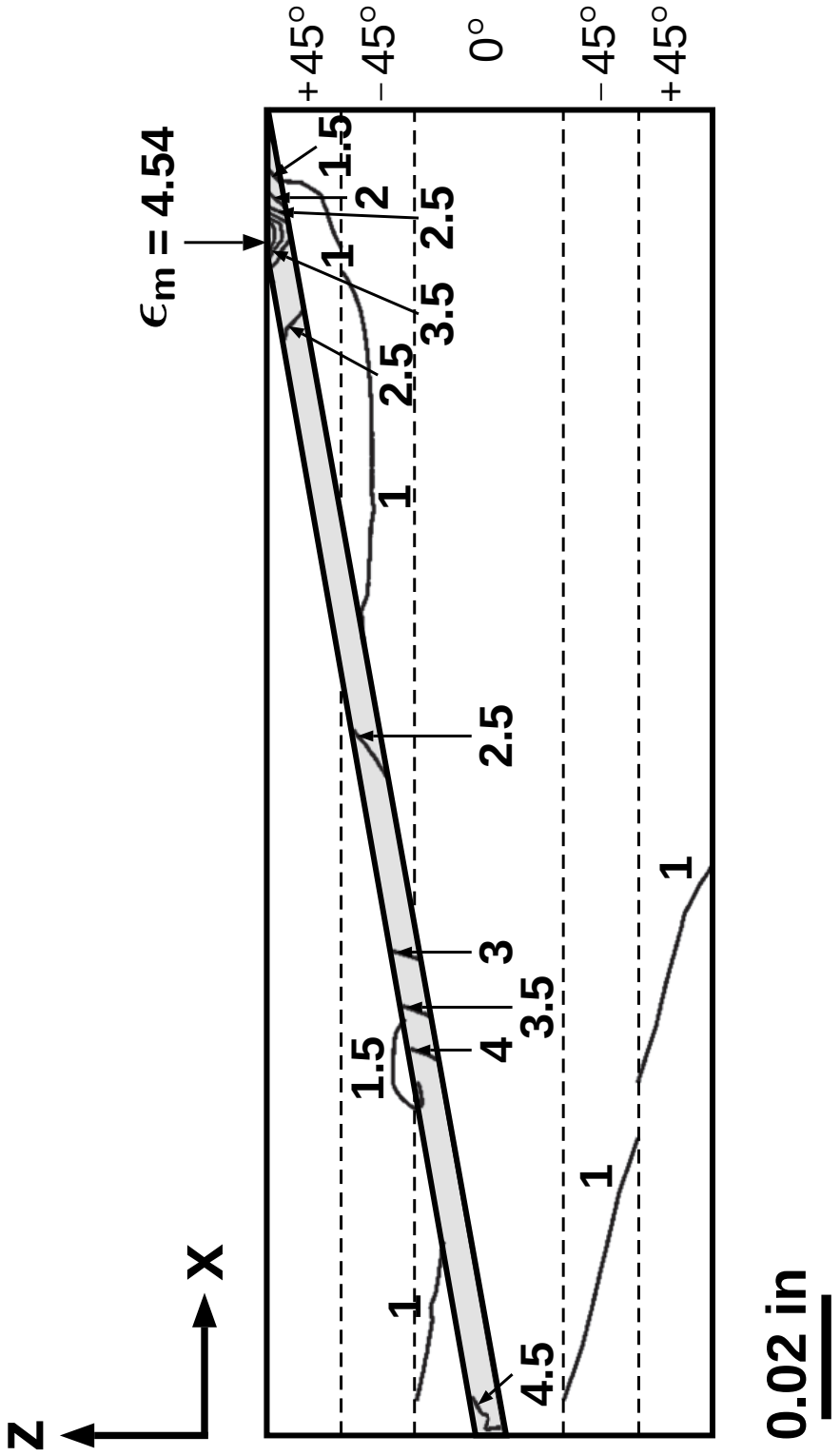

Figure B.22 Normalized isostrain contour field plot of ϵ_{11} for the two-dimensional composite scarf joint with equal scarf angles of 10°, adhesive thickness of 0.008 in, and laminate configuration of $[\pm 45_2/0_2]_S$.

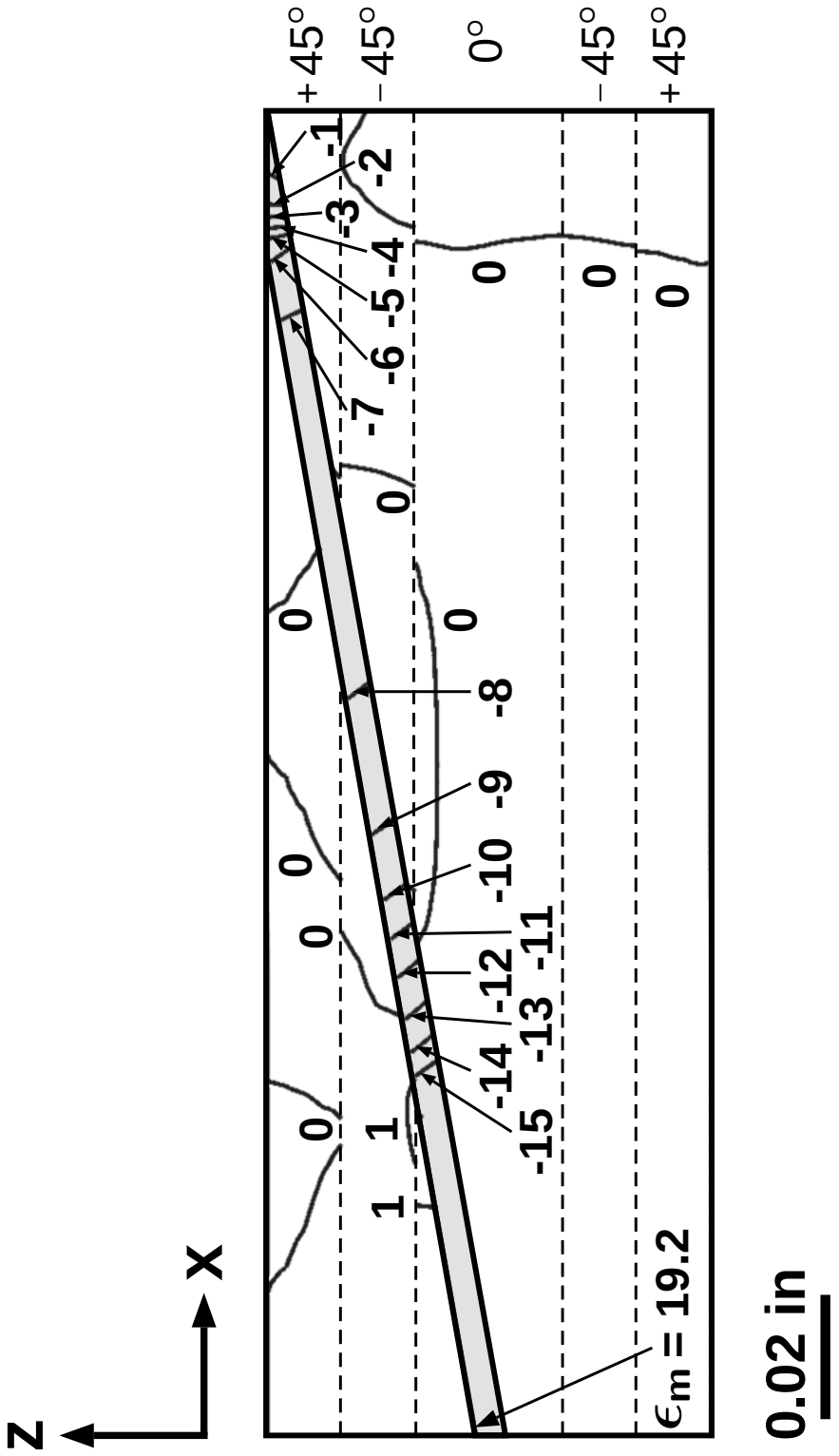

Figure B.23 Normalized isostrain contour field plot of ϵ_{13} for the two-dimensional composite scarf joint with equal scarf angles of 10°, adhesive thickness of 0.004 in, and laminate configuration of $[\pm 45_2/0_2]_S$.

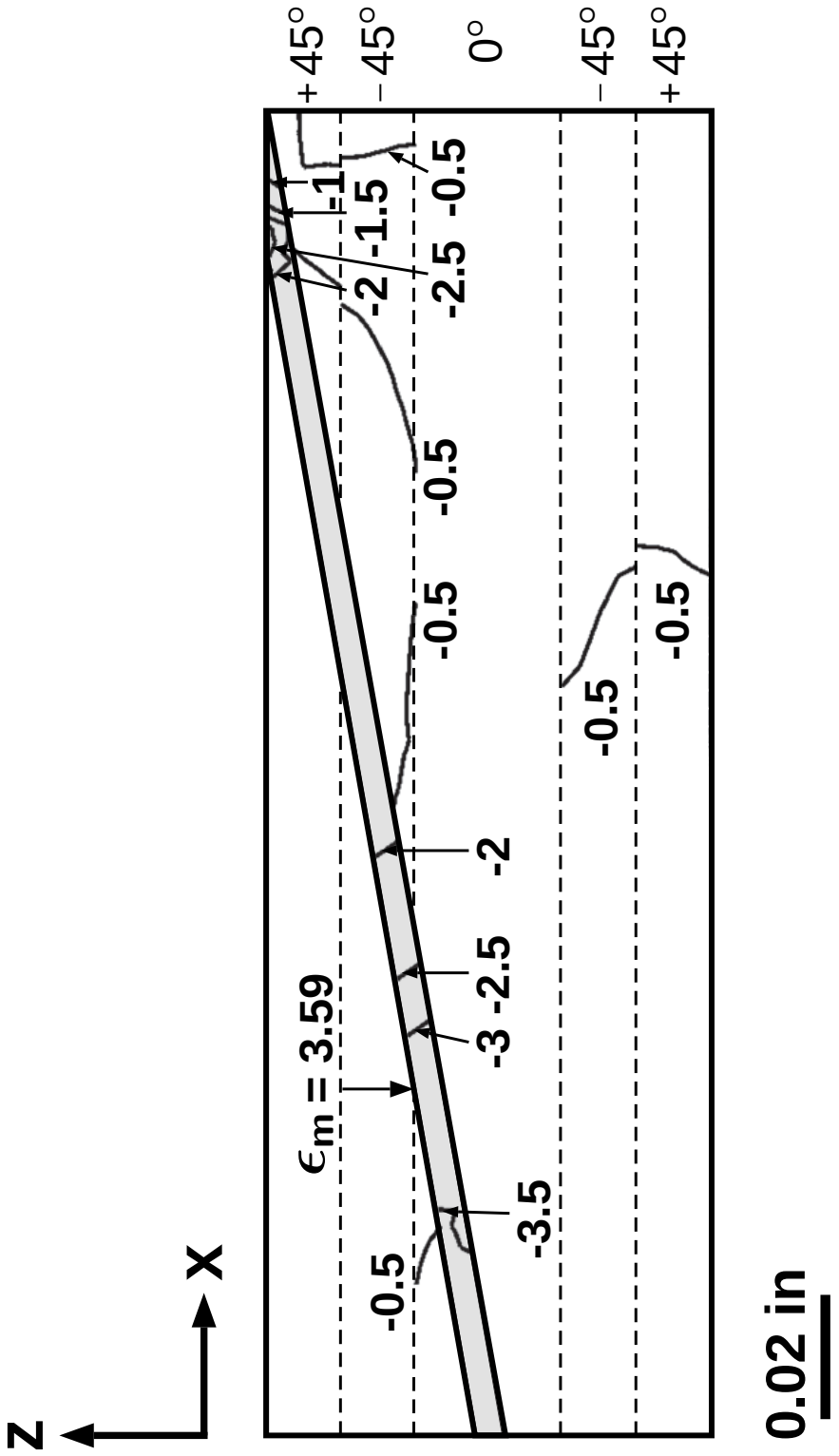

Figure B.24 Normalized isostrain contour field plot of ϵ_{33} for the two-dimensional composite scarf joint with equal scarf angles of 10°, adhesive thickness of 0.004 in, and laminate configuration of $[\pm 45_2/0_2]_S$.

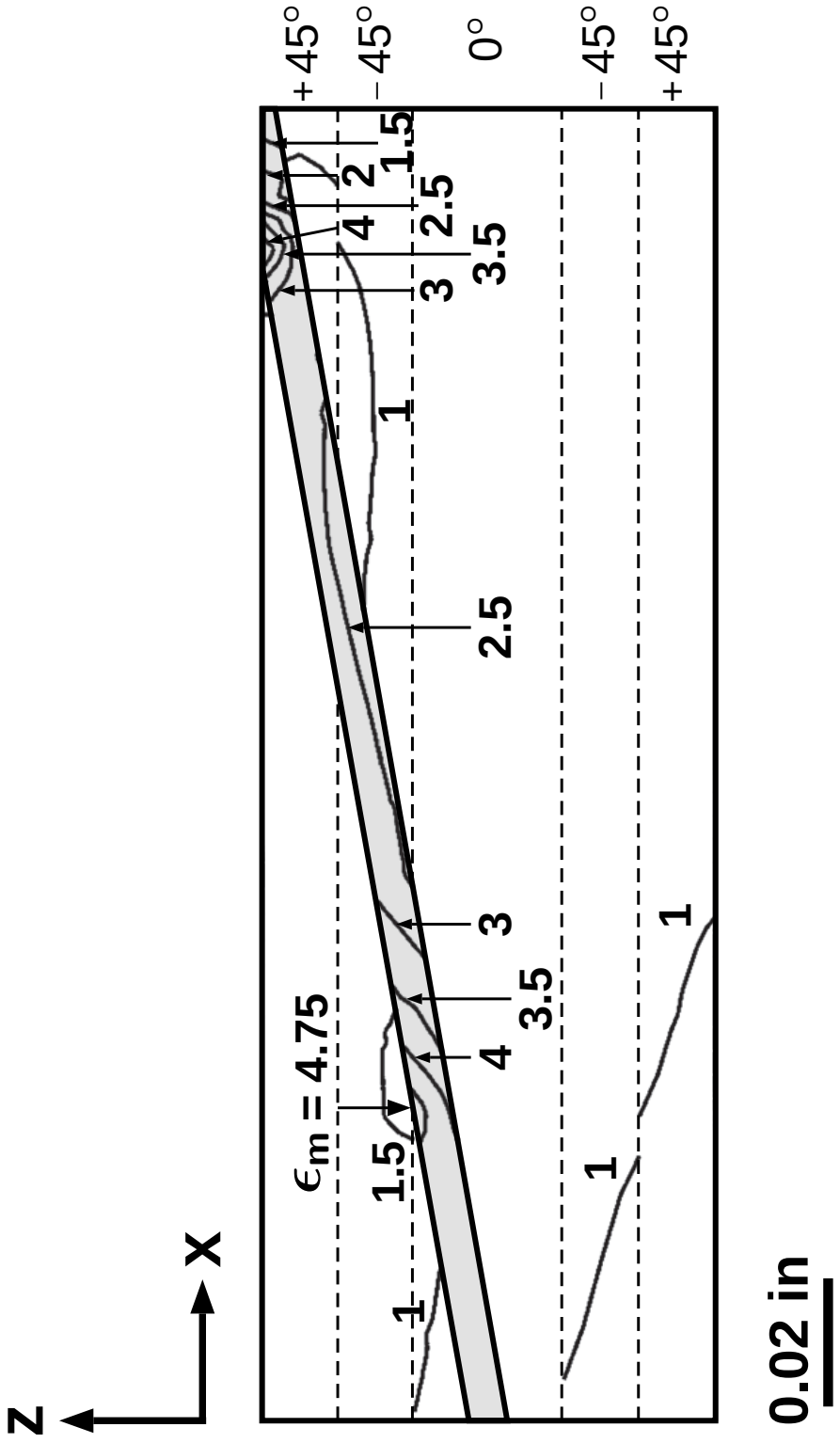

Figure B.25 Normalized isostrain contour field plot of ϵ_{11} for the two-dimensional composite scarf joint with equal scarf angles of 10°, adhesive thickness of 0.006 in, and laminate configuration of $[\pm 45_2/0_2]_S$.

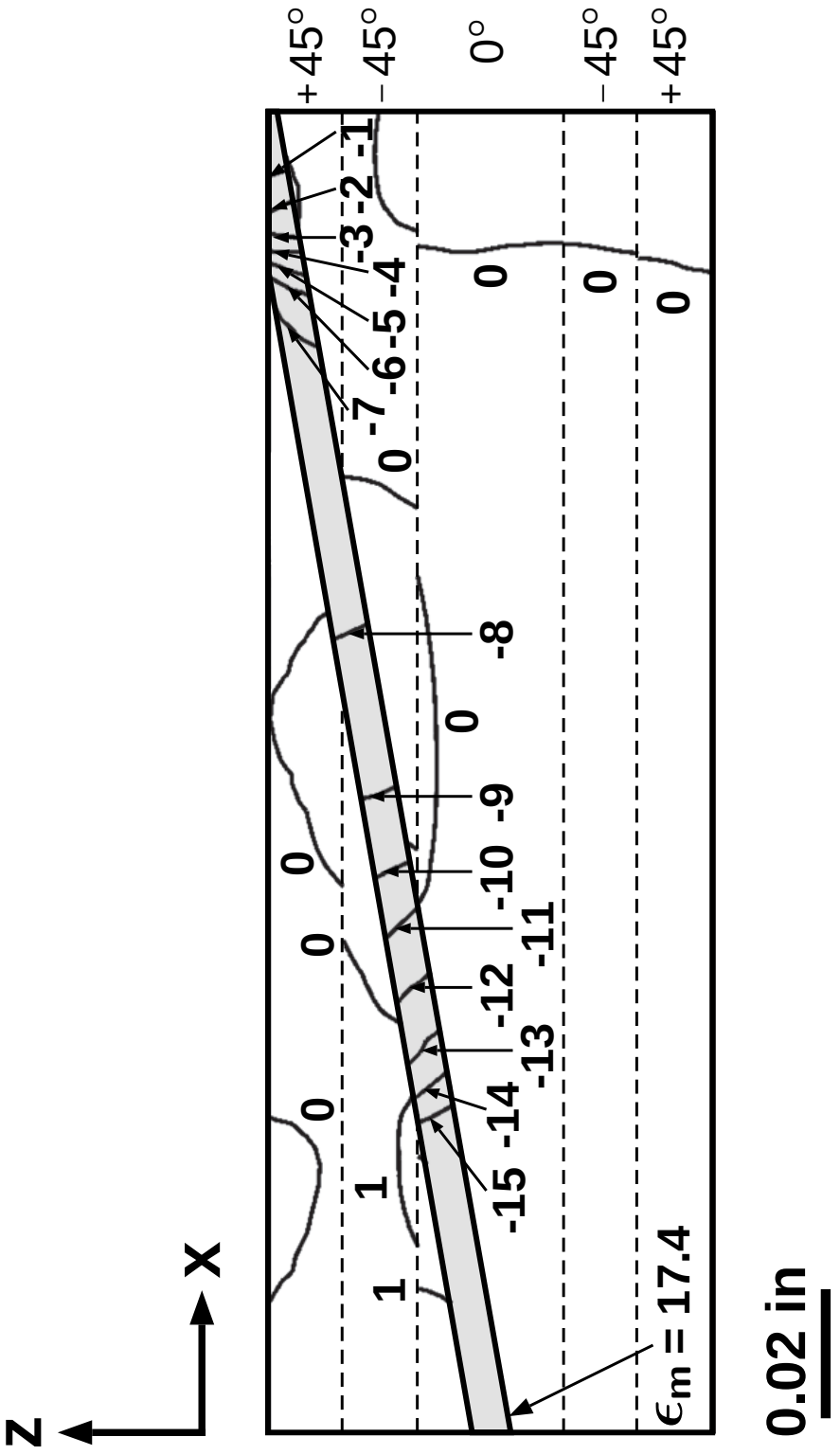

Figure B.26 Normalized isostrain contour field plot of ϵ_{13} for the two-dimensional composite scarf joint with equal scarf angles of 10°, adhesive thickness of 0.006 in, and laminate configuration of $[\pm 45_2/0_2]_S$.

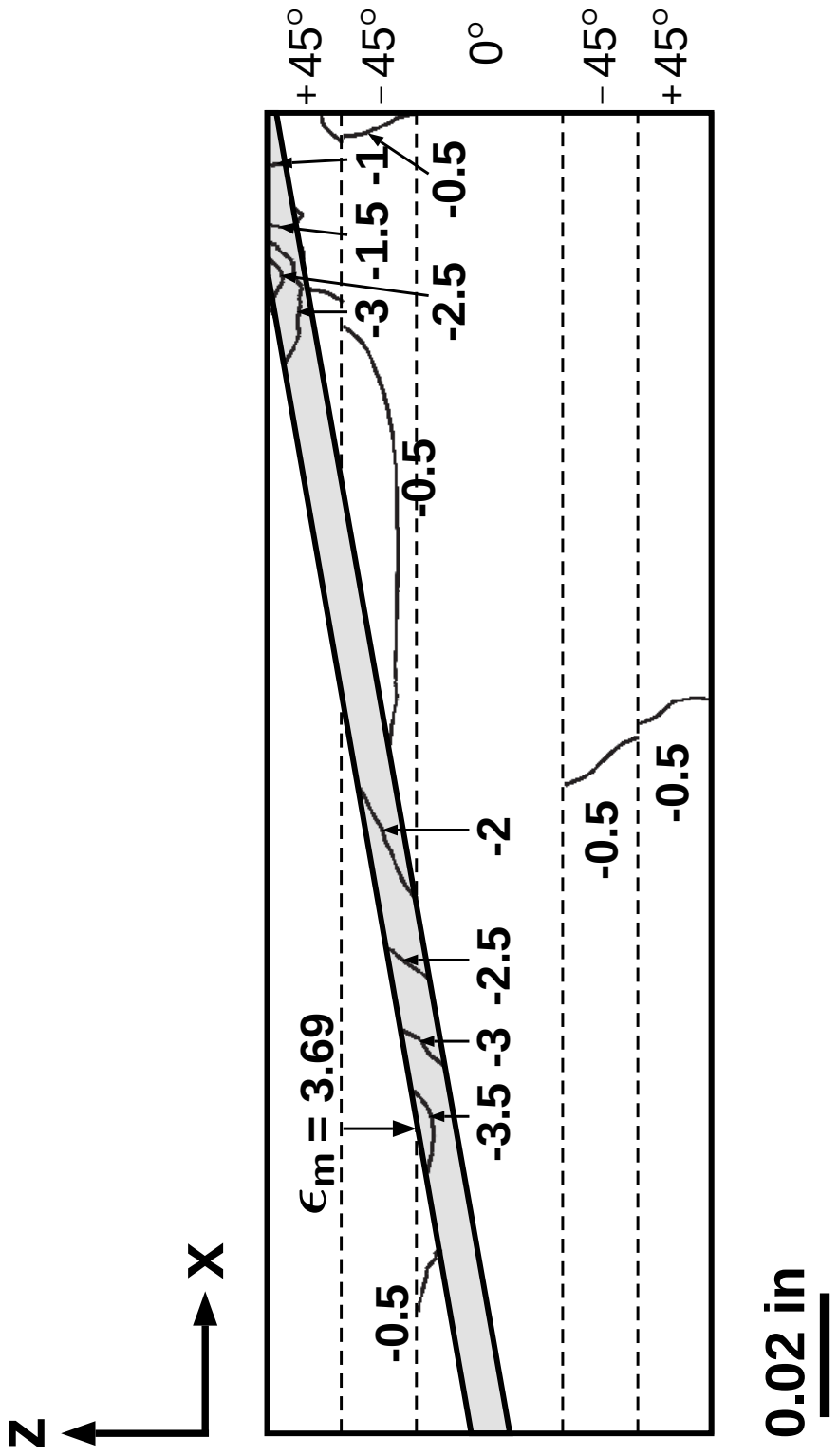

Figure B.27 Normalized isostrain contour field plot of ϵ_{33} for the two-dimensional composite scarf joint with equal scarf angles of 10°, adhesive thickness of 0.006 in, and laminate configuration of $[\pm 45_2/0_2]_S$.

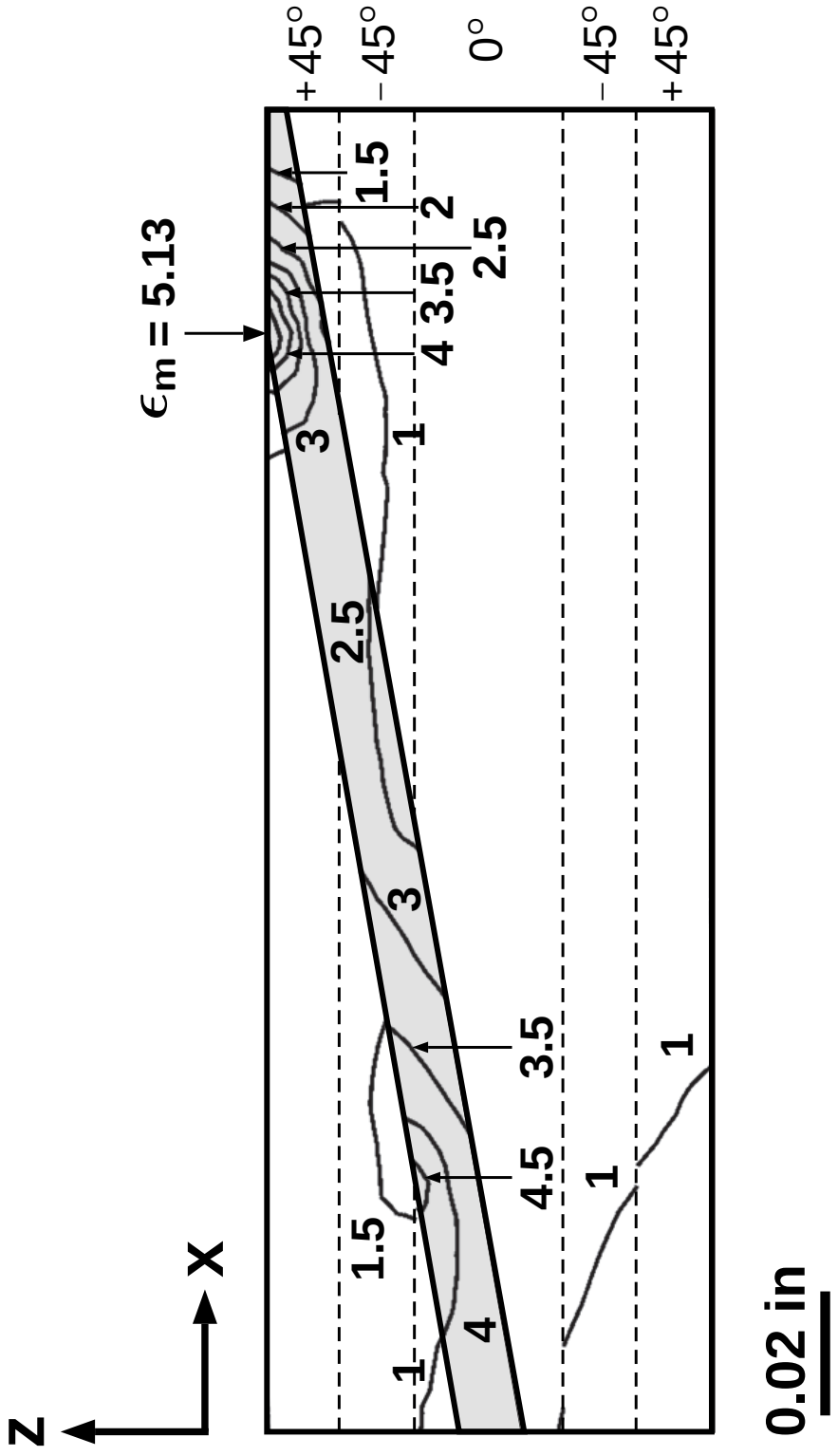

Figure B.28 Normalized isostrain contour field plot of ϵ_{11} for the two-dimensional composite scarf joint with equal scarf angles of 10°, adhesive thickness of 0.010 in, and laminate configuration of $[\pm 45_2/0_2]_S$.

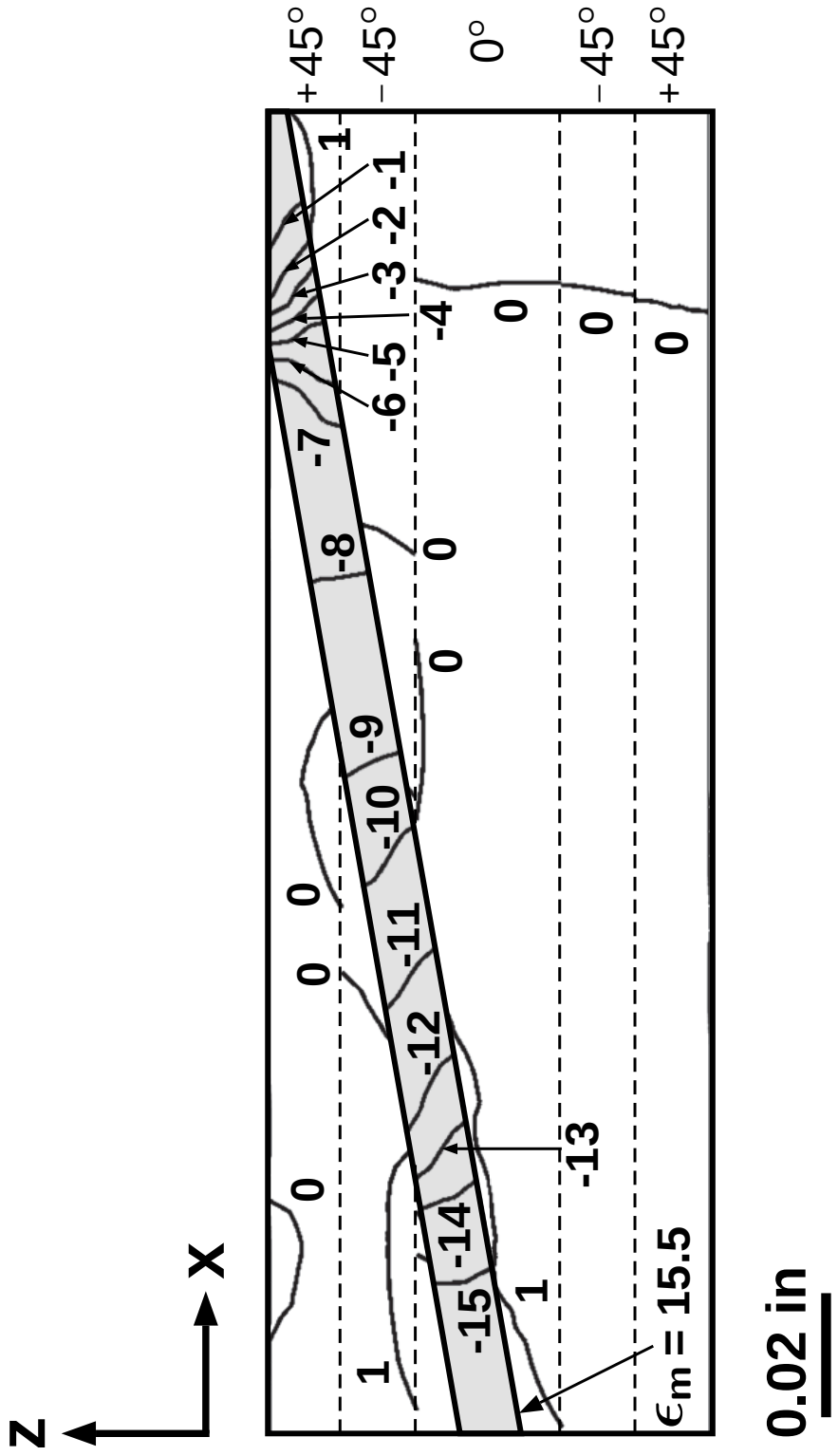

Figure B.29 Normalized isostrain contour field plot of ϵ_{13} for the two-dimensional composite scarf joint with equal scarf angles of 10°, adhesive thickness of 0.010 in, and laminate configuration of $[\pm 45_2/0_2]_S$.

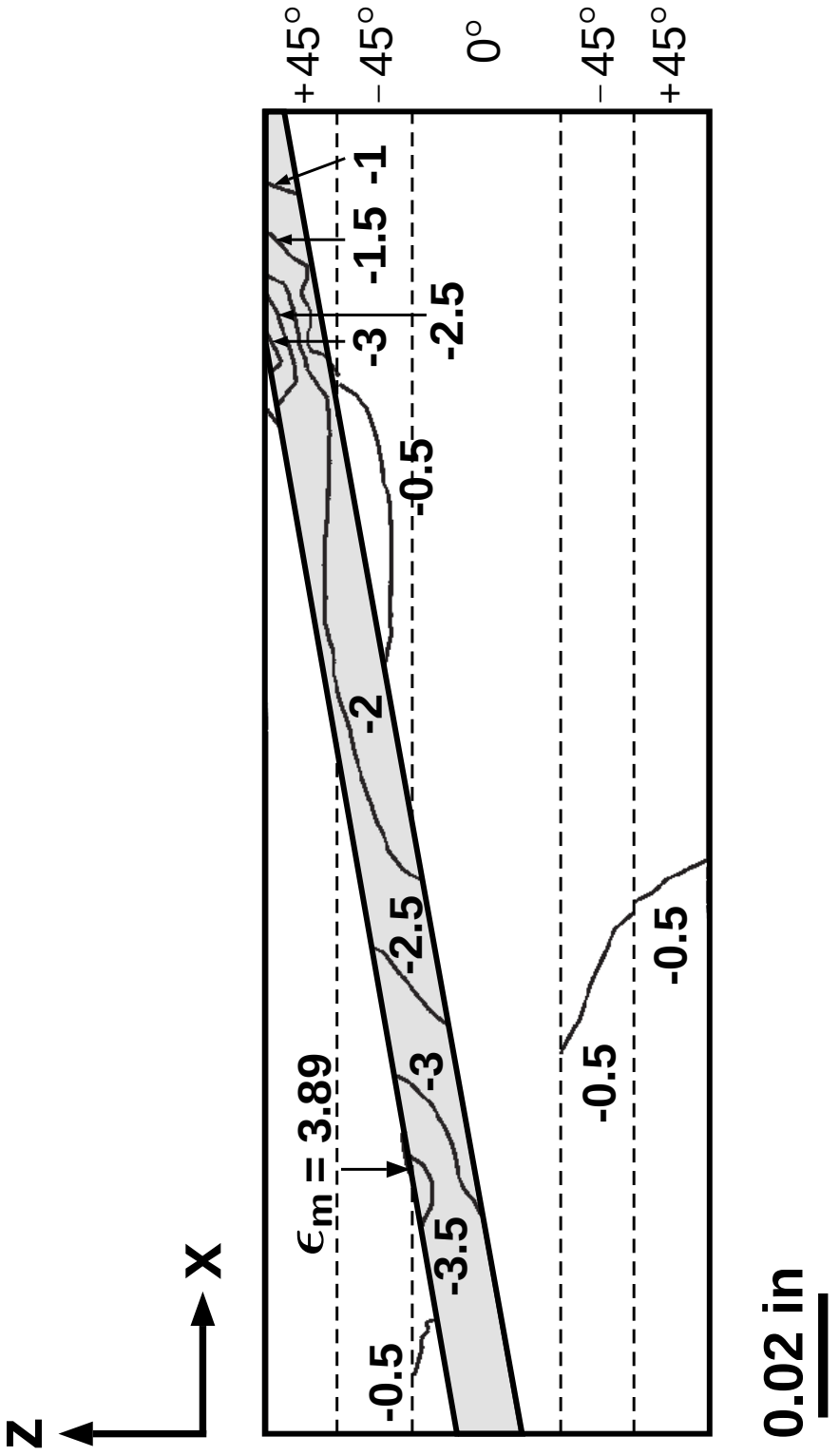

Figure B.30 Normalized isostrain contour field plot of ϵ_{33} for the two-dimensional composite scarf joint with equal scarf angles of 10°, adhesive thickness of 0.010 in, and laminate configuration of $[\pm 45_2/0_2]_S$.

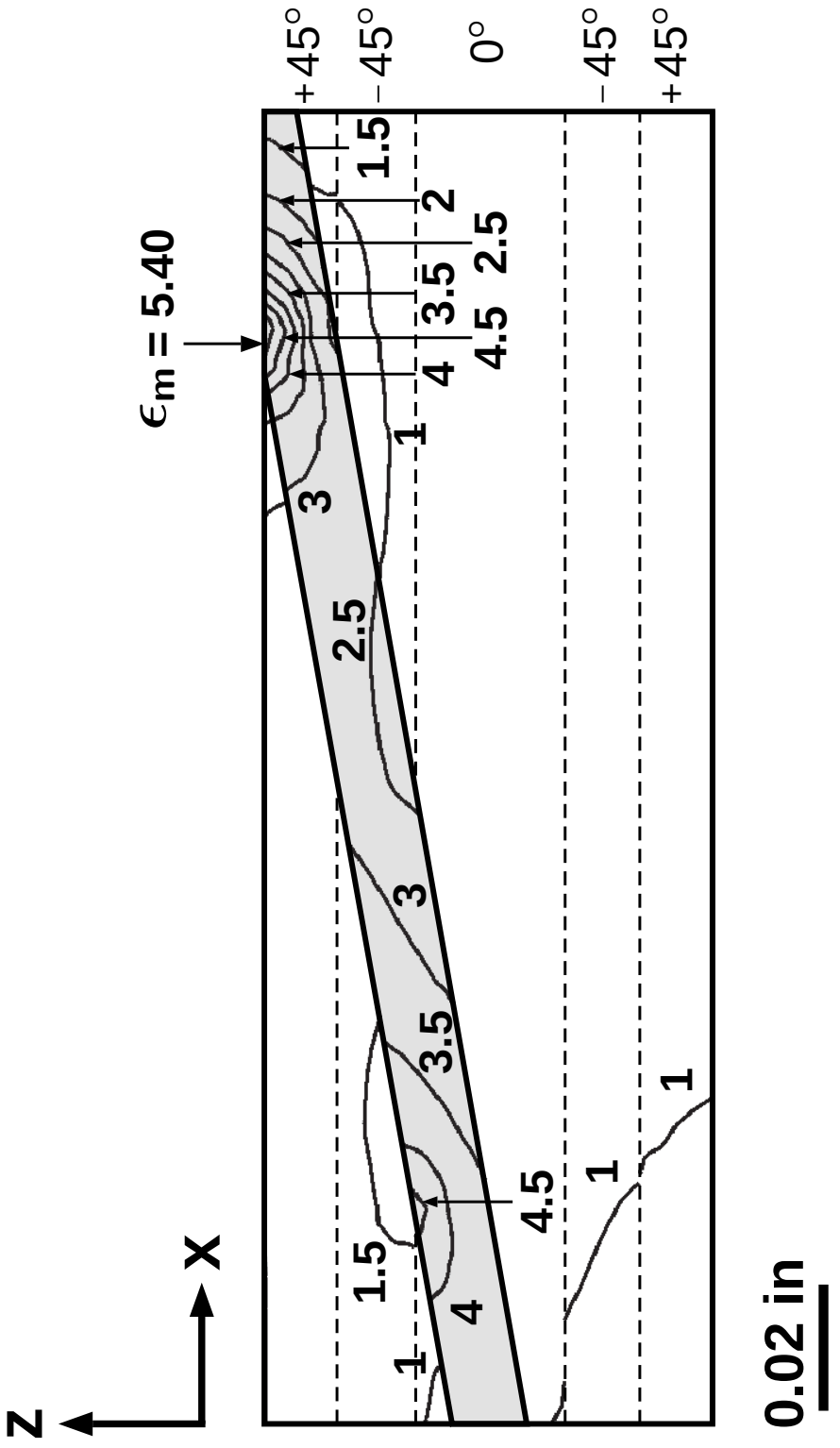

Figure B.31 Normalized isostrain contour field plot of ϵ_{11} for the two-dimensional composite scarf joint with equal scarf angles of 10°, adhesive thickness of 0.012 in, and laminate configuration of $[\pm 45_2/0_2]_S$.

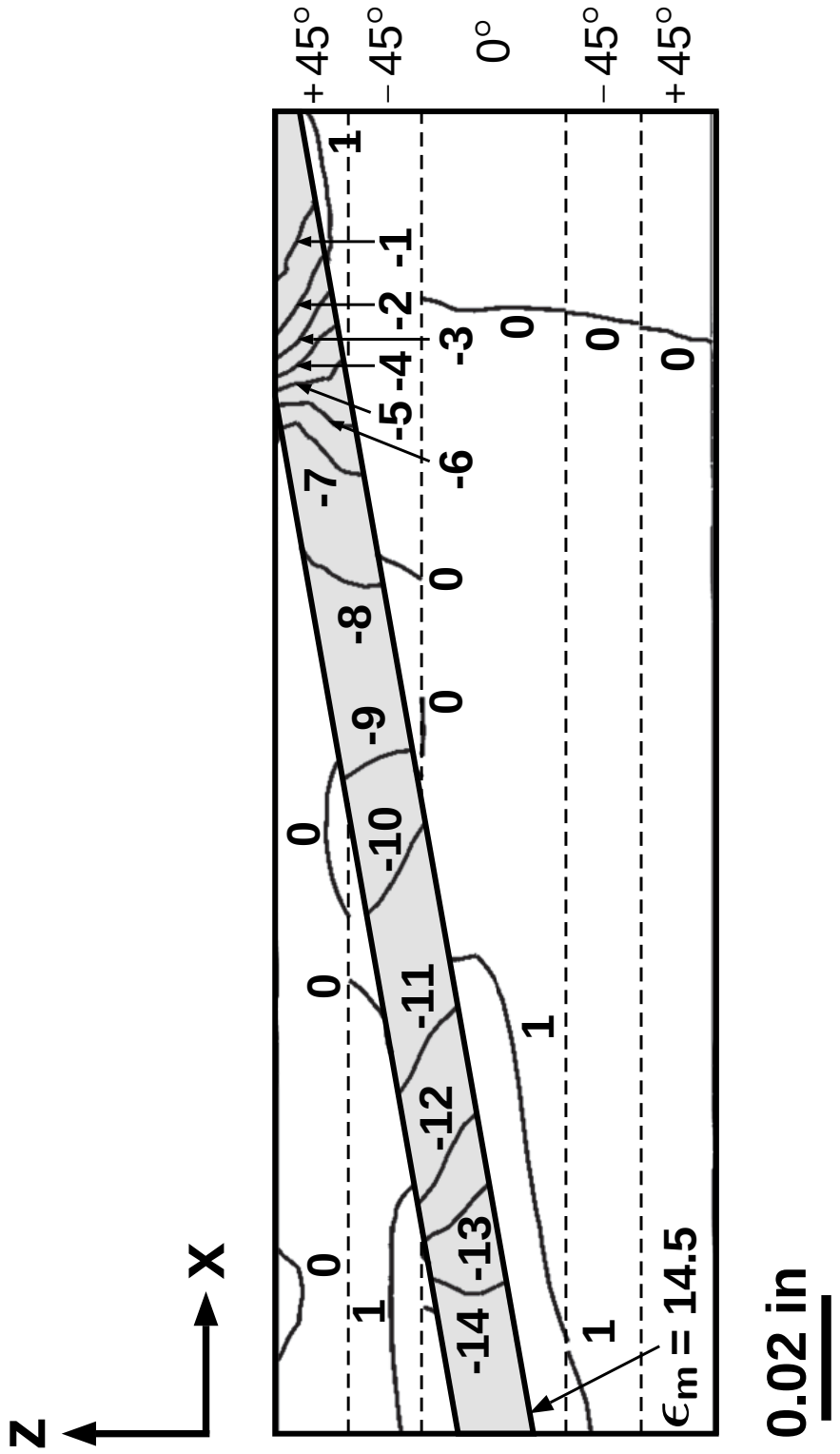

Figure B.32 Normalized isostrain contour field plot of ϵ_{13} for the two-dimensional composite scarf joint with equal scarf angles of 10°, adhesive thickness of 0.012 in, and laminate configuration of $[\pm 45_2/0_2]_S$.

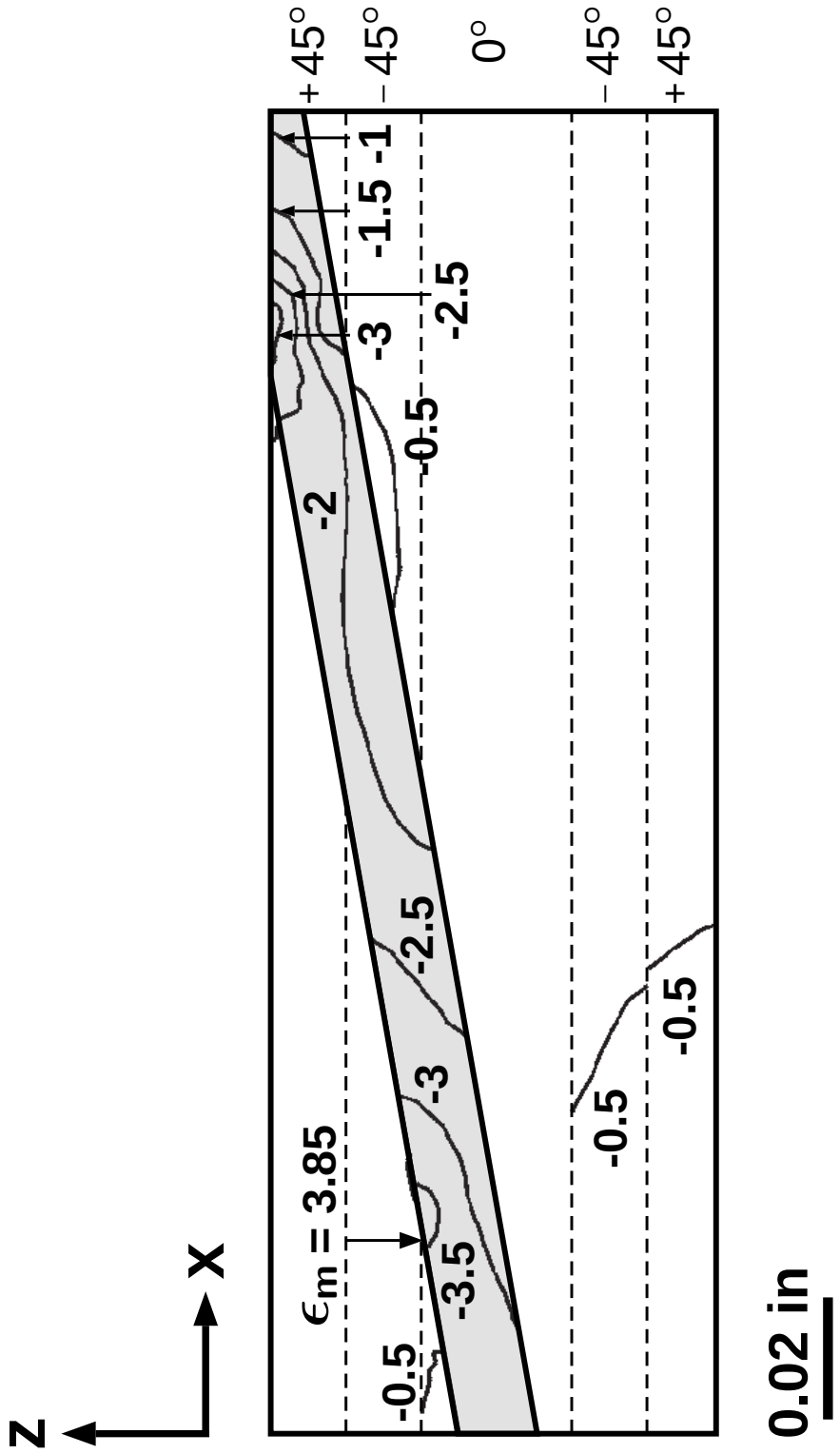

Figure B.33 Normalized isostrain contour field plot of ϵ_{33} for the two-dimensional composite scarf joint with equal scarf angles of 10°, adhesive thickness of 0.012 in, and laminate configuration of $[\pm 45_2/0_2]_S$.

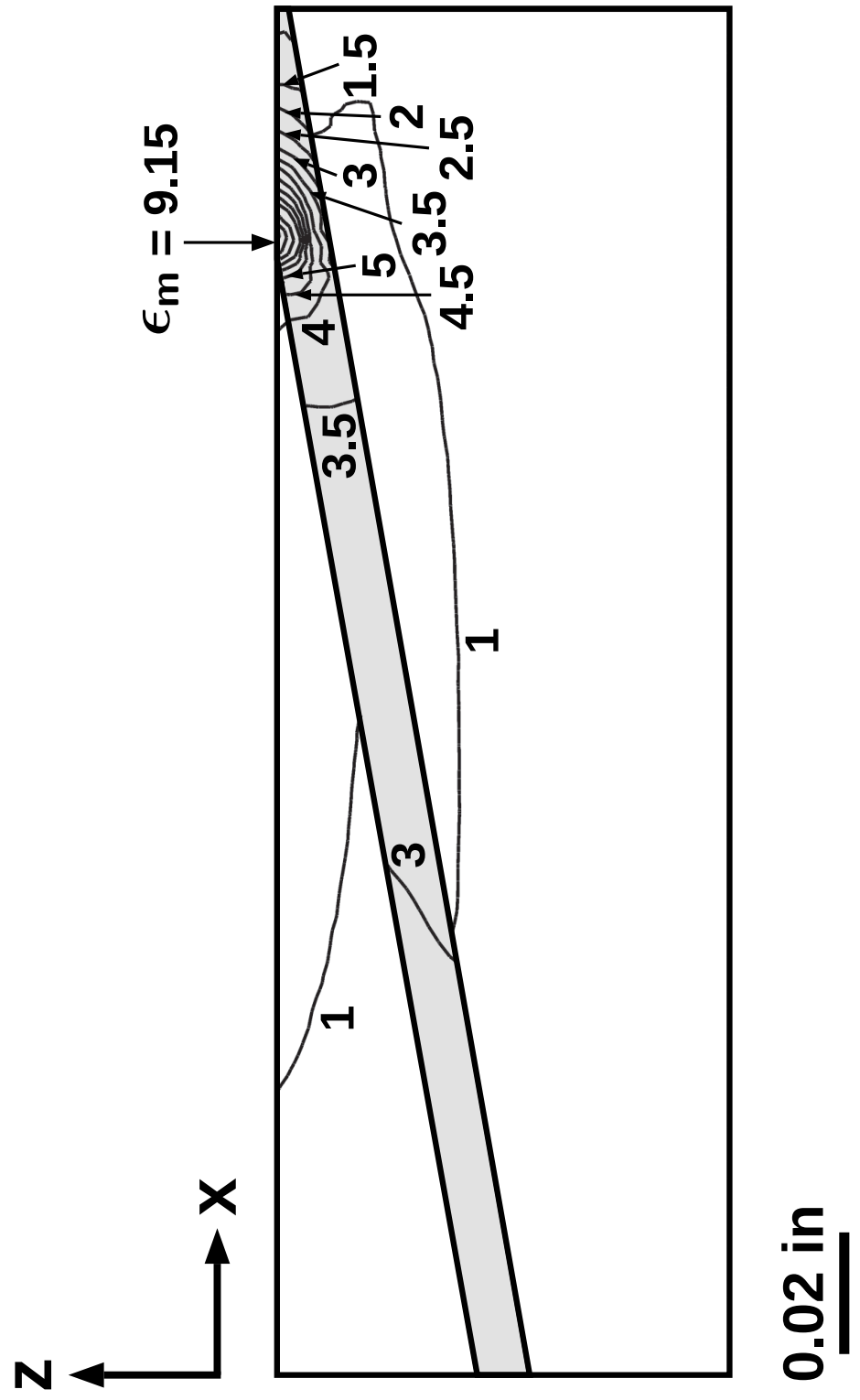

Figure B.34 Normalized isostrain contour field plot of ϵ_{11} for the two-dimensional composite scarf joint with equal scarf angles of 10°, adhesive thickness of 0.008 in, and laminate configuration of *homogenized* $[\pm 45_2/0_2]_S$.

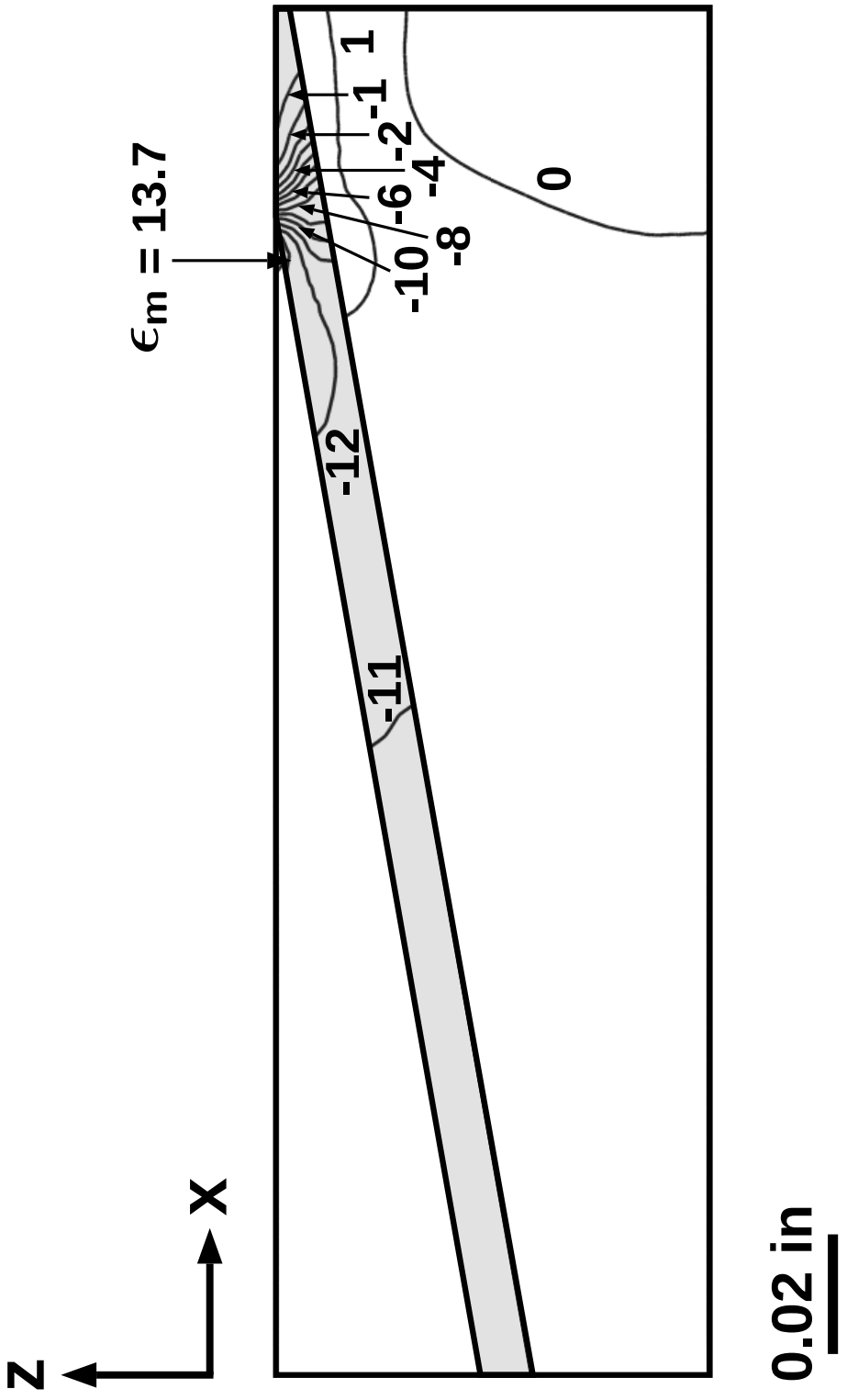

Figure B.35 Normalized isostrain contour field plot of ϵ_{13} for the two-dimensional composite scarf joint with equal scarf angles of 10°, adhesive thickness of 0.008 in, and laminate configuration of *homogenized* $[\pm 45_2/0_2]_S$.

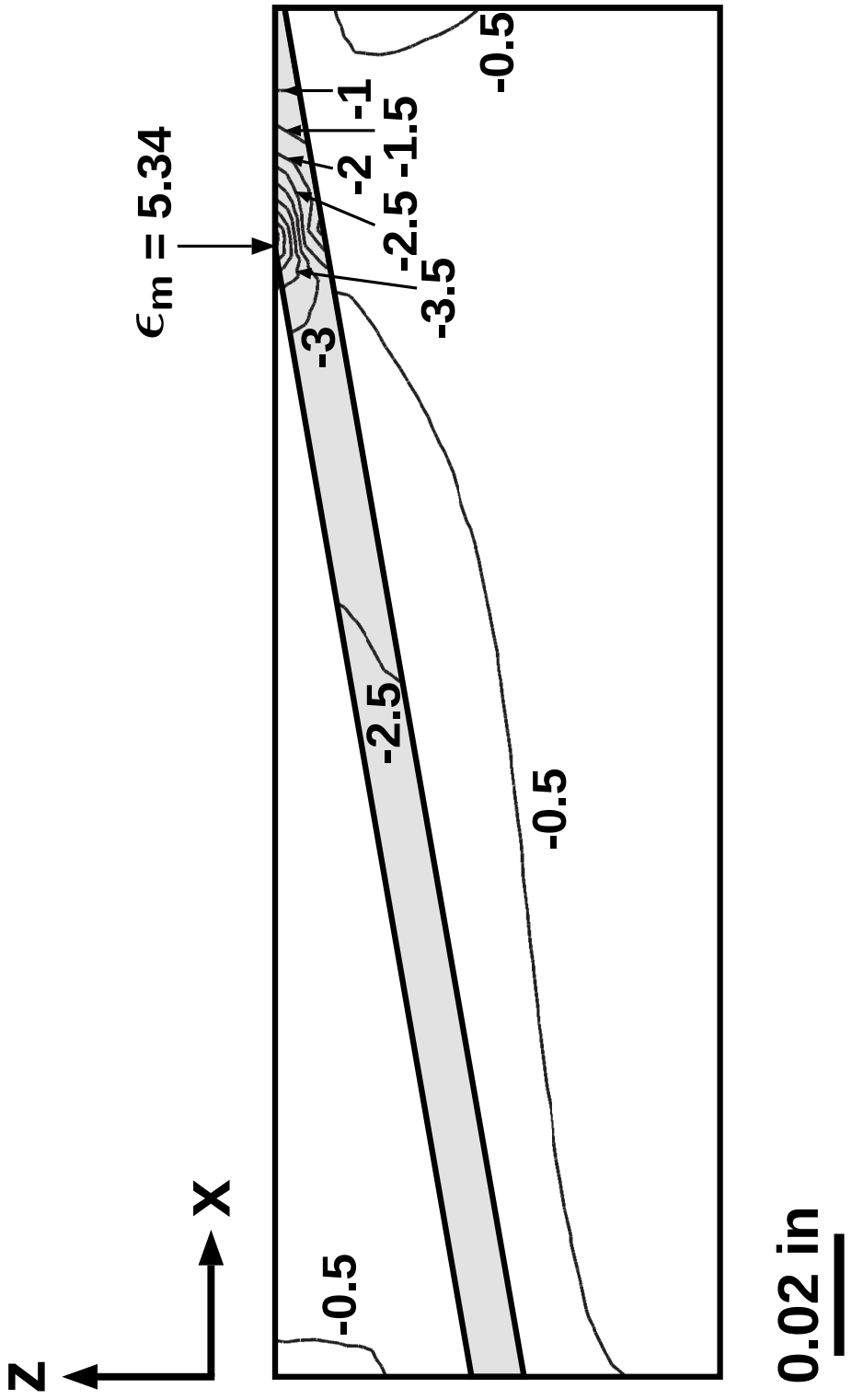

Figure B.36 Normalized isostrain contour field plot of ϵ_{33} for the two-dimensional composite scarf joint with equal scarf angles of 10°, adhesive thickness of 0.008 in, and laminate configuration of *homogenized* $[\pm 45_2/0_2]_S$.

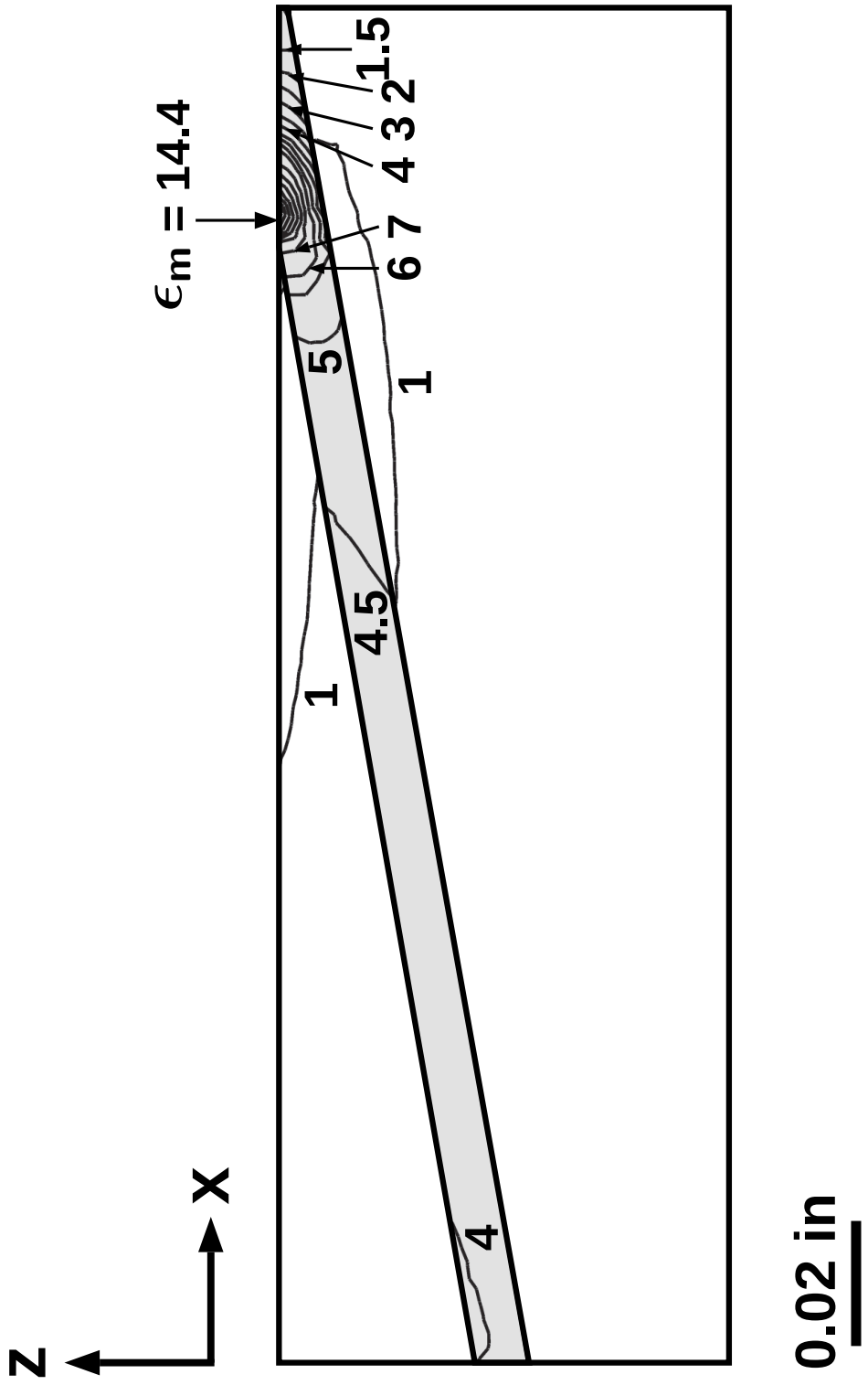

Figure B.37 Normalized isostrain contour field plot of ϵ_{11} for the two-dimensional composite scarf joint with equal scarf angles of 10°, adhesive thickness of 0.008 in, and laminate configuration of *homogenized* $[\pm 15_2/0_2]_S$.

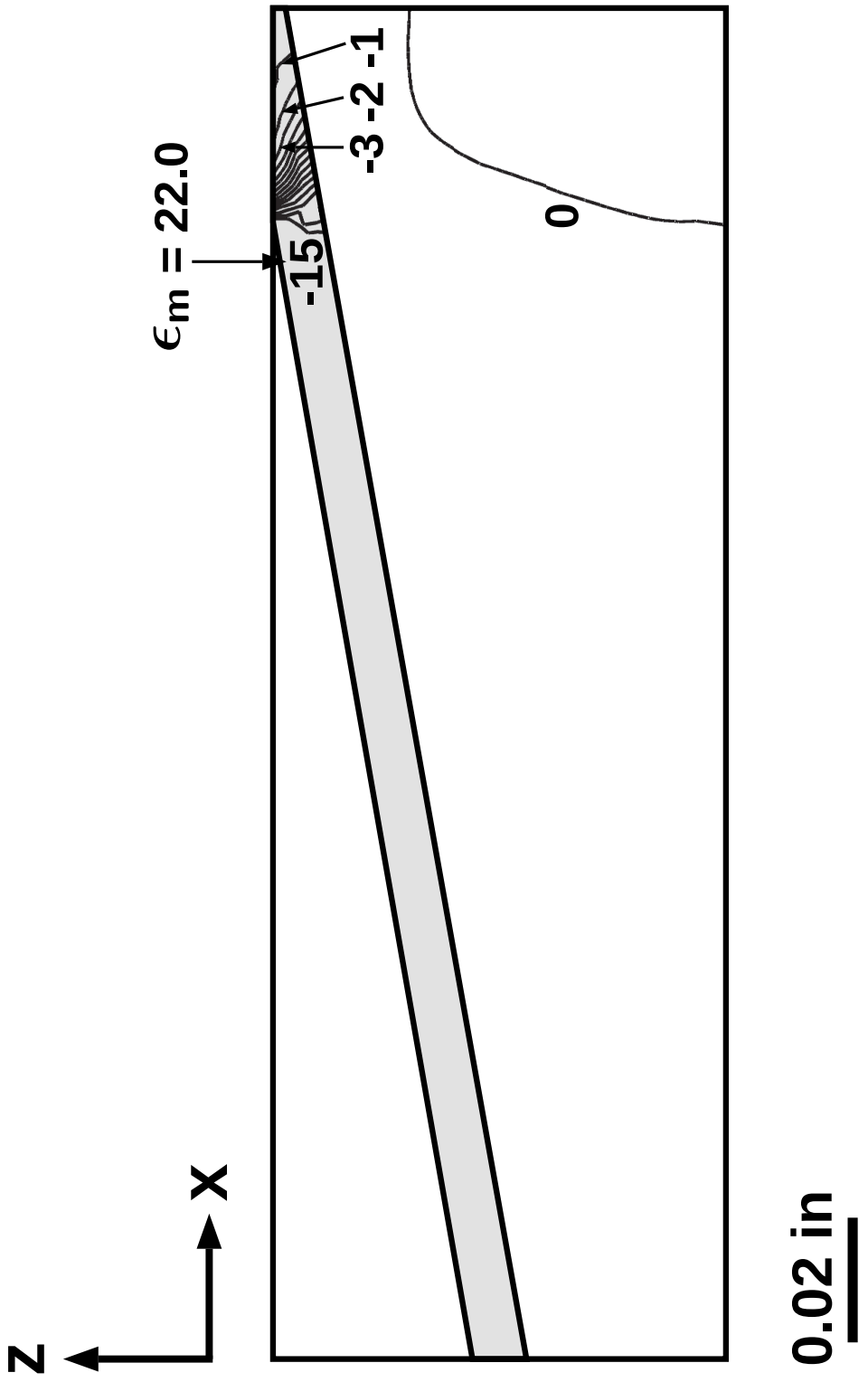

Figure B.38 Normalized isostrain contour field plot of ϵ_{13} for the two-dimensional composite scarf joint with equal scarf angles of 10°, adhesive thickness of 0.008 in, and laminate configuration of *homogenized* $[\pm 15_2/0_2]_S$.

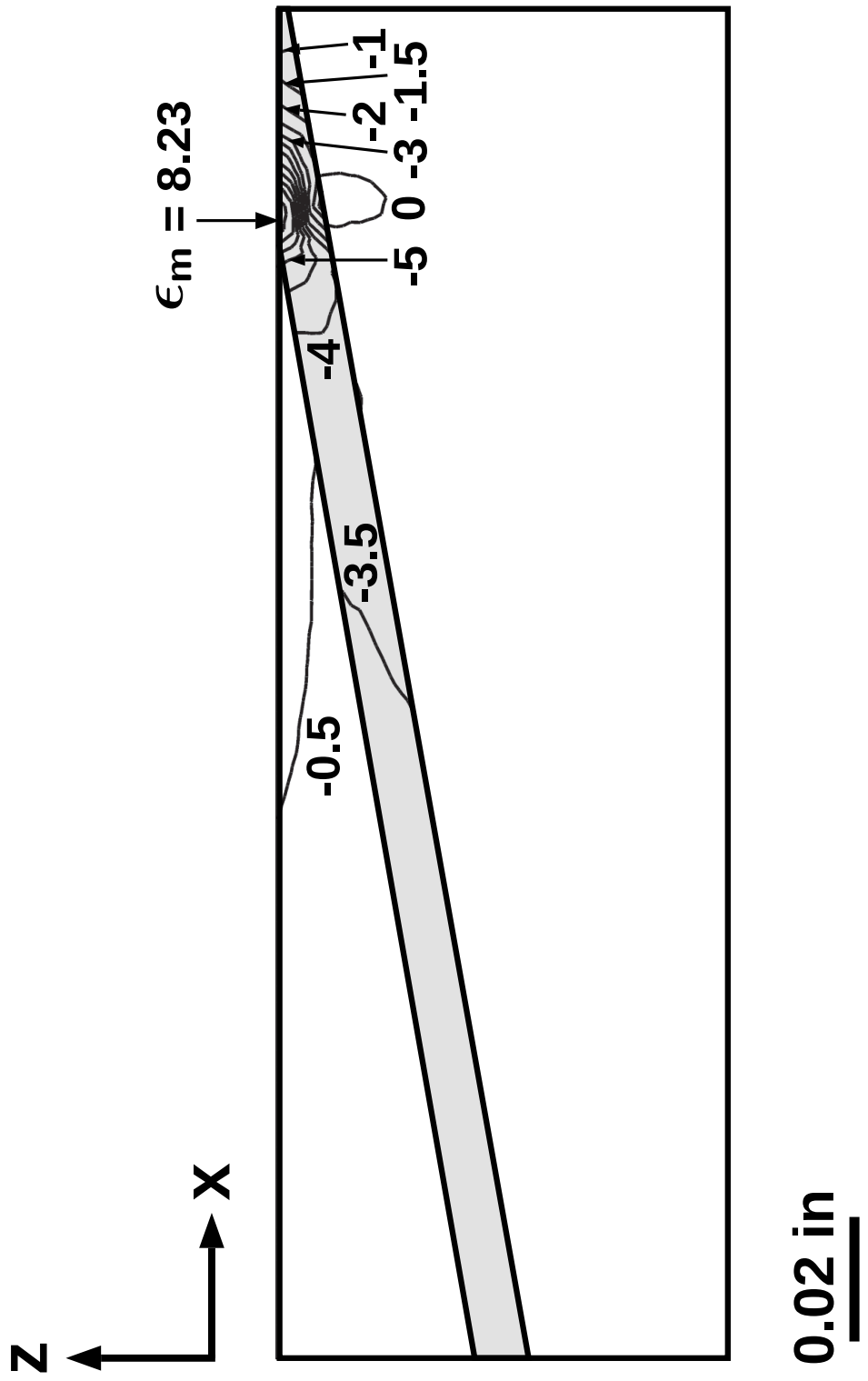

Figure B.39 Normalized isostrain contour field plot of ϵ_{33} for the two-dimensional composite scarf joint with equal scarf angles of 10°, adhesive thickness of 0.008 in, and laminate configuration of *homogenized* $[\pm 15_2/0_2]_S$.

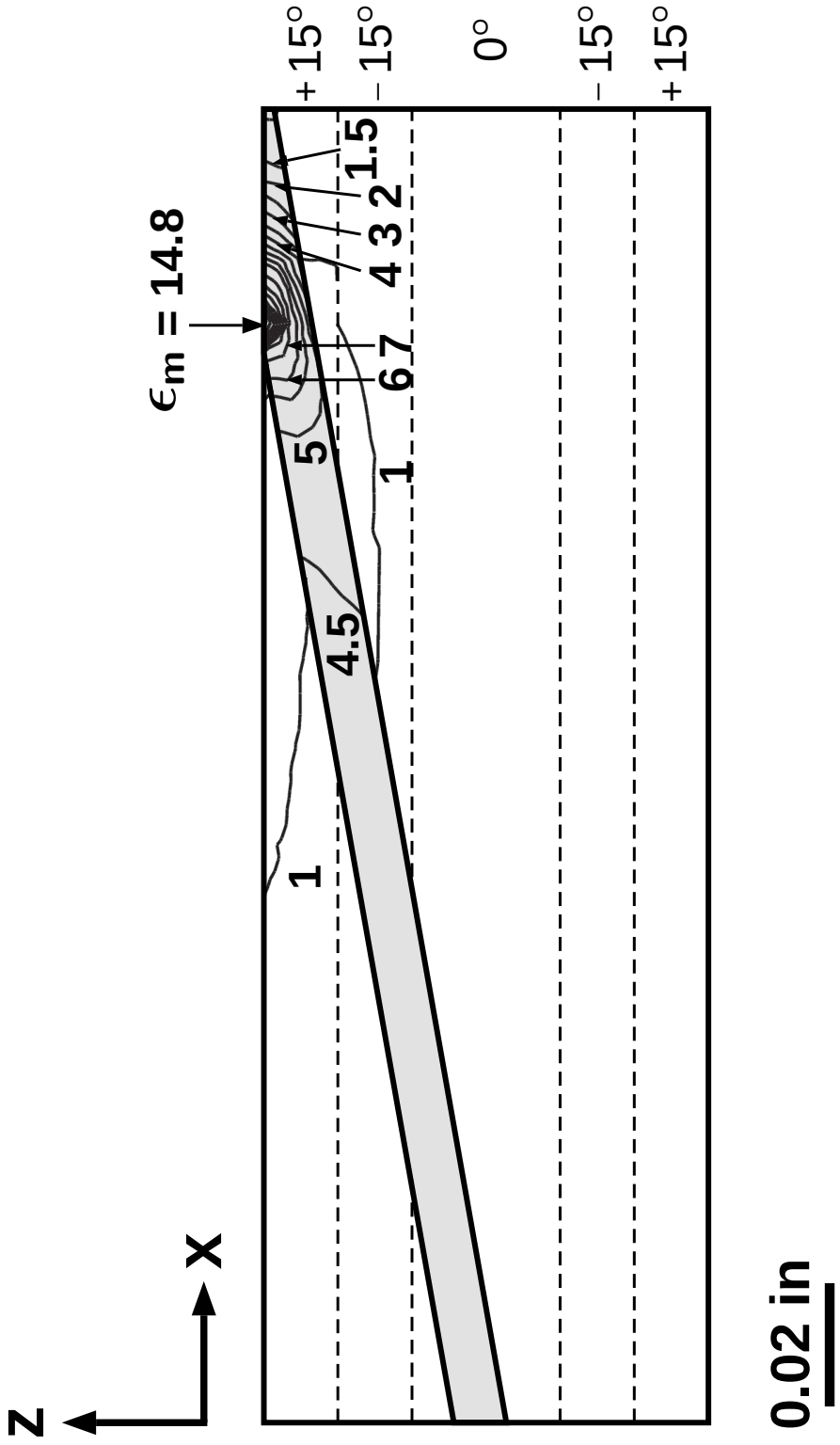

Figure B.40 Normalized isostrain contour field plot of ϵ_{11} for the two-dimensional composite scarf joint with equal scarf angles of 10°, adhesive thickness of 0.008 in, and laminate configuration of $[\pm 15_2/0_2]_S$.

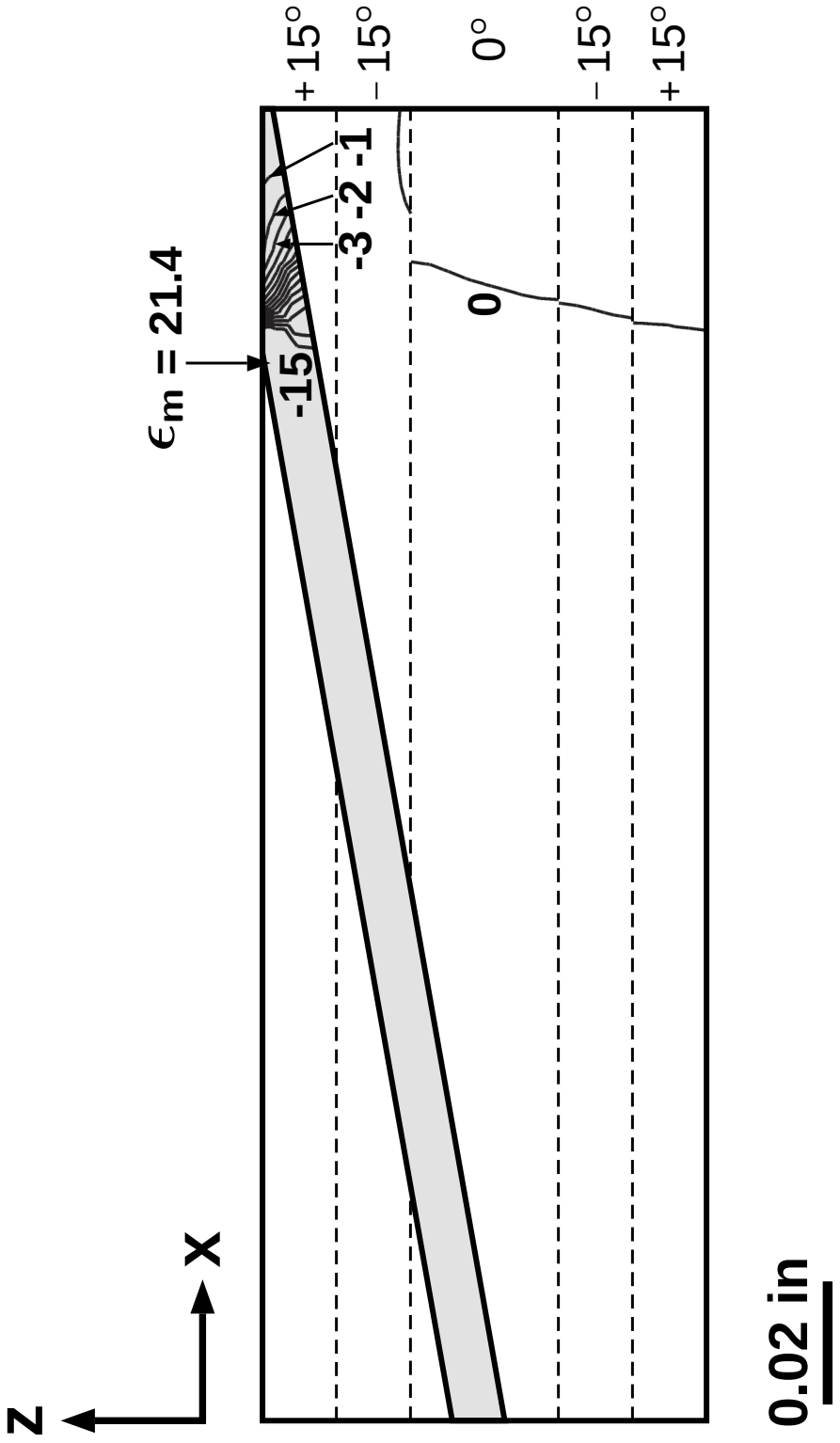

Figure B.41 Normalized isostrain contour field plot of ϵ_{13} for the two-dimensional composite scarf joint with equal scarf angles of 10°, adhesive thickness of 0.008 in, and laminate configuration of $[\pm 15_2/0_2]_S$.

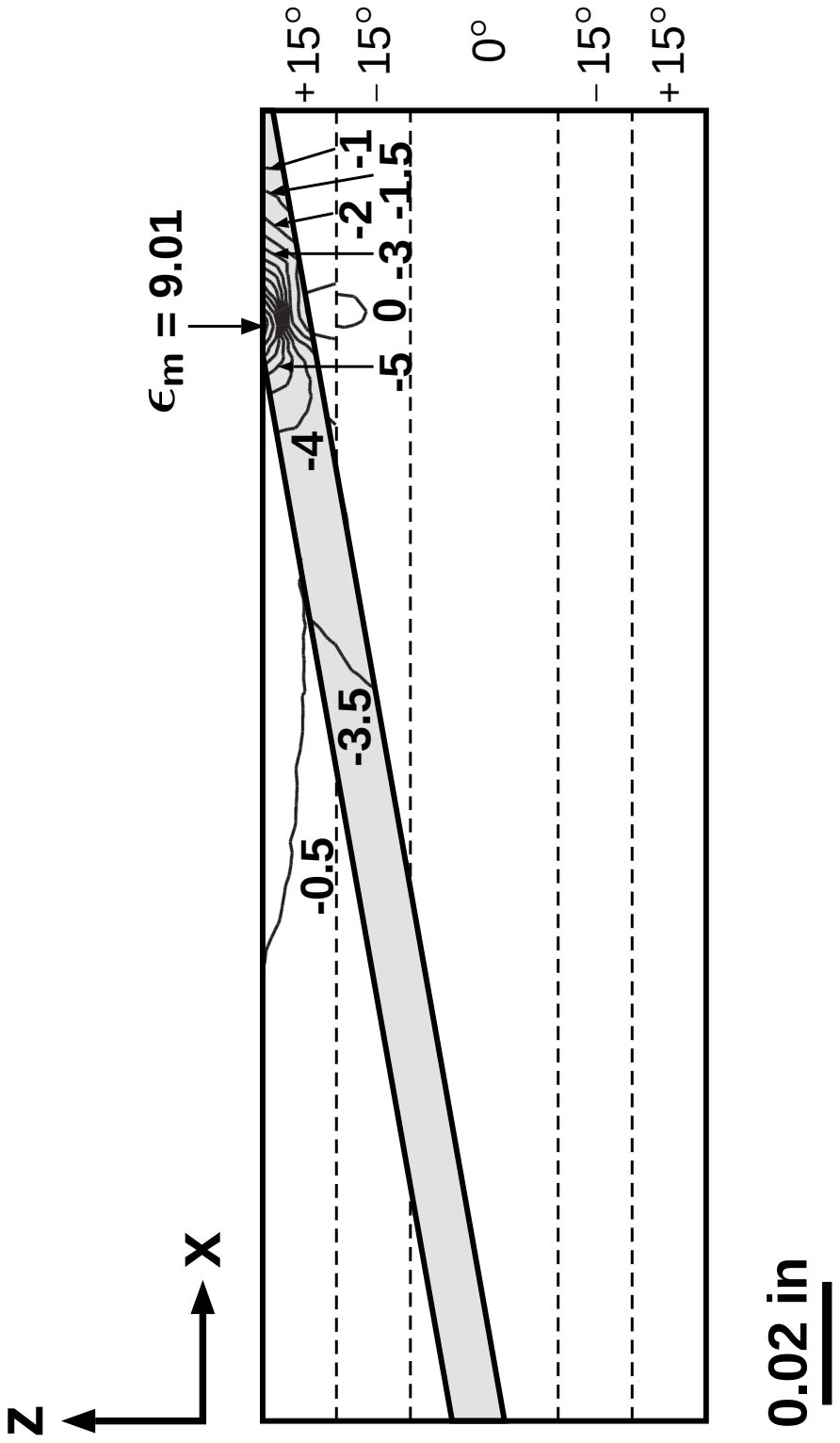

Figure B.42 Normalized isostrain contour field plot of ϵ_{33} for the two-dimensional composite scarf joint with equal scarf angles of 10°, adhesive thickness of 0.008 in, and laminate configuration of $[\pm 15_2/0_2]_S$.

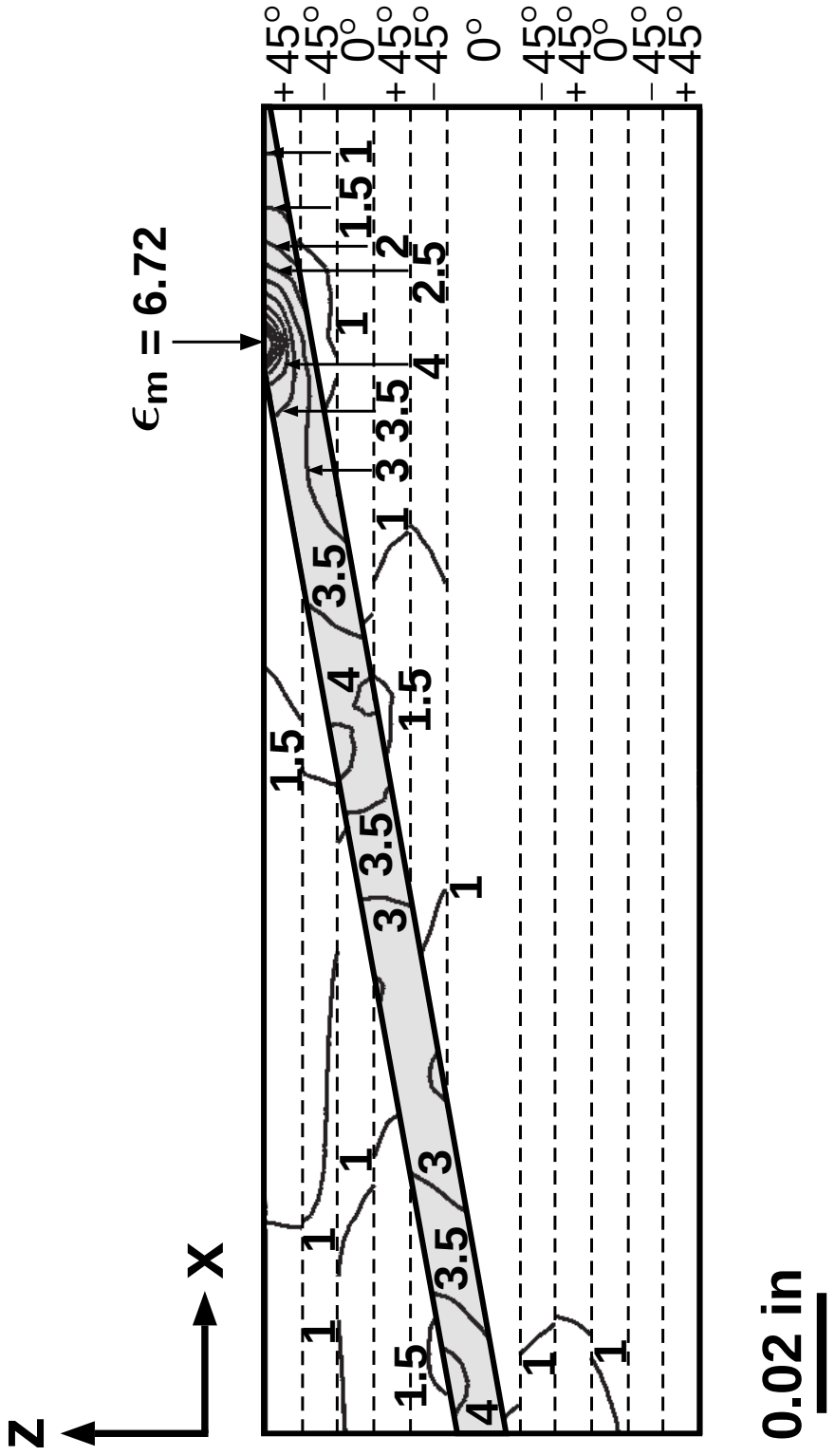

Figure B.43 Normalized isostrain contour field plot of ϵ_{11} for the two-dimensional composite scarf joint with equal scarf angles of 10°, adhesive thickness of 0.008 in, and laminate configuration of $[\pm 45/0]_{2S}$.

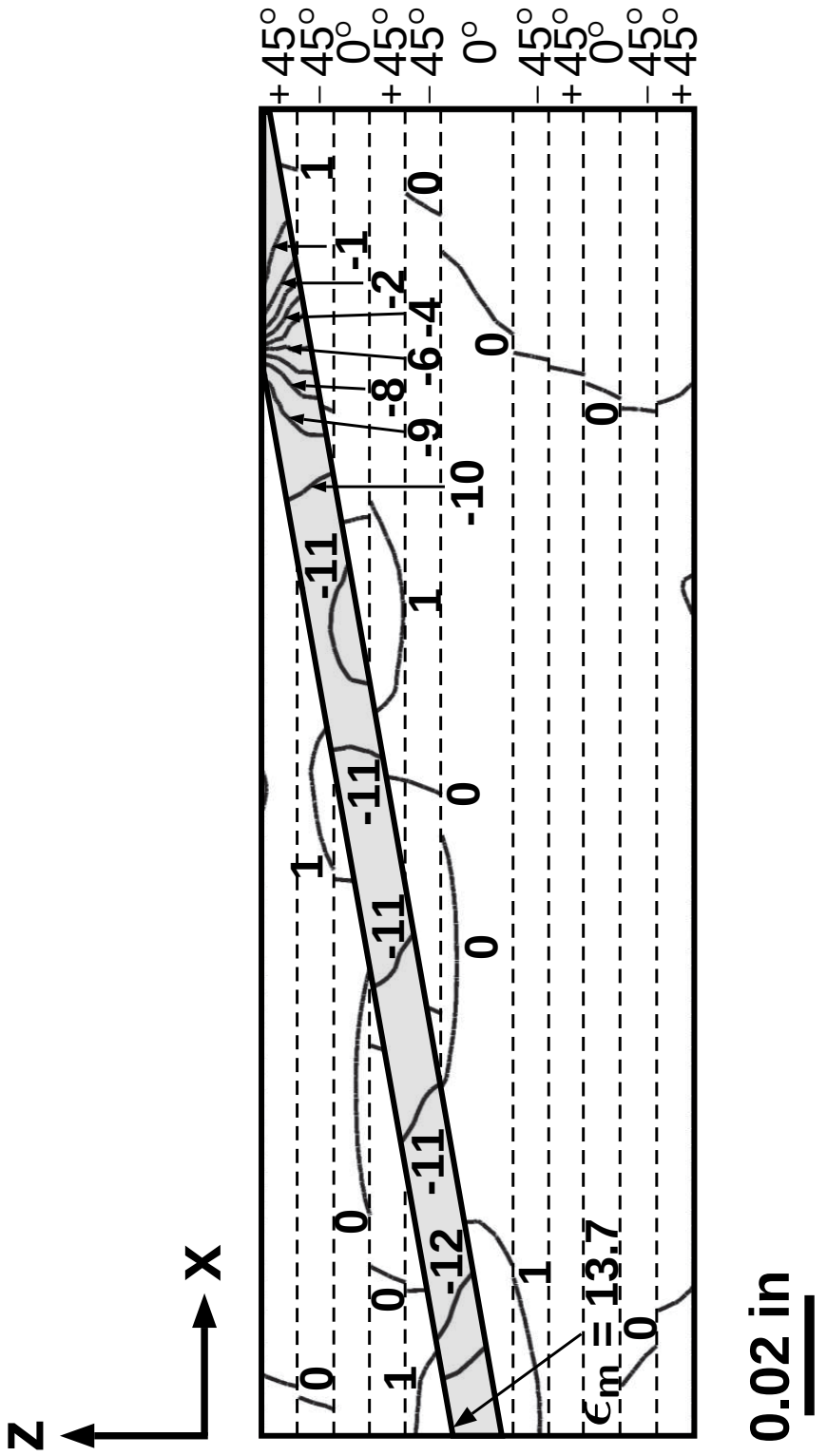

Figure B.44 Normalized isostrain contour field plot of ϵ_{13} for the two-dimensional composite scarf joint with equal scarf angles of 10°, adhesive thickness of 0.008 in, and laminate configuration of $[\pm 45/0]_{2S}$.

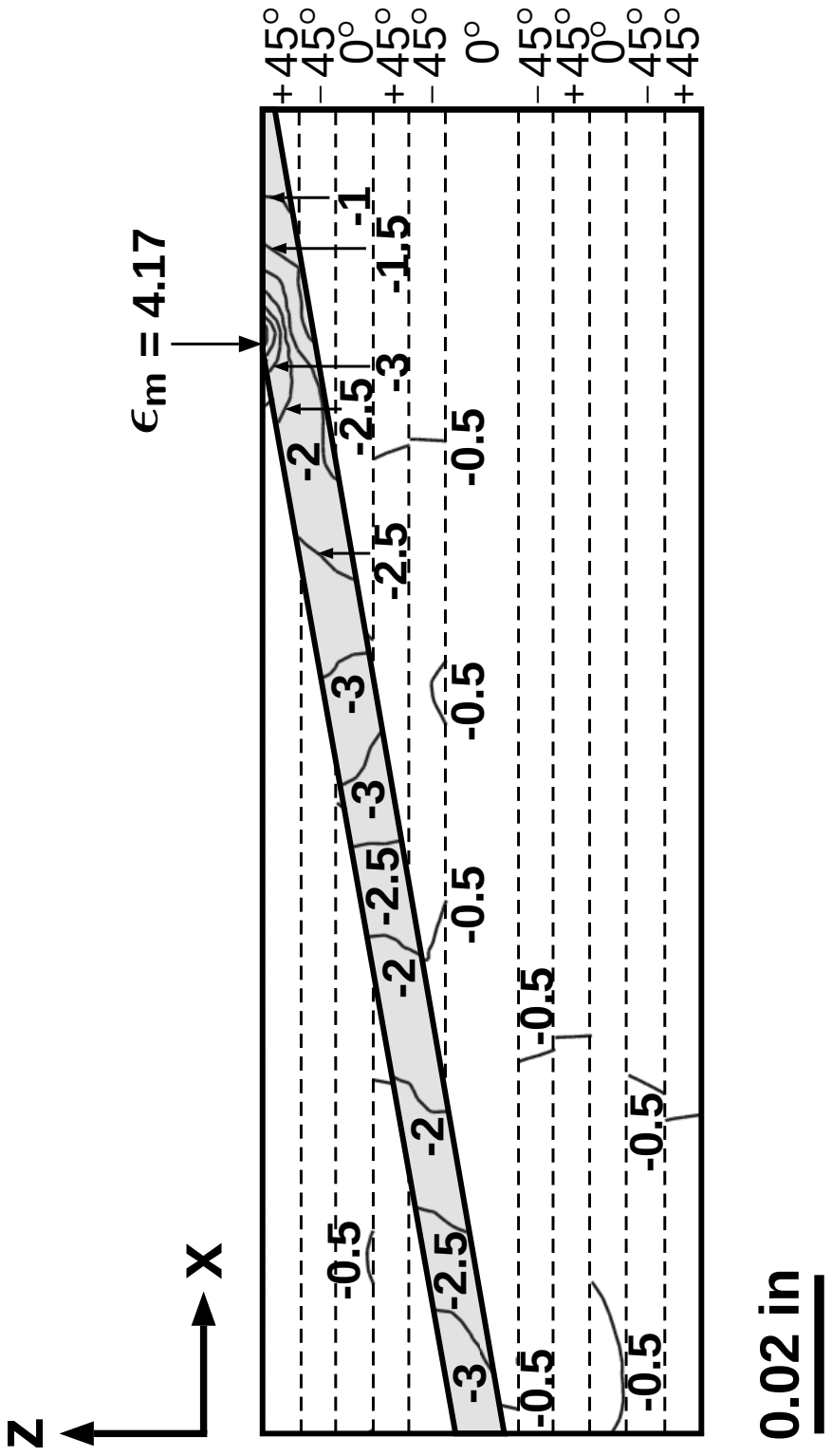

Figure B.45 Normalized isostrain contour field plot of ϵ_{33} for the two-dimensional composite scarf joint with equal scarf angles of 10°, adhesive thickness of 0.008 in, and laminate configuration of $[\pm 45/0]_{2S}$.

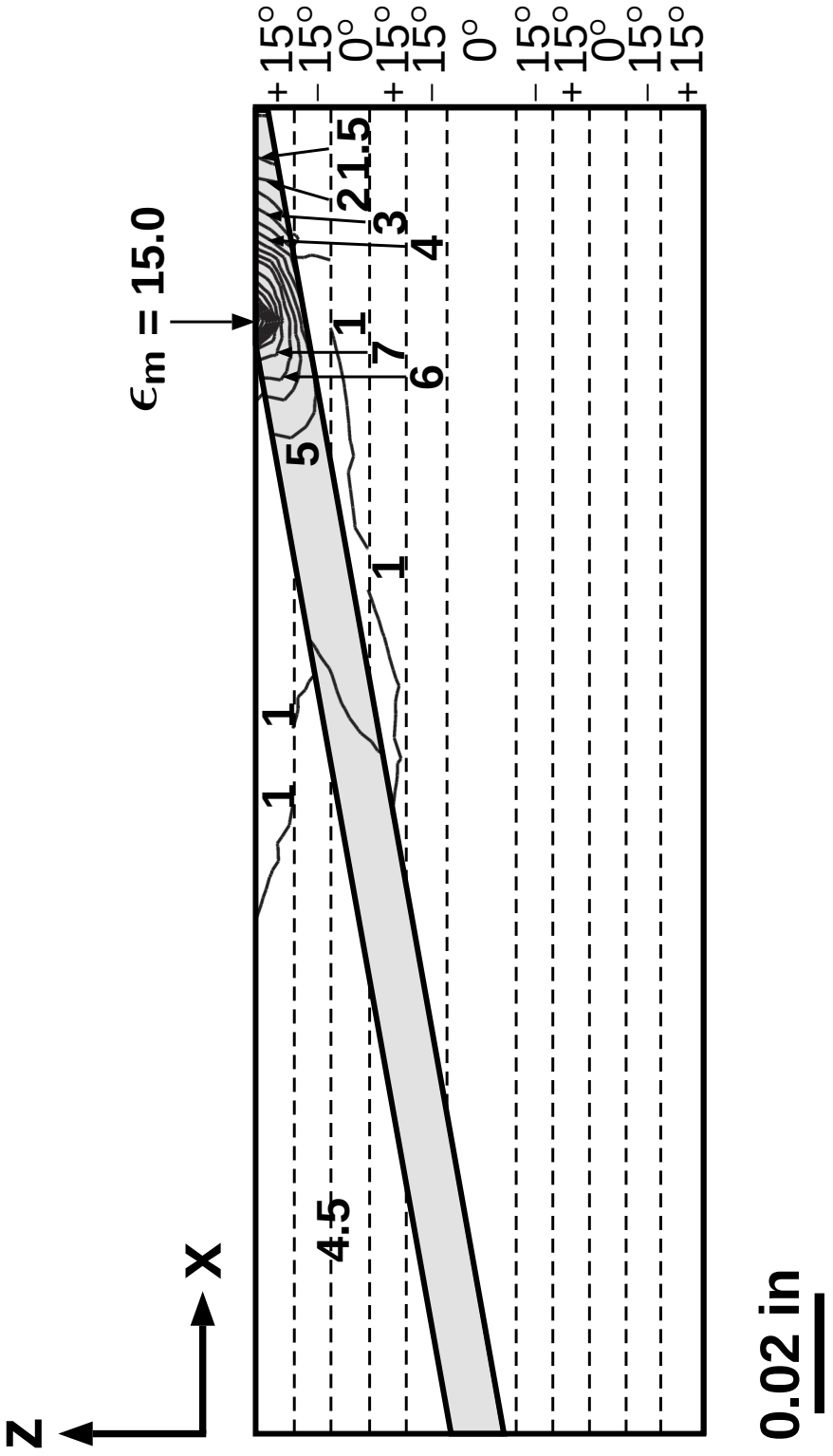

Figure B.46 Normalized isostrain contour field plot of ϵ_{11} for the two-dimensional composite scarf joint with equal scarf angles of 10°, adhesive thickness of 0.008 in, and laminate configuration of $[\pm 15/0]_{2S}$.

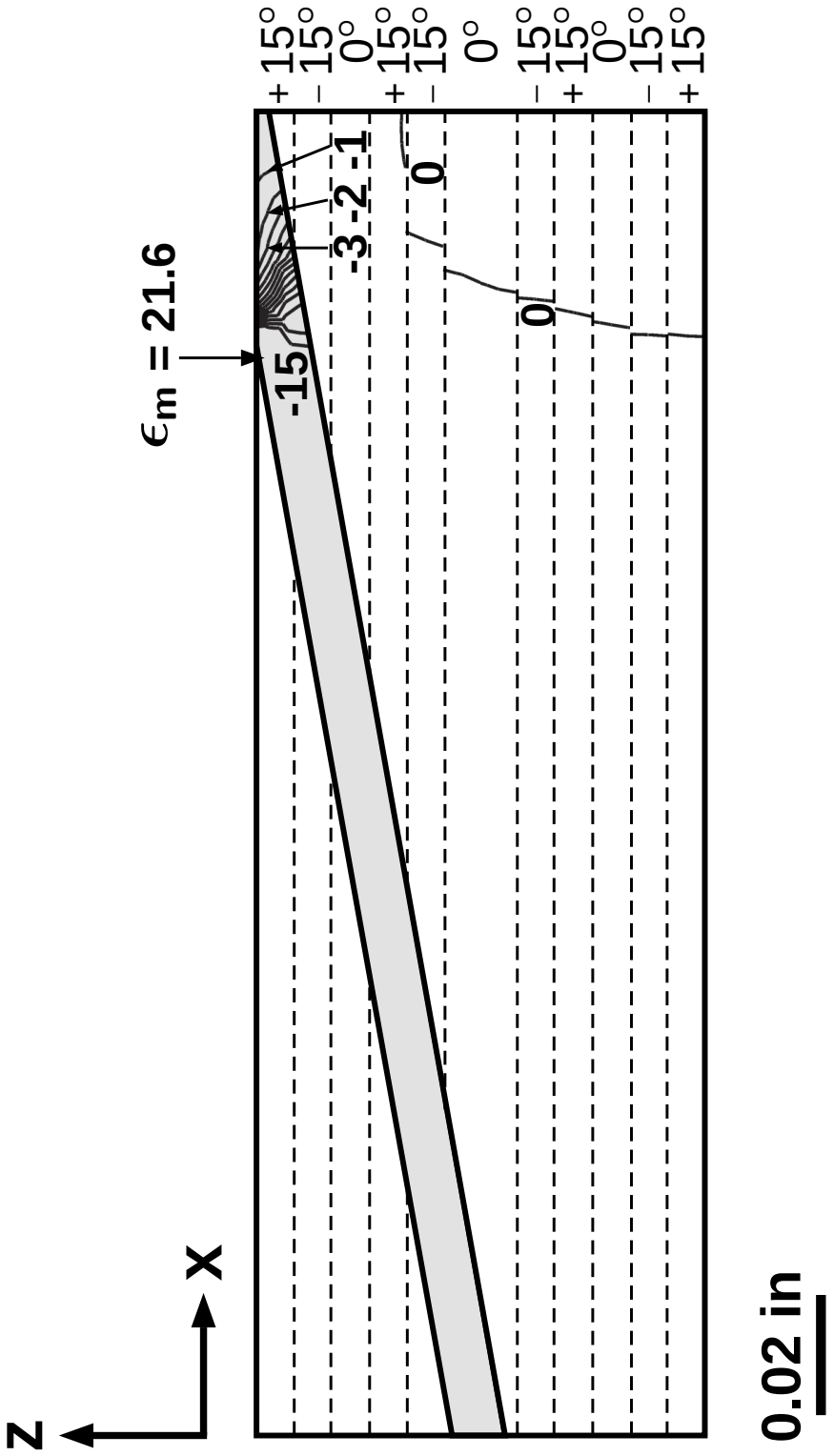

Figure B.47 Normalized isostrain contour field plot of ϵ_{13} for the two-dimensional composite scarf joint with equal scarf angles of 10°, adhesive thickness of 0.008 in, and laminate configuration of $[\pm 15/0]_{2S}$.

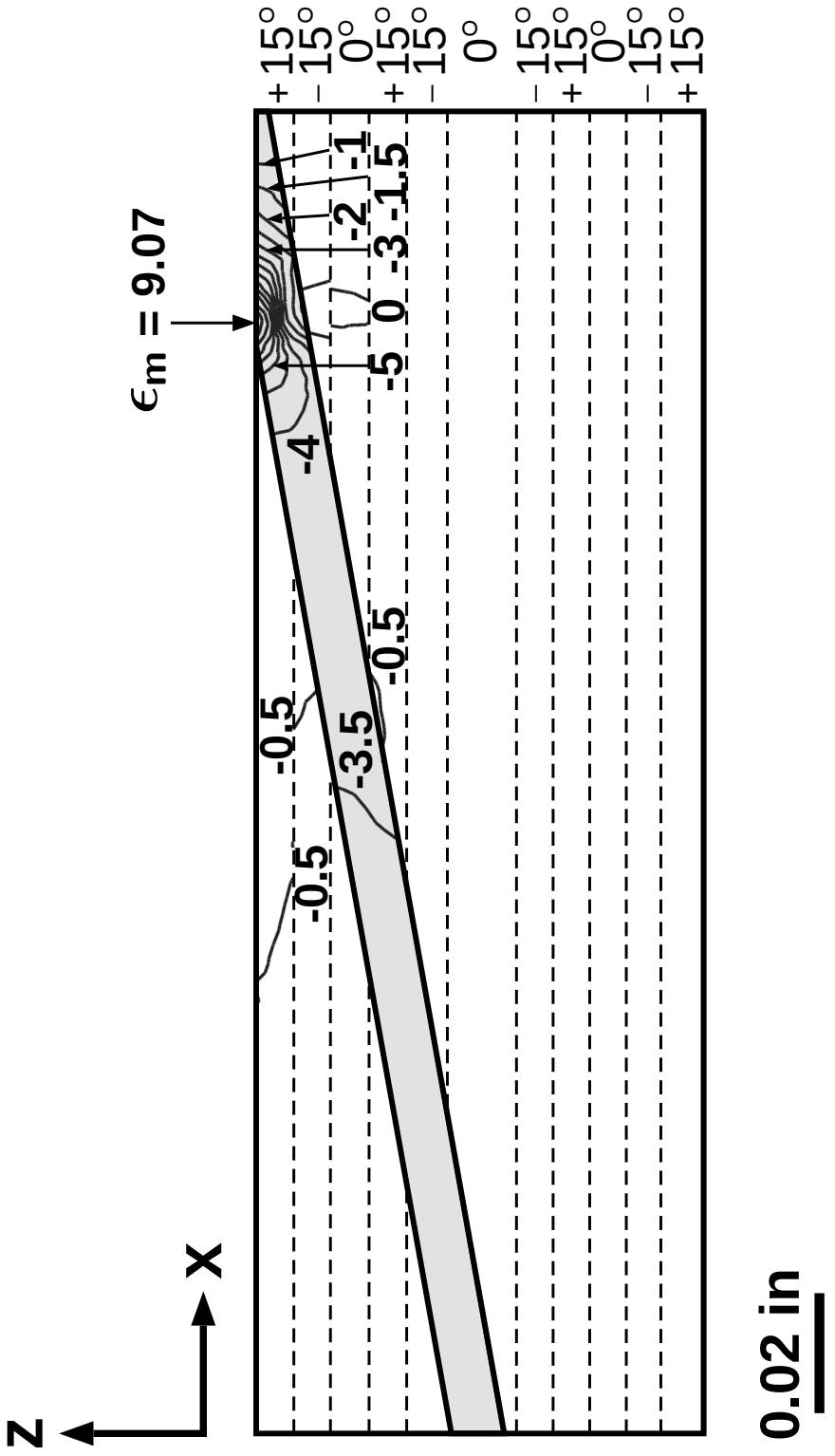

Figure B.48 Normalized isostrain contour field plot of ϵ_{33} for the two-dimensional composite scarf joint with equal scarf angles of 10°, adhesive thickness of 0.008 in, and laminate configuration of $[\pm 15/0]_{2S}$.

Appendix C

Equilibrium Considerations in the Adhesive

As discussed in Section 6.1, the macroscopic equilibrium along any x_j-axis in the adhesive, particularly along the bondline, is a key consideration in establishing the mechanics of the response and the associated load transfer mechanisms. The specifics of this equilibrium formulation are presented in this appendix.

The equilibrium of differential triangular elements in the adhesive along an arbitrary x_j-axis for an arbitrary x_j-y plane of unit width in the y-direction is considered. The schematic for one such differential triangular element in the x-z (or 1-3) plane located along the bondline in the adhesive is illustrated in Figure C.1. The differential length, dx_j, denotes the length of the hypotenuse of the differential triangular element along the bondline. The differential forces acting on the faces of this element in the 1-direction and the 3-direction are denoted by dF_1 and dF_3, respectively. The associated differential lengths of the horizontal (normal to the 3-direction) and vertical (normal to the 1-direction) edges of the differential triangular element are related to the scarf angle of the configuration, α, as $dx_j \cos\alpha$ and $dx_j \sin\alpha$, respectively.

The expressions for the net resultant forces in the 1-direction and the 3-direction acting on the x_j-y plane, of unit width in the y-direction, are obtained by integrating the expressions for each of the differential forces along the length of the x_j-axis, $[t_{adherend}/\sin\alpha]$, which is also the length of the bondline. The expressions for these

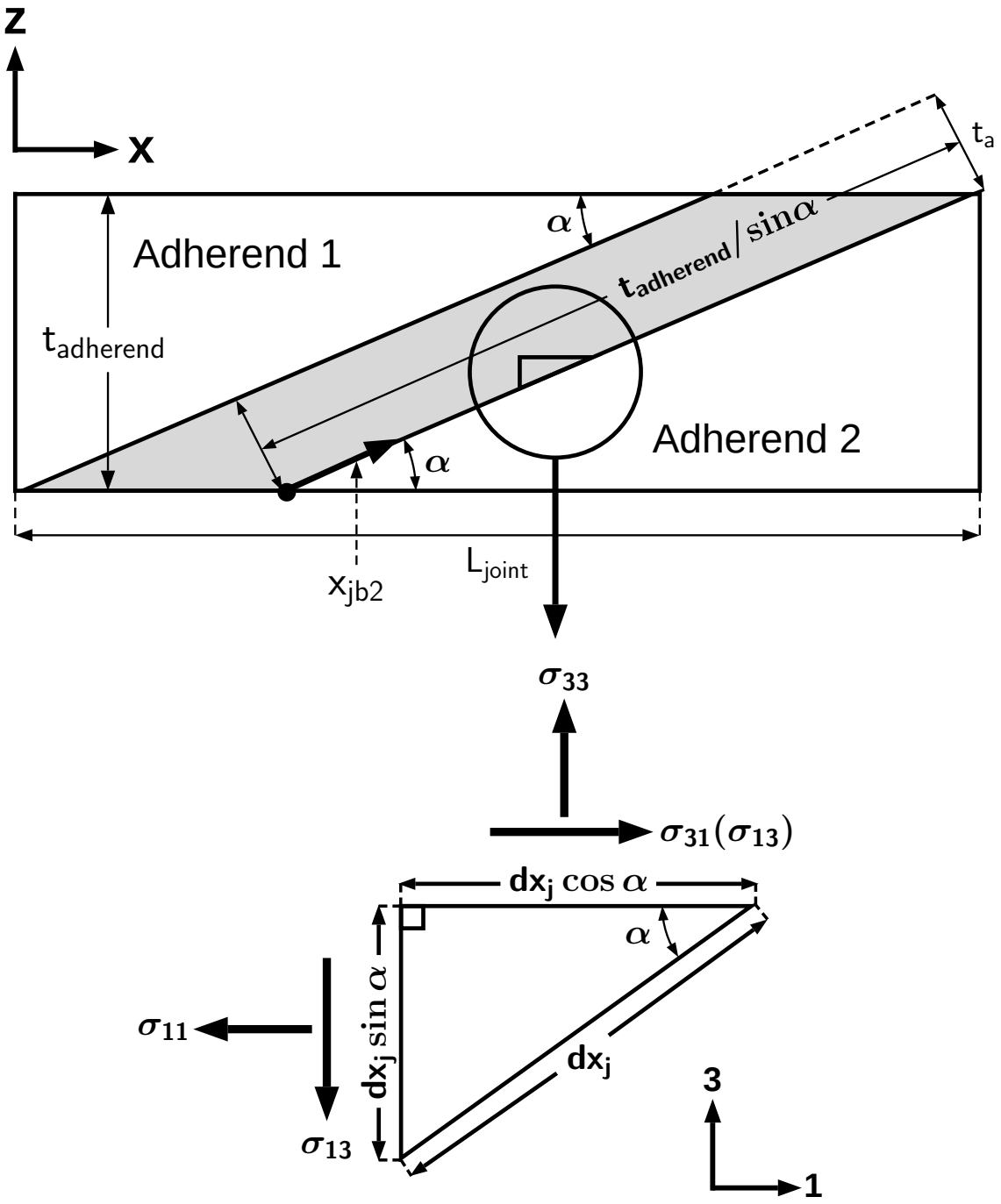

Figure C.1 Equilibrium schematic of a differential triangular element located along the bondline in the adhesive of a two-dimensional composite scarf joint.

differential forces depend on the stresses acting in those directions, and on the scarf angle of the configuration through the differential lengths of the edges:

$$\mathrm{d}F_1 = -\sigma_{11}(\mathrm{d}x_j \sin\alpha) + \sigma_{13}(\mathrm{d}x_j \cos\alpha), \tag{C.1}$$

$$\mathrm{d}F_3 = -\sigma_{13}(\mathrm{d}x_j \sin\alpha) + \sigma_{33}(\mathrm{d}x_j \cos\alpha). \tag{C.2}$$

Taking the integral along the length of the $\mathrm{x_j}$-axis, $[\mathrm{t_{adherend}}/\sin\alpha]$, yields macroscopic equilibrium relations for the net longitudinal and transverse forces. These equilibrium relations for the net longitudinal and transverse forces must be equal and opposite to the equivalent far-field conditions of pure extensional load in the 1-direction, and no load in the 3-direction:

$$F_1 = \int_0^{\frac{\mathrm{t_{adherend}}}{\sin\alpha}} [\sigma_{11}(x_j)\sin\alpha - \sigma_{13}(x_j)\cos\alpha]\,\mathrm{d}x_j = \int_0^{\mathrm{t_{adherend}}} \sigma_{11}^{\infty}(z)\,\mathrm{d}z, \tag{C.3}$$

$$F_3 = \int_0^{\frac{\mathrm{t_{adherend}}}{\sin\alpha}} [\sigma_{13}(x_j)\sin\alpha - \sigma_{33}(x_j)\cos\alpha]\,\mathrm{d}x_j = 0. \tag{C.4}$$

The resulting equilibrium Equation C.3 for the net longitudinal force can also be expressed in terms of the corresponding strain components by using the constitutive relations for plane strain:

$$\begin{pmatrix} \sigma_{11} \\ \sigma_{33} \\ \sigma_{13} \end{pmatrix} = \lambda \begin{pmatrix} 1-\nu & \nu & 0 \\ \nu & 1-\nu & 0 \\ 0 & 0 & 1-2\nu \end{pmatrix} \begin{pmatrix} \epsilon_{11} \\ \epsilon_{33} \\ \epsilon_{13} \end{pmatrix}, \tag{C.5}$$

where E and ν are the Young's modulus and Poisson's ratio of the adhesive, and the constant λ relates to these via:

$$\lambda = \frac{\mathrm{E}}{(1+\nu)(1-2\nu)}. \tag{C.6}$$

This results in the following expression for the net longitudinal force:

$$F_1 = \int_0^{\frac{t_{adherend}}{\sin\alpha}} [\lambda(1-\nu)\epsilon_{11}(x_j)\sin\alpha - \frac{E}{1+\nu}\epsilon_{13}(x_j)\cos\alpha + \lambda\nu\epsilon_{33}(x_j)\sin\alpha]dx_j. \quad (C.7)$$

This is worked to give:

$$F_1 = A\int_0^{\frac{t_{adherend}}{\sin\alpha}} \epsilon_{11}(x_j)\,dx_j + B\int_0^{\frac{t_{adherend}}{\sin\alpha}} \epsilon_{13}(x_j)\,dx_j + C\int_0^{\frac{t_{adherend}}{\sin\alpha}} \epsilon_{33}(x_j)\,dx_j, \quad (C.8)$$

where:

$$A = \lambda(1-\nu)\sin\alpha, \quad (C.9)$$

$$B = -\frac{E}{1+\nu}\cos\alpha, \quad (C.10)$$

$$C = \lambda\nu\sin\alpha. \quad (C.11)$$

The constants E, ν, λ, A, B, and C are the same for any x_j-axis for a given scarf angle in the adhesive.

As discussed in Section 6.1, the longitudinal load transmitted across any x_j-y plane of unit width in the y-direction must be the same for mechanical equilibrium to hold. Thus, for two different x_j-axes in the adhesive, x_{jb2} and x_{jm}, the areas bounded by the (normalized) distributions of strains, $\epsilon_{ij}(x_j)$, must be approximately equal for all configurations having similar effective longitudinal adherend stiffness, and thus similar average far-field longitudinal strain, ϵ_{11}^{∞}, thereby indicating equality of load transfer. This is expressed as:

$$\int_0^{\frac{t_{adherend}}{\sin\alpha}} \epsilon_{ij}(x_{jb2})\,dx_{jb2} = \int_0^{\frac{t_{adherend}}{\sin\alpha}} \epsilon_{ij}(x_{jm})\,dx_{jm}. \quad (C.12)$$

This also holds true when comparing distributions of normalized strains in the adhesive along similar x_j-axes, x_{jb2} or x_{jm}, for two or more different configurations that have similar effective longitudinal adherend stiffness. These aspects are exhibited

in all distributions of strains along the bondline and the midline in the adhesive in Section 5.1 for the different configurations of adherend investigated in this work.

The equilibrium Equations C.3 and C.4 thus indicate the specific dependence of the decomposition of the in-plane state of stress along an arbitrary x_j-axis, associated with the scarf angle of a two-dimensional composite scarf joint configuration, α.

References

[1] The Boeing Company, "787 Dreamliner - Program Fact Sheet." http://www.boeing.com/commercial/787family/background.html, 2011.

[2] W. R. Broughton, L. E. Crocker, and M. R. L. Gower, "Design Requirements for Bonded and Bolted Composite Structures," NPL Report MATC(A)65, NPL Materials Centre, National Physical Laboratory, Teddington, Middlesex, UK, January 2002.

[3] S. M. Spearing, P. A. Lagacé, and H. L. N. McManus, "On the role of lengthscale in the prediction of failure of composite structures: Assessments and needs," *Applied Composite Materials*, vol. 5, pp. 139–149, May, 1998.

[4] D. W. Adkins and R. B. Pipes, "End effects in scarf joints," *Composites Science and Technology*, vol. 22, pp. 209–221, 1985.

[5] F. Erdogan and M. Ratwani, "Stress Distribution in Bonded Joints," *Journal of Composite Materials*, vol. 5, pp. 378–393, 1971.

[6] M. N. Reddy and P. K. Sinha, "Stresses in Adhesive-bonded Joints For Composites," *Fiber Science and Technology*, vol. 8, pp. 33–47, 1975.

[7] O. Volkerson, "Die Nietkraftverteilung in Zugbeanspruchten Nietverbindungen Mit konstanten Laschenquerschnitten," *Luftfahrtforschung*, vol. 15, pp. 41–47, 1938.

[8] S. Marcolefas, V. Kostopoulos, and S. A. Paipetis, "Non-linear Analysis of a Metal-to-composite Scarf Joint," *Int. J. Mech. Sci.*, vol. 33, pp. 961–973, 1991.

[9] D. M. Gleich, "Stress Analysis of Structural Bonded Joints," Master's thesis, Imperial College, 2002.

[10] A. J. Gunnion and I. Herzberg, "Parametric Study of Scarf Joints in Composite Structures," *Composite Structures*, vol. 75, pp. 364–376, 2006.

[11] C. H. Wang and A. J. Gunnion, "On The Design Methodology of Scarf Repairs to Composite Laminates," *Composites Science and Technology*, vol. 68, pp. 35–46, 2008.

[12] A. B. Harman and C. H. Wang, "Improved Design Methods For Scarf Repairs to Highly Strained Composite Structures," *Composite Structures*, vol. 75, pp. 132–144, 2006.

[13] T. Breitzman, E. Iarve, B. Cook, G. Schoeppner, and R. Lipton, "Optimization of a Composite Scarf Repair Patch Under Tensile Loading," *Composites: Part A*, vol. 40, pp. 1921–1930, 2009.

[14] S. B. Kumar, S. Sivashanker, A. Bag, and I. Sridhar, "Failure of Aerospace Composite Scarf Joints Subjected to Uniaxial Compression," *Materials Science and Engineering A*, vol. 412, pp. 117–122, 2005.

[15] S. B. Kumar, I. Sridhar, S. Sivashanker, S. Osiyemi, and A. Bag, "Tensile Failure of Adhesively Bonded CFRP Composite Scarf Joints," *Materials Science and Engineering B*, vol. 132, pp. 113–120, 2006.

[16] Z. Hashin, "Failure Criteria for Unidirectional Fiber Composites," *Journal of Applied Mechanics*, vol. 47(2), pp. 329–334, 1980.

[17] J. D. Lee, "Three-Dimensional Finite Element Analysis of Damage Accumulation in Composite Laminate," *Computers and Structures*, vol. 15(3), pp. 335–350, 1982.

[18] J. Goh, S. Georgiadis, A. Orifici, and C. Wang, "Effects of Bondline Flaws on The Damage Tolerance of Composite Scarf Joints," *Composites: Part A*, vol. 55, pp. 110–119, 2013.

[19] M. Kim, D. Elder, C. Wang, and S. Feih, "Interaction of Laminate Damage and Adhesive Disbonding in Composite Scarf Joints Subjected to Combined In-plane Loading And Impact," *Composite Structures*, vol. 94, pp. 945–953, 2012.

[20] H. Kawakami and P. Feraboli, "Lightning Strike Damage Resistance and Tolerance of Scarf-repaired Mesh-protected Carbon Fiber Composites," *Composites: Part A*, vol. 42, pp. 1247–1262, 2011.

[21] Y. Jen, "Fatigue Life Evaluation of Adhesively Bonded Scarf Joints," *International Journal of Fatigue*, vol. 36, pp. 30–39, 2012.

[22] R. D. S. G. Campilho, M. F. S. F. de Moura, A. M. G. Pinto, J. J. L. Morais, and J. J. M. S. Domingues, "Modelling The Tensile Fracture Behavior of CFRP Scarf Repairs," *Composites Part B: Engineering*, vol. 40, pp. 149–157, 2009.

[23] A. M. G. Pinto, R. D. S. G. Campilho, M. F. S. F. de Moura, and I. R. Mendes, "Numerical Evaluation of Three-dimensional Scarf Repairs in Carbon-epoxy Structures," *International Journal of Adhesion and Adhesives*, vol. 30, pp. 329–337, 2010.

[24] C. H. Wang and A. J. Gunnion, "Optimum Shapes of Scarf Repairs," *Composites Part: A*, vol. 40, pp. 1407–1418, 2009.

[25] A. Kimiaeifar, H. Toft, E. Lund, O. T. Thomsen, and J. D. Sorensen, "Reliability Analysis of Adhesive Bonded Scarf Joints," *Engineering Structures*, vol. 12, pp. 281–287, 2012.

[26] Cytec Engineered Materials, "FM® 300-2 Film Adhesive Technical Data Sheet." http://www.cemselectorguide.com/pdf/FM_300-2_092711.pdf, 2011.

[27] J. T. J. Sherraden, W. Seneviratne, and K. S. Raju, "A- Basis and B-Basis Design Allowables for Epoxy-Based Prepreg Toray T700GC-12K-31E 2510 Unidirectional Tape [US Units]," Advanced General Aviation Transport Experiments AGATE-WP3.3-033051-132, National Institute for Aviation Research, National Institute for Aviation Research Wichita State University Wichita, KS 67260-0093, November 2002.

[28] P. A. Lagacé, "Delamination in composites: Is toughness the key?," *SAMPE Journal*, vol. 22, pp. 53–60, November/December, 1986.

[29] Dassault Systémes, Simulia Corp., *Abaqus/CAE User's Manual v6.11*, 2011.

[30] J. S. Iqbal, "Response of Grooved Composite Laminates to Out-of-Plane Contact Loading via Numerical Models," Master's thesis, Massachusetts Institute of Technology, 2011.

[31] M. J. Donough, A. J. Gunnion, A. C. Orifici, and C. H. Wang, "Critical Assessment of Failure Criteria for Adhesively Bonded Composite Repair Design," *28th International Congress of the Aeronautical Sciences*.

[32] C. Shih-Pin, *Role of Delamination and Interlaminar Fatigue in the Failure of Laminates With Ply Dropoffs*. Ph.d., Massachusetts Institute of Technology, 2002.